UCRL-53945
Distribution Category UC-701

UCRL--53945
DE90 008015

Time-Dependent Failure of Silver Interlayer Welds

Robert S. Rosen

(Ph.D. Thesis)

Manuscript date: February 1990

LAWRENCE LIVERMORE NATIONAL LABORATORY
University of California • Livermore, California • 94551

ABSTRACT

Silver interlayer diffusion welds exhibit very high tensile strengths, despite the soft interlayer, because of the constraint provided by the stronger base metals. However, despite the high tensile strength, diffusion-welded-silver joints undergo time-dependent failure, or creep rupture at relatively low tensile stresses at ambient temperature, apparently by a ductile microvoid-coalescence mechanism at the coated and welded interfaces. Two classes of time-dependent tensile failure were investigated. In the first case, the applied stress does not produce any plastic deformation in the base metal, and rupture appears to be controlled by time-dependent plasticity within the silver interlayer as a result of the effective stress in the interlayer. The plasticity causes cavity nucleation and, eventually, coalescence and rupture. In the second case, time-dependent plasticity is observed in the base metals, and concomitant shear occurs within the soft silver interlayer under a high triaxial stress state. Here, the time-dependent plasticity of the base metal accelerates rupture. These models were substantiated by analyses of the stress and temperature dependence of the rupture times, finite-element analysis of the stress state within the interlayer, and microscopy of the fracture surfaces and interfaces loaded to various fractions of the expected rupture times. The procedures for preparing silver interlayers by planar-magnetron sputtering were developed in this research. This process was preferred over other interlayer fabrication methods, such as brazing, electrodeposition, and other physical vapor deposition processes, because of the more reproducible results obtained using planar-magnetron sputtering. The findings of this research, however, are applicable to joints in which the interlayers are prepared by these and other processes.

ACKNOWLEDGMENTS

I would like to dedicate this dissertation to my wife, Cindy, and to our children: Scott, Jay, and Kelsey; they have endured many sacrifices during my graduate studies. I would also like to express my sincerest appreciation to Professor Mike Kassner for the invaluable guidance he provided me with throughout this project. In addition, I would like to thank Greg Henshall for performing the finite-element analysis and for the many thoughtful discussions we held during this project. Finally, I would like to acknowledge the valuable contributions of Leroy Schrawyer for preparing coated specimens for diffusion welding, Mark Wall for performing transmission electron microscopy of the coated and diffusion-welded interlayers, and the National Center for Electron Microscopy at Lawrence Berkeley Laboratory for use of the 1.5 MeV High Voltage Electron Microscope. There are many other people who have contributed their efforts toward this project and toward the preparation of this dissertation. For each and every one who has helped me along the way, I thank you. This work was performed under the auspices of the U.S. Department of Energy by Lawrence Livermore National Laboratory under contract W-7405-Eng-48.

TABLE OF CONTENTS

LIST OF TABLES

LIST OF FIGURES

(Unless otherwise noted, micrographs shown were taken using scanning electron microscopy).

CHAPTER 1
INTRODUCTION

1.1. Background

1.1.1. Diffusion-Welded Interlayers

The utilization of metal interlayers for diffusion welding has been reported by numerous investigators. This joining method may be appropriate when brittle intermetallic compound formation, differential thermal contraction during cooling, or oxide dissociation and dissolution temperatures preclude conventional methods such as fusion welding, brazing, and direct diffusion welding of the base metals. An interlayer can be in the form of a foil,[1–4] or it can be applied to one or both of the base-metal surfaces by various coating methods (e.g., electrodeposition,[1,2,4,5] plasma spraying,[2] or vapor-deposition methods). Methods utilizing coated interlayers require a two-step joining procedure (coating and welding) as opposed to joints fabricated with foil interlayers, which may only require a single diffusion-welding step. However, methods utilizing coated interlayers have the advantage over foil interlayers in not requiring diffusion welding at the interlayer-base-metal interface. Diffusion welding of some interlayer-base-metal combinations may require high temperatures and/or pressures, due to the high dissociation temperatures of the surface oxides, which may preclude or restrict the use of foil interlayers.[6–8]

Various base-metal combinations have been diffusion welded using coated silver as the interlayer metal. The principal advantage of silver as an interlayer for diffusion welding is that high-strength joints can be fabricated at relatively low temperatures (473–673 K) and pressures (100–200 MPa) due to the low dissociation temperature (<460 K) for silver oxide. Depending on the strength of the base metals and the method (hydrostatic or uniaxial stress) by which pressure is applied to the silver-silver interface, the joining process may result in little or no deformation in the base metals.

Silver interlayers for diffusion welding are usually applied to one or both of the base metals by deposition using electrodeposition[9–12] or vacuum-coating methods. The vacuum-coating methods have included electron beam evaporation,[13] hot-hollow cathode (HHC) evaporation,[11,14–21] and ion-plating using sputtering.[22–24] Prior to deposition, the surface oxide layer may require removal from the base metal so as to achieve adequate adhesion of the silver. The surface oxide layer is usually removed by chemical- or sputter-etching methods. One advantage of vacuum coating over electrodeposition is the ability to sputter-etch the base metal *in situ* . This permits silver deposition with minimal oxygen re-contamination of the base-metal surface.[25]

1.1.2. Creep Rupture of Interlayer Joints

It has long been known that thin (e.g., 1 μm - 1 mm) interlayer welds, or brazes between stronger base materials may have high ultimate tensile or rupture strengths despite the relatively low strength of the filler metal.[26–28] The high strength of the joint results from the mechanical constraint provided by the (plastically) nondeforming base metals, which restricts transverse contraction of the interlayer. The constraint produces a triaxial state of stress and reduces the effective (von Mises) stress thus reducing the tendency for the joint to plastically deform.[26–28] The degree of mechanical constraint in the joint is generally known to increase with decreasing thickness-to-diameter ratio (t/d) of the interlayer.[26–39] Other factors, such as plasticity of the base metal, reduce the constraint.[36] Higher joint strength is associated with higher constraint.

Recent work[20,21,40] has verified an earlier observation[41] of time-dependent tensile failure, or creep rupture of diffusion-welded-interlayer joints at stresses substantially less than the ultimate tensile strength (UTS). In the first study,[41] Co-alloy and Ni-alloy foils were utilized as interlayers to join thoria-dispersed-nickel for high-temperature (1311–1477 K) application. Results showed that creep rupture occurred at stress levels at about 25% UTS when the joints were tested at 1366 K. Although fracture occurred within

the interlayer or at one of the interlayer-base-metal interfaces, base-metal creep plasticity was reported to occur at this test temperature. Creep ruptures times, ranging from several minutes to several days, were found to increase with decreasing applied stress.[41]

In another study,[20,40] diffusion-welded-silver interlayers between uranium and type 304 stainless steel base metals, prepared using hot-hollow-cathode vapor-deposition, were tested in tension to determine the ambient- and near ambient-temperature creep-rupture properties. Results showed that creep rupture of the silver occurred at stress levels as low as 50% UTS when the joints were tested from 269–345 K. Creep rupture times, ranging from several hours to several months, were found to increase substantially with decreasing applied stress or test temperature. Creep rupture fracture surfaces exhibited classic ductile microvoid coalescence in the vicinity of the diffusion-welded-silver (silver-silver) interface, and also evidence of plasticity at the silver-base-metal interfaces. The investigators suggested[20,40] that the rate-controlling mechanism of creep rupture is the nucleation of cavities by creep deformation within the silver interlayer.

In a more recent study,[21] further testing of diffusion-welded-silver interlayers between uranium and type 304 stainless steel, prepared identically to those of the previous study, was performed to compare the tensile creep-rupture behavior to that of the torsional behavior. The preliminary conclusions indicated that the ambient-temperature time-dependent plasticity or creep of the base metals (e.g., to plastic strains of about 0.01 or less) under tensile stresses relieves the interlayer constraint, and the joint strength may be correspondingly degraded. That is, base-metal creep induces concomitant shear within the interlayer under a state of high triaxial stress that causes ductile failure within the interlayer. Failure occurs after relatively small plastic strains, at the center-plane of the interlayer or near the interlayer-base-metal interfaces. Therefore, the creep rate of the base metal is believed to control the rupture time of joints loaded in tension. An analysis of torsional creep-rupture tests showed that the rate-controlling mechanism for torsional failure is steady-state creep plasticity in the silver interlayer. The creep-rupture phenomenon for the

general case of diffusion-welded interlayers utilizing elastic or nonplastically deforming base metals was not investigated.

1.2. Objectives

In this study, dc planar-magnetron (PM) sputtering (also known as magnetically enhanced sputtering) has been used to deposit silver interlayers on various base metals for subsequent diffusion welding. Sputtering is a vacuum process whereby atoms are ejected from a cathode surface as the result of bombardment by an ionized gas. Sputter-coating is the use of this process to deposit a film onto a substrate in vacuum. Planar-magnetron sputtering, described in detail elsewhere,[42] consists of a planar cathode (silver target from which atoms are ejected) with permanent magnets arrayed behind the cathode to confine the glow-discharge plasma (argon ions) directly in front of the silver-target surface. This design results in a high-rate sputtering source that can deposit thick coatings onto the substrate (base-metal) surface. Additionally, a separately-controlled dc power supply has been used to sustain a second glow-discharge plasma that sputter-etches the negatively-biased substrate prior to deposition.

The purposes of this work were as follows. First, the microstructural and mechanical properties of PM sputter-deposited silver interlayers used for diffusion welding were evaluated and compared with results previously reported using other types of silver interlayer methods (HHC deposition, electrodeposition, brazing, foils, etc.). Second, the validity of the "base-metal controlled" theory of creep rupture of diffusion-welded-silver joints between plastic base materials was checked. Creep rupture tests were performed on diffusion-welded-silver joints between stainless steel base metals fabricated using PM sputter-deposition. These specimens were loaded below the UTS to various applied tensile stresses. The creep rates of the base metals and the silver interlayer would be measured. There should be some correspondence between these creep rates if a base-metal controlled theory of creep rupture of diffusion-welded-silver joints is viable. The role of plastic base

metals in the fracture process was further investigated by conducting creep rupture tests of diffusion-welded-silver joints between stainless steels of different yield strengths. The base-metal control theory predicts that the rupture times should be related to the base-metal strength. This is because higher strength is associated with lower creep rates in the base metal and lower corresponding creep rates within the interlayer, thus, longer times-to-rupture, t_r.

Third, a determination was made as to whether creep rupture occurs in diffusion-welded-silver joints between elastic base metals, which do not show evidence of time-dependent plasticity over the range of applicable stresses. This question is particularly relevant as this may be the most common case for metals, ceramics, and composites during service. Again, ambient and near-ambient temperature creep rupture tests were performed at a variety of stresses below the UTS of the joint. A determination of the mechanism would be attempted for the case in which creep rupture is observed. Such a determination would include analyses of the stress and temperature sensitivity of the rupture time, an analysis of the fracture surface using scanning electron microscopy (SEM), and transmission electron microscopy (TEM) and microscopy of the interfaces unloaded after various fractions of the expected creep-rupture time, $t_{r,exp}$. Fourth, a determination was made as to whether creep rupture occurs in joints fabricated using interlayers prepared by processes other than physical vapor deposition, such as electrodeposition and brazing. These results would be used to confirm the general application of a failure mechanism to interlayer joints between various base metals independent of fabrication method. The existence of a general theory of creep rupture of interlayers is particularly relevant because joints fabricated by brazing far outnumber those fabricated by diffusion welding of either coatings or foils.

CHAPTER 2
EXPERIMENTAL PROCEDURES

2.1. Base-Metal Specimen Fabrication

2.1.1. Materials

Specimens to be silver-coated, joined, and tested to determine ultimate tensile strengths were fabricated from the following base metals: (1) maraging steel (A538 Grade C; nominally 18% Ni, 9% Co, 5% Mo), (2) type 304 (UNS S30400) stainless steel (SS), (3) type 316 (UNS S31600) SS, (4) depleted uranium (0.3% U^{235}), and (5) 8091 aluminum alloy (nominally 2.5% Li, 2.0% Cu, 0.8% Mg). Additional specimens to be silver-coated, joined, and tested to determine torsional strength were fabricated from maraging steel base metals. The maraging and stainless steels, readily weldable using conventional fusion welding methods, were selected to determine the behavior of silver interlayer welds using elastic and plastic base metals. Uranium and Al-Li alloy were selected as base metals for silver interlayer diffusion welding in order to utilize this process on materials which are difficult to weld using conventional methods. The thermal history and yield stresses of the various base metals are listed in Table 2.1.

Table 2.1. Base-metal properties.

Base Metal	Thermal History	Tensile Yield Stress[a]
Maraging steel	Aged at 873 K for 5 h	1518 MPa
Type 304 stainless steel	Annealed at 1323 K for 2 h	221 MPa
Type 304 stainless steel	Cold-worked	359 MPa
Type 316 stainless steel	Cold-drawn	745 MPa
Uranium (depleted)	Quenched from 998 K; annealed at 823 K for 4 h	241 MPa
8091 aluminum alloy	As-cast	269 MPa

[a] Determined using a 0.2 percent plastic strain offset at a strain rate of ~3×10^{-4} s^{-1}.

Specimens to be silver-coated, joined, and tested to determine creep rupture properties were fabricated from the following base metals: (1) maraging steel and (2) type 304 SS (annealed and cold-worked). Maraging steel is an ultrahigh-strength steel which exhibits only elastic deflections over the relevant range of applied stress (less than 760 MPa). This was confirmed from strain-gage testing of a maraging steel tensile specimen stressed to 758 MPa, which was found to exhibit less than 10^{-6} plastic strain (detectability limit) in 10^6 s. However, time-dependent plasticity or ambient-temperature creep is observed in the stainless steels at these stresses, even when significantly below the yield stresses.[43] The base-metal chemical analyses for maraging and type 304 stainless steels are listed in Table 2.2. Base-metal specimens to be coated with electrodeposited silver, diffusion welded, and tested to determine the creep rupture properties, were fabricated from hot-rolled type 304 stainless steel (as-received condition, σ_y = 296 MPa) and depleted uranium (σ_y = 354 MPa). The base-metal properties and chemical analyses are given elsewhere.[20–40]

The annealing and cold working of type 304 SS was accomplished prior to machining into specimens to be coated. The procedures for obtaining two sets of different strength material from the single heat (composition) were as follows. Some of the as-received 25.4-mm-diameter SS bars were sectioned into 813-mm lengths for annealing in a vacuum furnace. The remaining material was machined into 19.05-mm-diameter and 762-mm-long reduced- (or gage-) section threaded-end specimens (889 mm overall length). These long tensile rods (shown in Fig. 2.1) were then prestressed to 365 MPa at a crosshead rate of 12.7 mm per min. Figure 2.2 shows the (a) annealed type 304 SS, (b) cold-worked type 304 SS, and (c) maraging steel microstructures, viewed optically with polarized light.

2.1.2. Tensile Specimens for Base-Metal Properties Tests

Standard 6.35-mm-diameter and 25.4-mm-long reduced- (or gage-) section, threaded-end specimens (77.7 mm overall length) were machined from the base-metal bars for

Table 2.2. Base-metal chemical analyses.

	Weight Percent[a]	
Element	**Maraging Steel**	**Type 304 SS**
C	0.014	0.06
Si	0.06	0.46
Mn	0.01	1.23
S	0.001	0.020
P	0.002	0.025
Cu	0.12	0.25
Cr	0.08	18.37
Mo	4.85	0.30
Co	9.35	0.07
Ni	18.35	9.05
Al	0.11	
Ti	0.65	
W	0.01	
B	0.002	
Zr	0.012	
Ca	0.05	
N		0.042
Fe	Balance	Balance

[a] From manufacturer's chemical test report.

determination of mechanical properties. The gage section was ground to ±1.3 μm diametral tolerance. Figure 2.3 shows the standard tensile specimen configuration. Stress-strain behavior was determined using two strain gages (350 ohms, 2.14 gage factor, 5% maximum strain) placed 180 degrees apart to average the displacement data. Figure 2.4 shows the stress-strain behavior of the (a, b) annealed and (c) cold-worked type 304 stainless steels used in this study. Additionally, creep behavior of the type 304 stainless steels was determined by loading the base-metal tensile specimens in simple lever dead-weight type creep rupture testing machines to the desired stress level, and measuring the average strain versus time using the strain gages.

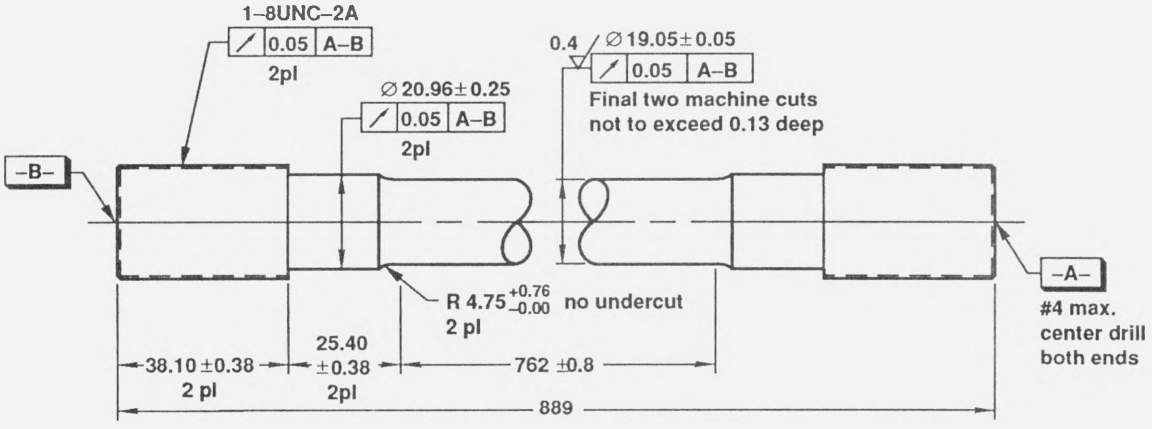

Figure 2.1. Long tensile bar utilized to obtain cold-worked type 304 stainless steel. Bars were loaded (prestressed) to 365 MPa prior to machining specimens out of them.

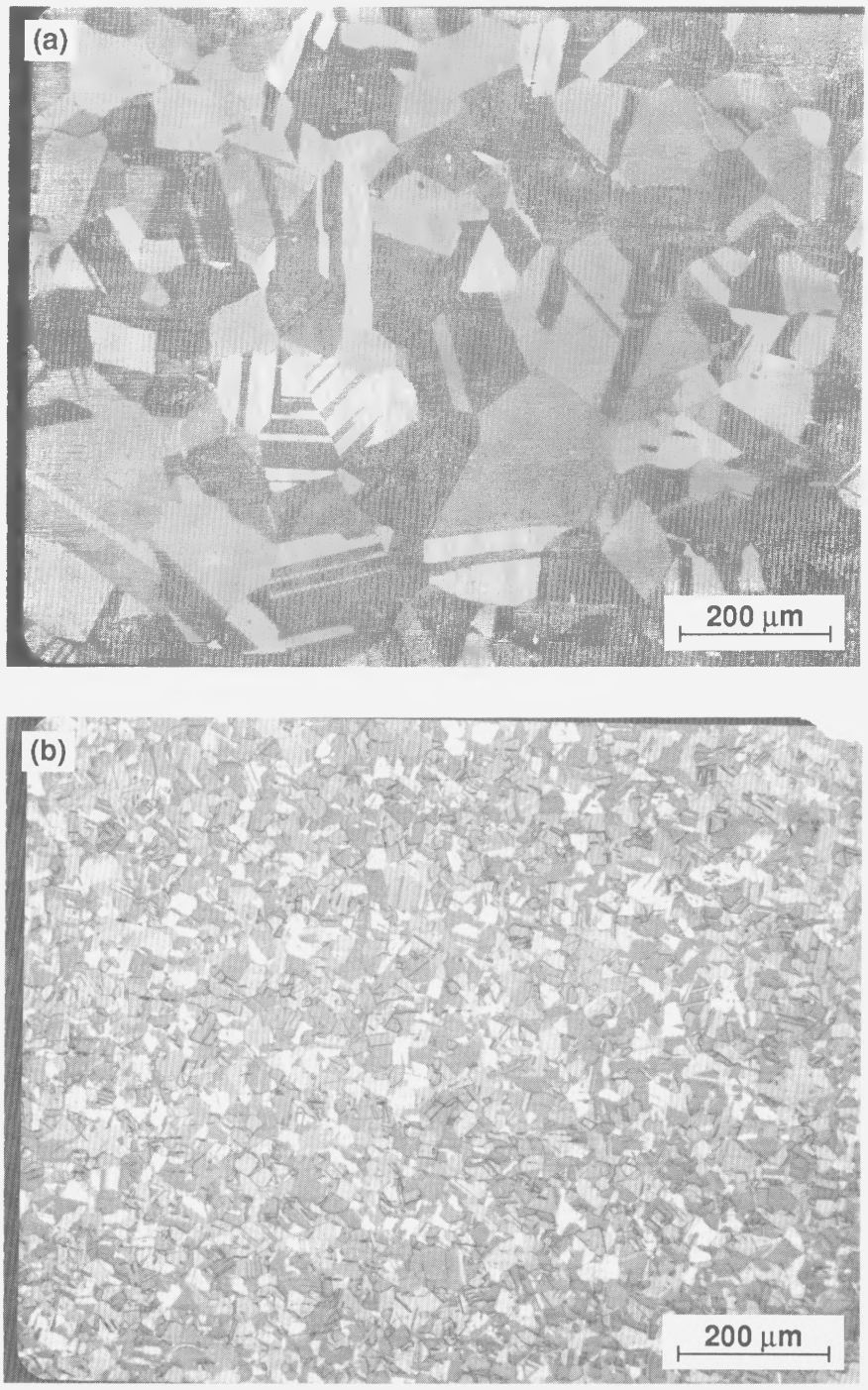

Figure 2.2. Optical micrographs showing microstructures of (a) annealed and (b) cold-worked type 304 stainless steel base metals.

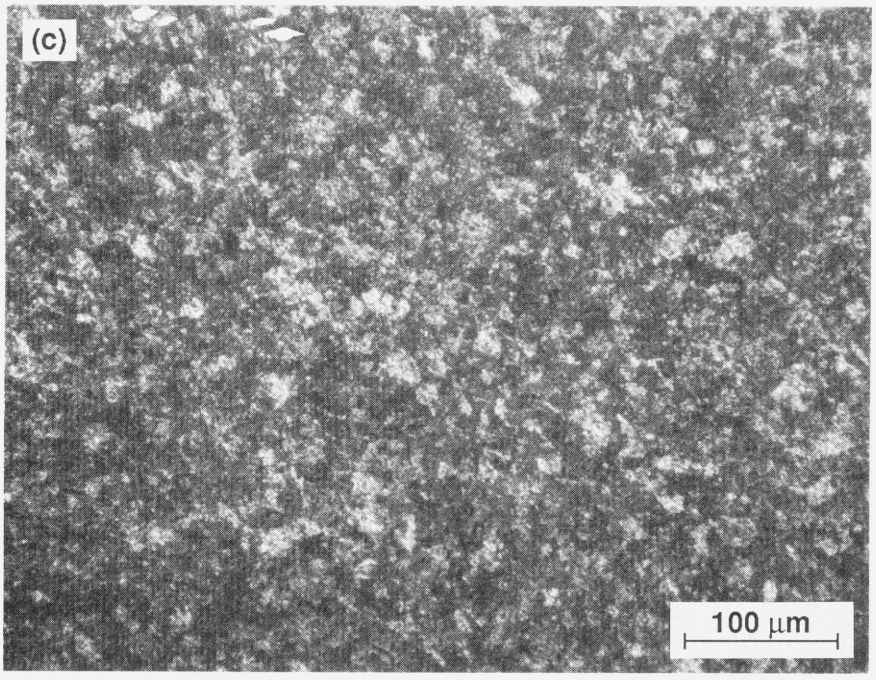

Figure 2.2. (c) Optical micrograph showing the microstructure of maraging steel base metal.

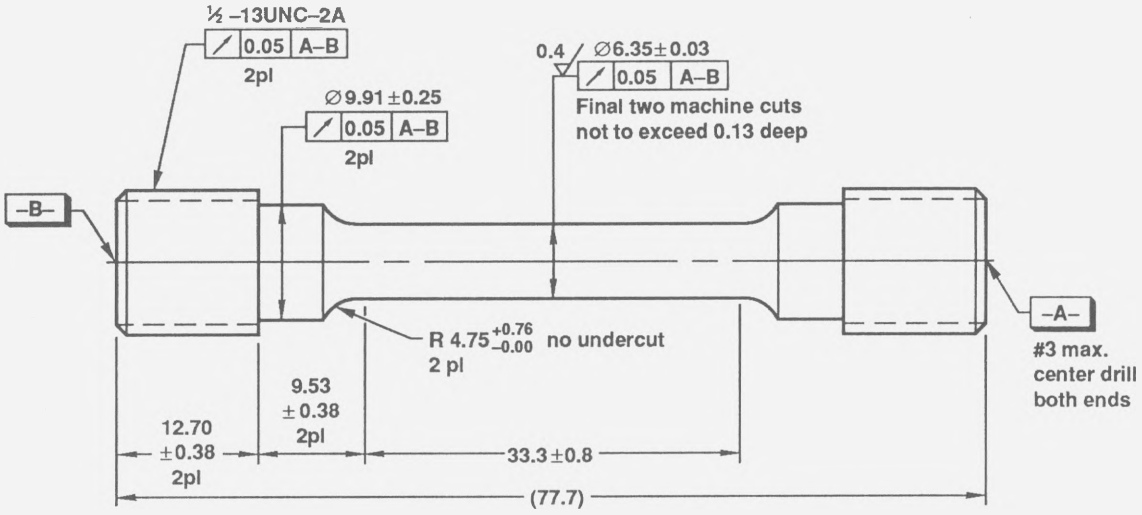

Figure 2.3. Standard tensile specimen used for determining base-metal mechanical properties. This same specimen geometry was utilized for creep rupture testing of interlayer joints.

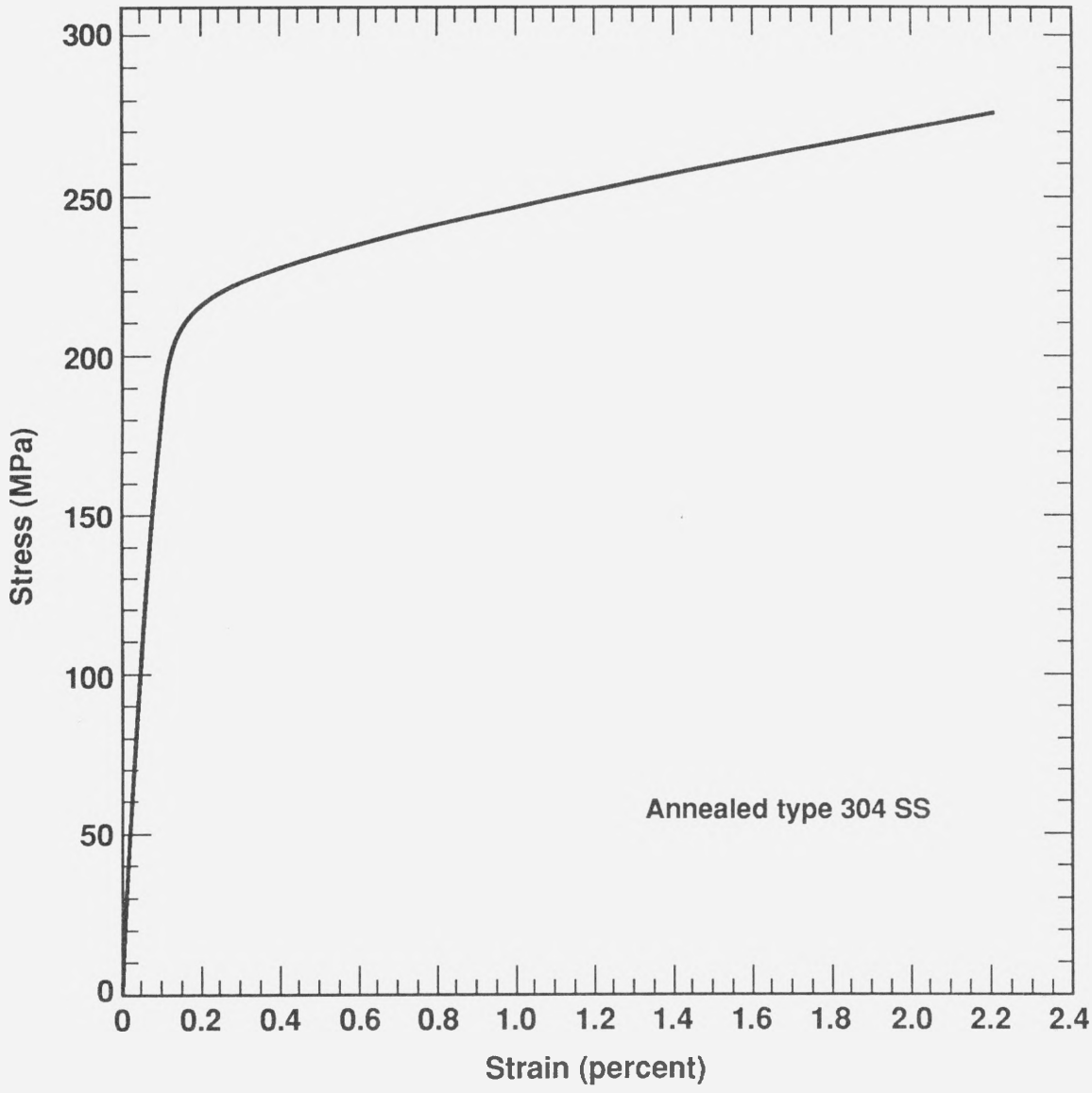

Figure 2.4. (a) Stress-strain behavior of annealed type 304 stainless steel base metal to strains of 2.2%.

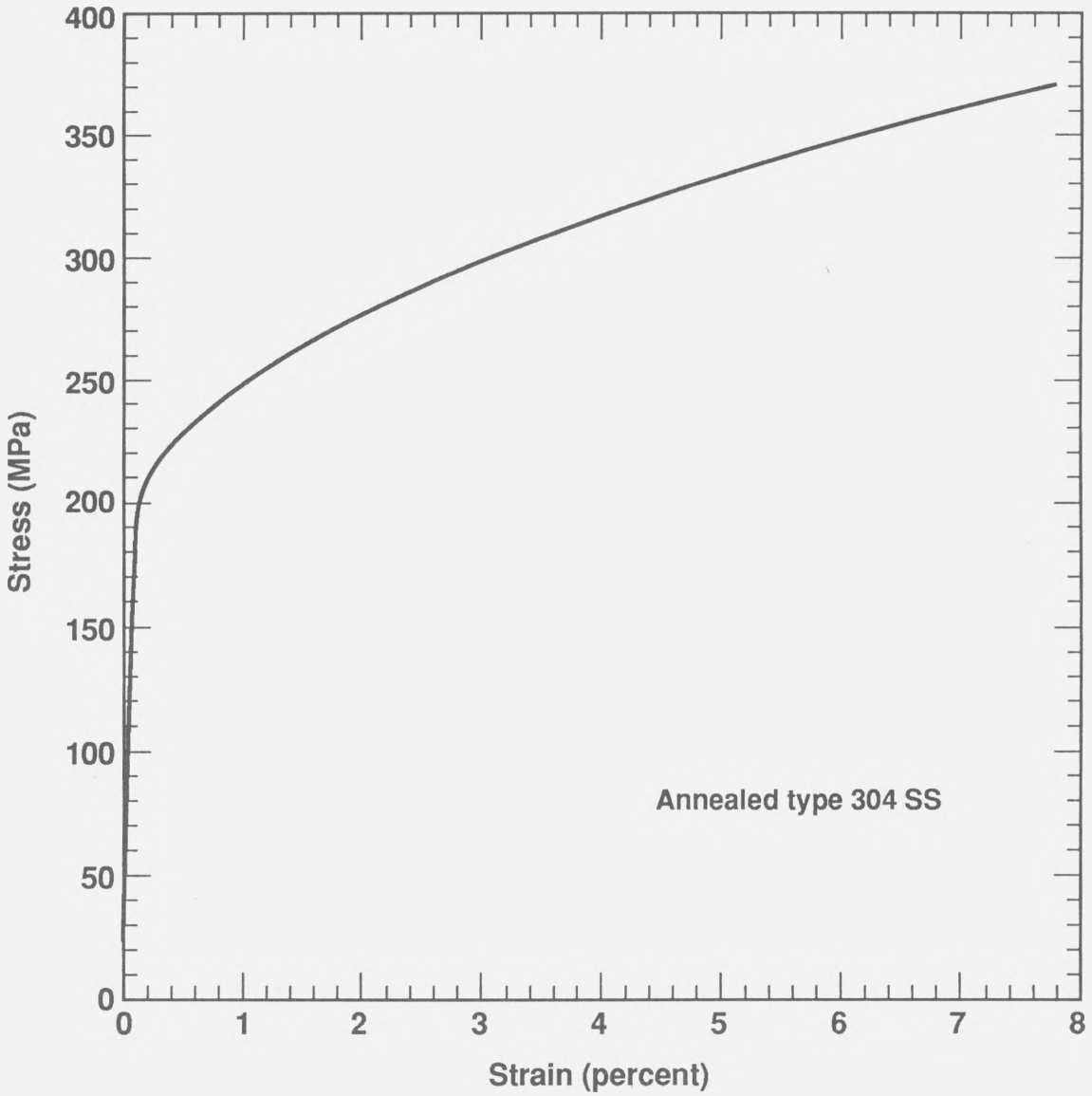

Figure 2.4. (b) Stress-strain behavior of annealed type 304 stainless steel base metal to strains of 7.8%.

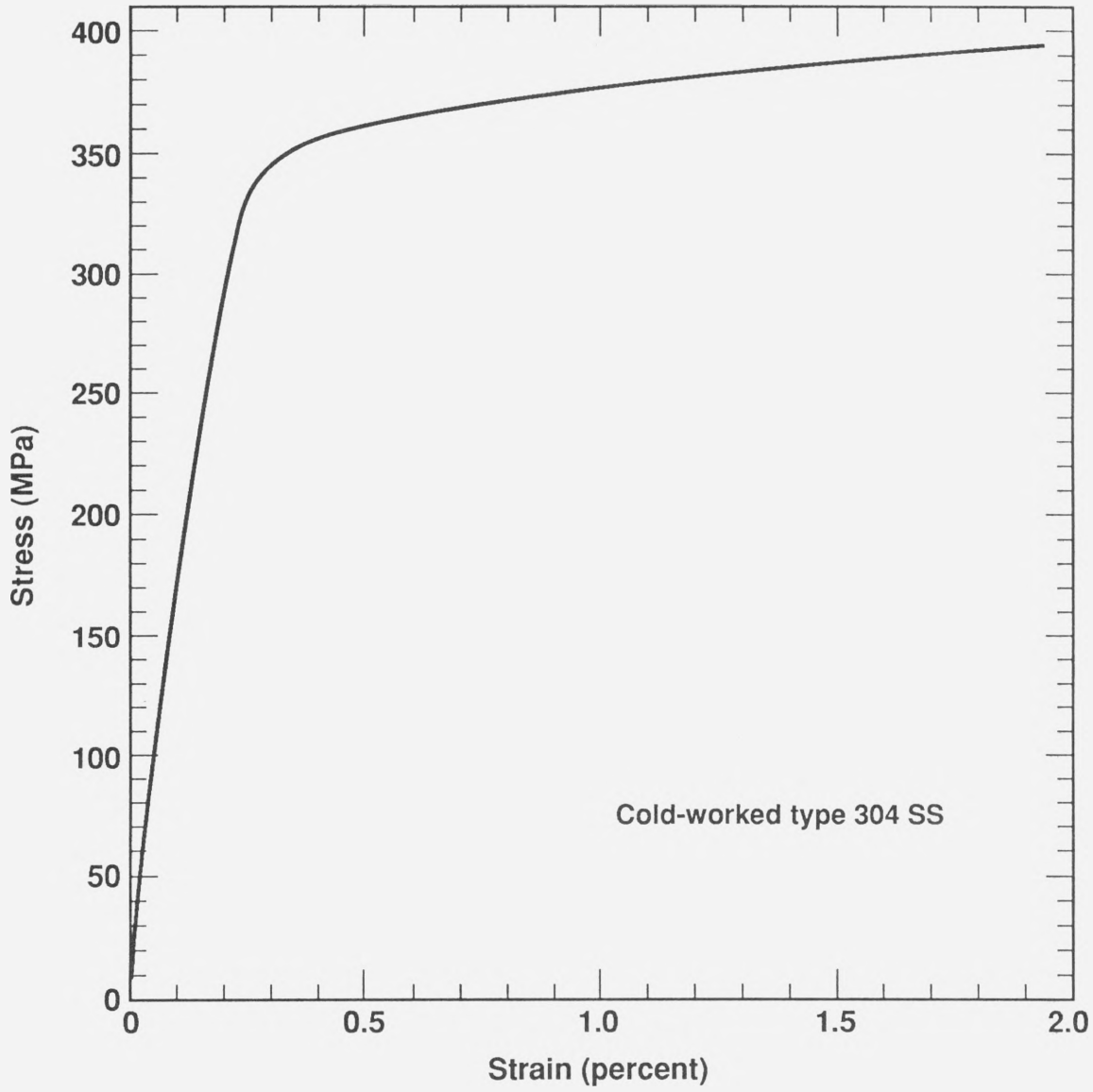

Figure 2.4. (c) Stress-strain behavior of cold-worked type 304 stainless steel base metal.

2.1.3. Coating Specimens

The base-metal specimens to be coated were machined into right cylinders with a diameter of 15.3 mm and a length of 38.8 mm. Type 304 SS specimens were machined from the annealed and cold-worked (prestressed) bars such that the ends to be coated and joined were taken from adjacent locations as shown in Fig. 2.5a. The surfaces to be coated were initially machined flat by single-point turning to 5 μm, and to a surface roughness of 0.4 μm arithmetic average (AA). The uranium and hot-rolled type 304 SS base metals to be coated with electrodeposited silver, and the 8091 Al-alloy specimens to be coated with PM sputter-deposited silver, were not machined further. All other base metals were finish-machined as follows. Specimens designated as "machined surfaces" were subsequently machined flat to 2 μm, and to a surface roughness of 0.1 μm AA using a precision air-bearing lathe with a cermet tool. This procedure required two facing passes of 0.02 and 0.01 mm deep at a feed rate of 0.009 mm per revolution at 1400 RPM. Figure 2.5b shows the machined specimen prior to coating. Specimens designated as "lapped surfaces" were lapped flat to 0.15 μm, and to a surface roughness of 0.03 μm AA using the following polishing procedure. First, the specimens were mounted into a fixture with the ends held flat against a surface plate. Second, the specimens were machine-lapped using 10-μm alumina paste on a cast-iron lapping surface followed by 9-μm alumina paste on an anodized aluminum lapping surface. Finally, the specimens were hand-polished using 1-μm diamond paste on standard photocopy paper placed on a surface plate.

2.1.4. Encapsulating Cans

Tubing used for the hot-isostatic-pressing cans was manufactured to specification MIL-T-8504A using type 304 SS. The specification called for a 15.37-mm (+ 0.07 mm, - 0.00 mm) ID and 0.25-mm (±0.02 mm) wall thickness. One end of the tube was sealed by electron beam welding a 0.25-mm-thick SS disk onto the tube. A small tube (1.55-mm OD and 0.41-mm wall thickness) was electron beam welded through the center of the disk,

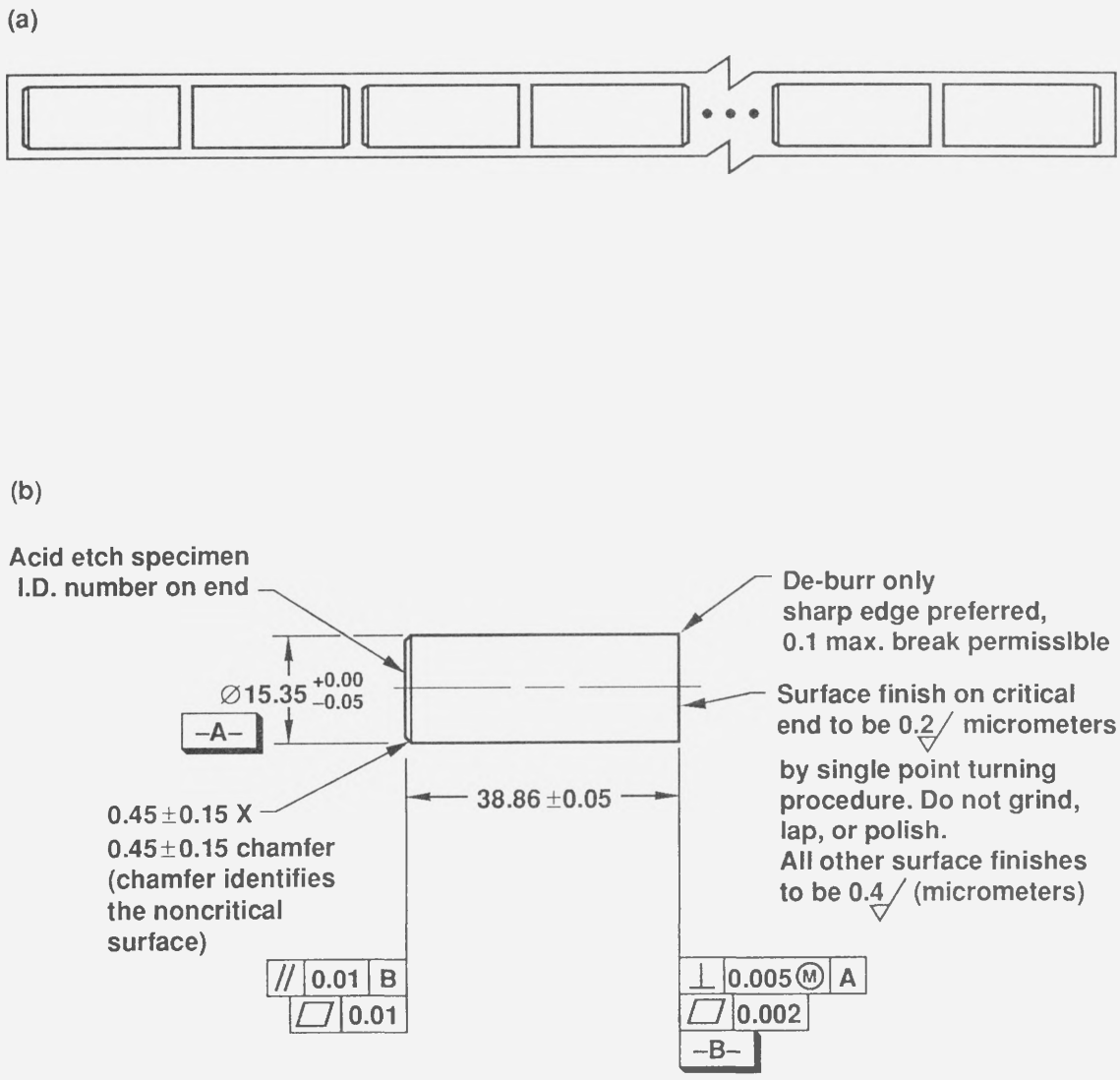

Figure 2.5. Schematic showing procedure for (a) machining specimens from type 304 stainless steel bars to be subsequently coated with silver. (b) Machined-surface coating specimen. Some specimens were finish-machined by lapping the surface to be coated.

protruding outward from the canned assembly. Figure 2.6 shows the encapsulating can assembly. Eventually, the coated specimens are inserted in the encapsulating can and sealed with a lid using electron beam welding.

2.2. Vacuum Coating of Silver Onto Base Metals

2.2.1. Specimen Cleaning and Fixturing

Subsequent to machining, base-metal specimens were washed with an abrasive detergent followed by a hot-water rinse. The specimens were then rinsed in deionized water and ultrasonically cleaned for 20 minutes in ethyl alcohol. Drying of the specimens was accomplished by blowing with helium. The specimens were then loaded into a 150-mm-diameter copper fixture that positions 24 specimens for the coating operation. Each coating operation was performed using a single type of base-metal specimen to prevent any possibility of cross-contamination of atoms during the sputter-etching phase (the copper fixture was pre-coated with a thick layer of silver for the same reason). The fixture was designed to allow specimens to be placed within an annular area of 30 to 120 mm in diameter (see Fig. 2.7). It was determined that deposition thickness varied within ±10 % over this area. The specimen fixture was placed inside the vacuum-coating chamber and was threaded into a water-cooled fixture. The water-cooled fixture was positioned at the top of the vacuum chamber, without rotational capability. The specimen surfaces faced the PM-sputtering source, located 152 mm below at the bottom of the vacuum chamber. A 152-mm-diameter silver disk, used as the sputtering target, was attached to the internally-mounted magnetron. The vacuum-coating chamber was designed with a large half-cylinder door (sealed with an O-ring) to permit easy access into the chamber. Figure 2.8 shows a schematic of the vacuum chamber and the two-stage etching and coating procedure (to be discussed subsequently).

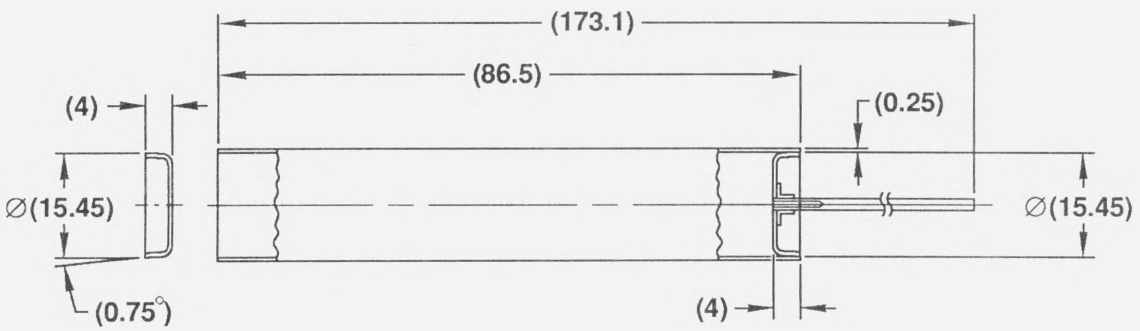

Figure 2.6. Encapsulating can assembly used in hot isostatic pressing procedure. The base-metal specimens are placed inside with the silver-coated surfaces contacting one another (dimensions are in millimeters).

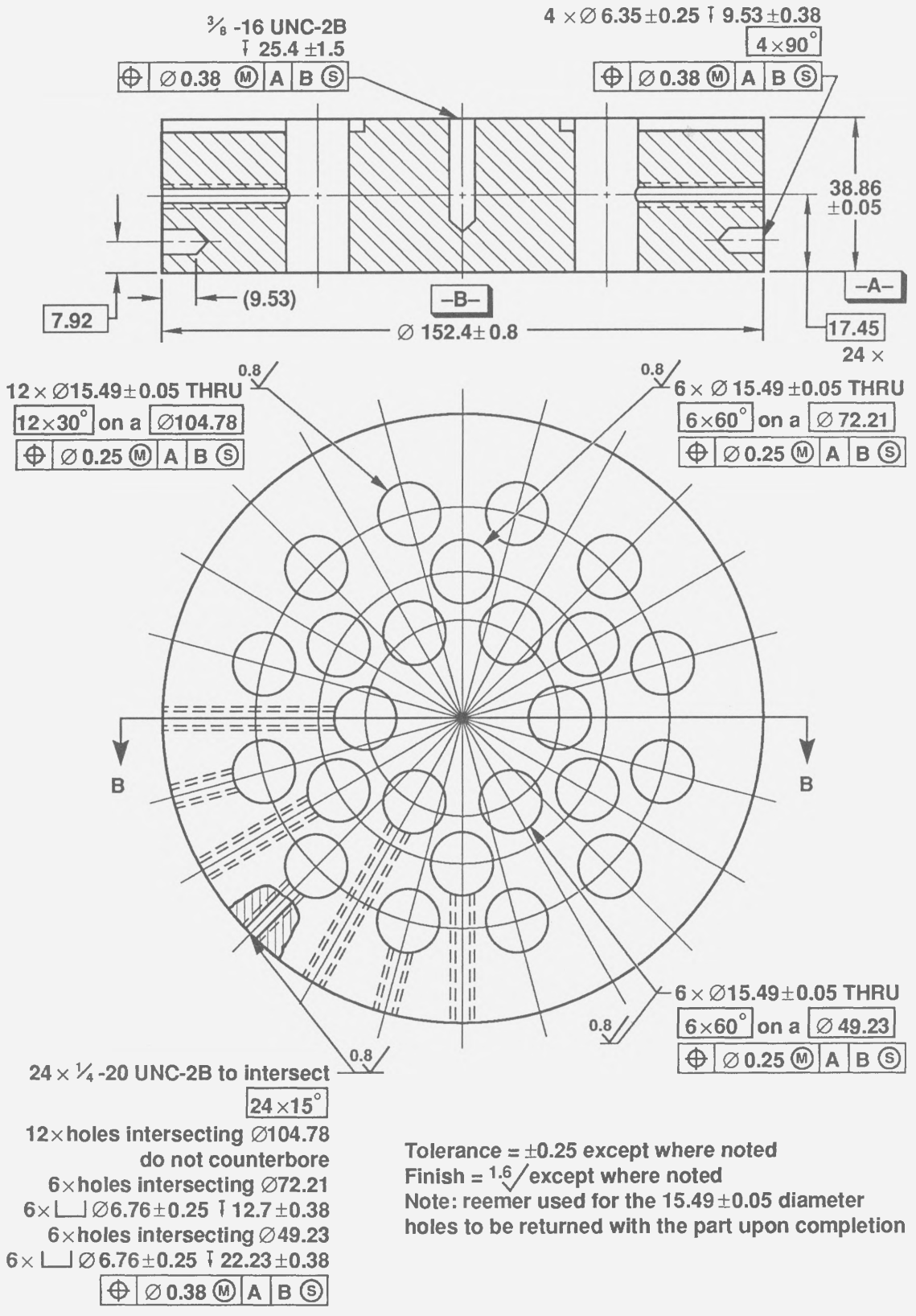

Figure 2.7. Fixture used to sputter-etch and deposit silver onto base-metal specimens.

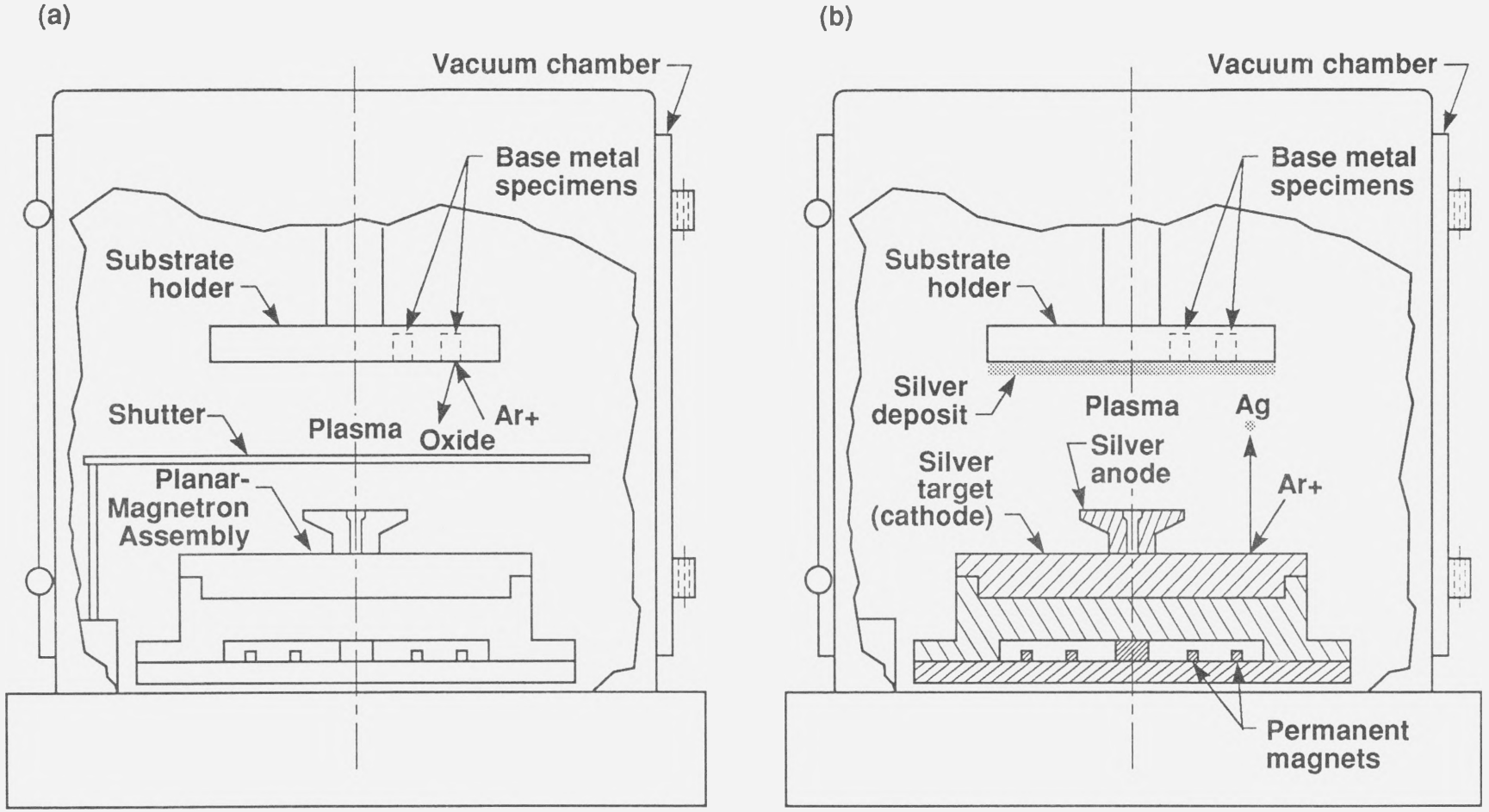

Figure 2.8. Schematic of vacuum chamber and associated hardware showing (a) ion-etching and (b) silver-deposition phases.

2.2.2. Chamber Evacuation

The chamber was evacuated using a Roots-type roughing pump in conjunction with an ultra-high vacuum turbomolecular pump (rated at 1500 liters/s). The chamber was heated using internally mounted quartz lamps to 383 K for 18 hours, allowed to cool for 4 hours, and then exposed to a liquid-nitrogen trap located in the high-vacuum line for an additional 16 hours. This procedure resulted in a base pressure of 4–8 μPa before the etching and coating cycles were initiated. A quadrapole mass spectrometer was used to analyze the residual gas in the vacuum chamber in order to detect any air leaks present prior to the etching and coating operation.

2.2.3. Sputtering-Etching Phase

Research-grade (99.999% pure) argon gas flowing through a thermal purifier (heated to 783 K) was introduced into the vacuum chamber for sputtering. The chamber pressure was regulated at 5.33 Pa argon pressure using a needle-orifice gas-flow controller and a high-vacuum bypass line. The maintenance of this pressure required approximately 21.8 SCCM (standard cubic centimeters per min.) argon flowing through the gas-flow controller. A dc glow-discharge power supply was used to initiate a plasma by ionizing the argon and maintain the plasma at 2000 V and 43 mA with reference to the coating fixture (base-metal specimens). The steel and uranium specimens were sputter-etched for 35 minutes; the aluminum-alloy specimens were sputter-etched for only 15 minutes. A total of 700 nm was etched from the steel specimen surfaces, corresponding to an average etching rate of 0.33 nm/s. Figure 2.9 shows the sputter-etch current versus time characteristics using stainless steel base metals. A shutter was placed between the target and specimen surfaces to prevent any deposition of sputtered atoms onto the silver surface during the etching phase.

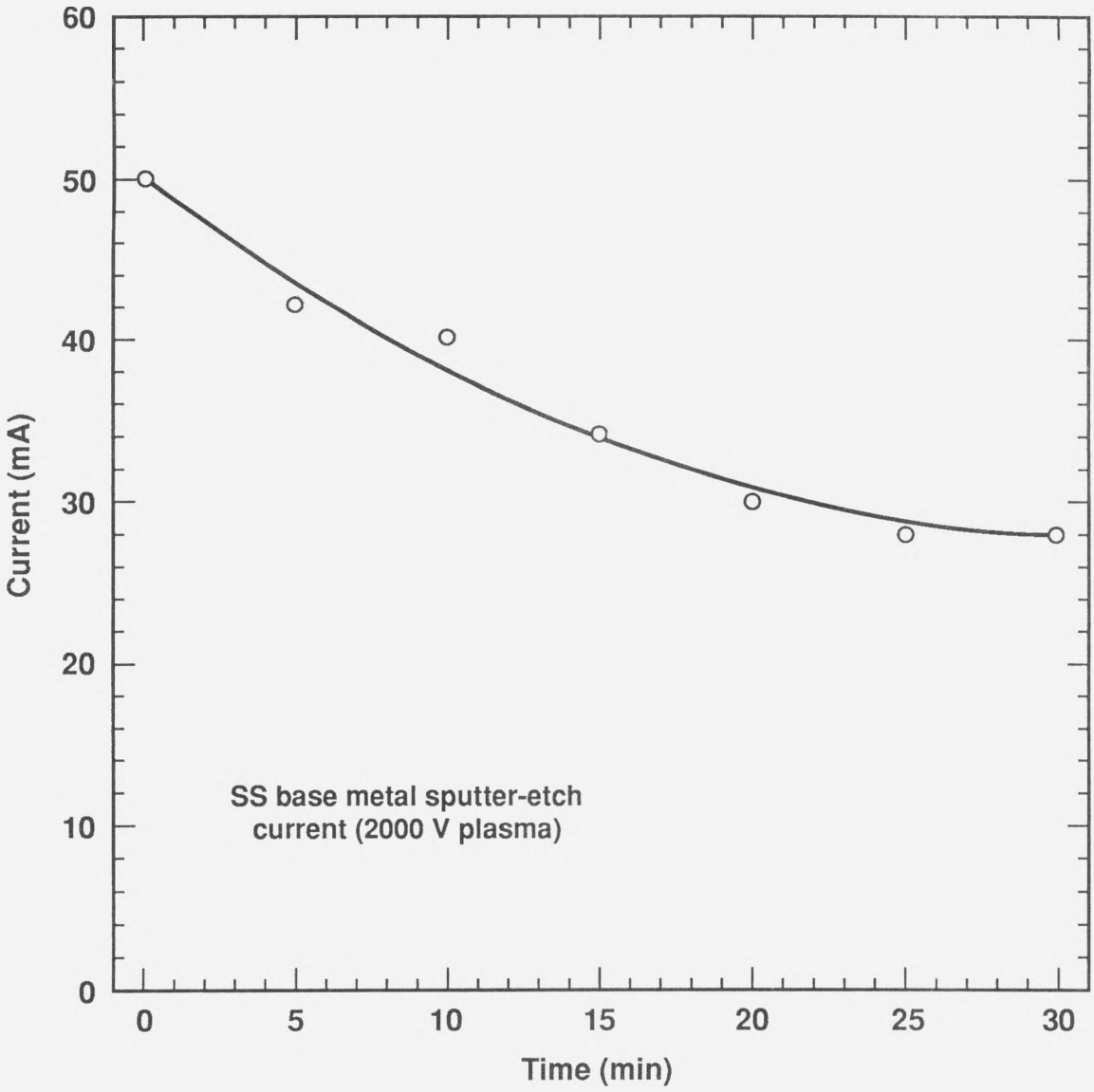

Figure 2.9. Sputter-etch current as a function of time, recorded using stainless steel base metals. The plasma is maintained at 2000 V with reference to the base-metal specimens.

2.2.4. Vapor Deposition Phase

The coating phase was initiated by using a separately-controlled dc power supply that applies a voltage to the PM source, thereby establishing a plasma adjacent to the silver-target surface. The power was linearly ramped by the controller during the final 5-minute etch period, reaching a steady-state value of 4.5 kW (625 V, 7.2 A). Deposition of silver onto the specimens was initiated by opening the shutter prior to switching off the sputter-etch power supply. This prevented any re-contamination of oxygen by adsorption of residual water vapor onto the specimen surfaces. The chamber pressure was reduced to 1.33 Pa by resetting the argon flow controller and closing the bypass line, causing the gas to flow through a chevron throttle valve located in the high-vacuum line. The silver-deposition rate at the specimen surfaces was determined to be 20 nm/s. Uranium and stainless steel specimens were coated for 60 minutes resulting in 75 μm of silver deposited onto the surfaces. Aluminum-alloy specimens were coated for 20 minutes (25 μm silver). Maraging steel specimens were coated for either 20, 60, or 420 minutes (25, 75, or 500 μm silver, respectively).

2.3. Electrodeposition of Silver Onto Base Metals

Uranium and hot-rolled type 304 SS specimens were electrodeposited with 75 μm of silver onto each of the base-metal surfaces to be used as an intermediate layer for diffusion welding (150 μm total thickness). The procedure for plating silver onto the uranium specimens differed from that of the SS specimens. Both specimens were masked to restrict the deposition to the surfaces to be joined. The uranium specimens were degreased, etched in ferric chloride solution, nickel-plated to a thickness of 6 μm, followed by silver plating at 43 A/m^2 to a thickness of 75 μm. The stainless steel specimens were degreased, electrolytically-etched in sulfuric acid, followed by a silver strike (215 A/m^2) and silver plate (43 A/m^2) to a thickness of 75 μm. Typical levels of impurities present in the silver plating solutions are given elsewhere.[12]

2.4. Diffusion Welding of Silver Interlayers

2.4.1. Uniaxial Pressing

The 8091 Al-alloy specimens were diffusion welded by uniaxially pressing the coated surfaces in a vacuum furnace. This was accomplished by placing pairs of specimens in the vacuum furnace and preloading the assembly using a hydraulic ram. The chamber was evacuated to below 100 μPa gas pressure prior to applying a pressure of 207 MPa to the coated surfaces in contact. The specimen temperature was elevated to 483 K using radiant heaters. Peak temperature and pressure were maintained for 10 minutes. The furnace was cooled to below 323 K before the pressure was relieved.

2.4.2. Hot-Isostatic Pressing

All other specimens in this study were diffusion welded by hot-isostastic pressing. The 24 specimens were removed from the coating fixture in pairs, their silver surfaces were placed in contact, and the pairs were encapsulated into 12 stainless steel cans (see Section 2.1.4). All specimens in this study (with the exception of electrodeposited-silver interlayers between uranium and type 304 SS) were fabricated by joining identical base materials. The cans were sealed with a lid using electron beam welding. The sealed assemblies were evacuated through the small tube welded on one end of the can using a vacuum pump. The resulting gas pressure was ~50 μPa. The tubes were sealed using a pinch-off tool, followed by electron beam welding to prevent rupture during the autoclave cycle. The evacuated assemblies were then placed in an autoclave and isostatically compressed with argon to a pressure of 138 MPa. The temperature was then raised to 673 K (873 K for electrodeposited-silver interlayers between uranium and SS base metals) while the gas pressure was increased to 207 MPa. The peak temperature and pressure were maintained for two hours. The autoclave was cooled to below 373 K before the gas was vented. Figure 2.10 shows the autoclave cycle.

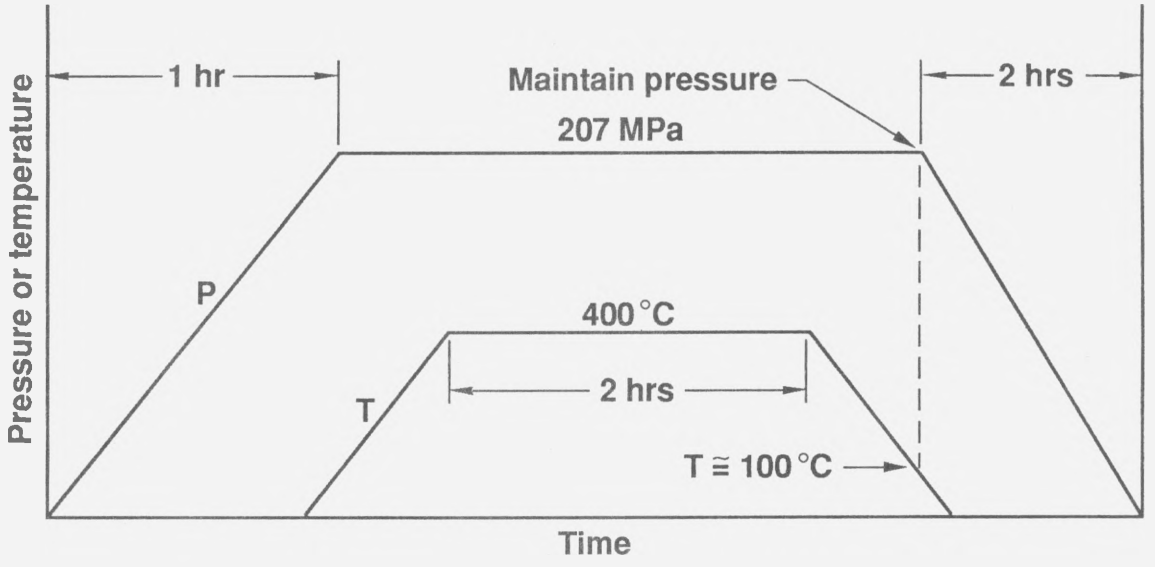

Figure 2.10. Autoclave cycle showing procedure for hot-isostatically pressing the encapsulated specimens to obtain diffusion welding of the silver interfaces.

2.5. Base-Metal Brazing With Silver

Maraging steel and annealed type 304 SS base-metal specimens (15.3 mm diameter by 38.8 mm long) were brazed with pure (99.995%) silver as follows. The surfaces to be brazed were first coated with titanium-hydride (Ti-H) flux. The flux consisted of Ti-H powder suspended in an isobutyl methyl metharcrylate (Lucite) solution thinned with butyl acetate. The desired joint spacing (150 μm) was obtained by spot-welding three thin strips of stainless steel spaced 120° apart onto the edges of one of the faying surfaces. A 250-μm-thick silver foil was used as the filler material. Three flat strips of stainless steel were spot-welded onto the outer diameter of the other specimen half such that they extended beyond the surface to be brazed. This enabled the assembly to be aligned axially, with the interlayer placed between the two specimen halves.

The assembly was placed in a vacuum furnace and evacuated to below 50 μPa. The temperature was then raised to 1223 K for 5 minutes of soak time using radiant heaters. Brazing was accomplished by increasing the temperature from 1234 K (T_m) to 1248 K during a 3-minute period. The brazed-specimen assembly was cooled slowly to below 373 K before removing from the vacuum furnace.

2.6. Microstructural Analysis of Interlayers and Base Metals

2.6.1. Optical Microscopy

Cross-sections for optical metallography of as-deposited and diffusion-welded silver were cut with a diamond abrasive radial saw, mounted in epoxy resin, and then ground successively from 240- through 600-grit silicon carbide. Vibratory polishing of the mounted specimens was accomplished using 1-μm diamond in kerosene on a silk cloth, followed by final polishing using 0.5-μm colloidal silica on a nylon cloth. The silver structure in optical metallography specimens was revealed by chemical etching for 20 seconds using a solution of 20 parts water, 10 parts ammonium hydroxide, and 1 part hydrogen peroxide (30% conc.).

2.6.2. Microhardness Measurements

Microhardness measurements of silver and type 304 stainless steels were obtained using a diamond pyramid hardness indenter set at either 50 or 100 g loads. The materials were mounted, polished, and etched to remove surface damage. The silver interlayers were etched with the same solution used for the metallography specimens, except etch times were increased to between 2–5 min. Stainless steel specimens were electrolytically etched in dilute oxalic acid (30% conc.) using 5 mV for 5 minutes. Vickers hardness values represent averages of 5–7 indentations taken randomly throughout the structure.

2.6.3. Scanning Electron Microscopy

Fractured specimens were analyzed using scanning electron microscopy (SEM) at 25 kV accelerating potential to characterize the separated surfaces. Energy dispersive spectroscopy (EDS) was used to determine the presence of silver on the steel base-metal side of silver-steel fractures. Stereoscopic photography using tilt-angle SEM was used to confirm the existence of microvoids at the silver-silver interfaces of mounted, polished, and etched cross sections of specimens previously loaded to varying fractions of their expected creep rupture times.

2.6.4. Transmission Electron Microscopy

All but one of the transmission electron microscopy (TEM) thin foils were extracted from tangential sections (perpendicular to the radial direction) containing the diffusion-welded-silver interlayer between steel base metals. The exception was an as-deposited silver coating extracted parallel to the coated interface. In either case, the procedure required cutting 0.4-mm-thick slices from specimens using a slow-speed cubic-boron-nitride abrasive radial saw (76 mm diameter) from which 3-mm-diameter disks were spark-cut. The disks were then ground using a succession of silicon-carbide polishing papers (40, 12, and 3 μm abrasive) to a thickness of 100 μm. Pre-thinning of the disks was

accomplished by mechanical dimpling with a phosphorous bronze wheel using cubic boron nitride abrasive (2 μm) in paste form. This procedure removed 65 μm from one side, followed by 25 μm from the opposite side of the disk. Final thinning of the 10-μm-thick disks was accomplished by ion-milling using an 11° angle of incidence with the disk placed on a cold stage. Crystallographic orientations were determined using both electron and x-ray diffraction.

2.7. Mechanical Testing of Interlayer Joints

2.7.1. Tensile and Creep Rupture Testing

Two types of mechanical tensile tests of the interlayer joints were performed: (1) ultimate tensile tests performed by monotonically increasing the load until the specimen fractured, and (2) creep rupture tests performed by loading in tension to a level below the UTS, and maintaining a constant load until the specimen fractured. Standard 6.35-mm-diameter and 25.4-mm-long reduced- (or gage-) section, threaded-end specimens (77.7 mm overall length) were machined from the autoclaved cylinders for eventual mechanical testing (see Fig. 2.4). The 50-μm-, 150-μm-, and 1-mm-thick silver joints were located in the center of the gage section. The gage section was ground to ±1.3 μm diametral tolerance to eliminate any notch effects at the silver joint from the single-point turning operation. Tensile testing of joints was accomplished by recording fracture load at a strain rate of $\sim 3\times10^{-4}$ s^{-1} based on the base-metal gage length. Both ends of the tensile specimens were threaded directly into universal joints to prevent bending stresses. Plastic strains in the gage section of the base metal was determined by extensometers during the tests, and also by direct measurements of the unloaded specimen gage diameter using an optical comparator at 100×. Plastic strains in the silver interlayer and the base metal near (<0.0076 mm) the interlayer were determined by unloading the specimen after various creep times, and measuring the joint diameter with the optical comparator.

Creep rupture tests were performed in tension at ambient temperature (295 K or 22 °C) and at 345 K (72 °C) using simple lever dead-weight type creep-rupture testing machines. Heating was accomplished by resistance furnaces that controlled the temperature within ±1 °C as measured by thermocouples spot-welded to the specimen surface. Plastic strain measurements of the interlayer and base metal were performed by measuring specimen diameters using the optical comparator. Additional creep (plastic strain vs. time) data for the stainless steel base metals were obtained using the final specimen gage diameter (after rupture of the joint) along with the time-independent plastic strain determined from stress-strain testing (see Section 2.1.2). Plastic strain measurement within the 150-μm-thick silver interlayer is estimated to be accurate within $\pm 10^{-3}$ strain. In some cases, plastic strain was measured by optically profiling the interlayer at high (500×) magnification. This is estimated to be accurate to within $\pm 2\times 10^{-4}$ strain. Tensile tests were performed in air of 30–40% relative humidity, and the effects of any stress corrosion cracking were determined not to be relevant.[44,45]

2.7.2. Torsion Testing

Torsion specimens were fabricated from untested tensile specimens by turning the threaded ends to 10.67 mm diameter, and then milling the ends flat to a thickness of 6.20 mm. Torsion tests of 150-μm- and 1-mm-thick silver joints between maraging steel, shown in Fig. 2.11, were performed at a constant twist-rate using a screw-driven testing machine. A 10-mm-gage torsional extensometer capable of measuring rotational displacements up to 4° was placed over the joint. The torque, M, was converted into shear stress, τ, using the solid-specimen torsion equation:[46]

$$\tau = \frac{M(3+n+m)}{2\pi r^3} . \qquad (1)$$

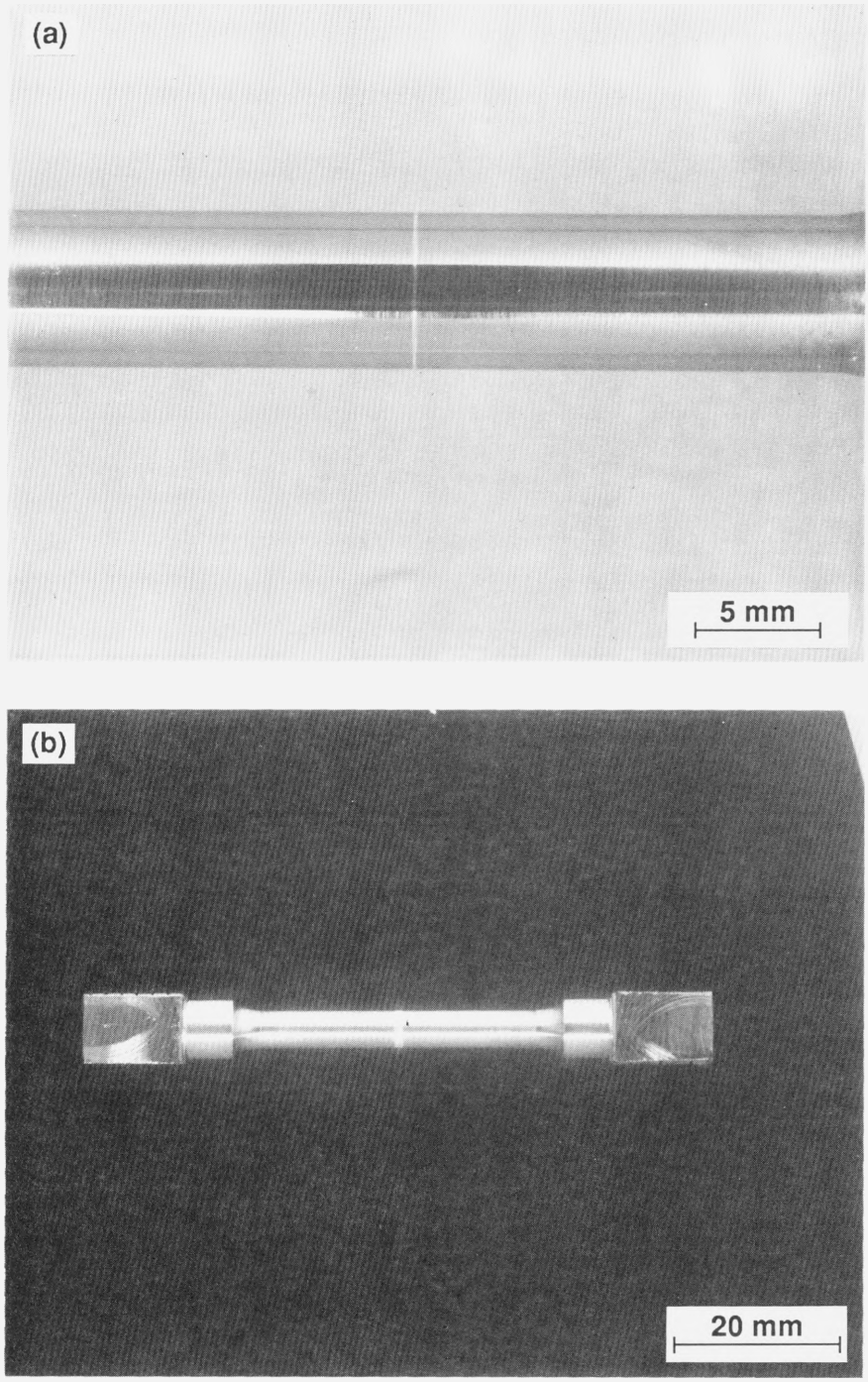

Figure 2.11. Optical photograph showing (a) 150-μm-thick silver interlayer and (b) 1000-μm-thick silver interlayer joining maraging steel base metals. Specimens have been machined into a torsion-test configuration.

The angle of twist, Θ, was converted into shear strain, γ, by the equation:

$$\gamma = \frac{r\Theta}{L} . \qquad (2)$$

In the above equations, r = radius of the specimen, L = gage length, n = strain-hardening coefficient, approximated by $(\partial \ln M)/(\partial \ln \Theta)$, and m = strain-rate sensitivity which has been reported[47] to be negligible (<1% effect on Eq. 1) in silver at 295 K. The strain in the silver joint was calculated by subtracting elastic displacements of the base metal from the total displacements measured by the extensometer. Torsion tests were performed at an effective (von Mises) strain rate of 3.3×10^{-4} s^{-1}.

CHAPTER 3
MICROEXAMINATION RESULTS

3.1. As-Deposited Silver Coatings

Figure 3.1 shows the structure of a PM sputter-deposited coating on type 304 SS base metal before the diffusion-welding cycle. This is termed the "as-deposited" structure. The fine-grained columnar structure, shown in Figs. 3.1a and 3.1b using optical metallography, appears similar to silver deposits on low-temperature substrates reported previously using HHC silver evaporation.[15] This type of structure has been characterized for sputter-deposited films as that of Zone T, or transition between porous (Zone 1) and dense, large columnar grains (Zone 2).[48] This structure commonly forms in coatings deposited onto low-temperature substrates (~0.3 T_m) using a low working-gas pressure (~1 Pa).[48] Figure 3.1c and 3.1d are TEM micrographs of the as-deposited structure. Transmission electron microscopy reveals that the as-deposited structure consists of columnar grains that are ~0.25 μm in diameter. The columns are perpendicular to the base-metal surface with the axes of the columns oriented along the [111] crystallographic direction. The columnar grains resulting from PM sputter-deposition contain a high density of growth twins approximately 15 nm thick. Transmission electron microscopy foils parallel with the coated surface reveal that the structure consists of clusters of approximately six columnar grains with each grain separated by a low-angle (<5°) grain boundary (see Fig. 3.1d). These 1-μm-diameter clusters are joined by high-angle grain boundaries that preferentially etch and become the dominant cross-sectional feature observed by optical metallography (see Fig. 3.1b). The as-deposited silver appears to be a fully dense structure, as voids were rarely observed in any of the TEM foils examined in this study.

The crystallographic orientation of the coatings was determined using x-ray diffraction. The results are shown in Table 3.1. The results are compared with bulk polycrystalline

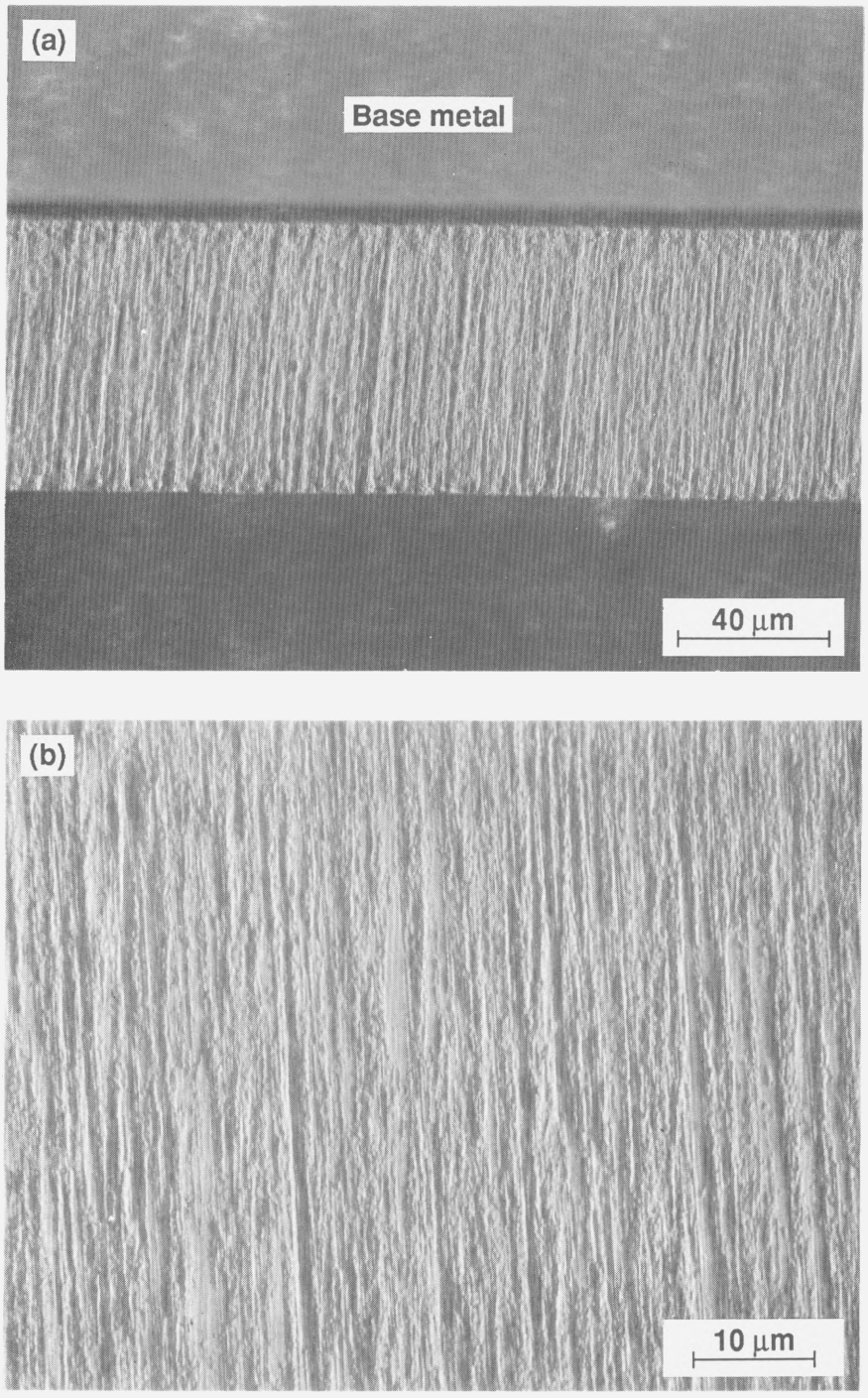

Figure 3.1. (a, b) Optical micrographs showing cross section of planar-magnetron-deposited silver structure. The fine-grained columnar structure appears similar to silver deposits on low-temperature substrates reported previously using HHC silver evaporation.[15]

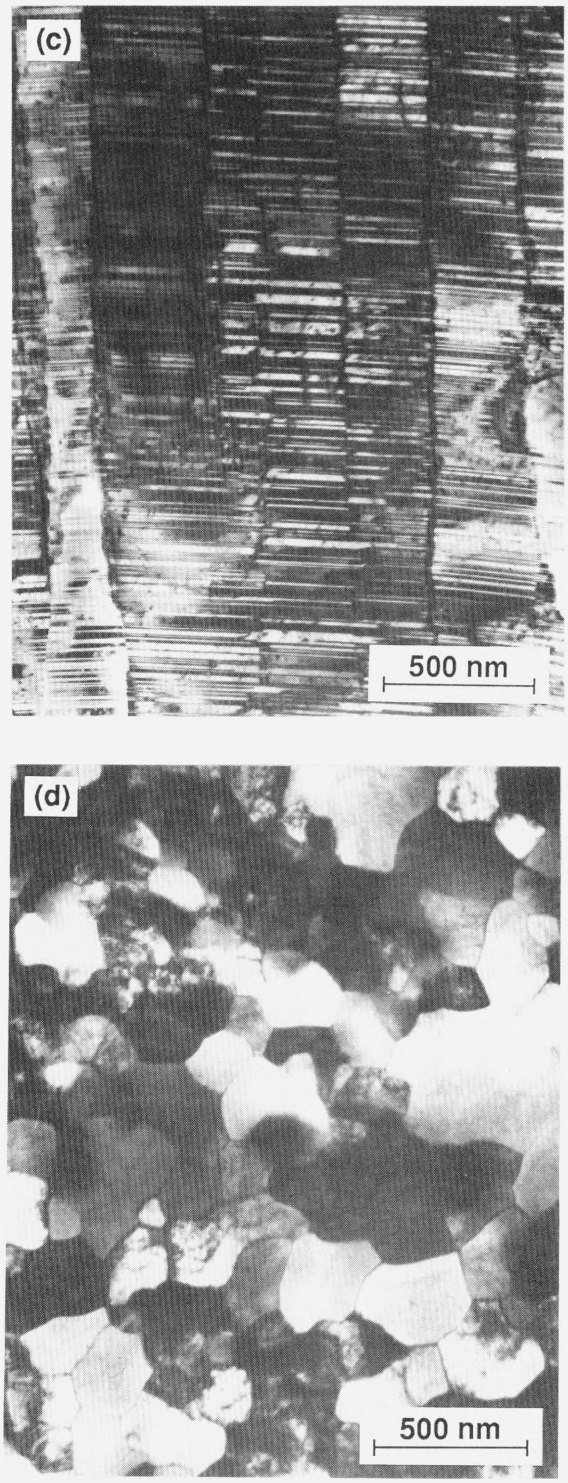

Figure 3.1. Transmission electron micrographs showing (c) the high twin-density in cross section of planar-magnetron-deposited silver structure, and (d) end view of the columnar grains taken perpendicular to the coated surface.

silver and with results reported[15] for silver deposited by HHC evaporation. The diffractometer rotates in a plane perpendicular to the specimen surface through Bragg angles from 2Θ = 24–100°. Reflections from the close-packed (111) planes give the highest intensities and are arbitrarily assigned a relative intensity of 100. Relative intensities of other planes represent ratios of the counter rate compared with that of (111) planes. Intensities of diffracted x-ray beams from crystallographic planes other than (111) are approximately 20 times stronger for bulk than for vapor-deposited silver (PM or HHC). The orientation of the [111] direction was determined to be perpendicular to the surface of the coating.

Table 3.1. Crystallographic orientation (Miller indices) of vapor-deposited silver.

	I/I_0 Relative Intensities (hkl)			
Type of Silver	**(111)**	**(200)**	**(220)**	**(311)**
Bulk silver (polycrystalline)	100	40	25	26
Silver deposited by PM sputtering[a]	100	2.2	0.5	2.5
Silver deposited by HHC evaporation[b]	100	2	1	1

[a] Type 304 SS base metal; this study.
[b] Type 304 SS base metal, no substrate bias (ion-bombardment) during deposition.[15]

3.2. Diffusion-Welded-Silver Interlayers

Figure 3.2 shows several examples of silver interlayers between steel base metals after diffusion welding at 673 K for 2 hours. Optical metallography revealed that the silver interlayer consists of two types of structures: (1) nonrecrystallized silver which has retained the columnar grains and fine microtwins of the as-deposited coating and (2) silver which has recrystallized into large grains (>1 mm in diameter) containing a high density of annealing twins. Approximately 50–75% of the silver structure consisted of recrystallized

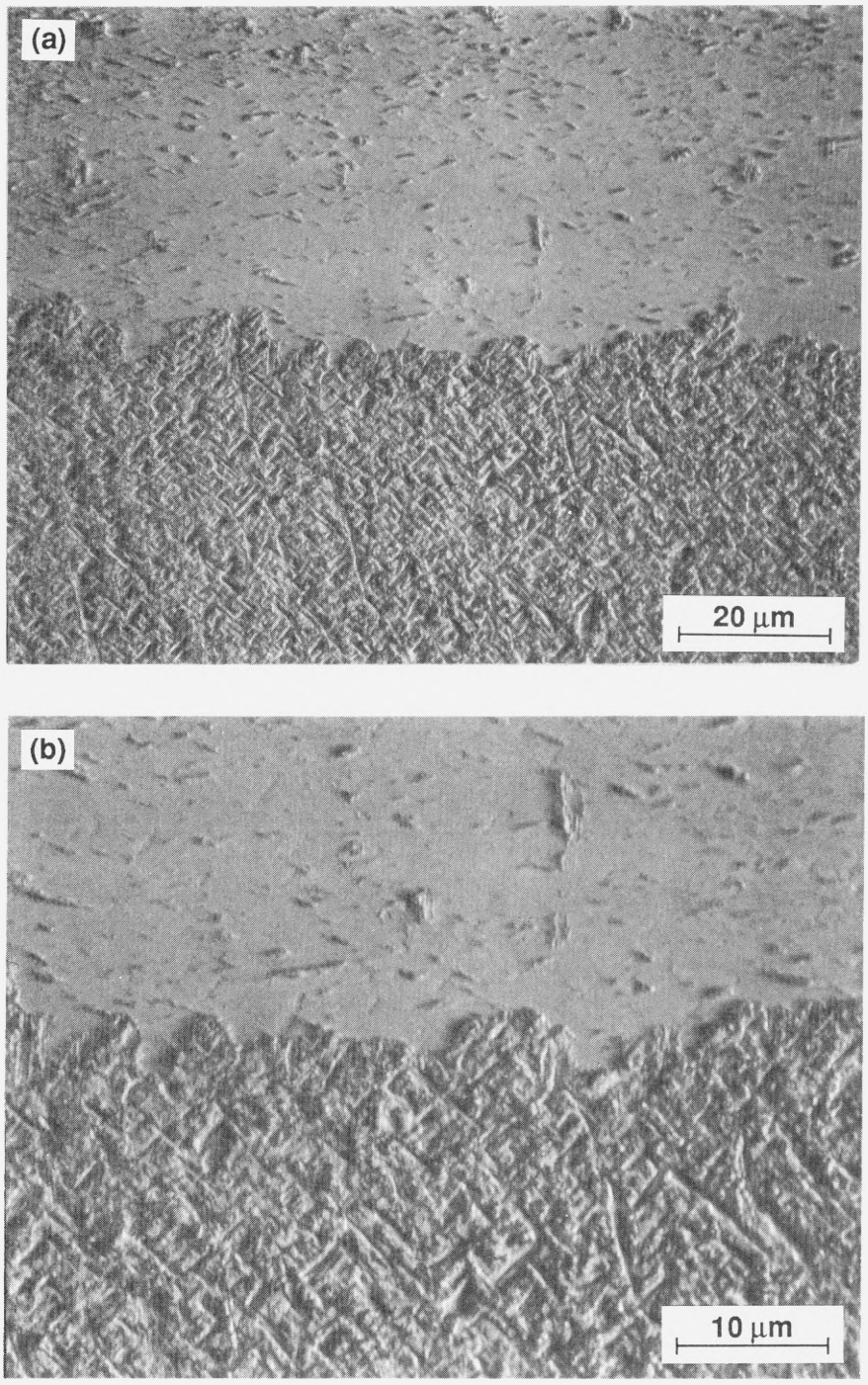

Figure 3.2. (a, b) Optical micrographs of diffusion-welded-silver interlayers joining steel base metals. Interlayers usually contain recrystallized grains with numerous annealing twins, shown on both sides of silver-silver interface.

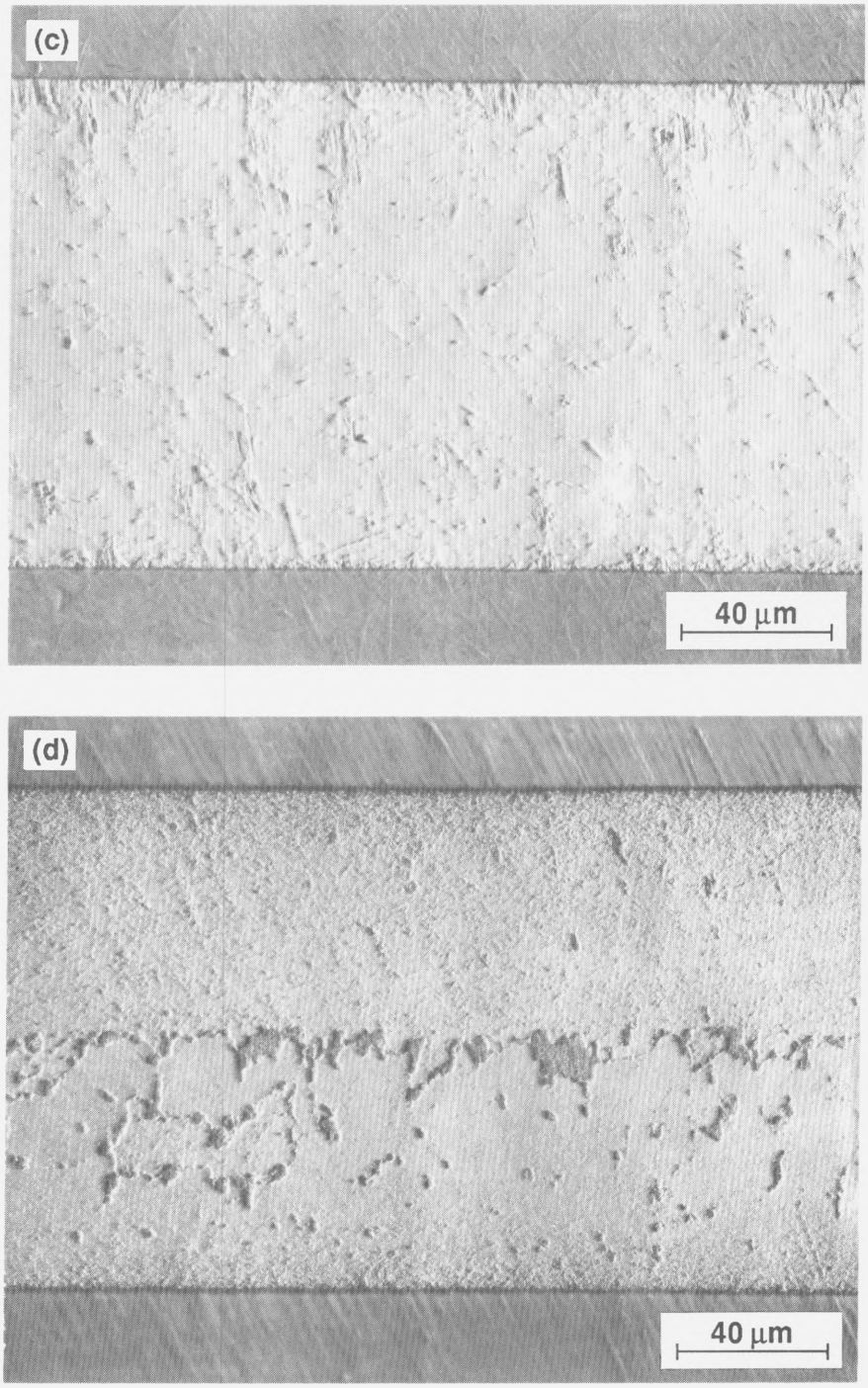

Figure 3.2. Optical micrographs of diffusion-welded-silver interlayers joining steel base metals. Some interlayers exhibit (c) nearly complete recrystallization while others (d) retain nonrecrystallized grains at the original diffusion-welded-silver interface.

grains, with some recrystallization across the silver-silver interface. Of course, the estimated percent of recrystallized silver represents the average for all silver structures analyzed. Figures 3.2a and 3.2b show the wavy silver-silver interface which forms between recrystallized interlayers each containing a high density of annealing twins. Some interlayers remained substantially nonrecrystallized, while other interlayers exhibited nearly complete recrystallization. An example of an interlayer for which recrystallization is nearly complete is shown in Fig. 3.2c. In some cases, only one side of the interlayer (one of the two coated halves) recrystallized, while in other cases, the nonrecrystallized regions remained in isolated patches, often at the original diffusion-welded-silver interface as shown in Fig. 3.2d.

The diffusion-welded-silver interface of all specimens utilizing steel base metals, which were examined by optical microscopy, appeared to be free of any large voids or nonbonded regions. Examination of the diffusion-welded-silver interlayer between 8091 Al-alloy base metals revealed large voids, or nonbonded regions, along the silver-silver interface. Figure 3.3 shows that these voids are predominantly associated with machining damage, or "pullout," of the base-metal surface prior to coating. Apparently, the silver-coated surfaces on top of these asperities failed to contact one-another during the diffusion-welding process.

Transmission electron microscopy revealed that the diffusion-welded-silver interlayer in the vicinity of the original coated silver surfaces consists of a high-angle grain boundary often with nonrecrystallized regions on one side of the interface (see Fig. 3.4a). The interface appears to be essentially free of defects such as voids or second phase particles. Only a few, isolated voids were found in diffusion-welded silver (at or near the silver-silver interface). The TEM micrograph of figure 3.4b shows the silver-base-metal interface. Most of the silver interlayers examined contain a nonrecrystallized region (~1 μm thick) along the silver-base-metal interface. It will be shown in Sections 6.4 and 8.4 that many of the fractures appearing to be "silver-base-metal" separations (where the bulk of the

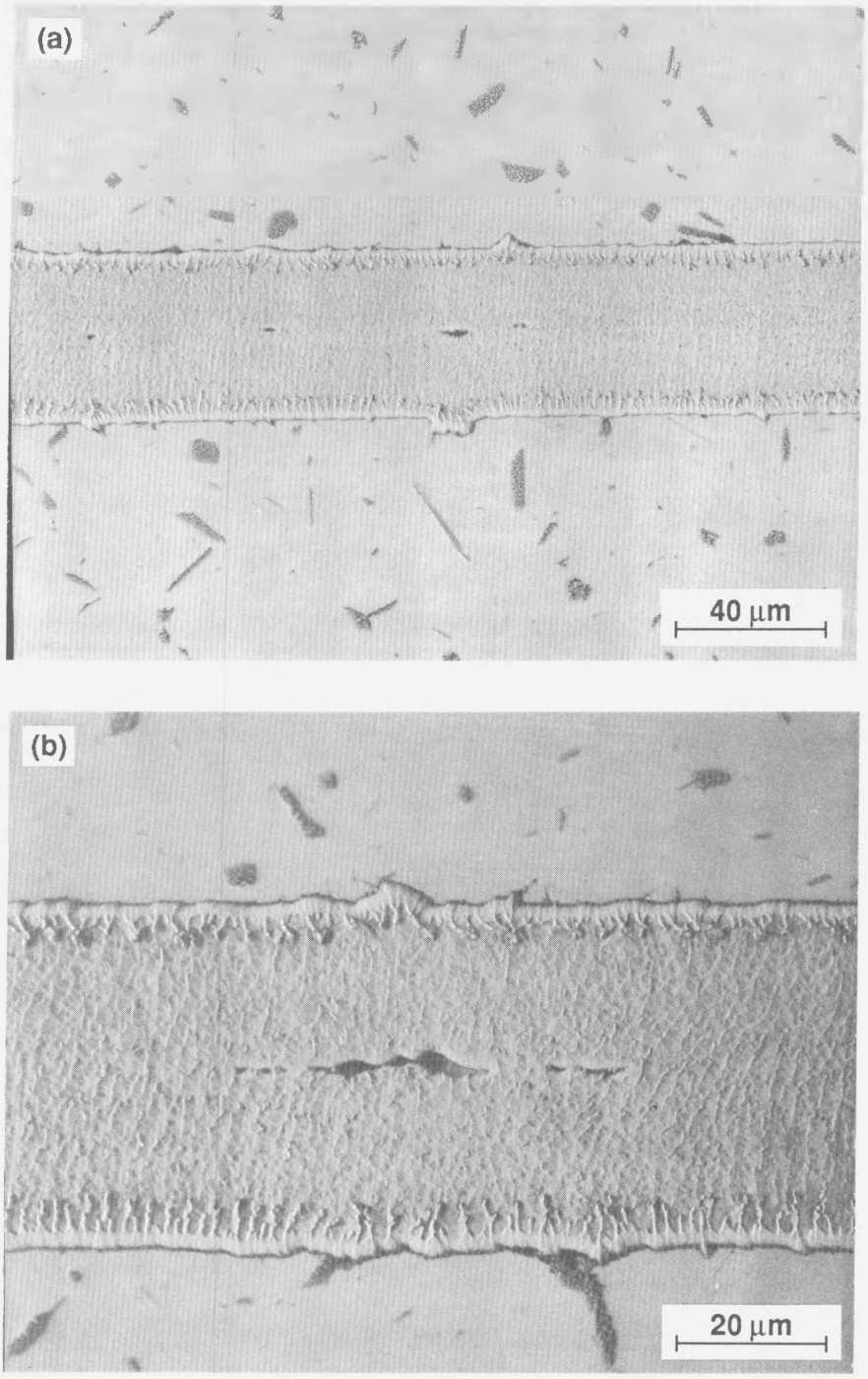

Figure 3.3. Optical micrograph of diffusion-welded-silver joint between 8091 Al-alloy base metals. Nonbonded regions at the silver-silver interface result from the joining of silver interlayers which were coated onto machining-damaged base-metal surfaces.

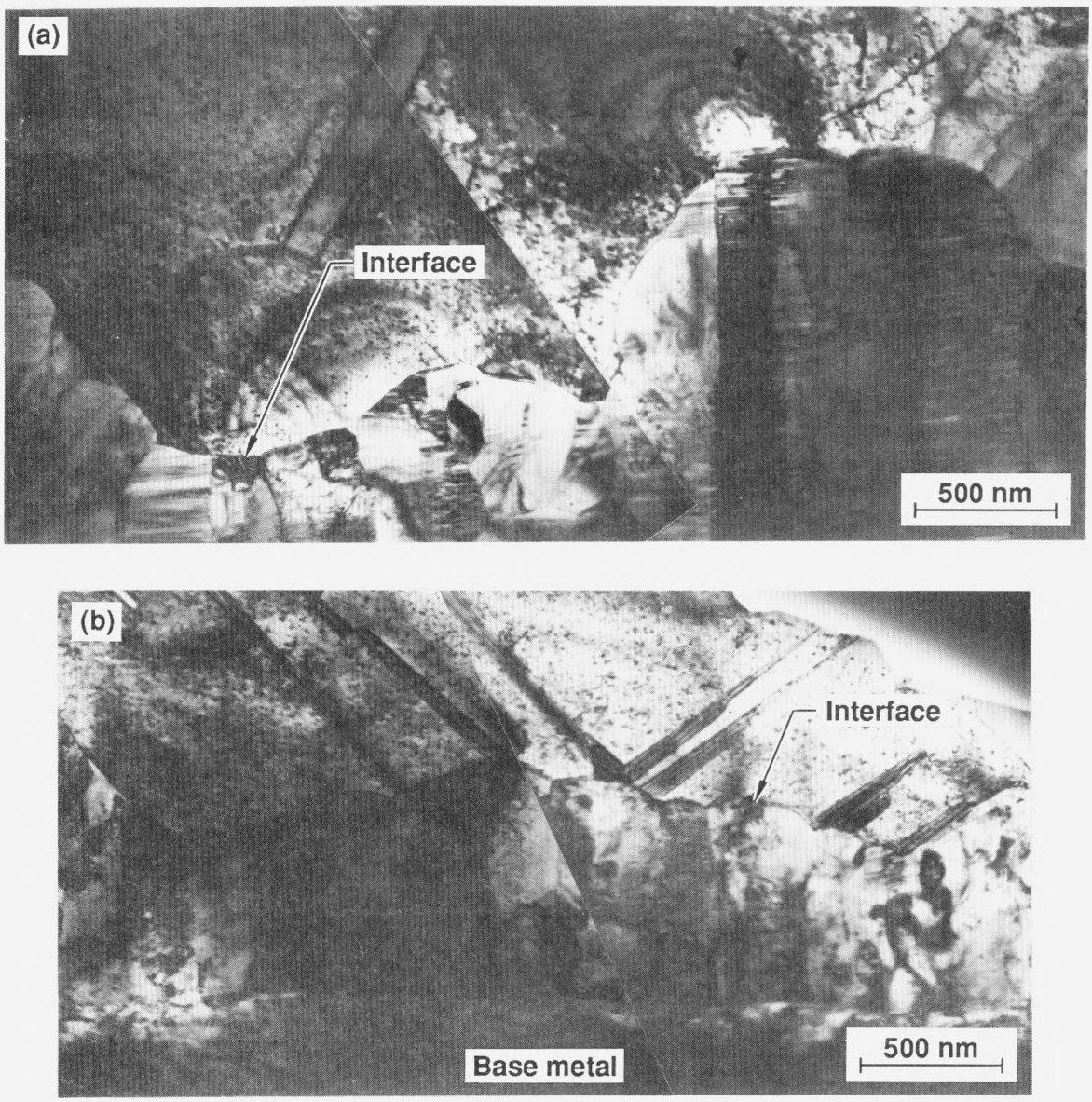

Figure 3.4. Transmission electron micrographs of diffusion-welded-silver interlayer joining steel base metals. (a) The diffusion-welded-silver interface consists of a high-angle grain boundary between a recrystallized grain (top half of photo) and a retained columnar grain structure. (b) Columnar grains are often retained along the silver-base-metal interface, resulting in a silver-silver interface near (~1 μm) the base-metal interface.

silver interlayer remains adhered to only one side of the base-metal surfaces) are actually silver-silver separations at this nonrecrystallized-recrystallized silver interface. As illustrated previously, some interlayers contained regions where a single recrystallized grain spanned the entire joint thickness. In these instances, small patches of nonrecrystallized (columnar) grains were often present within the interlayer. Besides containing a high density of annealing twins, the recrystallized structure may contain a relatively high dislocation density (seen in Fig. 3.4c along with twinned regions).

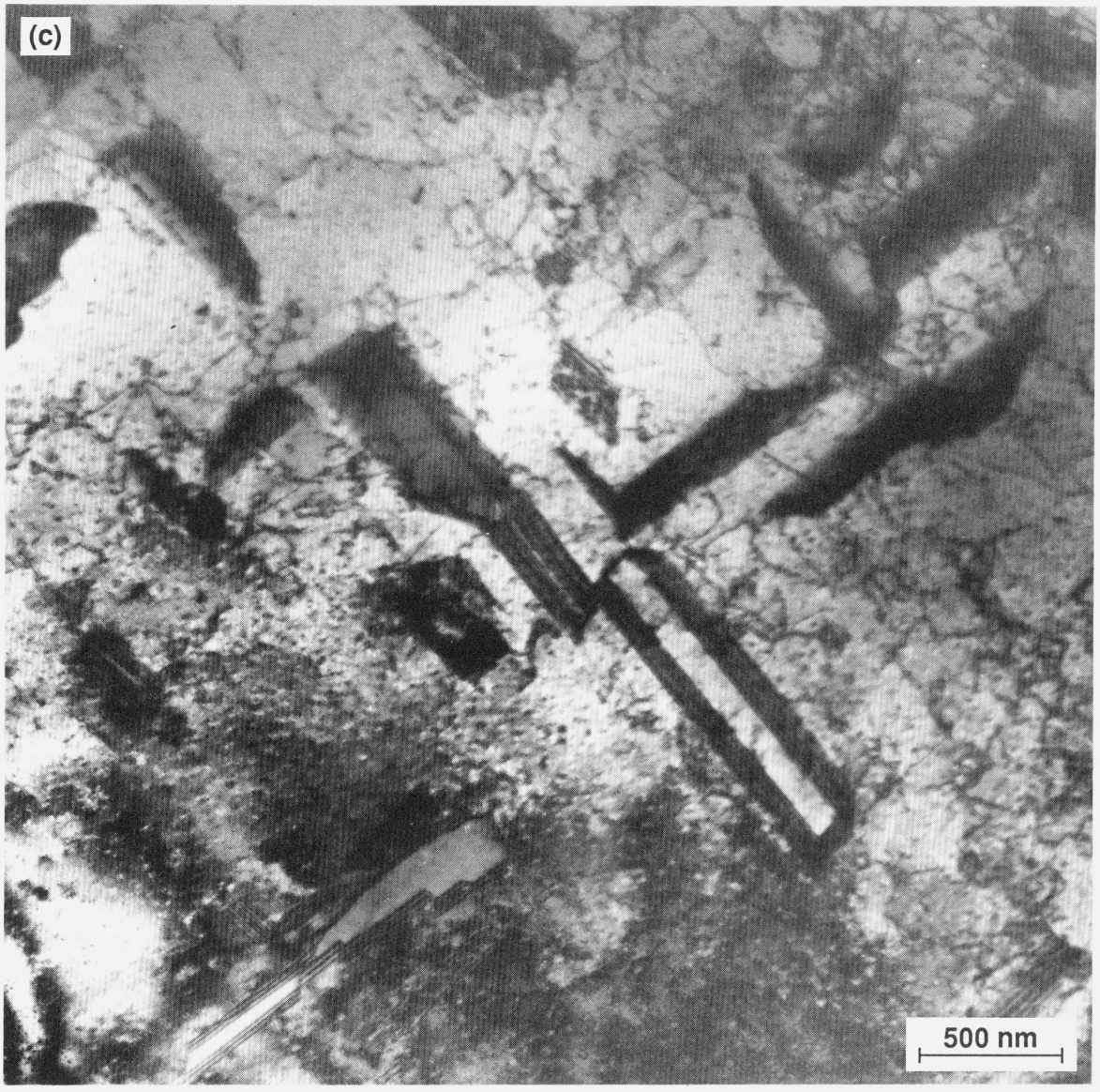

Figure 3.4. (c) Transmission electron micrograph of diffusion-welded-silver interlayer joining steel base metals, showing annealing twins and dislocations in the recrystallized region of the interlayer.

CHAPTER 4
TORSION TEST RESULTS

4.1. Effect of Interlayer Microstructure

The base metals provide relatively little mechanical constraint of the interlayer during torsional loading (shear stress is parallel to the interlayer plane). Therefore, torsion testing allows the mechanical behavior of the interlayer material itself to be studied. The behavior of the interlayer in shear can be converted to equivalent uniaxial tensile behavior using the von Mises stress and strain criteria, $\bar{\sigma} = \tau\sqrt{3}$, and $\bar{\varepsilon} = \gamma/\sqrt{3}$, where τ and γ are shear stress and strains, respectively. Effective (von Mises) stress-strain ($\bar{\sigma}$-$\bar{\varepsilon}$)behavior for a 150-μm-thick silver joint (between maraging steel) tested in torsion is shown in Fig. 4.1, along with results reported for bulk polycrystalline (annealed) silver.[49] The bulk-silver specimen yields (0.2% effective plastic strain offset) at 21 MPa and reaches a maximum (or steady-state) effective stress of 235 MPa at an effective strain of about 2.5. The yield stress (0.2%) of the diffusion-welded joint is 6 times greater (115 MPa) than the bulk-silver value. The strain-hardening rate, $d\sigma_{eff}/d\varepsilon_{eff}$, at an effective stress of 100 MPa is over 9 times greater (3800 vs. 400) than bulk polycrystalline silver.[49] The maximum interlayer stress of 259 MPa is attained after a strain of only 0.3 (99% of the maximum value is attained after a strain of only 0.1). Therefore, the interlayer silver strain-hardened at a higher rate and reached essentially the same maximum stress as the bulk silver specimen, although at a substantially lower strain.

Only a relatively mild increase in yield stress and strain-hardening rate above those of bulk silver were observed in torsion tests of brazed-silver joints between steel.[50] The yield stress of brazed joints (of comparable thickness to those tested in the present study) was only about 1-1/2 times greater than bulk polycrystalline silver; the strain-hardening rate was about 4 times greater. The investigators[50] suggested that higher interlayer yield stresses and strain-hardening rates result from a concentration of most of the plastic deformation in

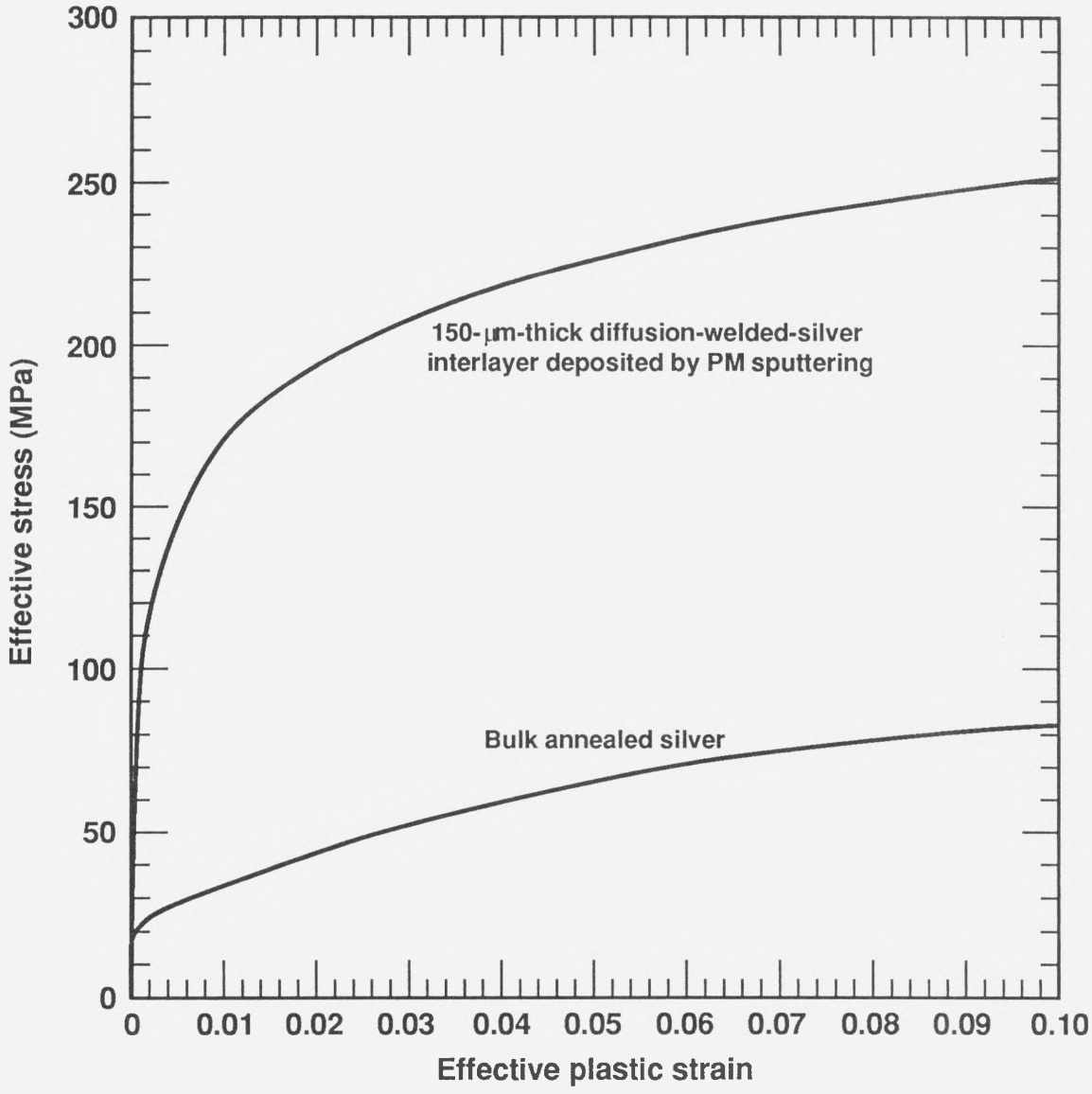

Figure 4.1. (a) Effective (von Mises) stress-strain behavior of silver tested in torsion. Substantial differences in yield stress between 150-μm-thick silver joints and bulk polycrystalline (annealed) silver[49] are shown for effective plastic strains to 0.1.

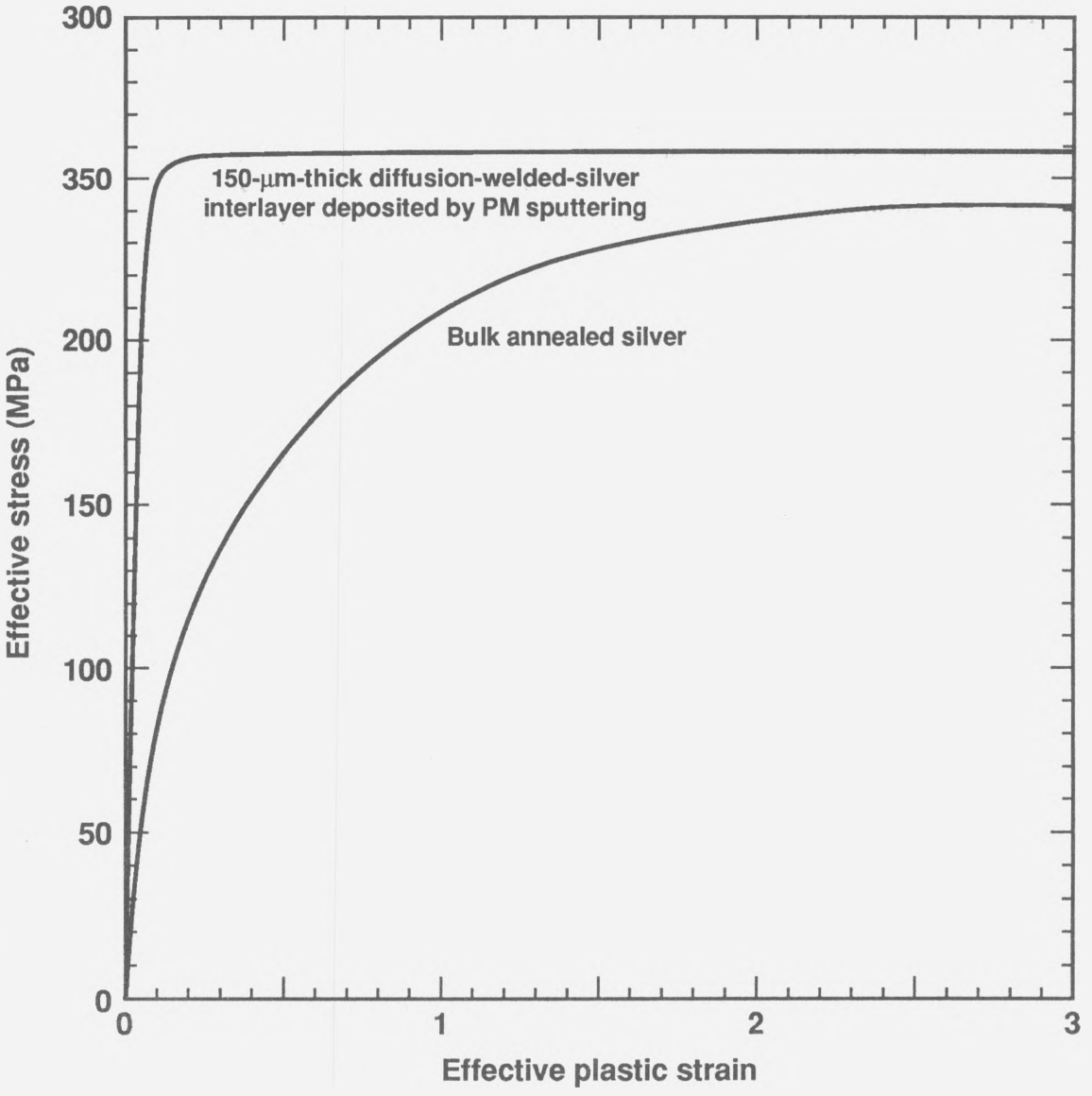

Figure 4.1. (b) Effective (von Mises) stress-strain behavior of silver tested in torsion. Substantial differences in strain-hardening rates between 150-μm-thick silver joints and bulk polycrystalline (annealed) silver[49] are shown for effective plastic strains to 3.0.

the central portion of the silver interlayer, whereas a region of only limited deformation extends outward from the steel interface. Scribe marks across the interlayer (parallel to the torsion axis) revealed that a region of limited deformation extends outward from the steel interface, giving rise to an "s-shaped" strain pattern (similar results were found in the present study for PM sputter-deposited silver joints which consisted of mostly recrystallized grains). This heterogeneous deformation may be due to a combination of effects: (1) complexity of slip near the base-metal interface resulting in a region of high strain-hardening and limited deformation, and/or (2) a structure gradient in the interlayers that is evident in the transmission electron micrographs of this study (see Fig. 3.4c). It should be noted that torsion testing of specimens with recrystallization on only one side of the interlayer (one of the two coated halves) resulted in a concentration of most of the plastic deformation in the recrystallized structure. These interlayers exhibited substantially higher strain-hardening rates, based on calculating strain over the entire interlayer gage length (this will be discussed further in the next section).

The relatively high concentration of barriers (strong nonrecrystallized grains, twins, and, perhaps, forest dislocations) to dislocation movement present in the diffusion-welded-silver structure may account for the higher yield stress (and, perhaps, the higher strain-hardening rate) of PM sputter-deposited interlayers compared with that of bulk silver specimens tested in torsion. Torsion tests of diffusion-welded silver interlayers coated by HHC evaporation have been reported using uranium-to-SS base metals.[21] The investigators reported increases in the yield stress and strain-hardening rates from bulk-silver values comparable to those found in the present study. However, they reported the steady-state stress of silver joints to be approximately 25% higher (311 MPa) than that of bulk silver, compared with 10% higher values found in the present study. One explanation for this difference may be the presence of tantalum impurities reported[19] in the silver of HHC deposits. Approximately 0.7–1.0% Ta (by weight) was analyzed in HHC-deposited silver using Auger spectroscopy.[51] The addition of impurities may raise the maximum, or

steady-state stress and, perhaps, explain the increase in steady-state stress of silver joints utilizing HHC deposition compared with those utilizing PM sputter-deposition. As discussed later in this chapter, the impurities may stabilize an "as-deposited" structure and preclude substantial recrystallization during the diffusion-welding process. This would also lead to higher yield and maximum stresses.

4.2. Effect of Interlayer Thickness and Annealing Temperature

Figure 4.2 shows the effective stress-strain behavior for 1000-μm-thick silver joints (between maraging steel) tested in torsion, as a function of prior annealing temperature (at an applied hydrostatic pressure of 207 MPa), compared with those of 150- or 1000-μm-thick interlayers with no additional annealing beyond that of the HIP cycle (673 K). (Torsion specimens annealed above 883 K at 1 atmosphere exhibited cracking at the silver-steel interfaces. These specimens failed in torsion testing at effective stress levels of only 60 Mpa, corresponding to effective plastic strain levels of ~0.03. Therefore, all annealing was accomplished by maintaining pressure at temperature using the standard hot-isostatic-pressing cycle shown in Fig. 2.10).

In general, the stress-strain behavior for a 1000-μm-thick silver interlayer tested in torsion was the same as that of a 150-μm-thick interlayer. It should be noted that in several tests of either thickness interlayer, the strain-hardening rate appeared to be higher than shown in Fig. 4.2, although the steady-state or saturation stresses were nearly identical. This phenomenon may be due to the presence of a more substantial nonrecrystallized structure in one side of the interlayer. Examination of fine scribe lines placed across these interlayers revealed that the strain in the silver was mostly concentrated in one side of the interlayer (one of the two coated halves). However, the maximum, or steady-state stresses of the two types of interlayers (fully or one-half recrystallized) are essentially the same.

Annealing the PM sputter-deposited-silver interlayers at temperatures ranging from 1073–1123 K resulted in only a modest decrease in yield stress and strain-hardening rate

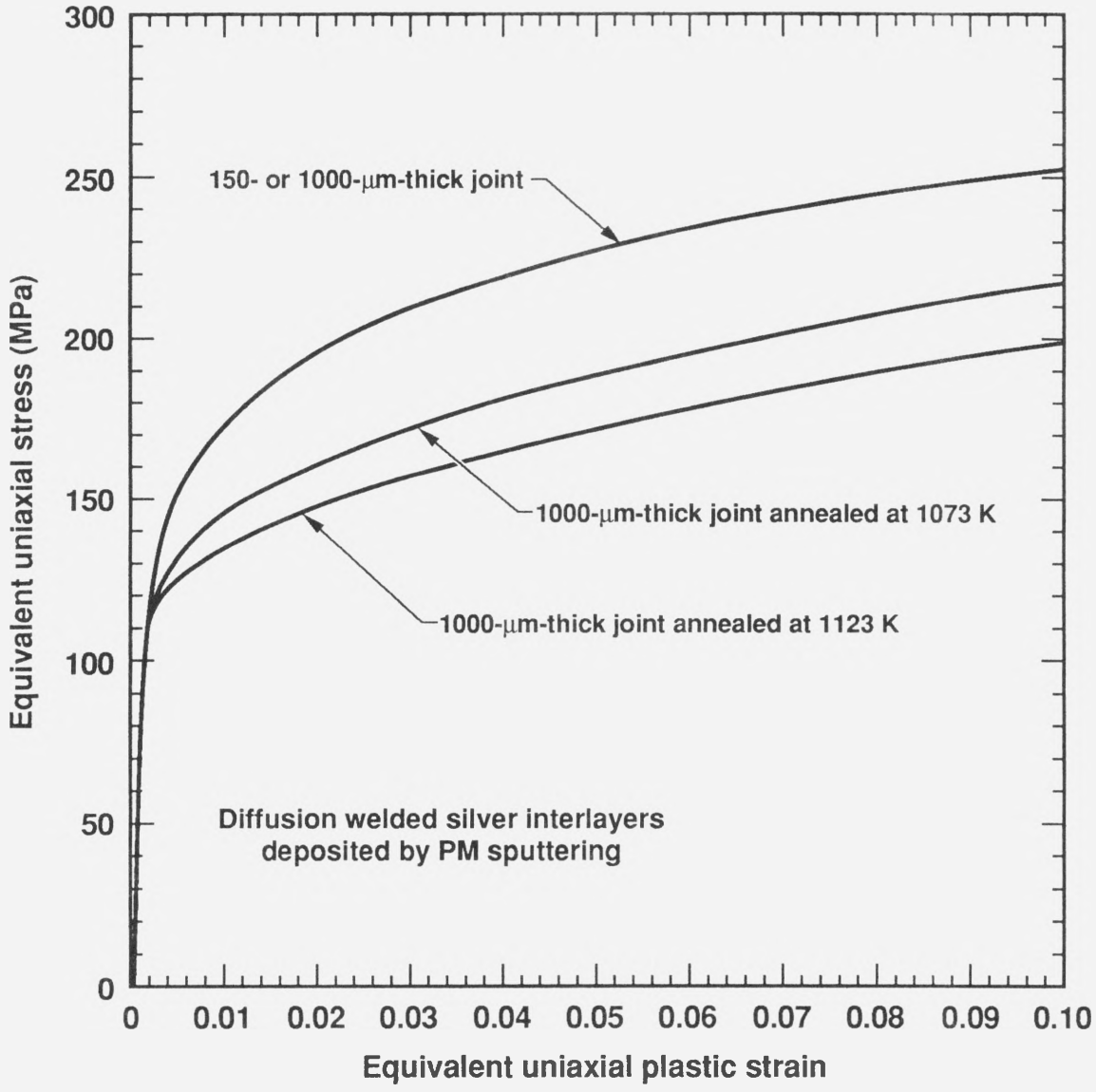

Figure 4.2. Effective stress-strain behavior of silver joints (between maraging steel) tested in torsion, as a function of prior annealing temperature (at an applied hydrostatic pressure of 207 MPa) Strain-hardening rates of 150-μm- and 1000-μm-thick interlayers are similar.

below those of "as-hipped" (673 K) specimens. However, the steady-state or saturation stresses are nearly the same as those of the "as-hipped" specimens. The yield stress and strain-hardening rate of the "annealed" diffusion-welded silver remain greater than those of bulk polycrystalline (annealed) silver (see Fig. 4.1). This may be explained by barriers (annealing twins, and, perhaps, nonrecrystallized grains) to dislocation movement that may still be present in the diffusion-welded-silver structure even after "annealing."

CHAPTER 5
TENSILE TEST RESULTS

5.1. Effect of Base-Metal Properties

Results from tensile tests of the diffusion-welded-silver joints are listed in Table 5.1. Diffusion welds of the maraging steel failed at stresses below the yield stress of the base metal. In contrast with the behavior of maraging steel, uranium and stainless steel base metals undergo plastic deformation prior to joint failure. Base-metal yielding is known to relax the triaxial constraint in the interlayer and cause increased plasticity which leads to failure of the joint at lower stresses.[34–36] Fracture occurred after ~2–3% plastic strain in the base-metal gage section for the 150-μm-thick joints in uranium or type 304 stainless steel. However, joints with cold-drawn type 316 SS (high yield stress) failed with only 0.1% plastic strain in the base-metal gage section. The mechanical constraint produced by the base metals with high yield stresses inhibits the development of shear stresses in the

Table 5.1. Tensile test results for diffusion-welded-silver joints between base metals.

Base-Metal (Surface Finish To Be Coated)	Ag Interlayer Thickness, μm	Ultimate Strength, MPa	Plastic Strain at Fracture, %[a]
Maraging steel (machined)	150	656	0.0
Maraging steel (machined)	1000	483	0.0
Maraging steel (lapped)	150	758	0.0
Maraging steel (lapped)	50	793	0.0
Annealed 304 SS (machined)	150	304	3.1
CW type 304 SS (machined)	150	400	2.2
CW type 304 SS (lapped)	150	414	2.8
CD type 316 SS (lapped)	150	704	0.1
Uranium (machined)	150	442	2.0
8091 Al alloy (machined)	50	269	0.2[b]

[a] Measured in the base-metal gage section.
[b] Fractured in base metal.

interlayer thereby increasing the strength of the joint. Concurrently, large hydrostatic stresses develop causing failure in the silver to occur with very low strain.[29,36]

In contrast with the behavior of ductile base metals, 8091 Al alloy is brittle in the as-cast condition (0.2% plastic strain-to-fracture), and fracture occurs in the base metal at stress levels lower than the strength of the joint. This phenomenon has also been observed in joints using silver interlayers between beryllium base metals (~1% plastic strain-to-fracture).[12,13,52]

The average plastic strain in the silver interlayer prior to fracture was determined to be ~3–4% for diffusion welds utilizing plastically-deforming base metals (~1% more than that within the base-metal gage section), and ~0.2% for diffusion welds utilizing elastic base metals. For a similar joint thickness-to-diameter ratio, plastic strain in silver brazes was reported to be ~12% for plastic base-metal specimens (~10% more than that within the base-metal gage section), and 1–1.5% for elastic base-metal specimens.[36] The difference in ductility between PM sputter-deposited silver and brazed silver may be due to differences in the microstructure as discussed in Section 3.3.

The observed trend of decreasing ultimate joint strength (UTS) with decreasing base-metal yield stress (see Tables 2.1 and 5.1) has been reported for joints fabricated with brazed interlayers.[29,36] Contrary to this trend, however, higher ultimate strengths were achieved with uranium (σ_y = 242 MPa) than with cold-worked (CW) SS (σ_y = 359 MPa). This anomaly is probably due to the higher strain-hardening rate of uranium, resulting in a higher stress at what appears to be a critical plastic strain (~2–3%) for fracture.

Improving the coated-base-metal surface finish (lapping vs. machining) was found to increase the joint strength. This observation is in agreement with previously reported results for vapor-deposited-silver interlayers between beryllium base metals utilizing either machined or lapped surfaces.[52] Diffusion-welded-silver joints between machined beryllium surfaces were reported[52] to fail in the silver at stress levels 20% below those of joints fabricated with lapped beryllium surfaces.

5.2. Effect of Interlayer Thickness

The effect of interlayer plastic constraint is known to increase with decreasing interlayer thickness-to-diameter (t/d) ratio.[29–39] This explains why the fracture stress is higher for the 150-μm- (vs. the 1000-μm-) thick interlayer joints using machined base-metal surfaces. The fracture stress is also higher, although only slightly, for the 50-μm- (vs. the 150-μm-) thick interlayer joints using lapped base-metal surfaces.

Joint strengths of both brazed-silver alloy[35,36] and diffusion-welded interlayers utilizing electrodeposited silver[11] between maraging steel base metals were also reported to increase with decreasing interlayer thickness. However, the diffusion-welded-(electrodeposited) silver joints exhibited a minimum thickness below which strengths decreased.[11] This decrease was attributed to incomplete diffusion welding of the silver caused by the increased effect of surface flatness deviation on very thin coatings. A decrease in strength for very thin joints was also observed in diffusion-welded-nickel foils between nickel-alloy base metals[38] and between various brazed joints (including pure silver) between steel base metals.[29,31,53] These studies reported that joint strengths in tension increased with decreasing interlayer thickness due to increased plastic constraint by the base metals. However, in one case,[38] interlayer-base-metal contact during diffusion welding was reported to decrease with decreasing interlayer thickness. This effect was attributed to the constraint produced by the base metals on the soft foil interlayer during compressive loading, which inhibited the deformation of the foil presumably required to close gaps at the interfaces. The investigators[38] were successful in decreasing the optimum interlayer thickness by increasing the diffusion-welding parameters (pressure, temperature, time), thereby increasing resultant joint strengths. For the case of brazed joints,[29,31,53] a decrease of the tensile strength in extremely thin joints ($t/d < 0.004$) was attributed[29] to incomplete wetting during brazing. Therefore, maximum strength thresholds for decreasing joint thickness-to-diameter ratios have been reported for diffusion-welded foils and coatings as well as brazed interlayers. It will be shown in Section 6.2.2 that the

occurrence of a strength plateau with decreasing t/d ratio for very thin interlayers ($t/d < 0.01$) may be due to a plateau in decreasing effective stress with decreasing t/d ratio as predicted by FEM analysis.

5.3. Comparison With Joints Fabricated by Other Processes

5.3.1. Diffusion-Welded Interlayers

In general, the tensile strengths of PM sputter-deposited-silver joints between various base metals from this study are equal to or greater than those previously reported utilizing other silver-coating methods and similar diffusion-welding parameters. For elastic base metals with lapped surfaces, tensile strengths of 758 and 793 MPa using 150-μm- and 50-μm-thick interlayers, respectively, in the present study are comparable with HHC-deposited-silver joints (758 MPa using 10-μm-thick interlayers) and greater than those of electrodeposited-silver joints (669 MPa using 25-μm-thick interlayers).[11] However, the tensile strength values for silver joints fabricated using these other two coating methods are achieved with considerably thinner interlayers having the advantage of greater plastic constraint produced by the base metals.

For type 304 SS plastic base metals with machined surfaces and 150-μm-thick joints, tensile strengths of 304 MPa ($\sigma_{y,\,SS}$ = 221 MPa) and 400 MPa ($\sigma_{y,\,SS}$ = 359 MPa) from the present study are comparable with electrodeposited-silver joint strengths of 321–367 MPa ($\sigma_{y,\,SS}$ = 296 MPa).[12] For uranium (plastic) base metals with machined surfaces, the tensile strength of 442 MPa ($\sigma_{y,\,U}$ = 242 MPa) from the present study exceeds electrodeposited-silver joint strengths of ~255 MPa (despite the higher base-metal yield stress; $\sigma_{y,\,U}$ = 345 MPa) and HHC-deposited-silver joint strengths of 345–373 MPa in other studies.[12, 52] However, the lower joint strength using HHC-deposited-silver[52] may have resulted from a lower diffusion-welding pressure (138 MPa) and temperature (589 K) than used in the present study. The tensile strength of diffusion-welded-silver joints between dissimilar metals, such as uranium (σ_y = 345 MPa) and type 304 SS

(σ_y = 296 MPa) fabricated using HHC deposition has been reported to average 442 MPa.[20] The tensile strength of electrodeposited-silver joints between the same uranium and SS base metals which were diffusion welded at the same pressure (207 MPa), temperature (873 K), and time (2 h) from the present study averaged only 345 MPa. Therefore, diffusion-welded-silver joints fabricated using electrodeposition appear to be weaker than those fabricated using HHC deposition or PM sputter-deposition. This observation will be confirmed in Section 9.1 where the creep-rupture times of diffusion-welded-silver joints fabricated using electrodeposition are compared to those using HHC deposition.

5.3.2. Brazed-Silver Interlayers

The tensile strengths of PM sputter-deposited-silver joints exceeded those previously reported using brazed-silver interlayers for similar thickness-to-diameter ratios and utilizing lapped maraging steel base metals (deforming only elastically). Joint strengths of 420 MPa were reported[36] using brazed silver-alloy (4% Pd) interlayers (t/d = 0.046) compared to strengths of 758 MPa (t/d = 0.024) from the present study. The lower joint strength of brazed silver compared to PM sputter-deposited silver is believed to be at least partially the result of a high concentration of microvoids in the brazed silver, caused by solidification shrinkage during the brazing cycle.[29,36,53–56] Brazed-silver joints between AISI 4340 steel (deforming only elastically) achieved tensile strengths as high as 758 MPa in "void-free" joints, although with considerably thinner interlayers than those of the present study.[53] Void-free joints of thickness-to-diameter ratio comparable to those of the present study (t/d = 0.024) were reported to fracture in tension at only 450 MPa.[53] Solidification shrinkage voids (present in most of the specimens fabricated) were responsible for reducing tensile strengths 10–90% below the void-free values at all joint thicknesses tested.[53] Degradation of tensile strength due to the presence of shrinkage voids was also observed in dental gold and lead-tin solders between brass base metals.[54] The investigators reported that void-free joints could be fabricated using thick interlayers, but

porous joints resulted when interlayer thickness-to-diameter ratios were reduced below 0.05.[54] Applying a post-braze hydrostatic-pressure annealing treatment has been reported in several studies to decrease the volume fraction of microvoids, thereby increasing joint strengths above those of furnace-cooled joints.[54,55] As was shown in Section 3.1, PM sputter-deposited interlayers do not contain voids, which may partly explain the higher joint strengths compared to those of brazed interlayers.

Another possible explanation for the increased strength of joints fabricated with PM sputter-deposited silver compared to brazed silver may be due to differences in yield stresses and strain-hardening rates of the interlayers. Increasing the flow stress of the interlayer is known to increase the ultimate joint strength in tension.[32,35,37,39,56] Diffusion-welded-silver interlayers fabricated using PM sputter-deposition contain a high density of barriers to dislocation movement (see Section 3.1) and therefore, would be expected to exhibit a higher yield stress than that of brazed-silver joints. The higher yield stress of diffusion-welded-silver interlayers compared to that of brazed-silver joints under torsional loading was discussed previously in Section 4.2.

5.3.3. Reproducibility Compared With HHC Deposits

One significant improvement in diffusion-welded-silver joints using PM sputter-deposited coatings as opposed to HHC-deposited coatings is the reproducibility of mechanical properties among specimens from both given and differing coating operations. The scatter reported in creep rupture time at any given applied stress level for silver joints between uranium and type 304 SS utilizing HHC deposition from three separate coating operations was a factor of ~50.[20,40] The scatter in creep rupture time at any given applied stress level for silver joints between annealed type 304 SS utilizing PM sputter-deposition from three separate coating operations in the present study (to be discussed in Section 8.1) is only a factor of ~10. This difference in reproducibility may be due to variations in silver-base-metal adhesion and/or variations in silver structures. Three possible causes of these

variations are: (1) silver deposits from PM sputtering are of high purity, whereas those of HHC evaporation contain tantalum impurities (this point will be discussed further), (2) deposition rates are extremely uniform during PM sputtering compared to HHC evaporation (the structure of the deposit is partially determined by the deposition rate), and (3) transition between etching and coating phases is relatively simple and controllable for PM sputtering compared to that of HHC evaporation (Ar^+, Ag^+, and Ag are all present during the etching phase for HHC evaporation and vary with gas flow and electron beam current to the crucible, thereby allowing varying amounts of oxygen to re-contaminate the base-metal surface). Mechanical comparisons of process reproducibility between PM sputtering and other coating methods, such as electrodeposition or electron beam evaporation, are not possible due to a lack of published test results of joint strengths fabricated with these latter processes.

5.3.4. Foil Interlayers

Although there is only a limited amount of published test results of joint strengths fabricated with foil interlayers, it appears that interlayer-base-metal adhesion is difficult to achieve at temperatures below ~0.7 T_m of the interlayer. Tensile strengths of silver joints between alumina and type 321 SS were reported to be only 40 MPa when diffusion-welding parameters were 1073 K and 50 MPa for 0.5 h.[7] The investigators reported threshold diffusion-welding temperatures below which no measurable bonding was produced for each of the foils utilized (Ag, Al, Cu, and Ni). The threshold temperature to achieve diffusion welding of silver foils to alumina and type 321 SS was reported to be 873 K (0.7 T_m of the Ag), considerably higher than the temperature required to achieve diffusion welding of silver to itself (0.35 T_m).[13] Joint strengths of the other metal interlayers were reported to be comparable (40–50 MPa) to those of silver foils.[7]

Copper foils between WC-Co base metals ($\sigma_{y,\ WC\text{-}Co}$ = 638 MPa) were diffusion welded at 1323 K (0.98 T_m), and tensile joint strengths of 287–311 MPa were achieved

using interlayer thickness-to-diameter ratios comparable to those of the present study (t/d = 0.041–0.22).[39] The mechanical properties (yield stress and strain hardening rate) of pure copper are similar to those of pure silver. Therefore, fractures at the interlayer-base-metal interface at stress levels lower than those achieved with PM sputter-deposited silver (483–656 MPa) indicate that higher strengths may be achieved with coated interlayers than with foil interlayers. This conclusion is further supported by tensile tests reported for silver foil interlayers between type 304L SS and Ti-6Al-4V alloy.[57] These joints were fabricated by diffusion welding a 125-μm-thick silver foil between the base metals at 1153 K (0.94 T_m). The investigators[57] reported average joint strengths of 280 MPa. For annealed type 304 SS and 150-μm-thick joints fabricated using PM sputter-deposition, the tensile strength of 304 MPa from the present study is higher despite the higher base-metal yield stress of Ti-6Al-4V alloy used in their study.

5.3.5. Silver Interlayer Hardness

Microhardness measurements of as-deposited silver (by PM sputtering) and diffusion-welded silver interlayers (utilizing PM sputtering, HHC evaporation, or ion-plating) were compared with those of bulk silver and were found to be consistent with the mechanical properties and microstructures discussed previously. The average Vickers hardness value for as-deposited silver (by PM sputtering) from the present study was 130 DPH (diamond pyramid hardness), whereas that of diffusion-welded (recrystallized) silver was 67 DPH. The microhardness of annealed polycrystalline silver (99.999% pure) was 30 DPH. By comparison, the microhardness of ion-plated silver in diffusion-welds between 7010 Al alloy was reported[24] to increase from 40–60 DPH in the as-welded (553 K) condition to 140–170 DPH after solution heat treatment (SHT) (753 K for 16 h).[24] The investigators[24] attributed the hardening after SHT to diffusion of Zn and Mg solutes from the Al alloy into the silver interlayer. Interlayer microhardness measurements of diffusion-welded silver joints fabricated using HHC deposition yielded average values of 110 DPH,[58] substantially

higher than those fabricated with PM sputter-deposited silver. The differences in hardness could be explained by impurity hardening from tantalum in HHC-deposited silver and the fact that the HHC-deposited interlayer remains substantially nonrecrystallized. There is evidence for this possibility from optical metallography performed on diffusion-welded interlayers utilizing HHC-deposited silver.[58] It was determined that HHC-deposited silver consists of columnar grains (nonrecrystallized) in approximately 75% of the interlayer after diffusion welding. In contrast, PM sputter-deposited silver consists of columnar grains in only about 25–50% of the interlayer after diffusion welding. Chemical analysis performed on PM sputter-deposited silver using secondary ion mass spectroscopy (SIMS) failed to detect any impurities exceeding those of "background" trace amounts. Therefore, silver coatings deposited by PM sputtering are believed to be of very high purity compared with those of HHC deposition (containing 0.7–1.0 wt.% Ta) or electrodeposition (known to contain many trace impurities[12]).

5.4. Fracture Surface Characterization

Fracture surfaces of the elastic (maraging steel) or plastic (SS or uranium) base-metal tensile specimens (excluding Al-Li alloy) consist mostly of silver-silver fracture (80–100% of the specimen surface area) at the diffusion-welded-silver interface. Fractures referred to as "silver-silver" occur at or near the center of the interlayer, and results in approximately 75 μm of silver adhering to both of the base-metal surfaces. The remainder of the separation occurs at or very near one or both of the silver-base-metal interfaces. Fractures very near the silver-base-metal interface appear to occur at the recrystallized-nonrecrystallized silver interface ~1 μm from the silver-base-metal interface. Fractures at locations other than at or very near the three interfaces have not been observed.

Figure 5.1 shows a silver-silver fracture surface between elastic base metals with machined surfaces. (Unless otherwise noted, micrographs shown were taken using scanning electron microscopy). Unlike the silver-fracture surfaces from tensile-test joints

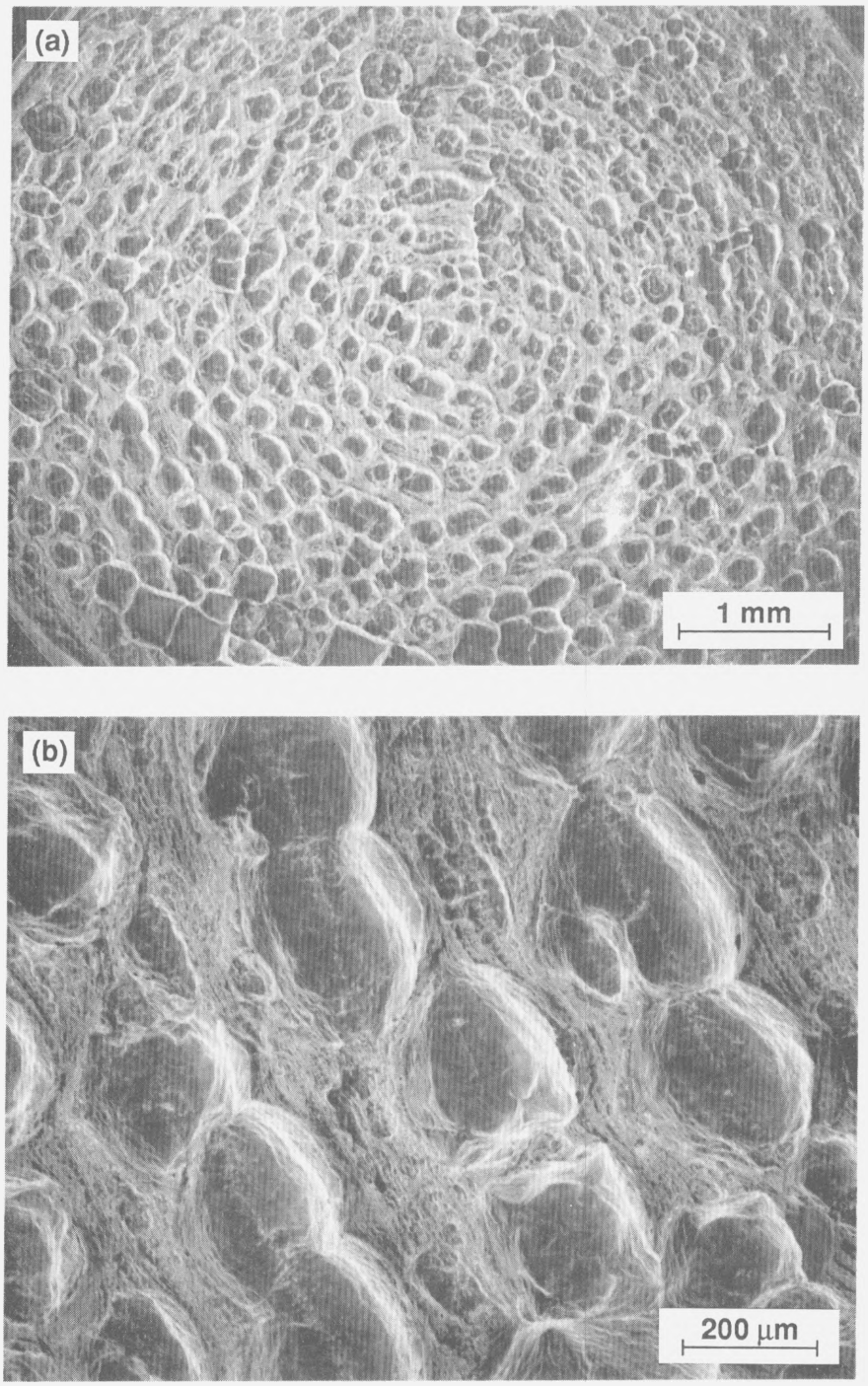

Figure 5.1. Typical high-stress fracture surface (621 MPa) of a diffusion-welded-silver joint between elastic base metals with machined surfaces. These type of separations exhibit heterogeneous cavitation (large cavities and small ductile dimples) parallel with the machining lay.

fabricated with plastic base metals (to be discussed next), large cavities formed during the fracture process in specimens utilizing machined maraging steel. These large cavities appear to have coalesced parallel to the machining lay of the coated-base-metal surface, and are separated by regions of small ductile dimples. In contrast with this fracture morphology, Fig. 5.2 shows a silver-silver fracture surface from a lapped type 316 stainless steel specimen. The dimpled surface is somewhat more uniform with no large cavities present. Although not pictured, silver-silver fractures between lapped surfaces of elastically-deforming base metals also consist mostly of the small, uniform-size dimples as shown in Fig. 5.2.

A typical fracture surface of specimens fabricated from plastically-deforming base metals which separated both at the silver-silver and at or near the silver-steel interfaces is shown in Fig. 5.3 (annealed type 304 SS). Silver-steel separations (seen as dark regions in Fig. 5.3a) occur along the outer circumference and in isolated (internal) areas. Fracture surfaces at the silver-silver interface of all specimens are characteristic of ductile fracture by microvoid coalescence. The fracture morphologies at the silver-silver interface may differ with the type of base metal (plastic vs. elastic) and, for the elastic base-metal case, the base-metal surface finish (machined vs. lapped). The ductile dimples along the silver-silver fracture surface of specimens with machined (elastic or plastic) base-metal surfaces corresponds with the circular machining tool marks of the base metal. Hence, microvoids at the silver-silver interface have nucleated and coalesced in a pattern closely related to the machining pattern. The silver coating replicates this pattern and heterogeneities at the diffusion-welded interface are produced that appear to serve as preferred nucleation sites for cavities that coalesce and cause failure. This is in contrast with the dimpled-fracture surfaces of lapped base-metal specimens, on which the voids tend to coalesce along the silver-silver interface without any apparent preferential sites of nucleation (see Fig. 5.2).

Fractures at the silver-base-metal interface do not usually show the same level of pronounced plasticity that was evident at the silver-silver interface in either the elastic or

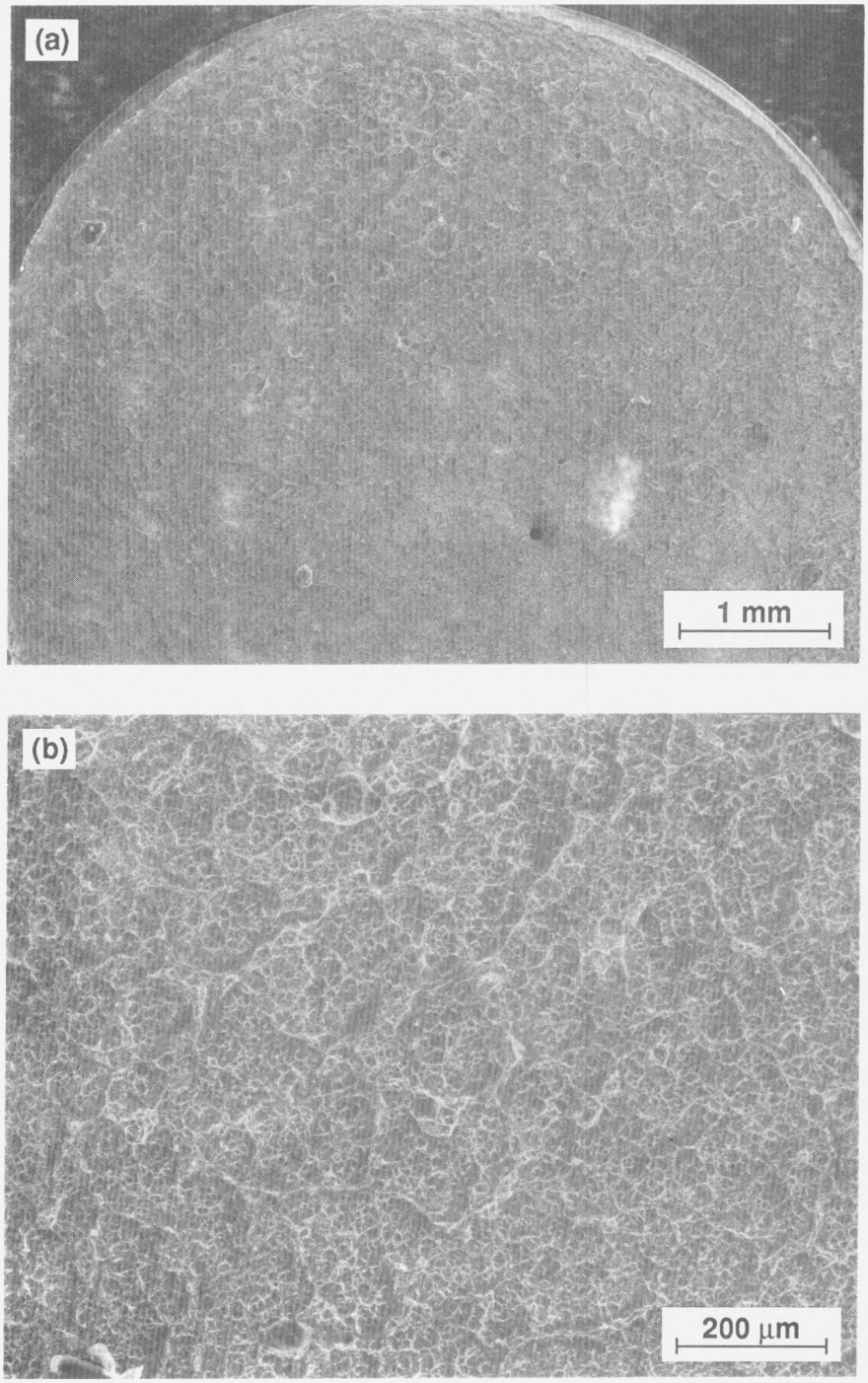

Figure 5.2. (a, b) Typical silver-silver fracture surface of a diffusion-welded joint between elastic or plastic base metals with lapped surfaces. These type of separations exhibit uniform-sized cavities (homogeneous cavitation). Specimen shown was fabricated from type 316 SS base metal, and fractured at 703 MPa.

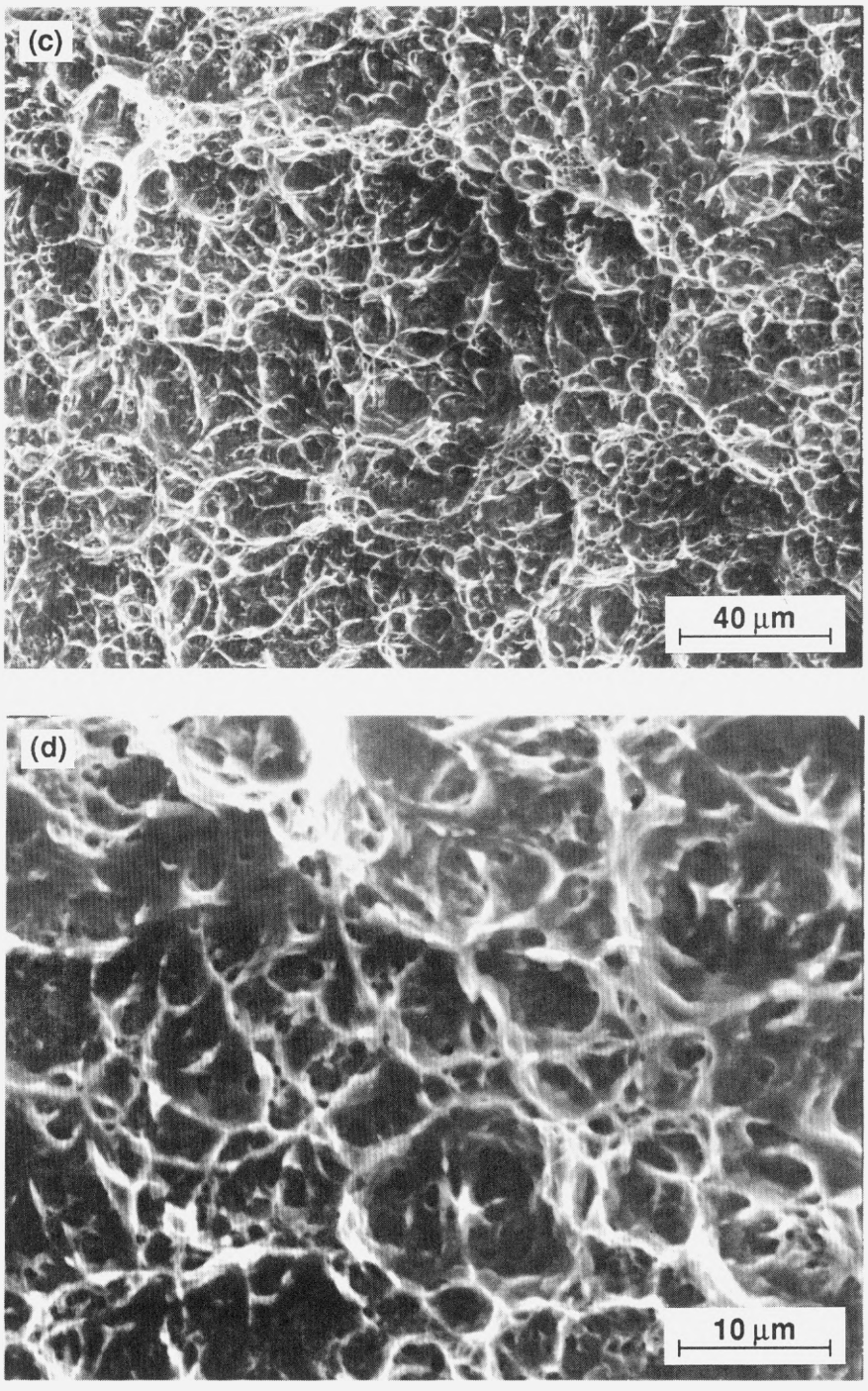

Figure 5.2. (c, d) Typical silver-silver fracture surface of a diffusion-welded joint between elastic or plastic base metals with lapped surfaces, resulting in uniform-sized ductile microvoid coalescence. Specimen shown was fabricated from type 316 SS base metal, and fractured at 703 MPa.

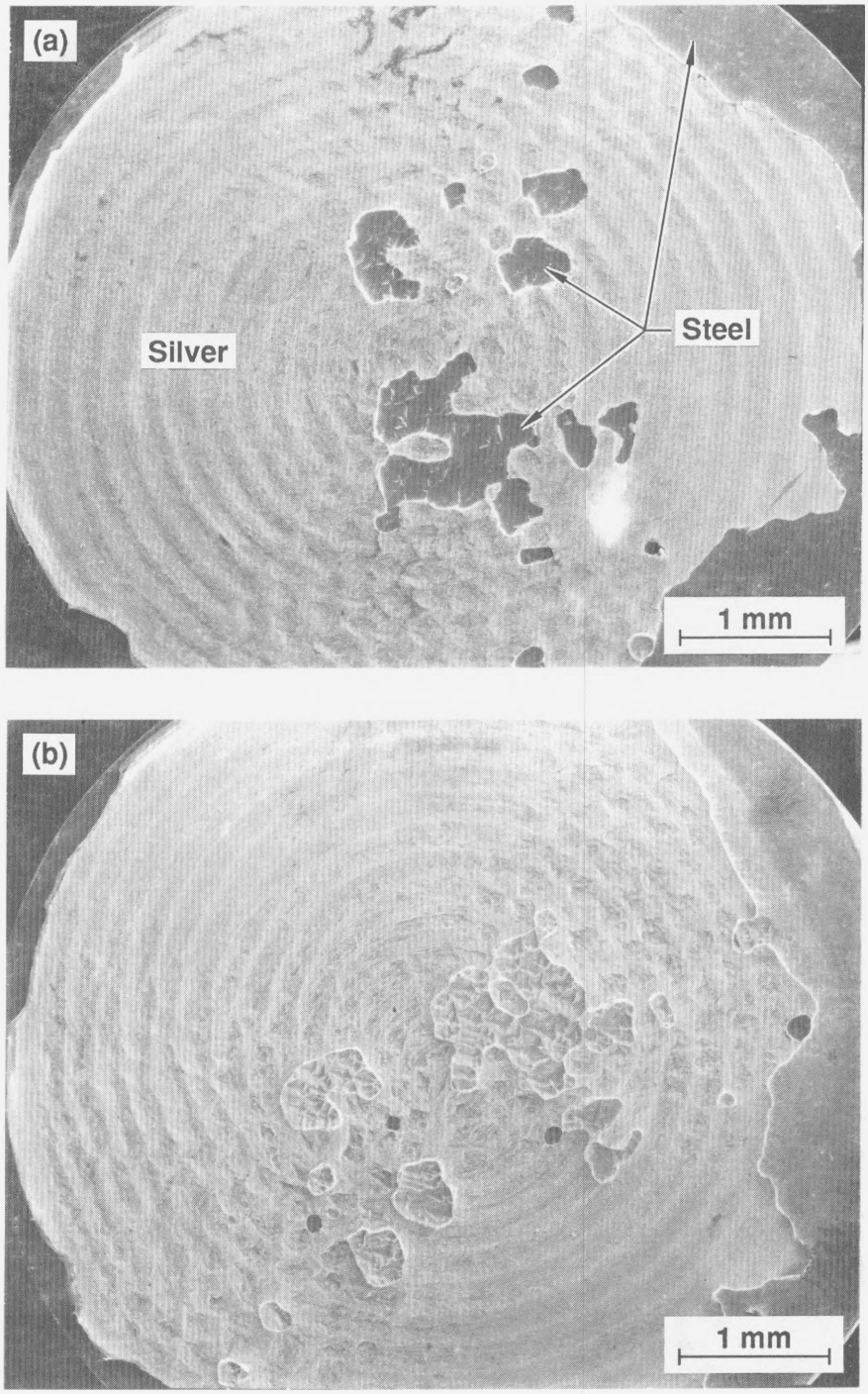

Figure 5.3. (a, b) Typical diffusion-welded-silver joint fracture (259 MPa) between plastic base metals (annealed type 304 stainless steel) with machined surfaces, showing both fractured halves.

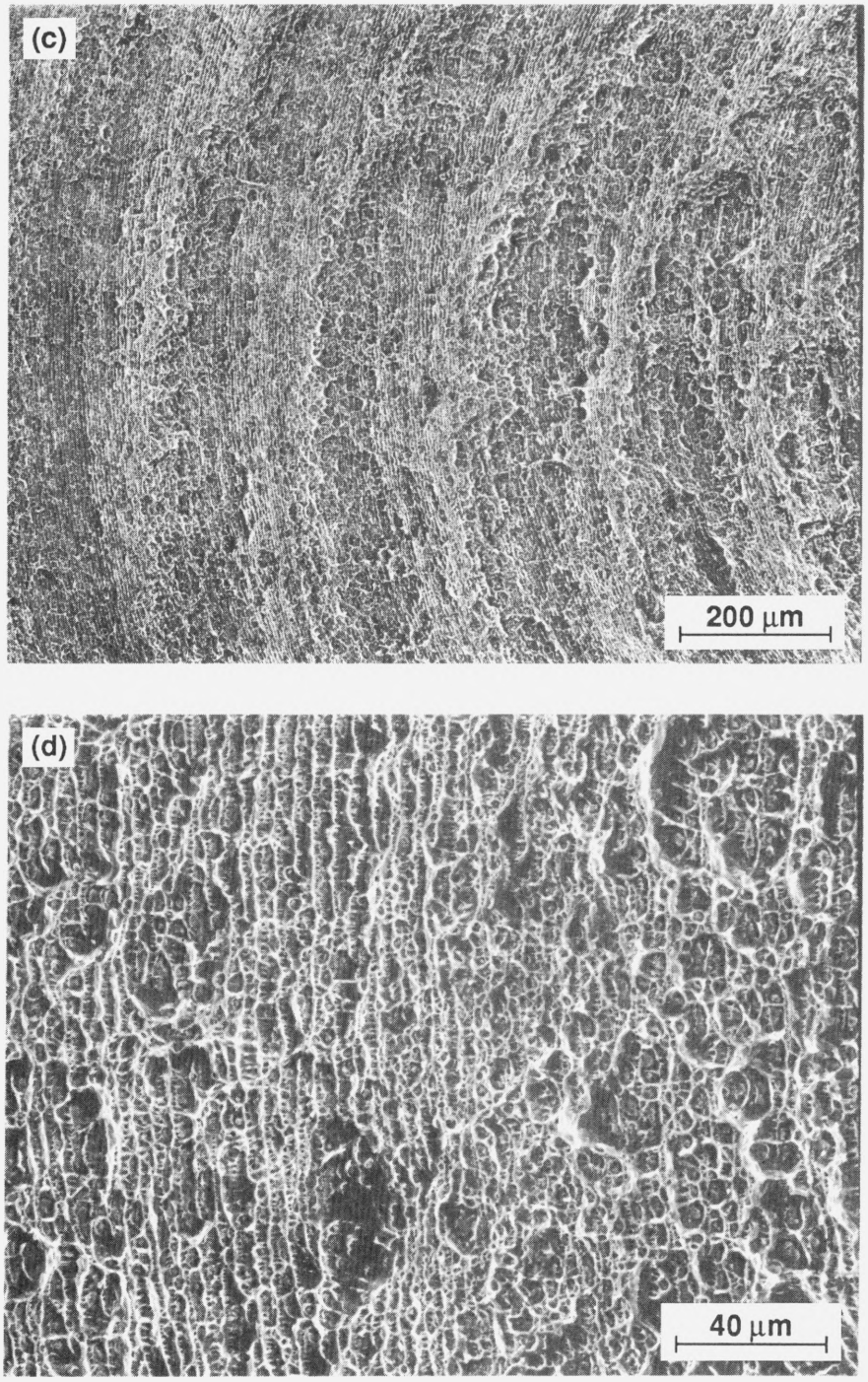

Figure 5.3 (c, d) Typical diffusion-welded-silver joint fracture (259 MPa) between plastic base metals (annealed type 304 stainless steel) with machined surfaces, resulting in ductile microvoid coalescence parallel with the machining lay.

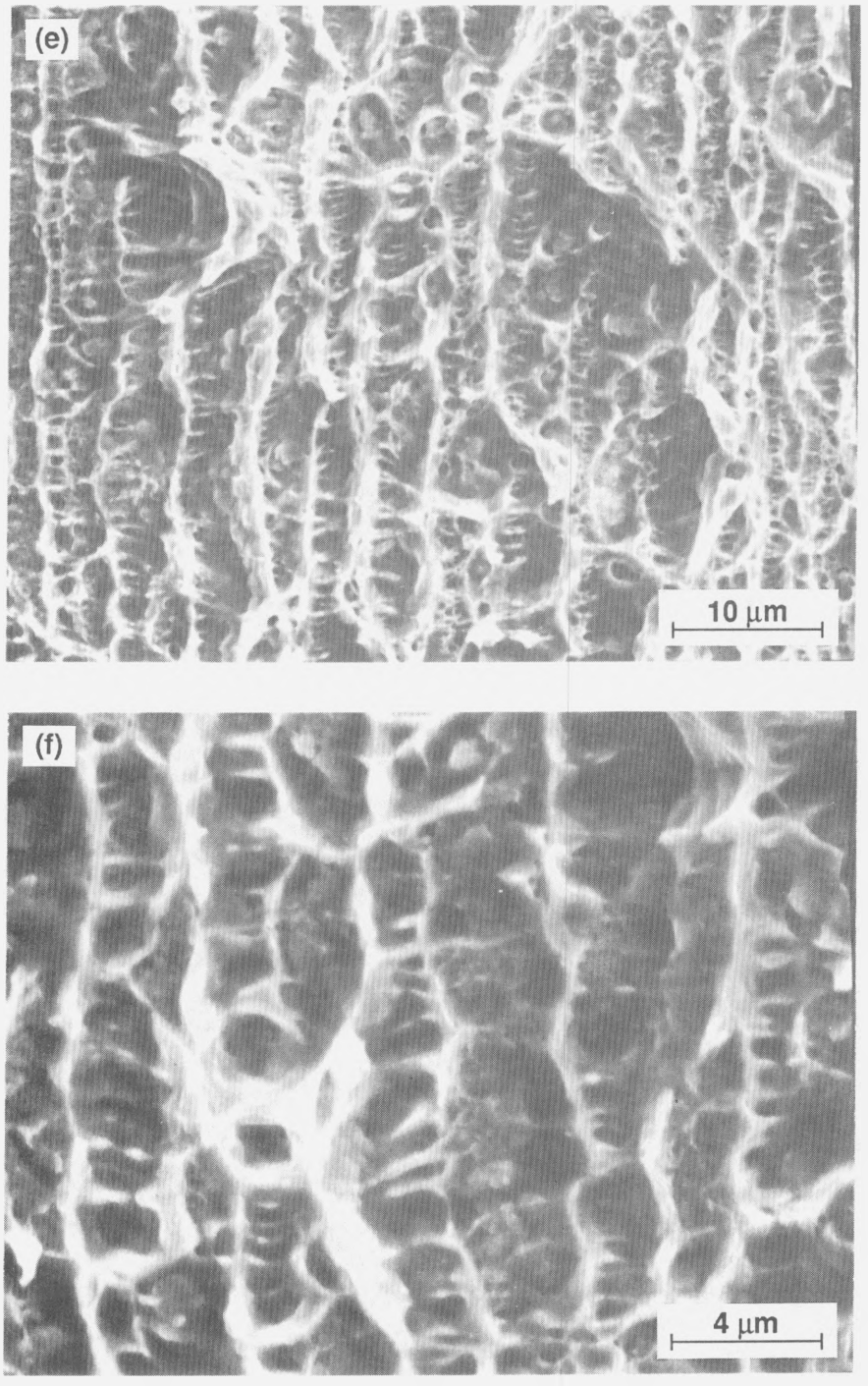

Figure 5.3 (e, f) Typical diffusion-welded-silver joint fracture (259 MPa) between plastic base metals (annealed type 304 stainless steel) with machined surfaces, resulting in ductile microvoid coalescence parallel with the machining lay.

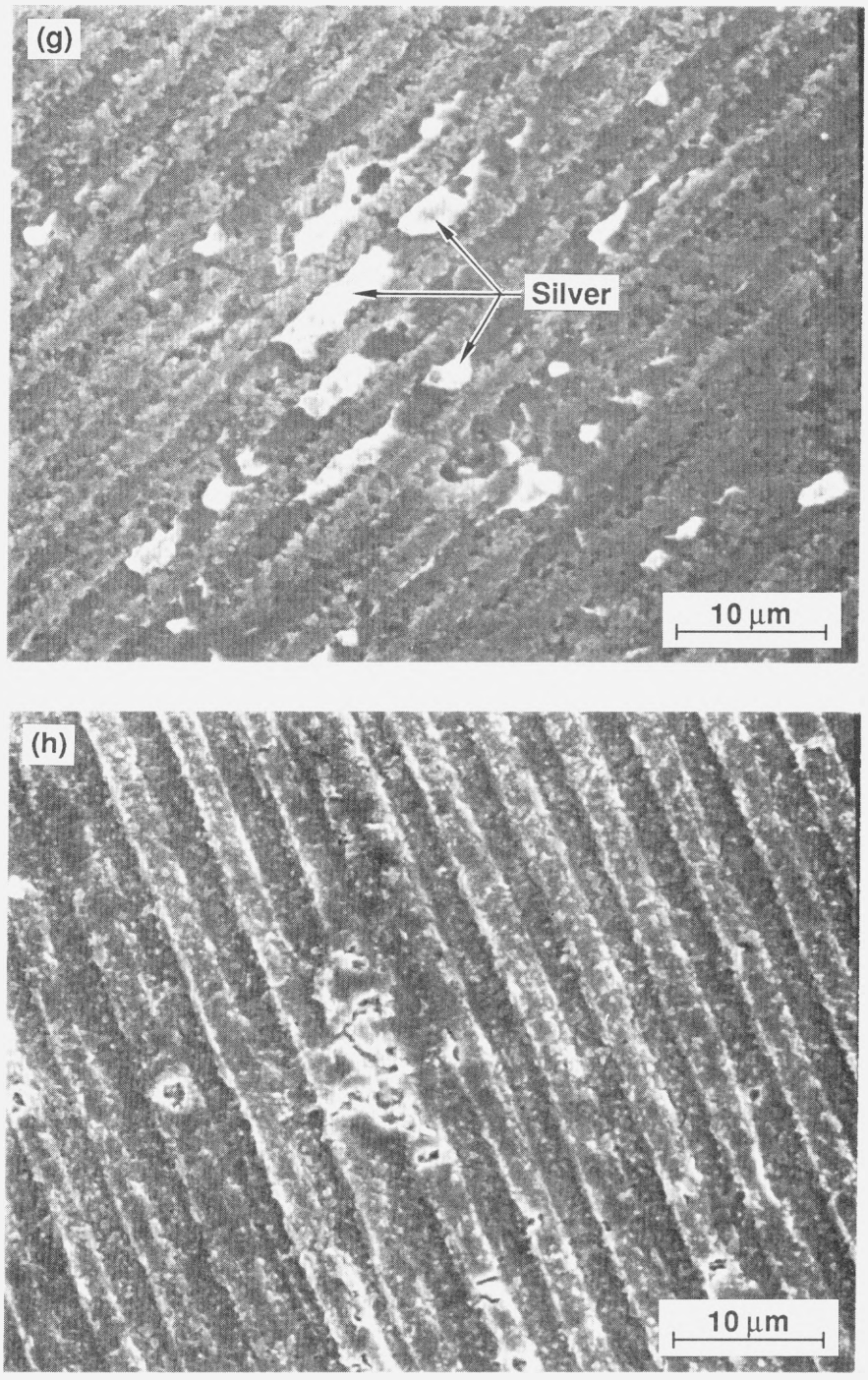

Figure 5.3. Very little silver appears to remain on the (g) steel side of silver-base-metal separations, shown replicated by the (h) silver side of the fracture surface.

plastic base-metal joints. Figures 5.3g and 5.3h are representative of one of the three types of silver-base-metal fractures observed for either elastic or plastic base-metal specimens. The other two types of fracture morphologies show more pronounced plasticity, and these will be discussed in Sections 6.4 and 8.4. The steel side of the fractured interface is shown in Fig. 5.3g, while the silver side is shown in Fig. 5.3h. Isolated regions of silver "pullout" remained on the steel surface, and obvious signs of plasticity are observed in those regions where the silver separated from the remaining interlayer. Energy dispersive spectroscopy revealed that the base-metal fracture surface consisted of predominantly stainless steel, with only isolated regions of the surface covered with silver. A previous study of tensile and creep rupture behavior of diffusion-welded-silver joints fabricated using HHC deposition demonstrated that the mechanical behavior or strength of interlayer joints is independent of the location of the fracture interface.[20] Therefore, the same damage mechanism may lead to failure at the silver-silver and silver-base-metal interfaces in spite of the differences in the general appearance of the fracture surfaces.

Figure 5.4 shows the fracture surface of a specimen fabricated using uranium base metals with machined surfaces. The silver-uranium fracture morphology shown in Fig. 5.4b (seen as dark regions in the micrograph) appears similar to the silver-steel fracture morphology shown in Fig. 5.3g. The silver-silver fracture surface shown in Figs. 5.4c and 5.4d appears similar to those of other silver-silver fractures between plastically-deforming base metals with machined surfaces, such as type 304 stainless steel shown in Figs. 5.3d and 5.3e.

The silver-fracture morphology of specimens utilizing the two different types of base-metal surfaces (machined vs. lapped) may be explained as follows. Silver deposition on the relatively rough machined surface results in a correspondingly rough silver surface, even after 75 μm of silver deposition. This phenomenon has also been reported for silver deposited by HHC evaporation onto machined base-metal surfaces.[20] The joining of the two rough surfaces during the diffusion-welding process may result in some kinds of

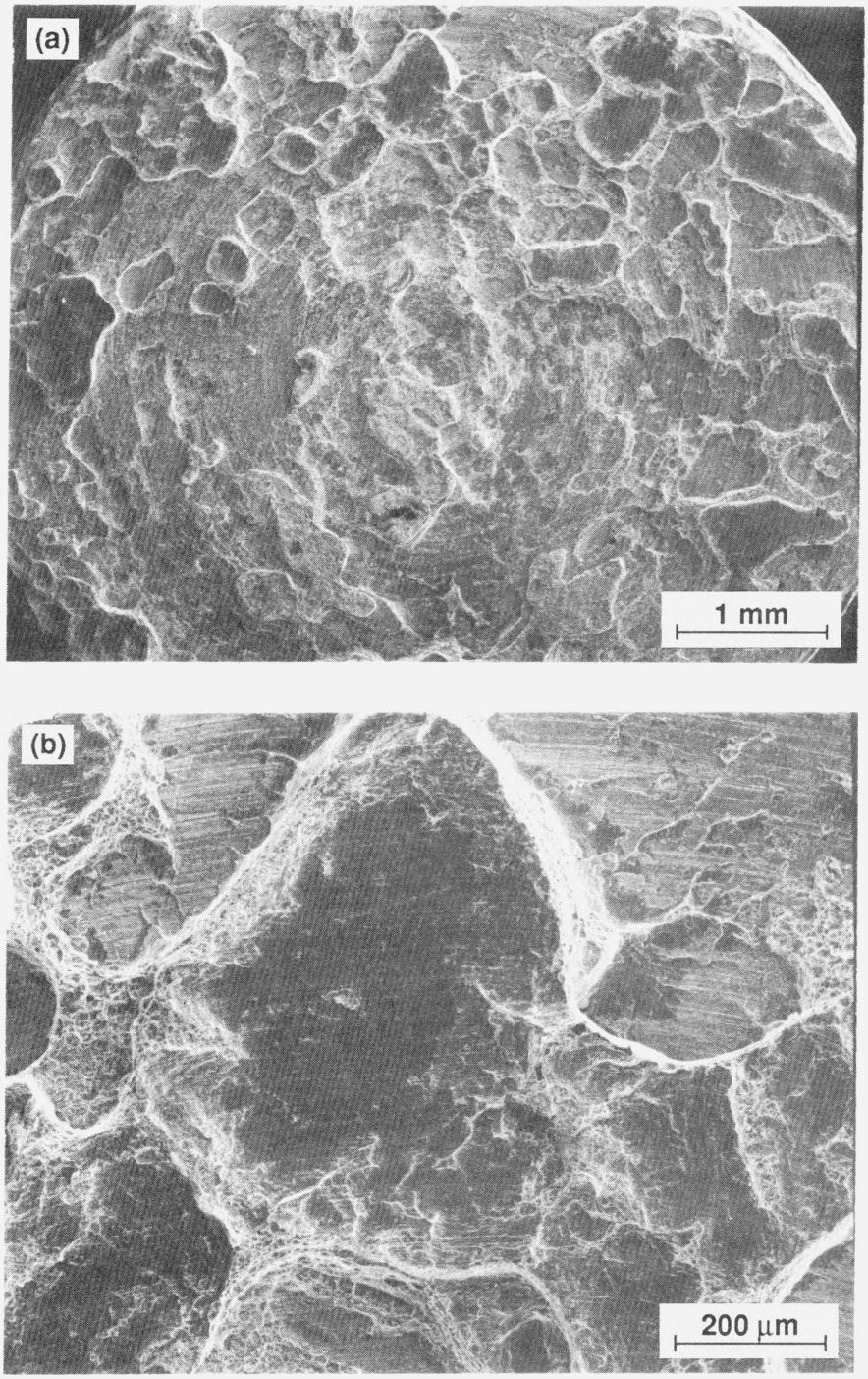

Figure 5.4. (a, b) Fracture surface of diffusion-welded-silver joint between uranium base metals with machined surfaces. The uranium side of silver-base-metal separations are the darker regions. Specimen fractured at 442 MPa.

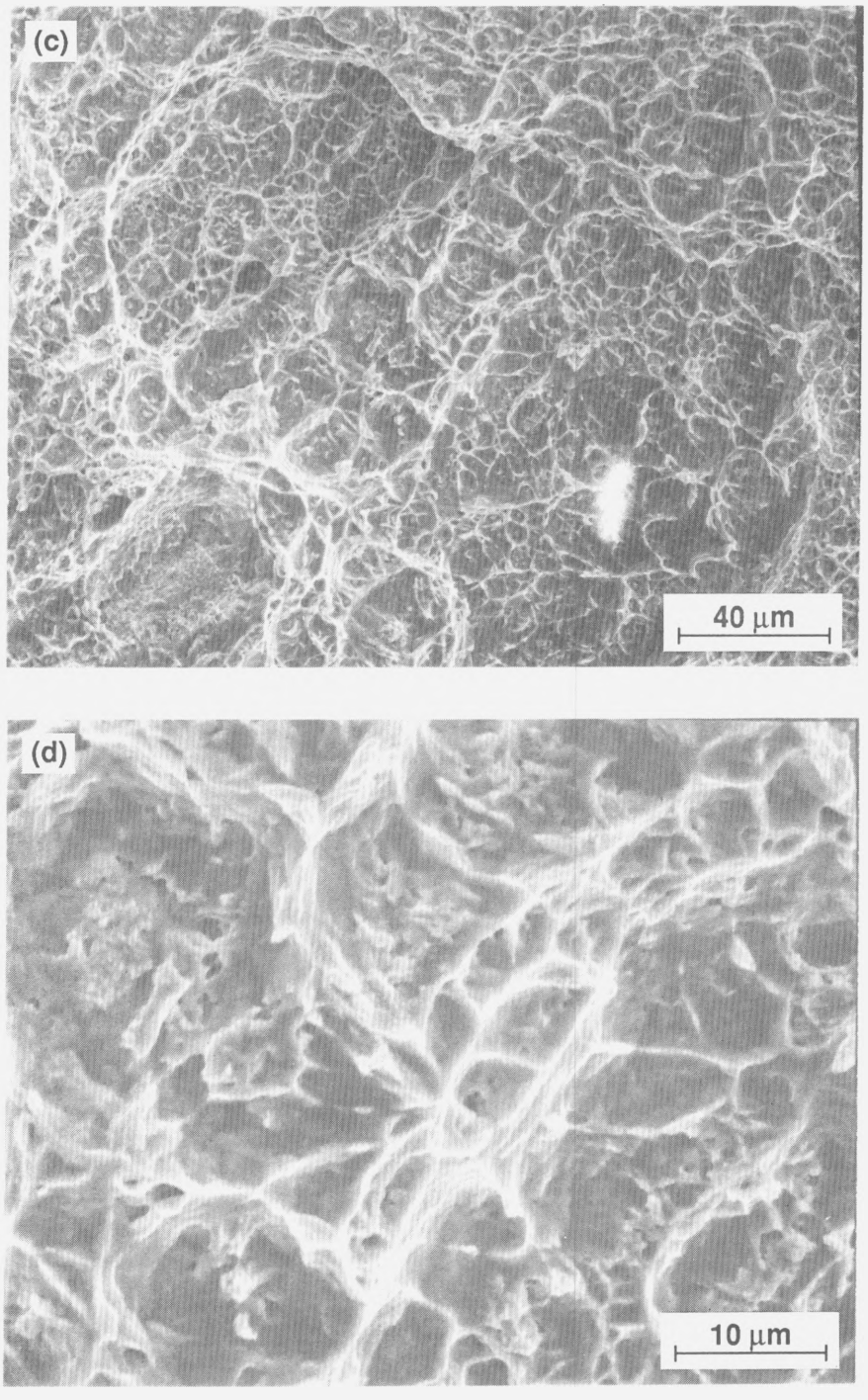

Figure 5.4. (c, d) Silver-silver fracture surface of diffusion-welded-silver joint between uranium base metals with machined surfaces. Specimen fractured at 442 MPa.

substructural heterogeneities (but not voids) at the diffusion-welded-silver interface that are less common in diffusion-welded joints fabricated using smoother surfaces of lapped specimens. In the case of specimens utilizing elastic base metals, the strain is not imposed by base metal deformation, but is indigenous to the interlayer. It is believed that the heterogeneities along the diffusion-welded-silver interface caused during the joining of the comparatively rough machined surfaces could result in regions which may be more resistant to plasticity than other regions. Cavities may form more easily in the regions less resistant to plastic strain leading to the formation of the very large, deep cavities of Fig. 5.1. When base-metal surfaces are lapped prior to coating, a more uniform silver-silver interface is created and the large cavities are not observed.

CHAPTER 6
CREEP RUPTURE RESULTS: ELASTIC BASE METALS

6.1. Effect of Surface Finish

Diffusion-welded-silver specimens utilizing either machined or lapped maraging steel base metals were tested in tension at constant stress levels less than 800 MPa, and these results confirmed that creep ruptures occur in the absence of base-metal plasticity, as shown in Fig. 6.1. As the applied stress (based on the original cross-sectional area) decreases, the time-to-rupture, t_r increases. Further, creep rupture is observed at stresses as low as 17% of the ultimate tensile strength (approximately equal to the stress level corresponding to a 1-second rupture time). Ambient temperature tests on maraging steel specimens for which the base-metal surfaces were lapped, rather than machined prior to coating, are indicated by circles with dots. At a given applied stress, lapped specimens fail at times approximately 50 times longer (range of 20–100) than those with machined surfaces. This difference between creep rupture times is consistent with the corresponding difference between ultimate tensile strengths (758 vs. 656 MPa for lapped vs. machined base-metal surfaces) as discussed earlier. Additionally, the slopes of the rupture time versus applied stress curves (or applied stress exponent, $n_{app} = [-\log t_r]/[\log \sigma]$) decrease with decreasing stress for both sets of data. This is in contrast with the results previously reported for creep ruptures between plastic base metals (uranium to SS), where the applied stress exponent was found to be constant over the range of stresses tested.[20,40] The significance of the creep-rupture stress exponent for elastic base metals will be discussed in Section 10.1.

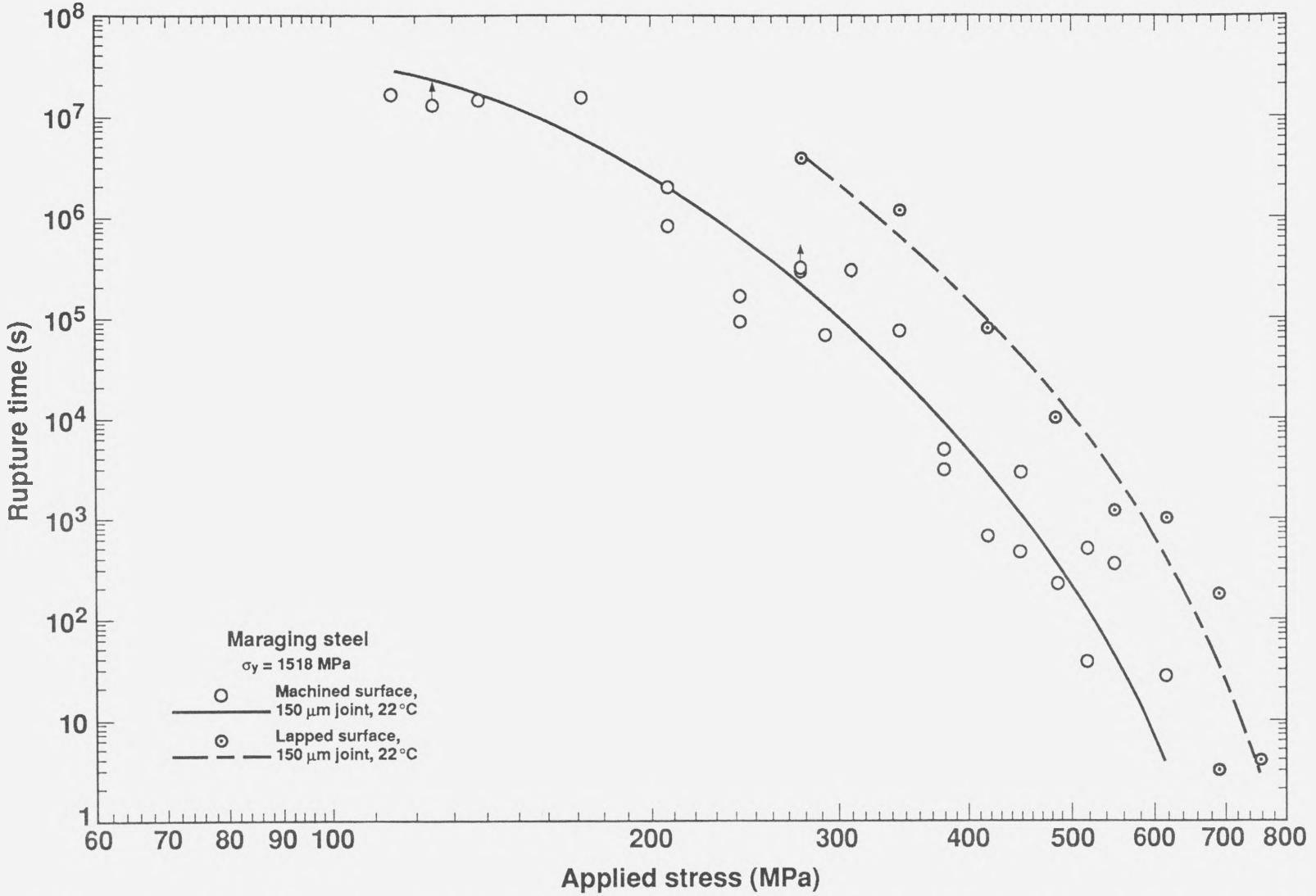

Figure 6.1. Effect of base-metal surface finish on creep rupture of diffusion-welded-silver joints between elastic base metals.

6.2. Effect of Interlayer Thickness

6.2.1. Experimental Results

Additional diffusion-welded-silver joints were fabricated using maraging steel and interlayer thicknesses of 50 μm (lapped base-metal surfaces) and 1000 μm (machined base-metal surfaces). These thicknesses correspond to substantial changes in the interlayer thickness-to-diameter (t/d) ratios (0.008 to 0.16). The effect of the changing interlayer thickness on the rupture time is indicated in Fig. 6.2. The figure also illustrates the rupture time versus applied stress behavior of 150-μm-thick diffusion-welded-silver interlayers using both lapped and machined maraging steel specimens that were presented in Fig. 6.1. Increasing the interlayer thickness by a factor of about 7 from 150 μm results in significantly decreased rupture times, but decreasing the interlayer thickness by a factor of 3 from 150 μm does not appear to substantially increase t_r or UTS, suggesting a possible trend of a limiting strength that is independent of decreasing thickness-to-diameter ratio. A trend of constant strength with decreasing t/d ratio has also been observed previously for ultimate tensile strengths of brazed-soft-metal interlayers between steel.[33] In this study, the investigators[33] noted that decreasing the t/d ratio resulted in no change in joint strength. This phenomenon may be different from that of a maximum strength threshold below which joint strengths decrease with decreasing t/d ratio, as discussed in Section 5.2. In those studies,[29,31,38,53] the investigators suggested that joining (brazing or diffusion welding) of base metals with surface flatness deviations may result in nonbonded regions which degrade the joint strength with decreasing t/d ratio for very thin interlayers. In contrast with this conclusion, an explanation for a possible plateau in strength (constant strength) with decreasing t/d ratio independent of surface flatness deviations will be given in the next section.

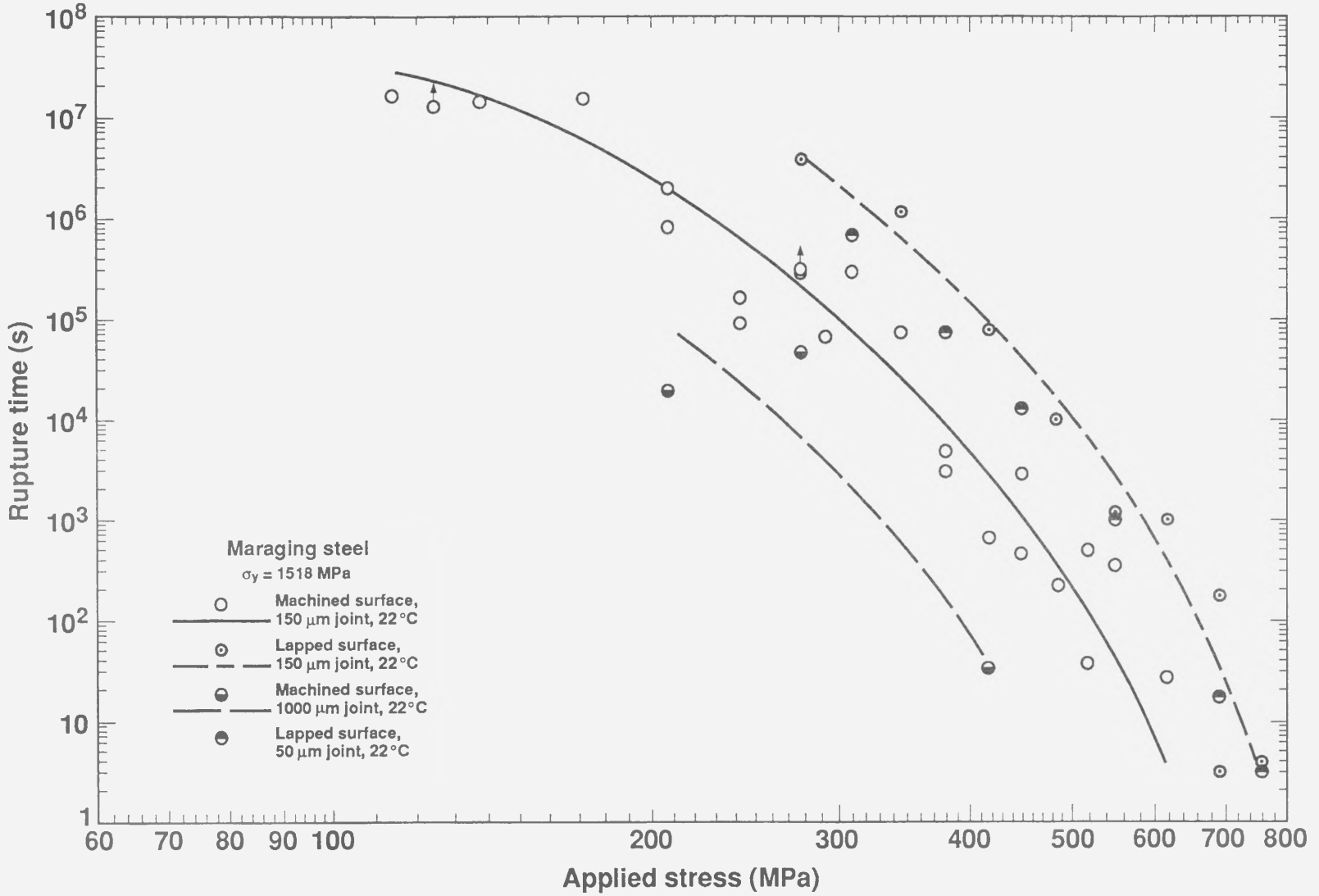

Figure 6.2. Effect of interlayer thickness on creep rupture of diffusion-welded-silver joints between elastic base metals.

6.2.2. Finite-Element Analysis

Figure 6.3 plots, for the interlayer thicknesses of (a) 50, (b) 150, and (c) 1000 μm, the axial, hydrostatic, and effective components of the stress in the center plane of the interlayer (original diffusion-welded-silver interface), from the center axis to the outer diameter of the maraging steel specimens at 345 MPa applied stress. These NIKE2D[59,60] finite-element analysis results were obtained using 948 elements for the 1000 μm interlayer and 4932 elements for the 50 μm interlayer. Generally, as the interlayer thickness (actually, t/d ratio) increases, the effective stress increases and the average hydrostatic stress decreases somewhat. The increase in the effective stress will cause increased shear within the interlayer and, apparently, creep rupture is accelerated. Estimates of the fracture strains in 1000-μm-thick joints, made using the optical comparator at 100×, indicated strains of 0.1–0.3, compared to measurements of 150-μm-thick joint fractures of <0.01 strain. This difference is a substantial increase in ductility and, perhaps, results from the reduced hydrostatic stresses in the thicker interlayer. The hydrostatic and effective stress states do not substantially change as thickness changes from 150 to 50 μm. This rationalizes the similarity of the rupture times shown in Fig. 6.2, and the ultimate tensile strengths discussed in Section 5.2. All this suggests that the effective stress, or plasticity, is an important consideration for the time-dependent failure of interlayer welds between elastic base metals.

6.3. Effect of Test Temperature

Figure 6.4 shows results of tests on diffusion-welded-silver interlayers between machined maraging base metals performed at ambient temperature (295 K or 22 °C; hollow circles) and at 345 K (72 °C; shaded circles). Ambient-temperature rupture times are nearly 50 times longer than 72 °C times over the entire range of stresses tested. Additionally, the slope of the rupture time versus applied stress curve at 72 °C appears to decrease with decreasing stress at least down to 100 MPa, consistent with the decreasing stress exponents

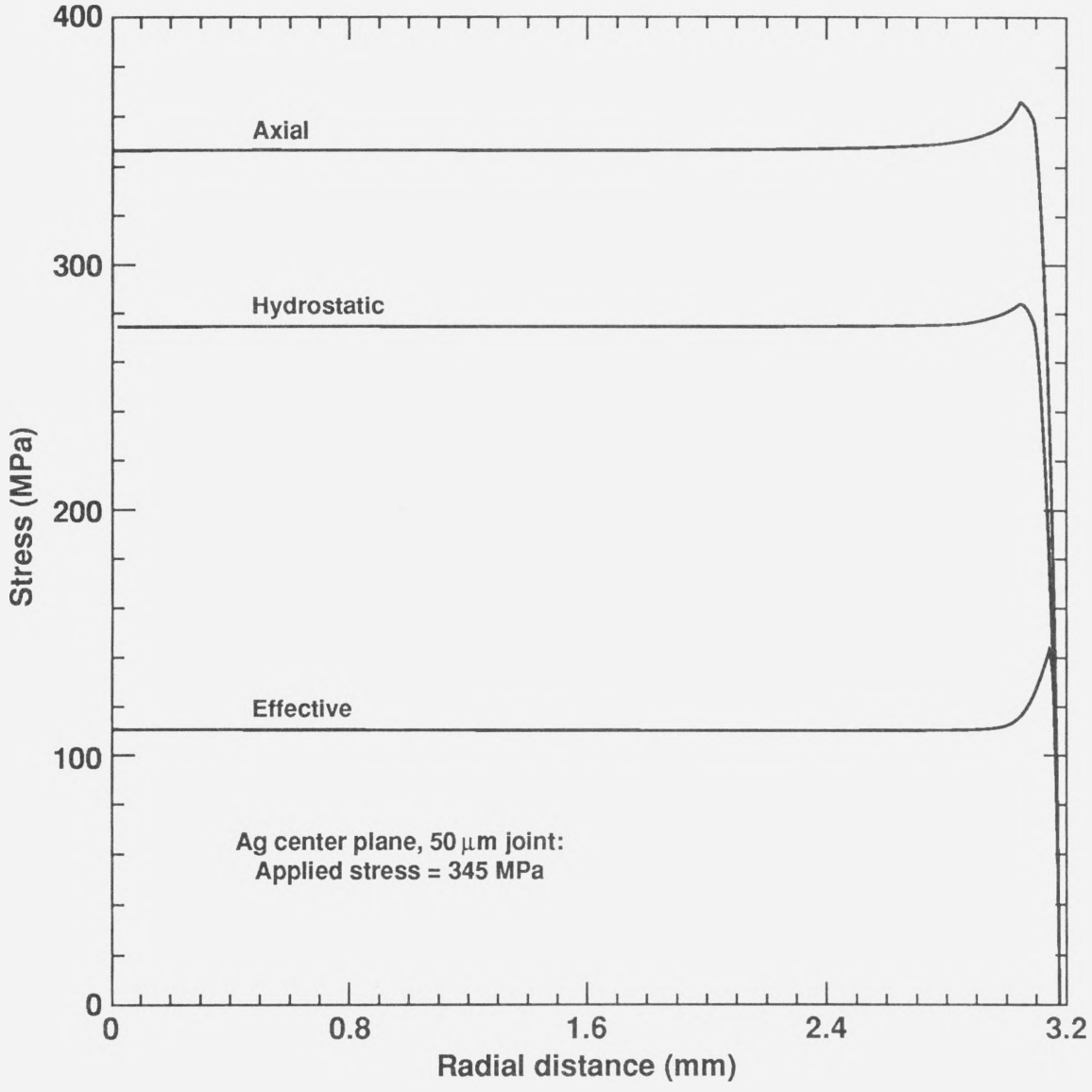

Figure 6.3. (a) Finite-element analysis of the axial, hydrostatic, and effective stresses at the center plane of a 50-μm-thick interlayer at an applied stress of 345 MPa.

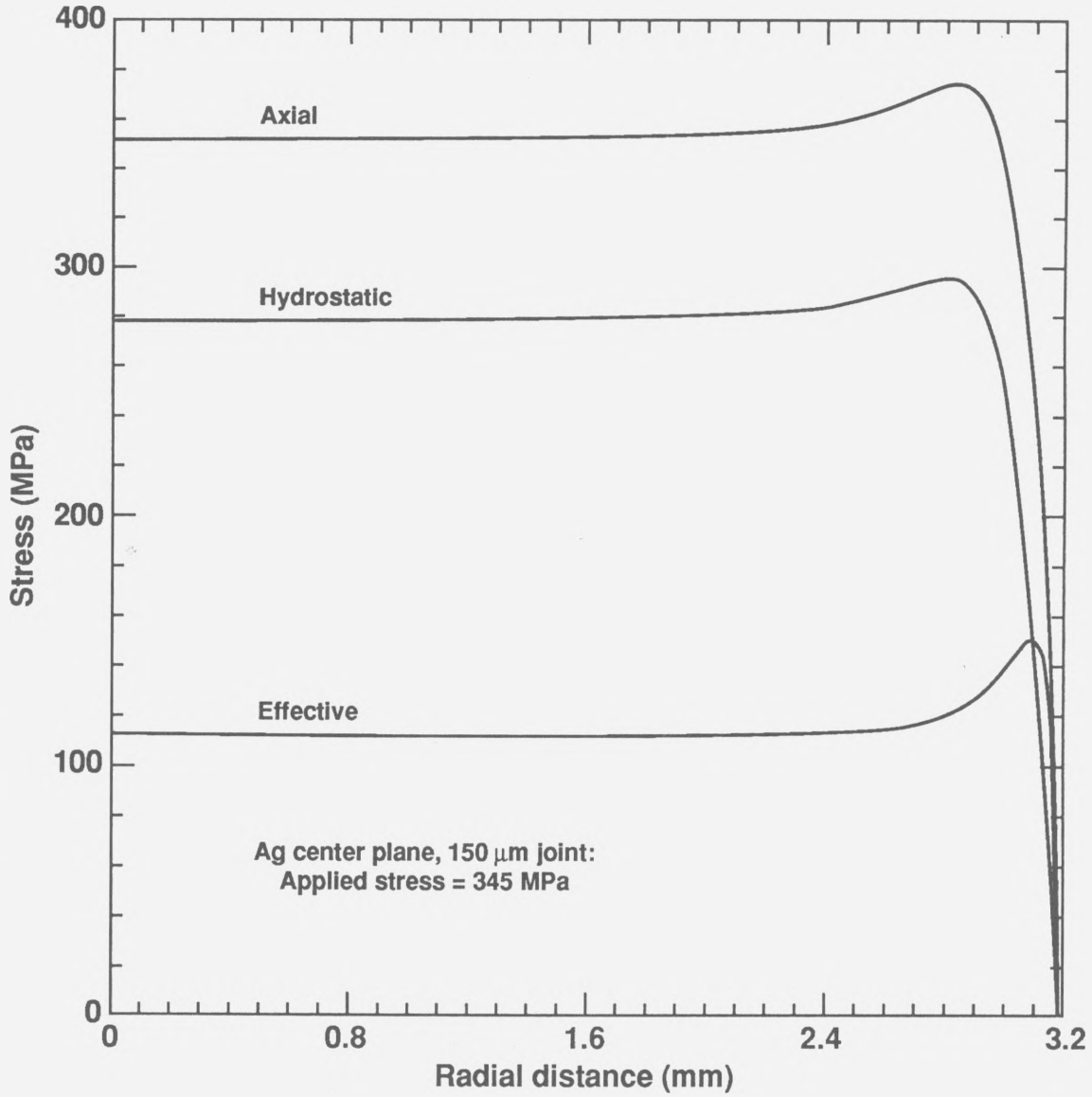

Figure 6.3. (b) Finite-element analysis of the axial, hydrostatic, and effective stresses at the center plane of a 150-μm-thick interlayer at an applied stress of 345 MPa.

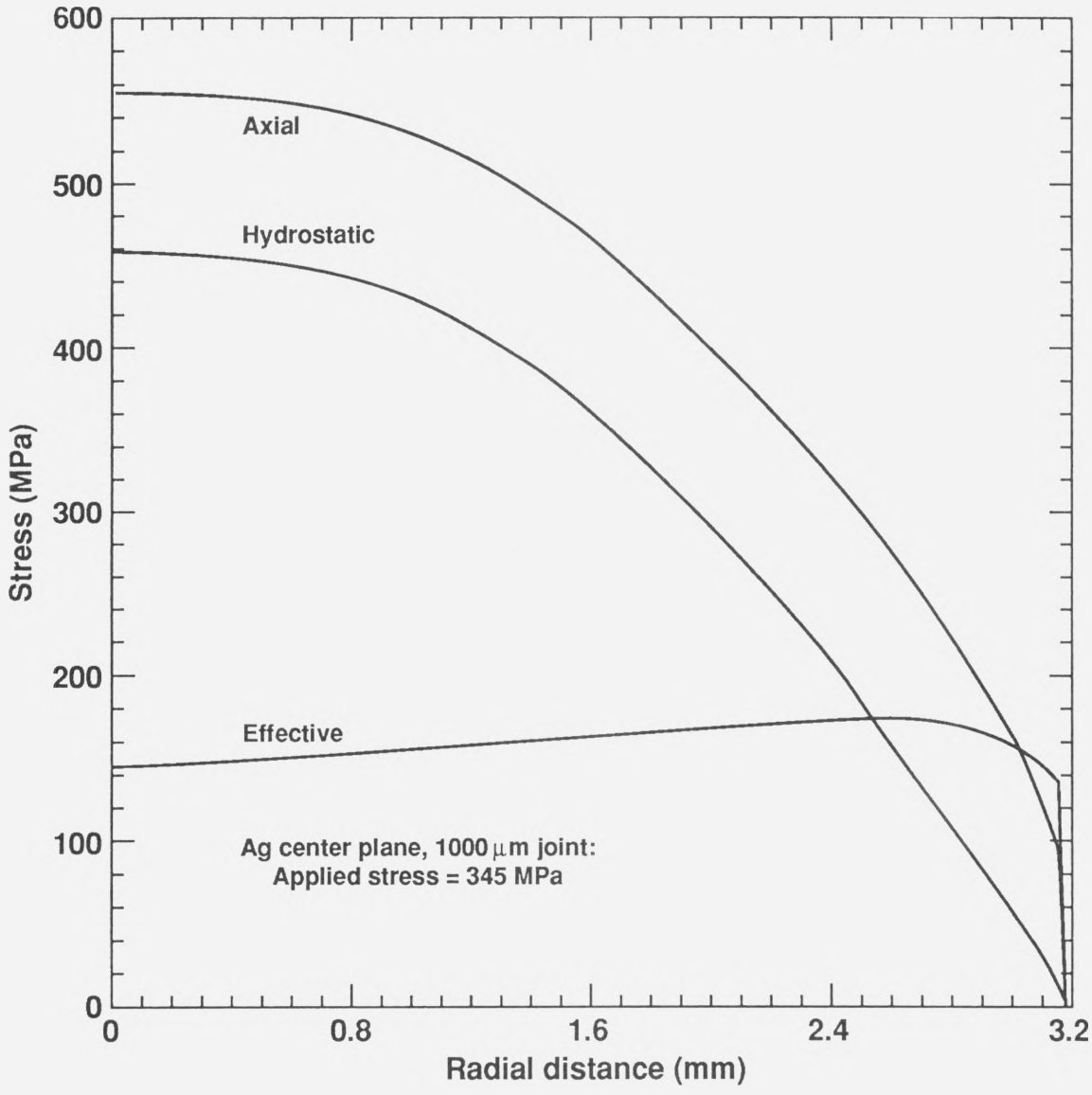

Figure 6.3. (c) Finite-element analysis of the axial, hydrostatic, and effective stresses at the center plane of a 1000-μm-thick interlayer at an applied stress of 345 MPa.

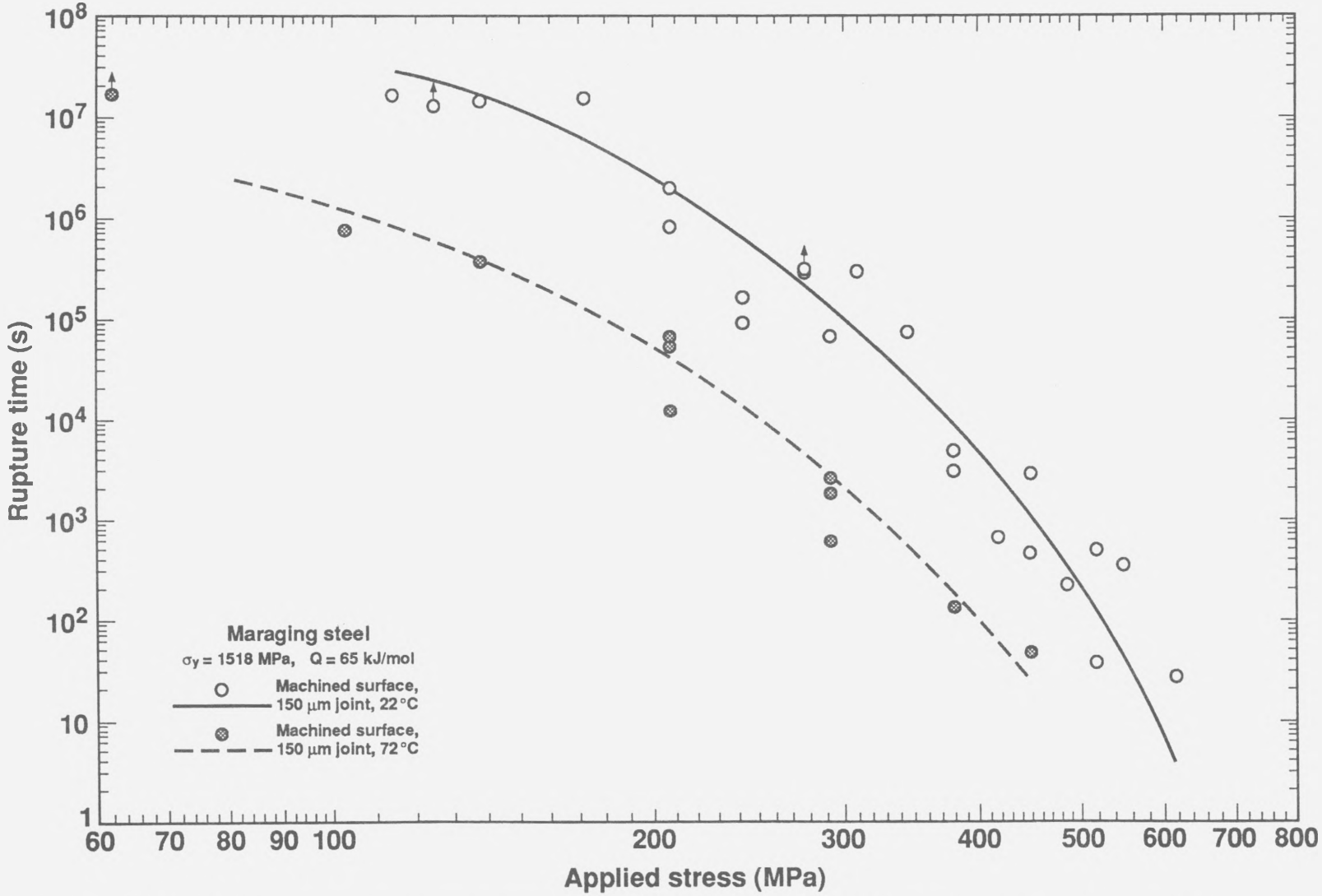

Figure 6.4. Effect of test temperature on creep rupture of diffusion-welded-silver joints between elastic base metals.

of specimens tested at 22 °C. The activation energy for creep rupture could be described by:

$$Q_r = \left[\frac{R\, \partial (\ln t_{r1})}{\partial \left(\frac{1}{T}\right)} \right]_{\sigma}, \tag{3}$$

where R is the universal gas constant, t_r is the rupture time, and T is the absolute temperature. The activation energy for creep rupture, equal to 65 kJ/mol, was found to be approximately constant over the range of stresses (103–379 MPa) tested. Although the significance of this value will be discussed more completely in Section 6.5, it can be mentioned now that this value is approximately the same as the activation energy for plastic deformation, or creep of silver.

As of the submission date of this document, the specimen loaded to 62 MPa at 72°C had not failed after 1.6×10^{-7} s, or approximately 4 times longer than expected based on an extrapolation of the higher-stress 72 °C creep-rupture curve. As will be discussed in Section 6.5, creep ruptures of interlayers joining elastically-deforming base metals appear to be caused by time-dependent plasticity within the interlayer (e.g., dislocation motion). It might be supposed that creep ruptures may not occur below applied stress levels necessary to cause dislocation motion. Plasticity within the silver interlayer may be observed, from ambient temperature torsion test results reported in Section 4.1, at stresses as low as 40 MPa (0.01% plastic strain). It is difficult to identify the precise stress level at which plasticity first occurs in the silver interlayer due the relatively poor sensitivity of the gage extensometer (total extensometer length-to-interlayer thickness ratios varied from 10–67:1). Because the yield stress of silver at 72 °C is nearly equal to the value at 22 °C, the specimen loaded to 62 MPa may be below a threshold stress level necessary to cause dislocation motion in the interlayer. Therefore, creep rupture may not occur at very low applied stress levels. This point will be discussed further in Section 10.2.2.

6.4. Fracture Surface Characterization

As in the case of UTS specimens, failure always occurs at or very near one of the three principal interfaces: the high angle grain boundary near the original diffusion-welded-silver (silver-silver) interface, or one or both of the two silver-base-metal interfaces. The silver-fracture morphology of creep rupture surfaces appear to be identical to those of ultimate tensile strength fractures. Energy dispersive spectroscopy (EDS) of the steel sides of the silver-steel fractures revealed that the steel surfaces are covered with a thin (~1 μm) layer of silver in nearly all of the specimens examined. It appears that these "silver-base-metal" separations are actually separations between the "bulk" (i.e., recrystallized) interlayer silver and the thin (~1-μm thick) nonrecrystallized silver layer adjacent to the base metal (see Fig. 3.4c). Fracture occurred between the silver interlayer and steel base metal surface in only a few specimens examined (as confirmed by EDS). As mentioned in Section 5.4, silver fractures at or near the base-metal interface occur as one of three types of morphologies: (1) silver which replicates the steel surface showing pronounced plasticity only where silver "pullout" remains adhered to the steel, (2) silver which shows pronounced plasticity in the form of ductile dimples, and (3) silver which exhibits a "pyramid-shaped" pattern of plastic deformation and shows pronounced plasticity (slip lines) when viewed in cross section. These second two types of fracture morphologies will be presented subsequently. The diffusion-welded-silver (silver-silver) fracture surfaces show the same evidence of a microvoid coalescence failure mechanism (ductile dimples) as observed in the fracture morphologies of ultimate strength specimens.

Figure 6.5 shows a plot of percent silver-silver fracture (at the diffusion-welded-silver interface) as a function of applied stress level for 150-μm-thick silver interlayers utilizing machined maraging steel base metals. At stresses between 350 and 700 MPa, the fracture surface typically consists of 85-100% silver-silver ductile separation, with the remaining separation occurring at or near the silver-base metal interface. Below 350 MPa, the fracture surface consists typically of 55-85% silver-silver separation. This plot suggests that the

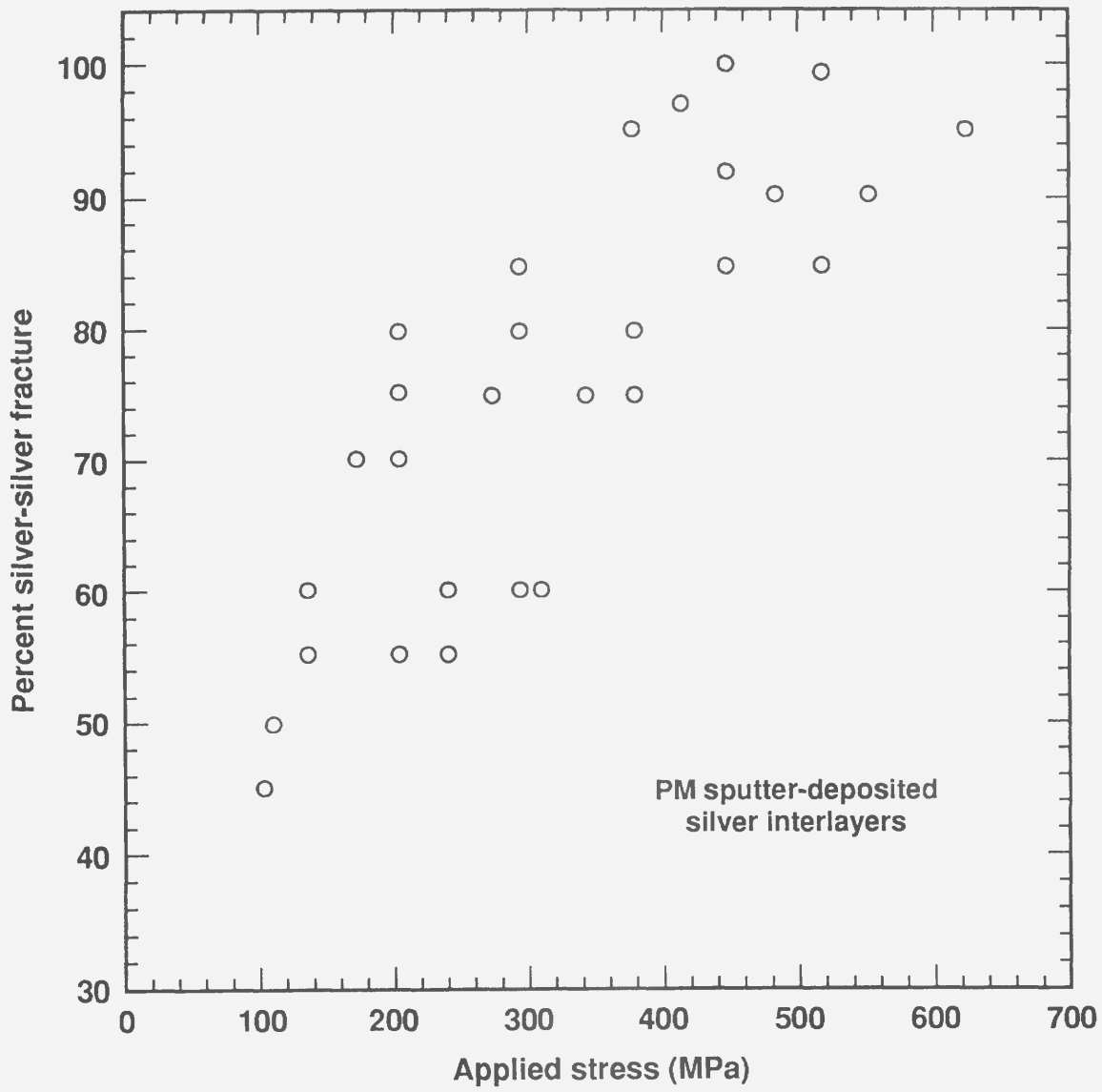

Figure 6.5. Percent silver-silver fracture as a function of applied stress level for PM sputter-deposited 150-μm-thick silver joints between machined maraging steel base metals.

percent silver-silver fracture decreases with decreasing applied stress (or increasing rupture time). The explanation for this phenomenon is not clear. A similar trend is observed for diffusion-welded-silver interlayer fractures between plastic base metals, and this trend will be discussed further in Section 8.4.

Figure 6.6 is the summary plot for creep rupture behavior of diffusion-welded-silver interlayers utilizing elastic base metals. The fracture surfaces of these specimens will be now be discussed. Figure 6.7 shows the typical silver-silver fracture surface of specimens in which the elastic base-metal surfaces were machined prior to coating. The silver-silver fracture surface has a duplex fracture morphology; relatively deep cavities separated by regions with smaller ductile dimples. This is the same fracture morphology as observed in tensile tests. The silver-silver fracture surface of this creep-rupture specimen, failing after nearly 10^6 s at 207 MPa, appears identical to that of the high-stress specimen failing at 621 MPa (see Fig. 5.1). Both specimens exhibit cavitation along the machining lay of the coated-base-metal surface. The only significant difference in the fracture morphologies between the high- and low-stress specimens is the percentage of silver-silver fracture as previously noted. Figure 6.7c shows a cross-sectional view of a large cavity at the silver-silver fracture surface. The diameter of these large cavities exceeds half the total interlayer thickness. The small dimples between the large cavities shown in Figs. 6.7d–6.7f are roughly comparable in size to those of the tensile or creep test silver-silver fracture surface of specimens in which the base metals were lapped prior to coating (e.g., Fig. 5.2).

The fracture morphologies of 1000-μm-thick interlayers between machined maraging steel base metals are shown in Figs. 6.8 (specimen exhibiting silver-silver separation) and 6.9 (specimen exhibiting silver-base-metal separation). The silver-silver fracture surface shown in Fig. 6.8 lacks the duplex morphology (relatively deep cavities separated by regions with smaller ductile dimples) of those using 150-μm-thick interlayers. However, cavitation is still observed to have coalesced along the machining lay. Therefore, the roughness of the original base-metal surface is replicated even after 500 μm

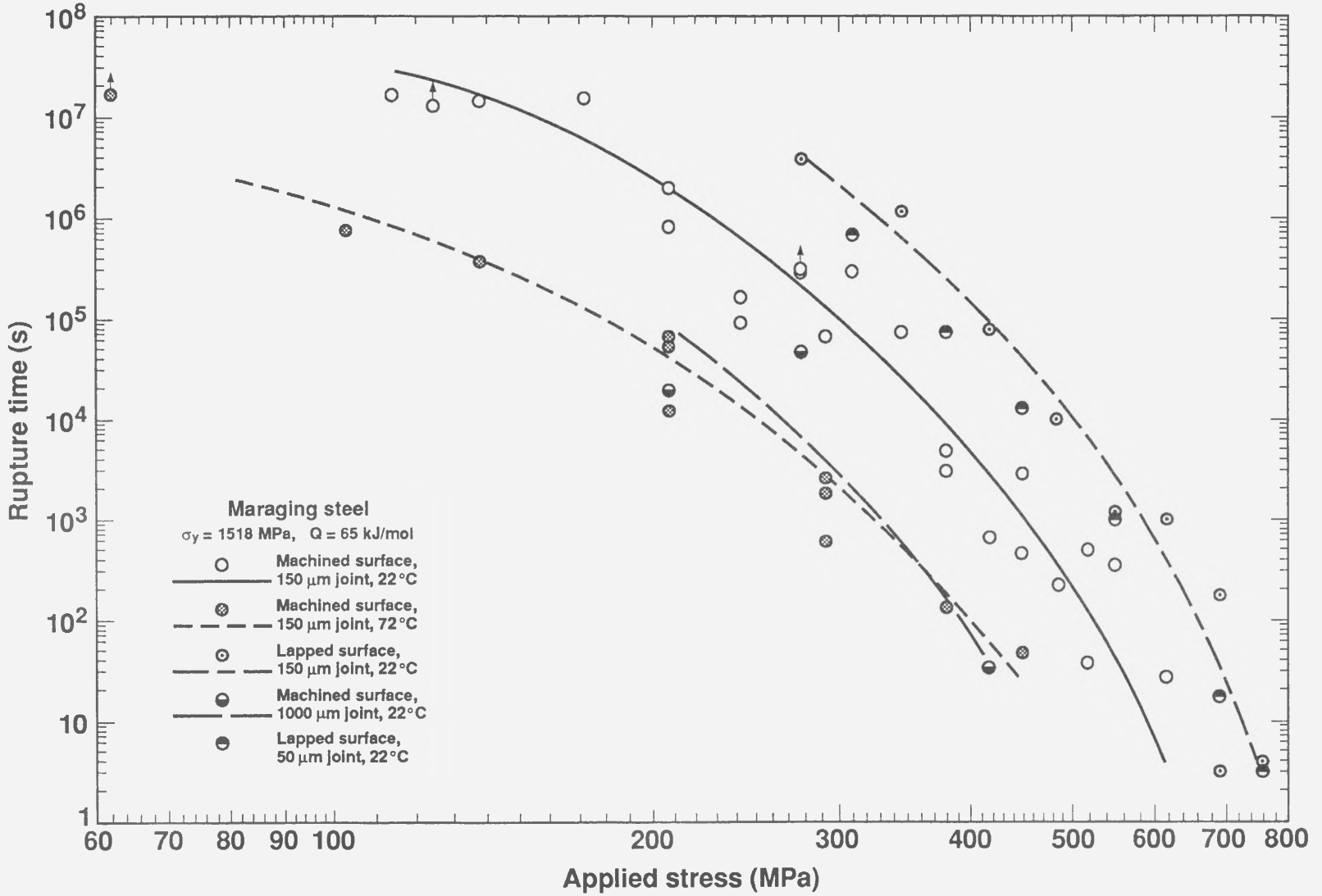

Figure 6.6. Summary plot for creep rupture behavior of diffusion-welded-silver joints between elastic base metals.

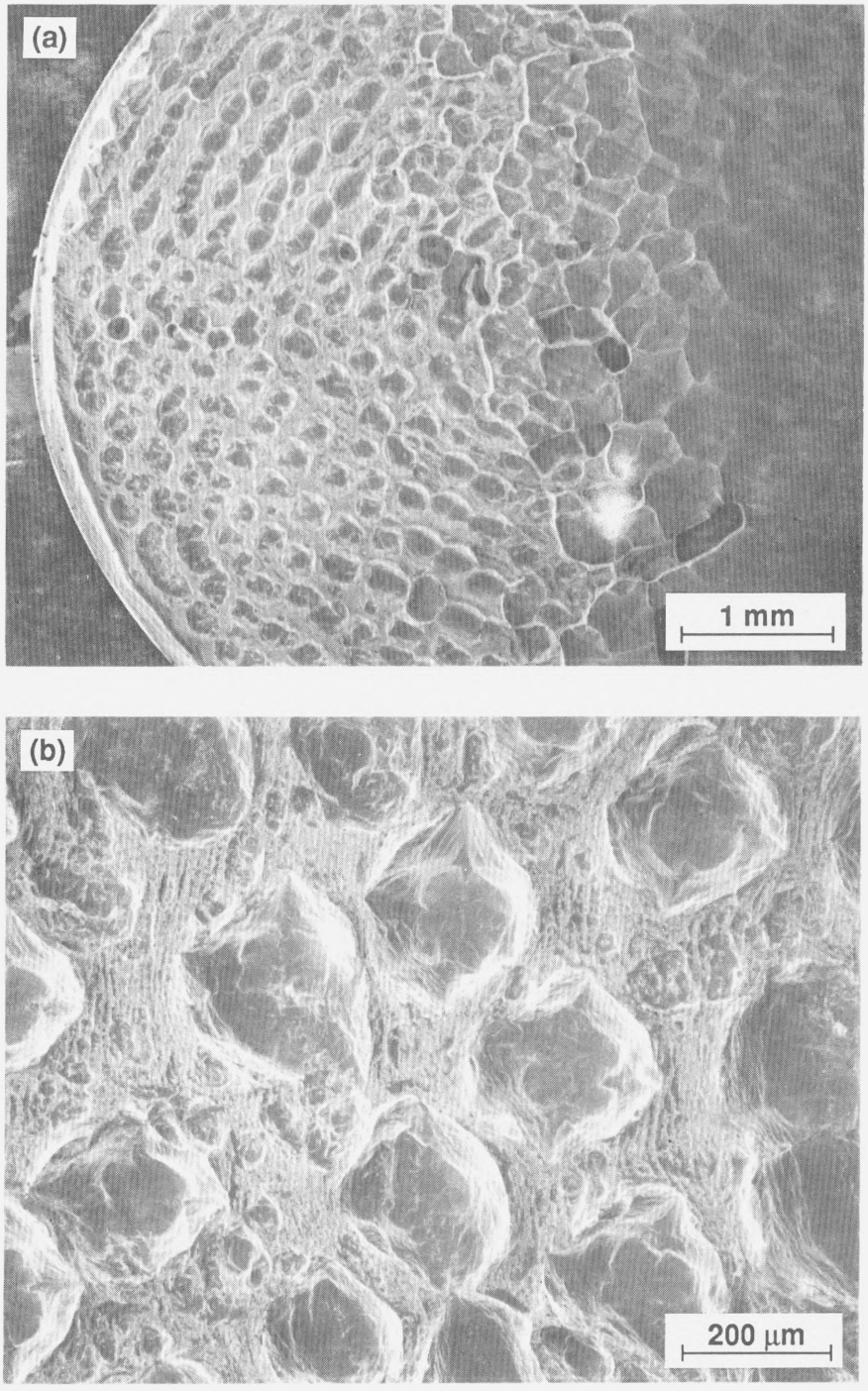

Figure 6.7. (a, b) Typical silver-silver fracture surface (207 MPa) of diffusion welds utilizing machined maraging steel base-metal surfaces. These type of creep ruptures exhibit the same heterogeneous cavitation (large cavities and small ductile dimples) parallel with the machining lay as those of high-stress specimens (see Fig. 5.1).

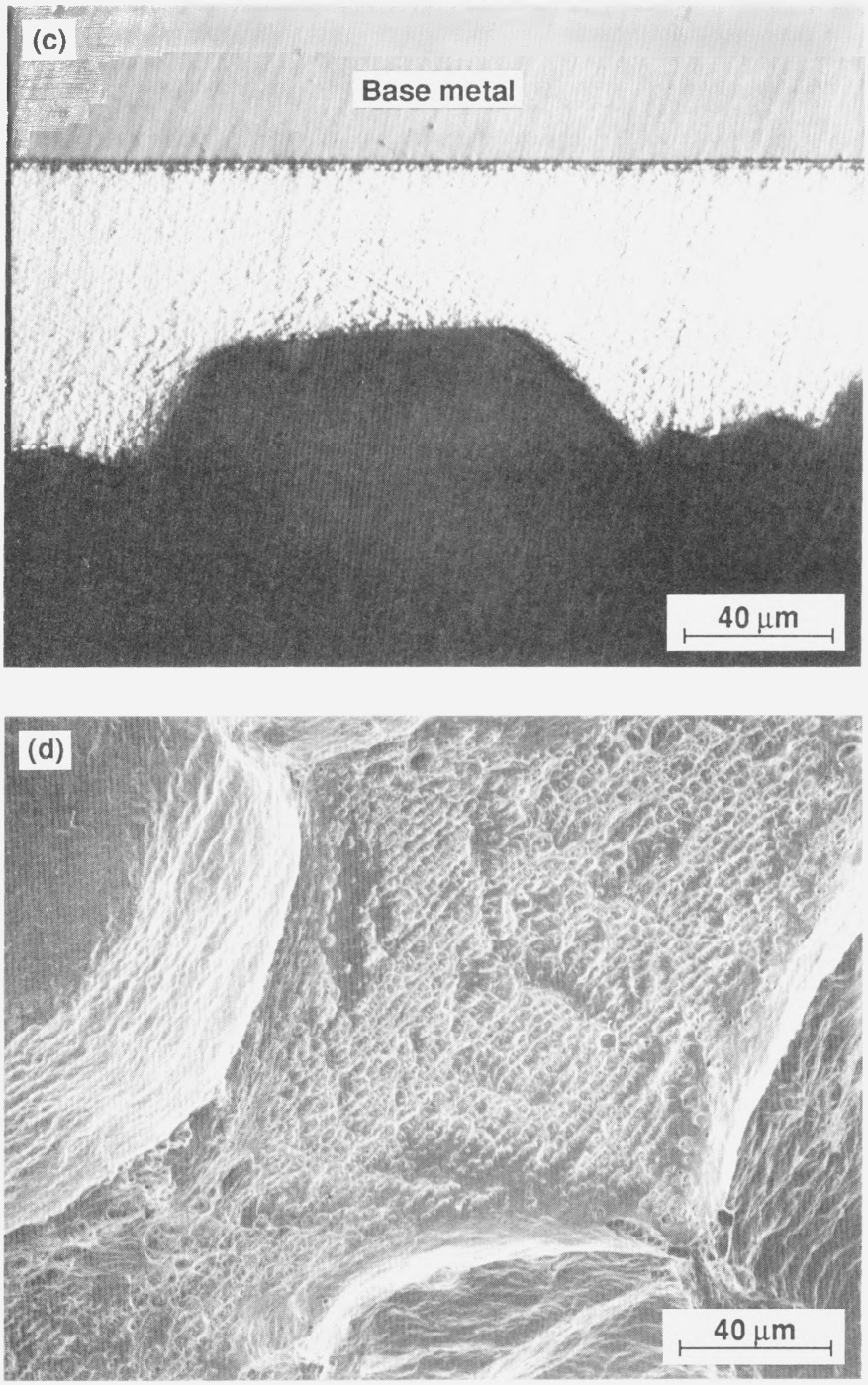

Figure 6.7. (c) Optical cross section of a large cavity at the silver-silver fracture surface (207 MPa) of diffusion welds utilizing machined maraging steel base-metal surfaces. (d) SEM micrograph of fracture reveals fine ductile microvoid coalescence between the large cavities.

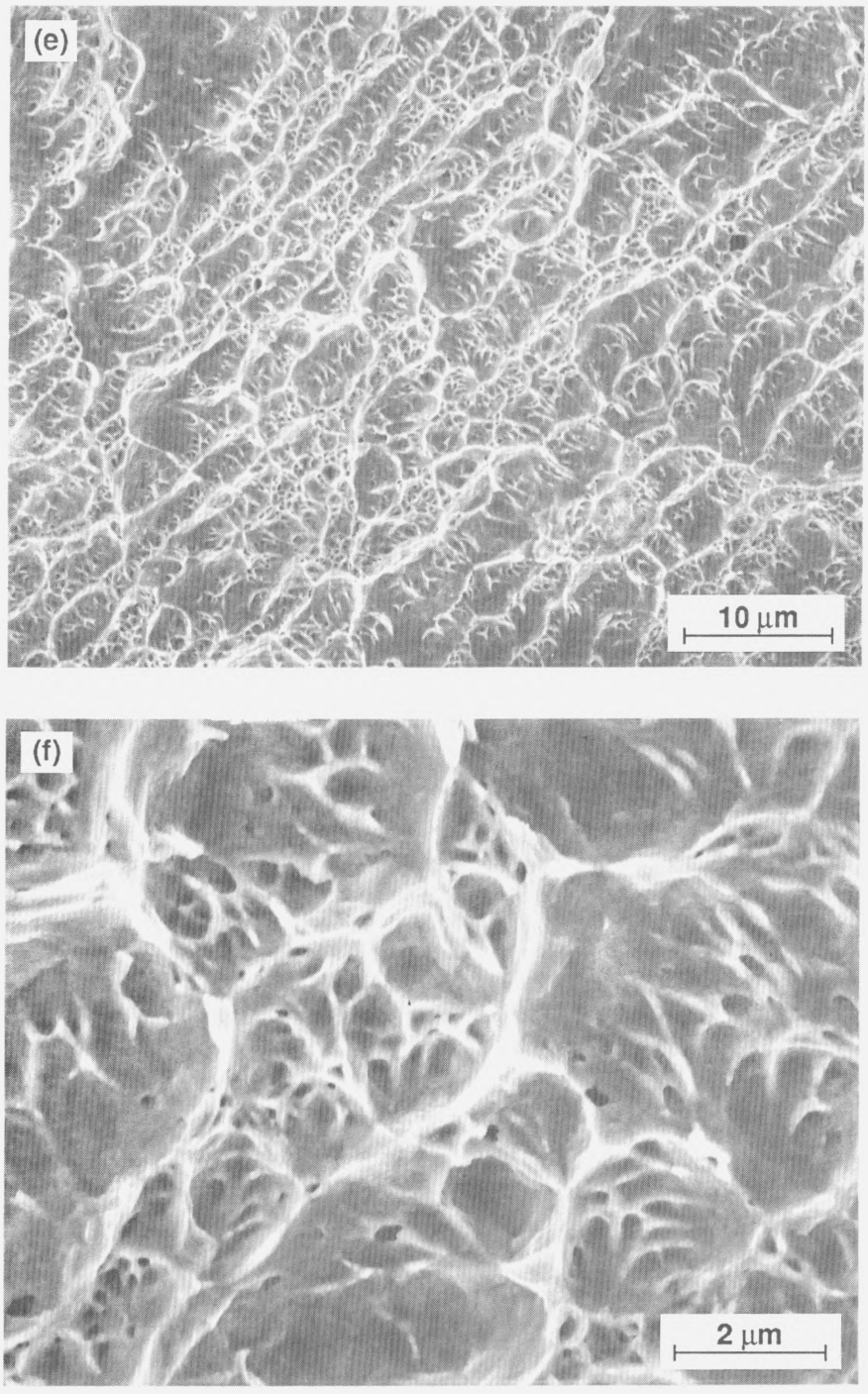

Figure 6.7. (e, f) Silver-silver fracture surface (207 MPa) of diffusion welds utilizing machined maraging steel base-metal surfaces.

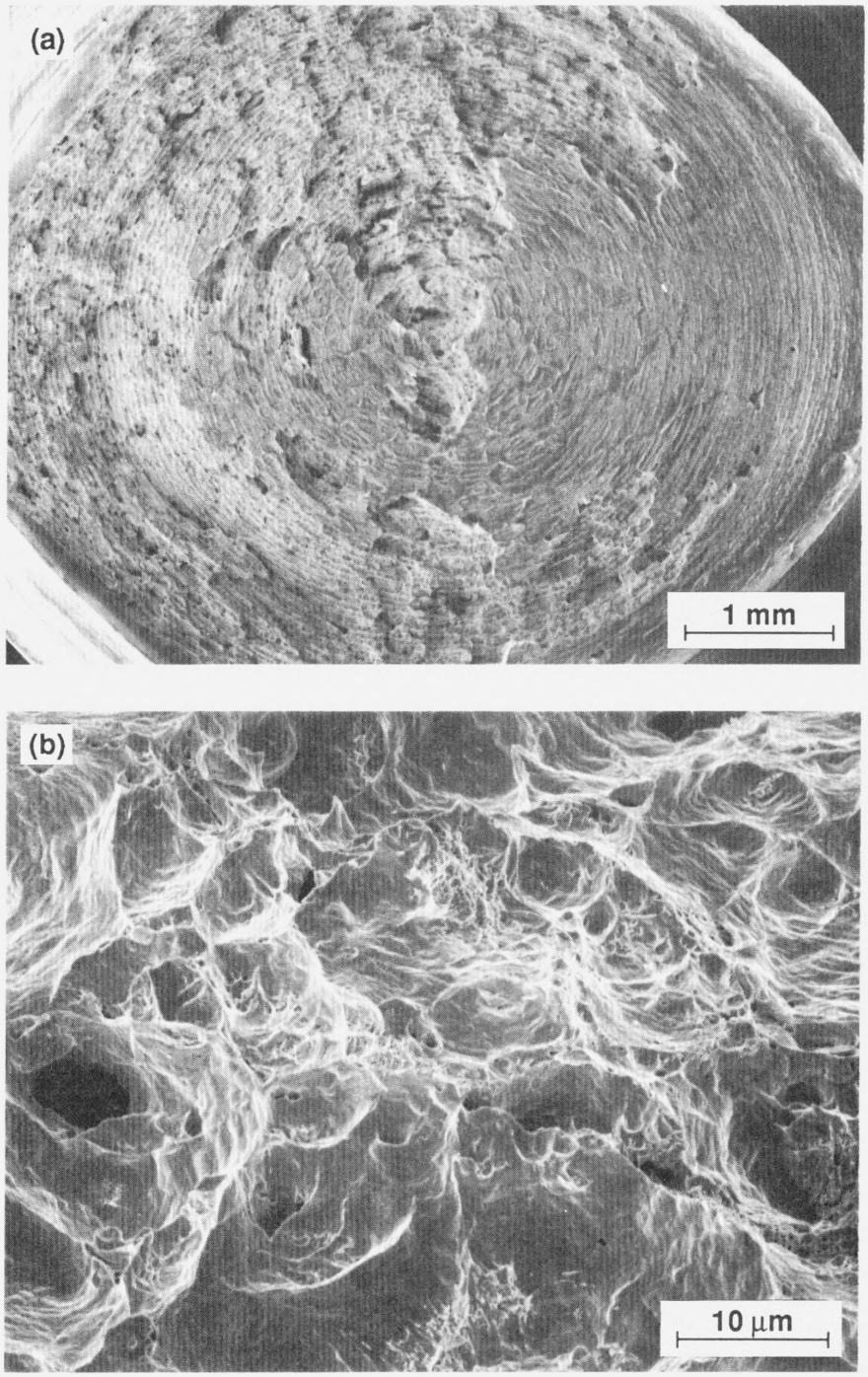

Figure 6.8. Silver-silver fracture surface (414 MPa) of a 1000-μm-thick interlayer between machined maraging steel base metals, exhibiting typical ductile microvoid coalescence.

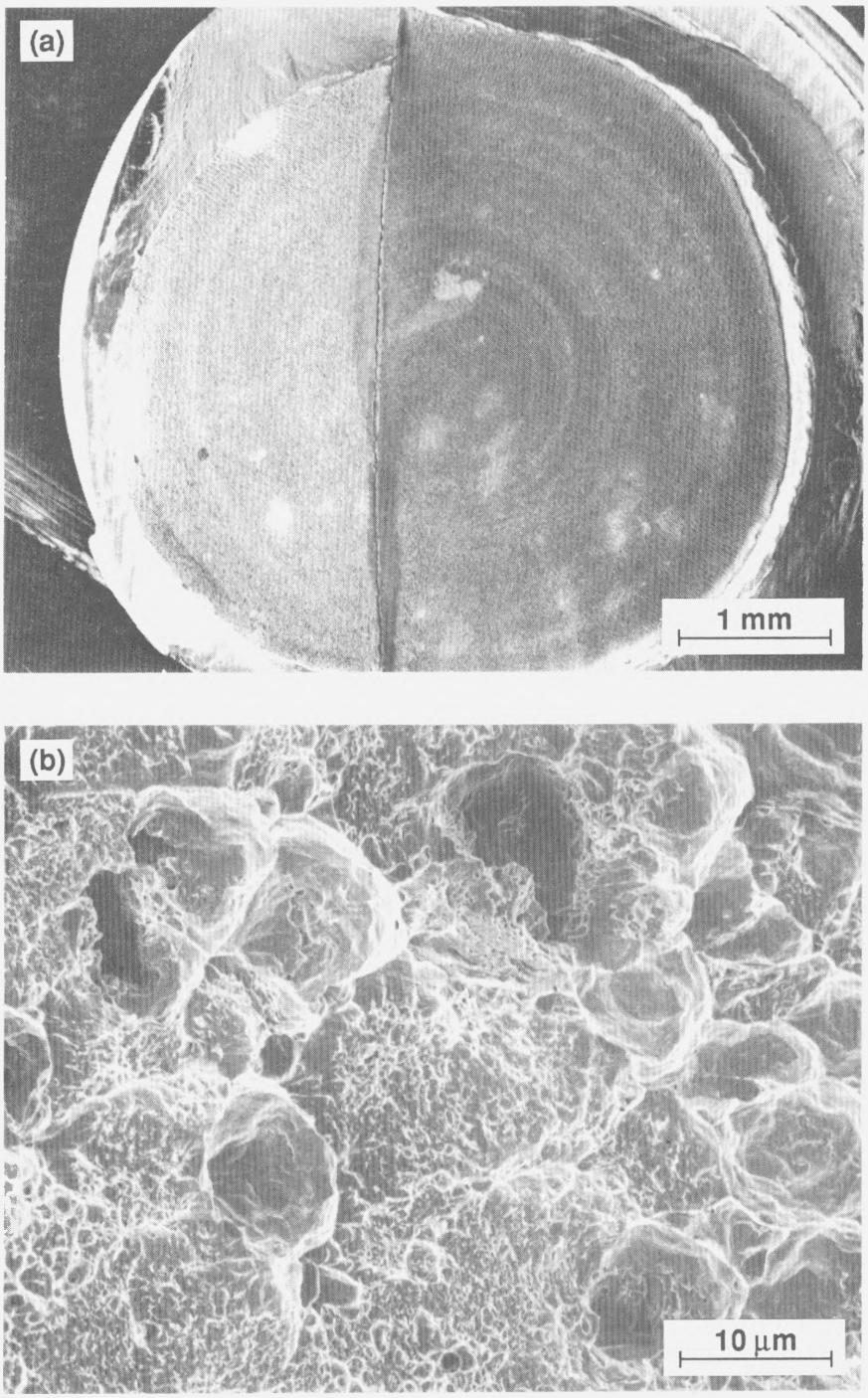

Figure 6.9. Silver-base-metal fracture surface (207 MPa) of a 1000-μm-thick interlayer between machined maraging steel base metals, exhibiting microvoid coalescence on the silver side.

of silver deposition. The second type of silver-base-metal fracture morphology (actually silver-silver fracture near the steel surface, as confirmed by EDS) is shown in Fig. 6.9. This type of silver-base-metal fracture morphology exhibits ductile microvoid coalescence, and is observed occasionally in other (150-μm-thick interlayer) specimens utilizing maraging steel.

Figure 6.10 shows the typical silver-silver fracture morphology of specimens utilizing lapped maraging steel surfaces. Analogous to the case of ultimate tensile strength specimens utilizing lapped base-metal surfaces, the fine-ductile-dimpled surface is extremely uniform with no large cavities present. An explanation for differences in silver-silver fracture morphology between UTS specimens utilizing machined versus lapped base metal surfaces was given in Section 5.4, and is believed to be applicable to creep rupture specimens. It will be shown later in this chapter that these differences in fracture surface morphologies are also consistent with a plasticity-controlled creep rupture failure mechanism.

Further evidence that the same, basic process leads to cavitation and rupture at all three principal interfaces is shown in Fig. 6.11. This figure shows a cross-sectional view of a diffusion-welded-silver interlayer between lapped maraging steel base metals. Fracture occurred at silver-silver (left-hand side of Fig. 6.11a) and silver-steel (right-hand side of Fig. 6.11a) interfaces. Extensive cavitation is observed at the silver-silver interface, leading to areas of local silver-silver failure in spite of fracture occurring at the silver-base-metal interface as shown in Fig. 6.11b. Additionally, the silver side of the silver-steel fracture shows evidence of plasticity, suggesting a ductile fracture process. In general, the silver-base-metal fracture surfaces do not appear dramatically different from the silver-silver fracture surfaces. Cavitation and plasticity are evident in both cases and the basic process that leads to separation appears to be the same. Finally, the morphology of the fracture surfaces of either type of specimen does not significantly change over the very wide range of applied stress.

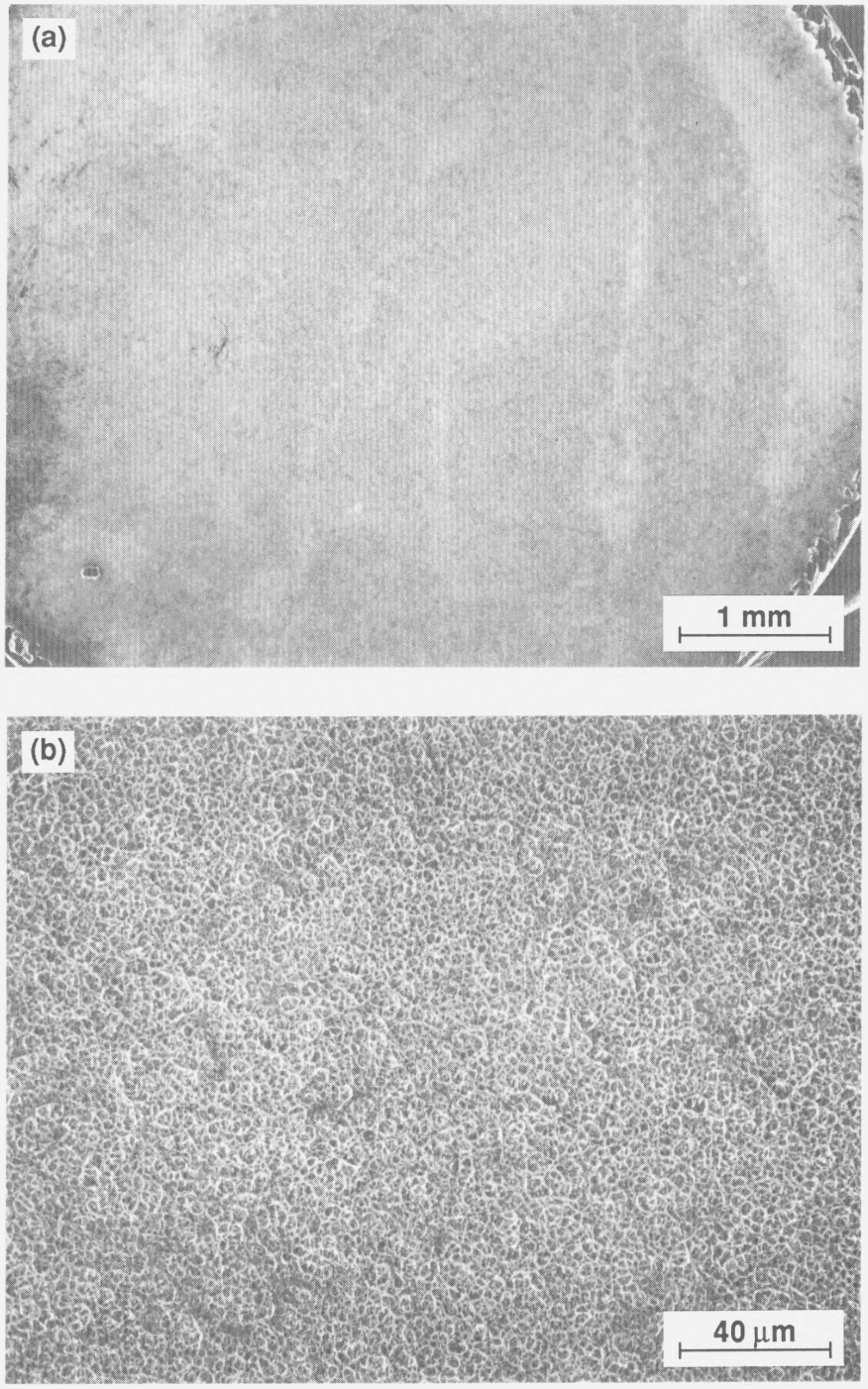

Figure 6.10. (a, b) Silver-silver fracture surface (310 MPa) between lapped maraging steel base metals. Creep ruptures exhibit the same uniform-sized cavities (homogeneous cavitation) as observed in high-strength fractures of specimens utilizing lapped base-metal surfaces.

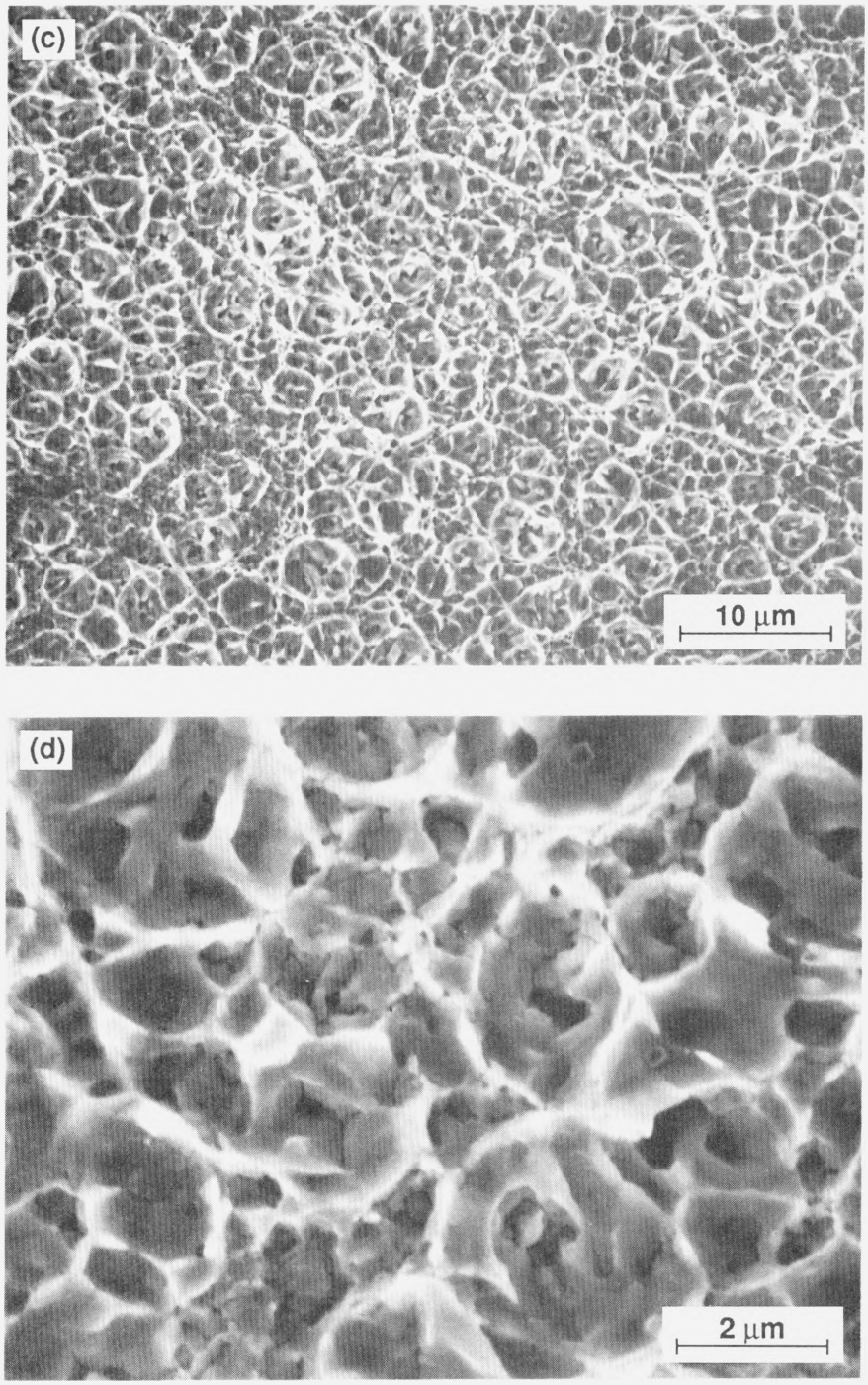

Figure 6.10. (c, d) Silver-silver fracture surface (310 MPa) between lapped maraging steel base metals. Creep ruptures exhibit the same uniform-sized cavities (homogeneous cavitation) as observed in high-strength fractures of specimens utilizing lapped base-metal surfaces.

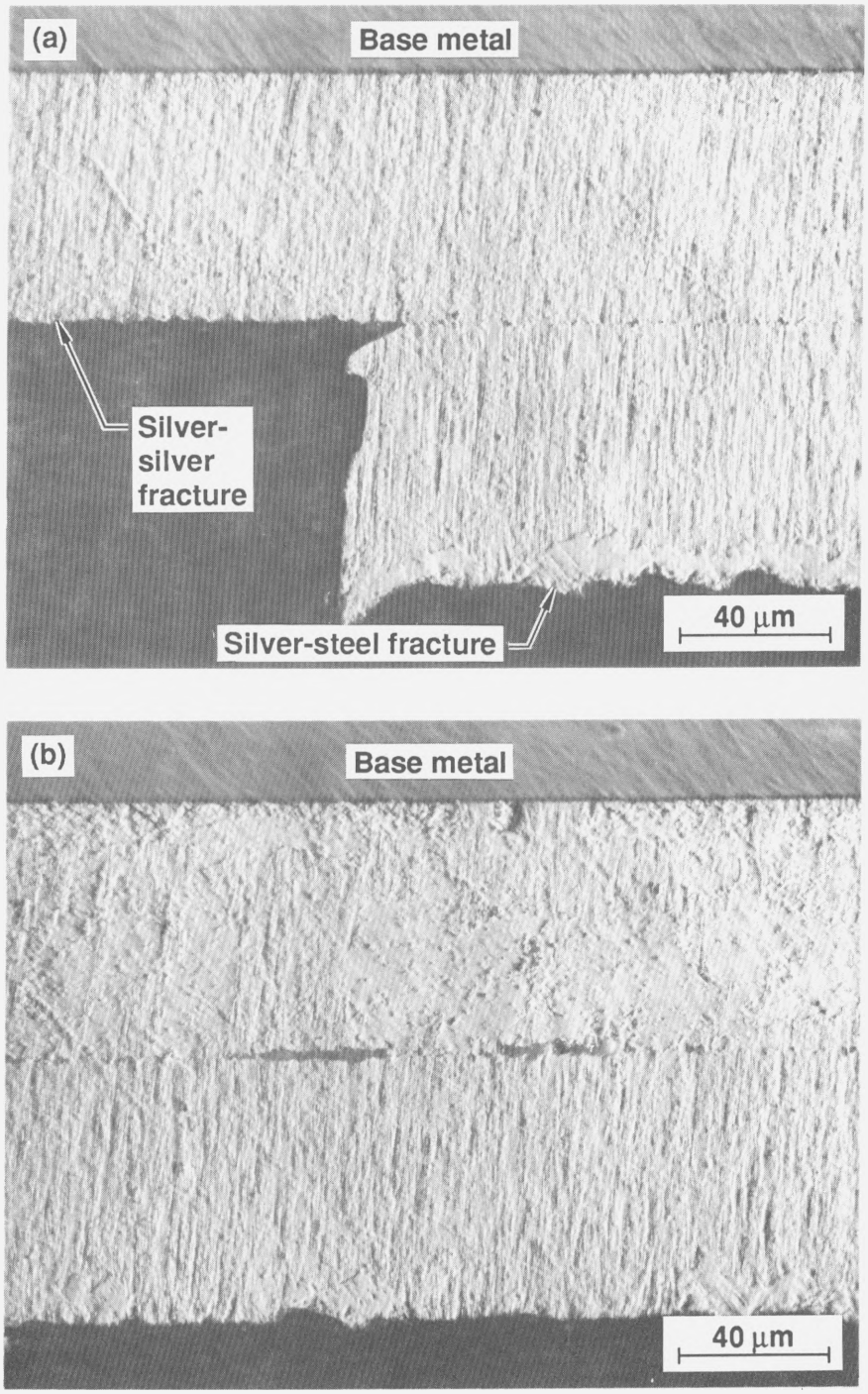

Figure 6.11. Optical cross section of a diffusion-welded-silver interlayer between lapped maraging steel base metals fracturing (689 MPa) at both silver-silver and silver-base-metal interfaces. Extensive cavitation is observed (a) at the silver-silver interface, (b) leading to areas of silver-silver failure in spite of fracture occurring at the silver-base-metal interface.

Fracture surfaces of elevated temperature (72 °C) test specimens appear similar to those of room temperature (22 °C) test specimens. Figure 6.12 shows a machined maraging steel specimen tested at elevated temperature, exhibiting the same type of heterogeneous cavitation at the silver-silver fracture surface as previously observed in specimens tested at ambient temperature. Large cavities, shown in Fig. 6.12c, are surrounded by small, uniform-sized dimples. Figure 6.12d shows a cross section of the transition from silver-silver to silver-base-metal fracture (seen in the lower half of Fig. 6.12a). Further evidence of ductile fracture at the silver-base-metal interface is shown by the slip lines, possibly indicating plasticity prior to fracture.

6.5. Discussion of Creep Rupture

Several mechanisms for creep rupture were considered. One mechanism to consider (despite the plasticity that is evident) is some type of environmentally-induced embrittlement at the interlayer-base-metal interface or within the interlayer. Previously reported results have shown that diffusion-welded-silver interlayers joining uranium base metals are susceptible to stress corrosion cracking at the silver-uranium interface in the presence of air saturated with water vapor.[61] However, the following observations seem to eliminate this kind of explanation for creep rupture. (1) Creep rupture appears to be a general phenomenon for interlayer joints. That is, creep rupture appears to be independent of base-metal and interlayer materials, and of the interlayer deposition processes (this point will be discussed further in Chapter 9). Creep ruptures have been observed at the interlayer-base-metal interfaces in joints utilizing austenitic (stainless) steel,[20,21,40] uranium,[20,21,40] beryllium,[62] and nickel[41] base metals. Further, interlayer separations have been observed with interlayers of silver,[20,21,40,62] cobalt,[41] and nickel.[41] Creep rupture has also been observed in interlayers fabricated using different processing procedures such as planar-magnetron sputter-deposition, as with the present study, hot-hollow-cathode deposition processes,[20,21,40,62] interlayer foils,[41] brazes, and

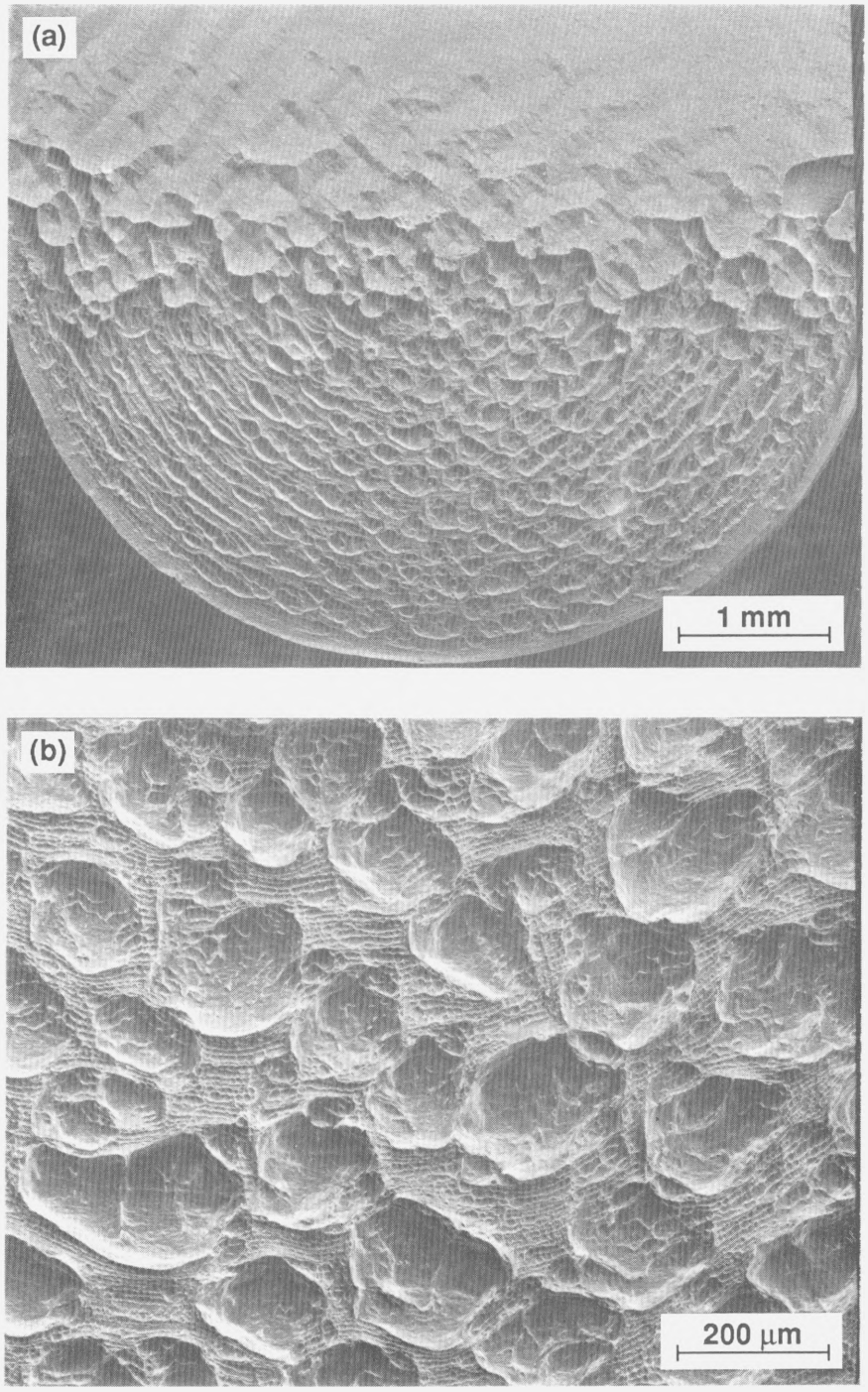

Figure 6.12. (a, b) Silver-fracture surface (103 MPa) of diffusion weld utilizing machined maraging steel base metals and tested at 72 °C, showing silver-steel and silver-silver separation. Fracture surface appears identical to those tested at 22 °C (see Fig. 6.7).

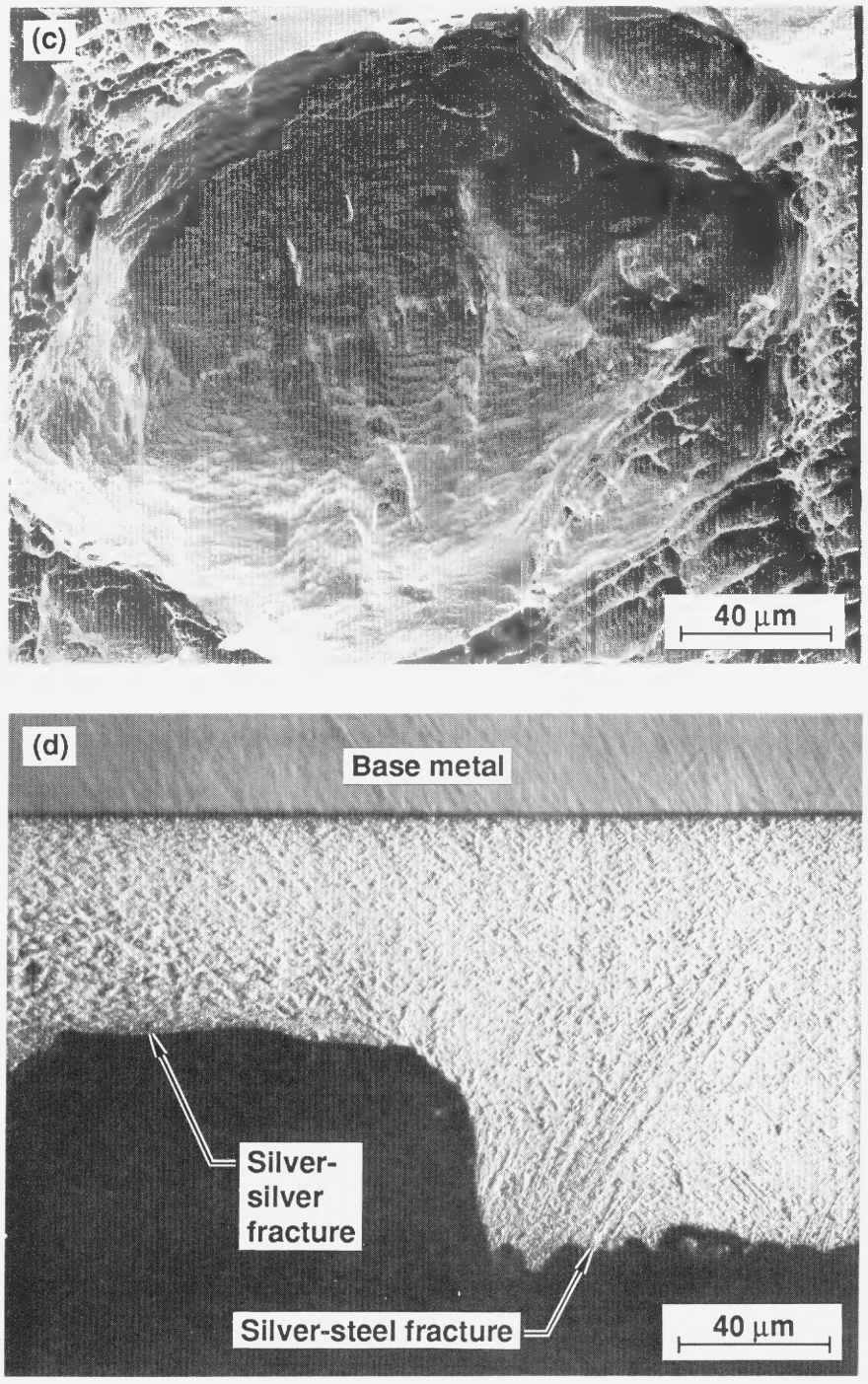

Figure 6.12. (c) Large cavity at silver-silver fracture of diffusion weld utilizing machined maraging steel base metals and tested at 72 °C. (d) Optical cross section of transition from silver-silver to silver-steel fracture reveals evidence of ductility (slip lines) at the silver-steel interface.

electrodeposition (these last two processes will be discussed in Chapter 9). Environmentally-induced embrittlement would not appear to be as general a phenomenon as mechanically-induced creep rupture. (2) The temperature and environmental conditions (e.g., relative humidity) are not expected to induce any external environmental cracking at the silver-silver or silver-SS interfaces.[44,45] (3) As will be discussed in the next section, external cracks have not been observed by dye penetrant or optical metallography prior to failure, suggesting that an external environment is not associated with failure. Additionally, as will be shown in the next section, extensive internal cavitation at is observed at the silver-interfaces of specimens loaded to substantial fractions of their expected creep rupture times. (4) The high-vacuum base pressure and high-purity argon sputtering gas (99.999% pure) are not expected to leave a significant quantity of impurities which could contribute to an internal embrittlement mechanism. This absence was confirmed by chemical (SIMS) analysis of the silver interlayer as mentioned in Section 5.3.5.

Instead, an attractive explanation for creep rupture is a rate-dependent mechanical process, such as plasticity of the silver interlayer resulting from the effective stress within the interlayer. The time-dependent plasticity can nucleate and expand cavities that eventually lead to coalescence and failure. The equilibrium vacancy concentration and diffusivity at ambient temperature appear much too low[63] to rationalize the short failure times at higher stresses at ambient temperature by a diffusive cavity growth mechanism.[64,65] Since the fracture surface morphology is independent of stress (or t_r), the detailed mechanism would also appear to be independent of stress, and a diffusive (or a coupled-diffusive[64,65]) mechanism would not appear to be relevant at any of the stress levels that induce failure.

Careful strain measurements in specimens that failed at stresses near the UTS indicate that the "macroscopic" plastic strain-to-failure in the silver interlayer is only about 0.2%. The strain appears to decrease with the applied stress. It is postulated that the, albeit small,

plastic strain on loading to the applied stress causes dislocation pile-ups at the three important interfaces (and at some other interface locations). At these high applied stresses, a small number of dislocations in a pile-up could be sufficient to concentrate the stress at the diffusion-welded-silver and silver-base-metal interfaces to nucleate a small cavity or crack. The hydrostatic component of the stress would prevent any "rewelding" of the fissure.

The silver-plasticity concept for rationalizing creep rupture is consistent with the temperature dependence of the time-to-rupture. The activation energy for creep of silver at ambient and near-ambient temperatures for various substructures, calculated by substituting $1/t_r$ by $\dot{\epsilon}$ in Eq. 3, falls within the range of 50–71 kJ/mole.[47,66] The activation energy for the creep rupture of diffusion-welded-silver joints between maraging steel, equal to 65 kJ/mole (see Section 6.3), falls within the range of activation energies for silver plasticity. This value is also smaller than the estimated value of 81 kJ/mole[67] for vacancy diffusion at low temperature which, again, suggests that classic diffusive cavity growth is not occurring.

The plasticity concept may also rationalize the silver-silver fracture surface morphology and rupture-time differences between specimens fabricated using base metals with machined and with lapped surfaces. Analogous to the case of UTS (as discussed in Section 5.4), silver deposition on the relatively rough machined surface results in a correspondingly rough silver surface which, after joining by diffusion welding, may result in substructural heterogeneities (but not voids) at the diffusion-welded-silver interface. These heterogeneities may be less common in joints fabricated from lapped specimens which have smoother coated silver surfaces. The heterogeneities in the machined specimens may provide for higher cavity nucleation rates (or possibly growth rates). Fracture may be accelerated in these regions as evidenced by the relatively large, deep cavities, and result in shorter rupture times for the machined base-metal specimens compared to those utilizing lapped base metals.

Microvoid coalescence, which may lead to catastrophic ductile fracture, may occur once a critical concentration of nuclei or cavities (which may be a function of the applied load) is attained at the interface(s). The nucleation, growth, and/or coalescence rate may be a function of the creep rate of the silver at locations in the vicinity of the interface. Finite-element stress analysis was performed on the 150-μm-thick silver interlayers between elastic base metals at applied stress levels corresponding to the experimental test results{using the NIKE2D code[59,60] with a total of 2256 elements (480 in the interlayer)}. Figure 6.13 shows the hydrostatic and effective stresses within the interlayer plotted as a function of applied stress (or engineering stress, load/area). Mechanical constraint, provided by the elastic base metals, results in radial and tangential stresses which restricts transverse contraction of the interlayer. After yielding (~0.1% effective plastic strain), the hydrostatic stress is shown to increase linearly with applied stress. As a result of this constraint, the effective stress within the silver increases only modestly with applied stress. Figure 6.14 shows the data of specimens that utilized maraging steel with machined surfaces from Fig. 6.1, plotted as a function of the effective stress (from Fig. 6.13) along with the applied stress. The analysis revealed that the effective stress within the interlayer is above the silver yield stress (defined for convenience as the 0.01% effective plastic strain offset stress) at all applied loads at which creep rupture is observed. Therefore, the nucleation of cavities, which is associated with time-dependent plasticity (creep) in the vicinity of the interfaces, could occur at any of the applied stresses at which creep rupture is observed. The effective stress versus t_r slopes in Fig. 6.14 are higher than the applied stress versus t_r slopes. The significance of this will be discussed in Section 10.1.

6.6. Interface Formation of Microvoids

An important test for the proposed theory to explain creep rupture is the examination of the silver-silver and silver-base-metal interfaces at various fractions of the creep-rupture time. If the observed creep ruptures are the result of silver creep under high triaxial

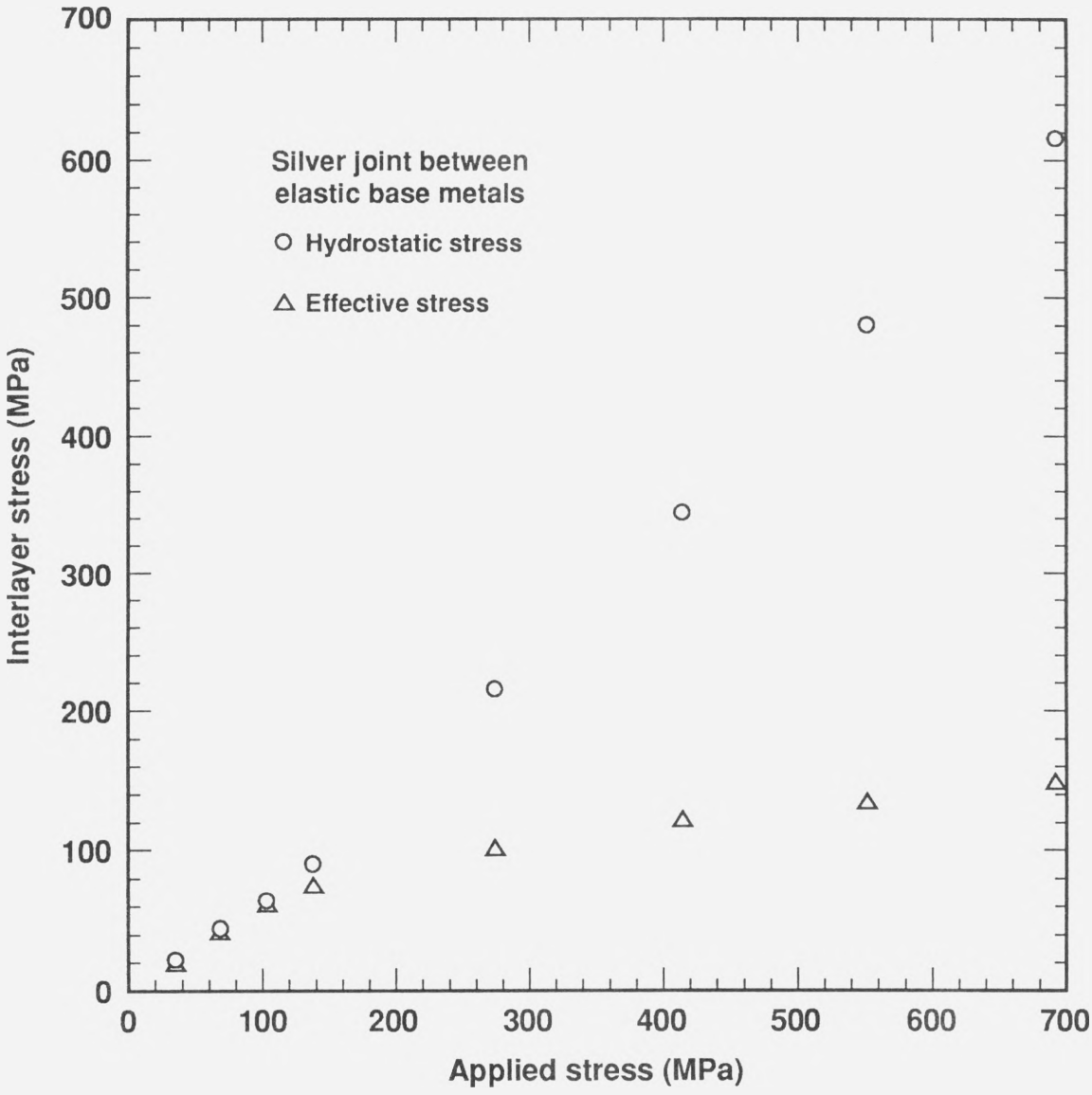

Figure 6.13. Finite-element analysis of average stress within a 150-μm-thick silver interlayer joining elastic base metals showing hydrostatic and effective stresses versus applied stress.

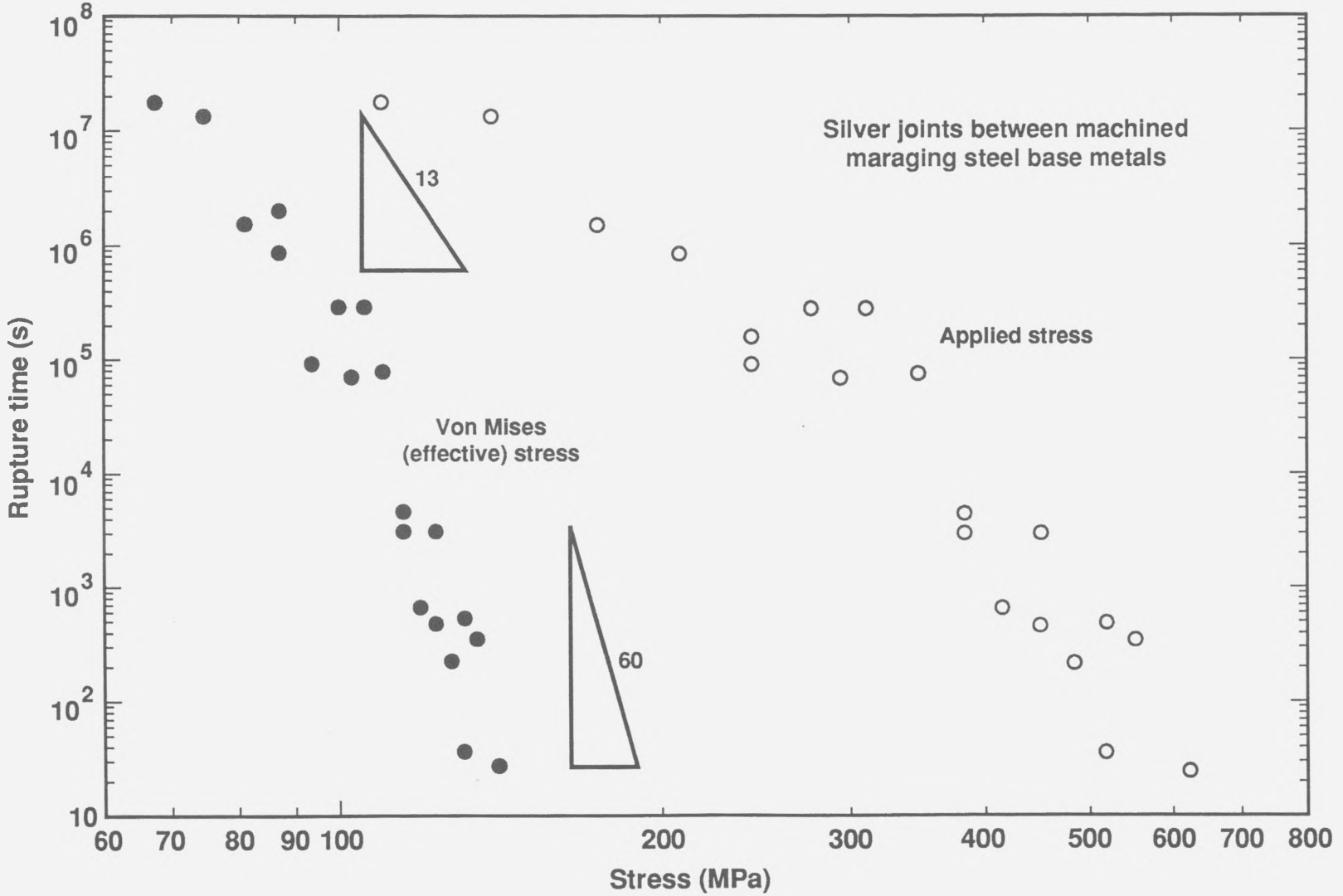

Figure 6.14. Rupture time versus applied and effective stresses for 150-μm-thick silver interlayers joining elastic base metals.

stresses that leads to microvoid nucleation and coalescence, then cavities should be increasingly evident at or very near the interfaces with an increasing fraction of the rupture time.

A number of specimens were loaded at different stresses to various fractions of the expected rupture time and examined for microvoids using SEM, TEM, and light (optical) microscopy. It was observed that small cavities, or microvoids were increasingly present in the vicinity of the three interfaces in previously loaded specimens. Figure 6.15 shows optical micrographs of the diffusion-welded-silver interlayer joining lapped maraging steel base metals, seen in the as-welded (nonloaded, or 0% rupture time) condition. Figures 6.16–6.21b (excluding the transmission electron micrograph of Fig. 6.20c) are optical micrographs showing the diffusion-welded-silver interlayers joining maraging steel base metals, loaded to 1, 10, 25, 50, 75, and 99% of the expected rupture times, $t_{r,exp}$. The specimens examined at 50 and 75% $t_{r,exp}$ were fabricated using machined base-metal surfaces, and were loaded to 124 and 483 MPa, respectively. The other specimens examined were fabricated using lapped base-metal surfaces, and were loaded to the relatively high stress level of 552 MPa.

Results of these examinations revealed that microvoids are only occasionally observed in nonloaded specimens. As the time-at-load increases, the microvoid concentration increases. After approximately 25% $t_{r,exp}$, strings of microvoids have begun to form at the silver-silver interface. Specimens loaded from 50–75% $t_{r,exp}$ exhibit extensive cavitation at the silver-silver interface as well as at the grain boundaries in nonrecrystallized regions. The specimen loaded to 99% $t_{r,exp}$ resulted in an high density of closely-spaced microvoids at the silver-silver interface, separated by an average distance of approximately 5 μm. Although the nonrecrystallized structure (both sides of the interlayer) also contains a high density of microvoids, failure will (always) occur at the silver-silver or silver-steel interfaces due to the high areal density of voids along these planes. As will be subsequently shown, microvoids have also been observed near the silver-steel interface

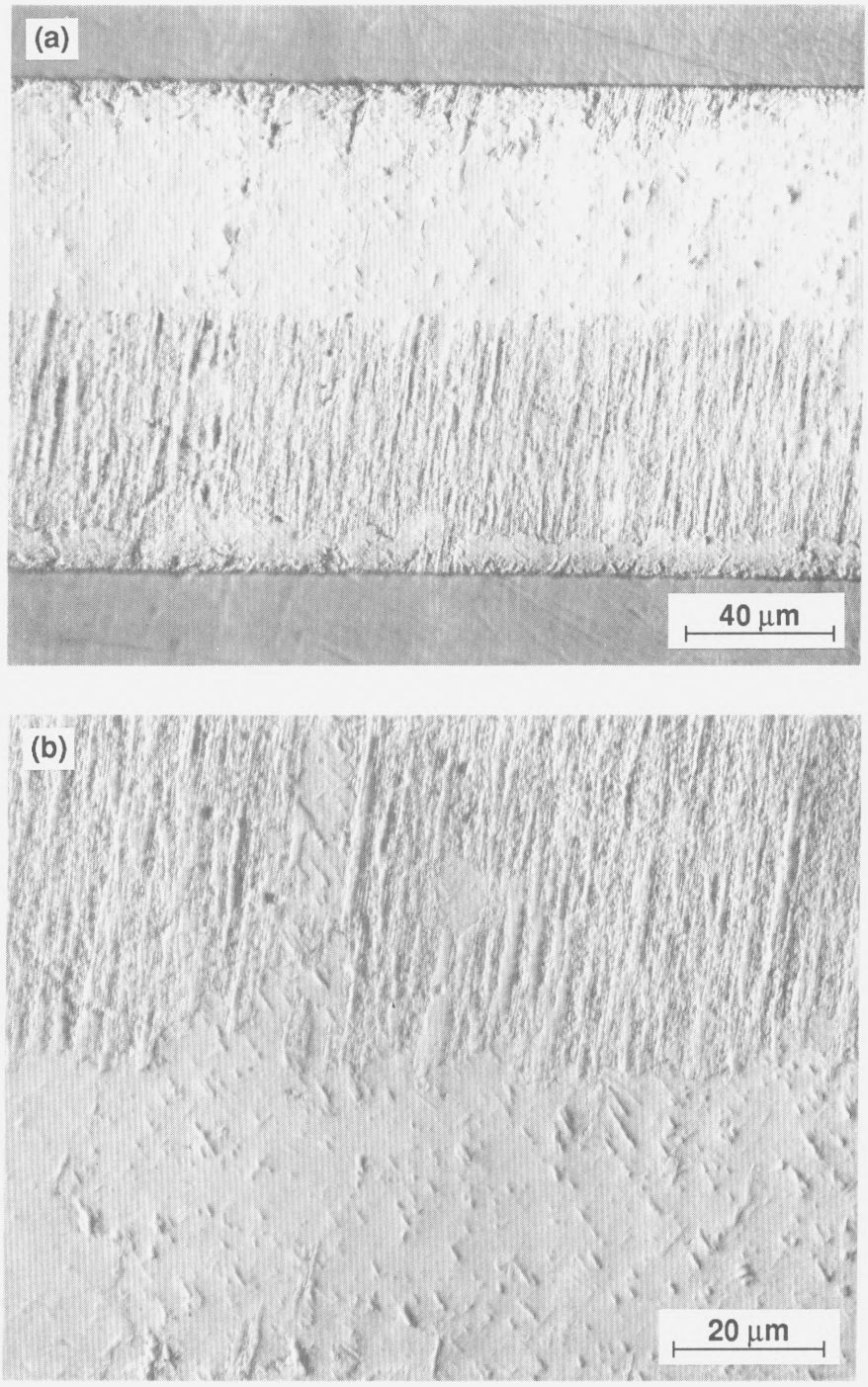

Figure 6.15. Optical micrographs showing the diffusion-welded-silver interlayer joining lapped maraging steel base metals seen in the as-welded (nonloaded) condition. Only a few, isolated microvoids are present in these structures.

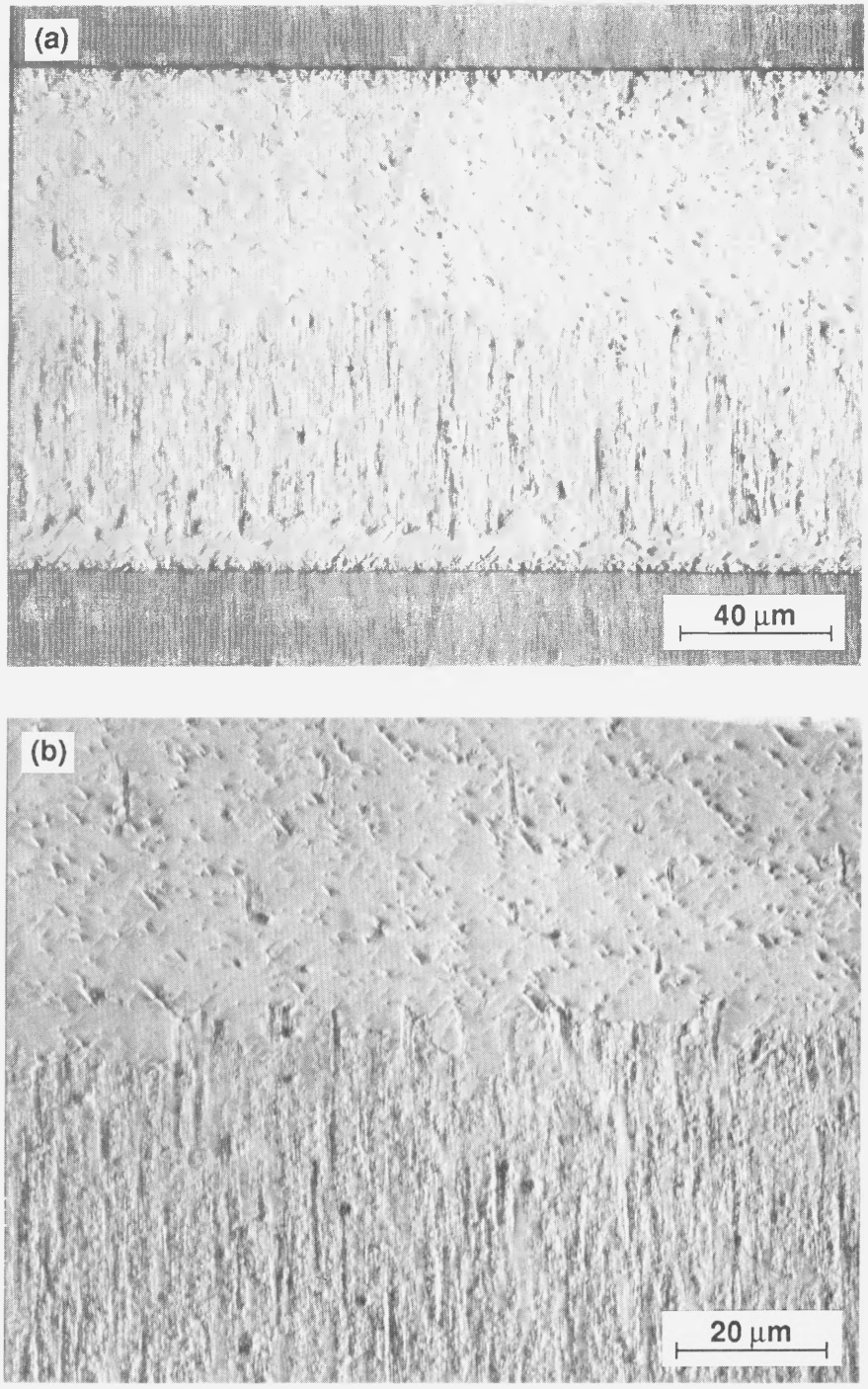

Figure 6.16. Optical micrographs showing the diffusion-welded-silver interlayer joining lapped maraging steel base metals, loaded to 1% of the expected rupture time at 552 MPa. The density of microvoids appears no greater than that of a nonloaded specimen.

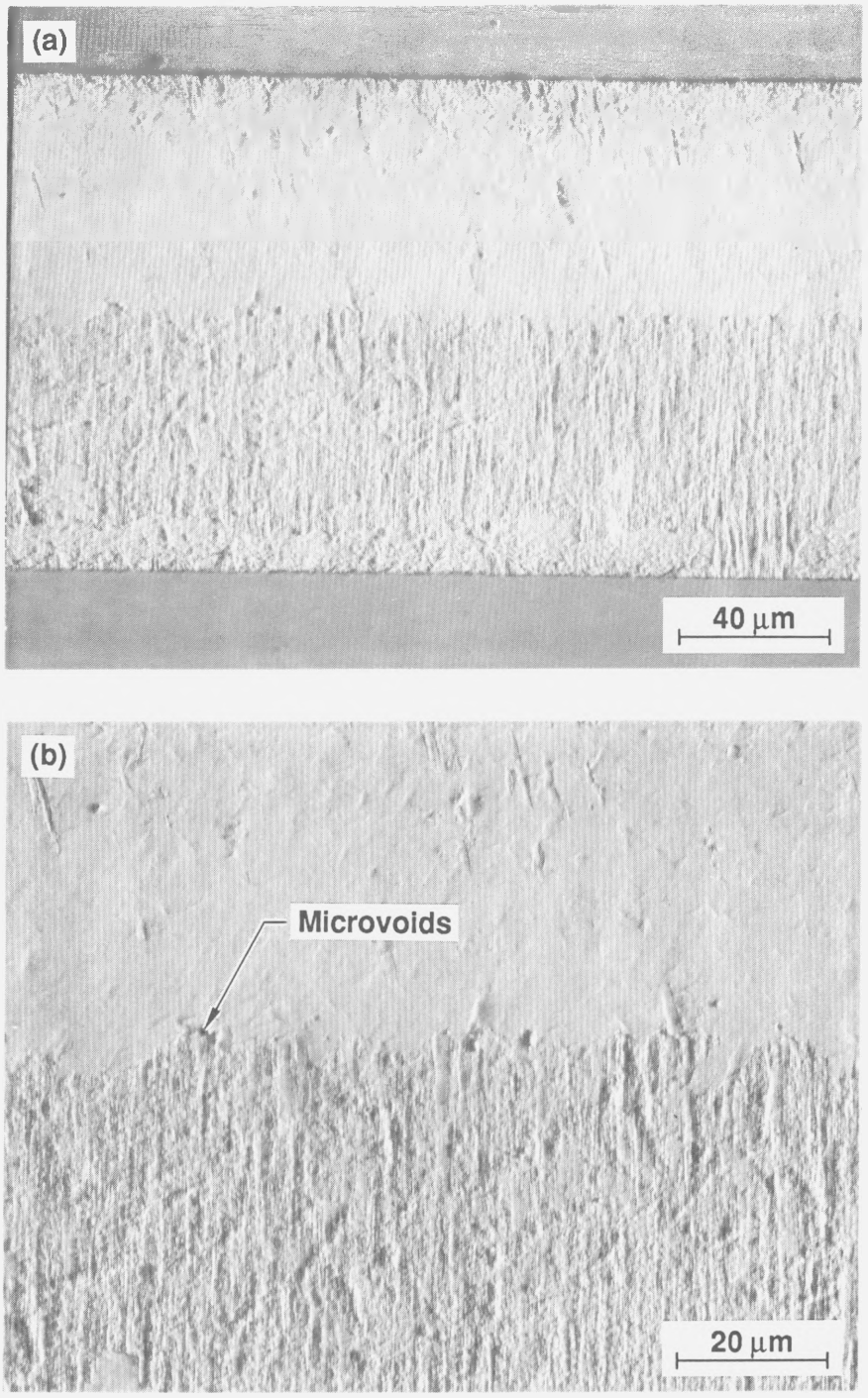

Figure 6.17. Optical micrographs showing the diffusion-welded-silver interlayer joining lapped maraging steel base metals, loaded to 10% of the expected rupture time at 552 MPa. Microvoids have begun to form at the silver-silver interface.

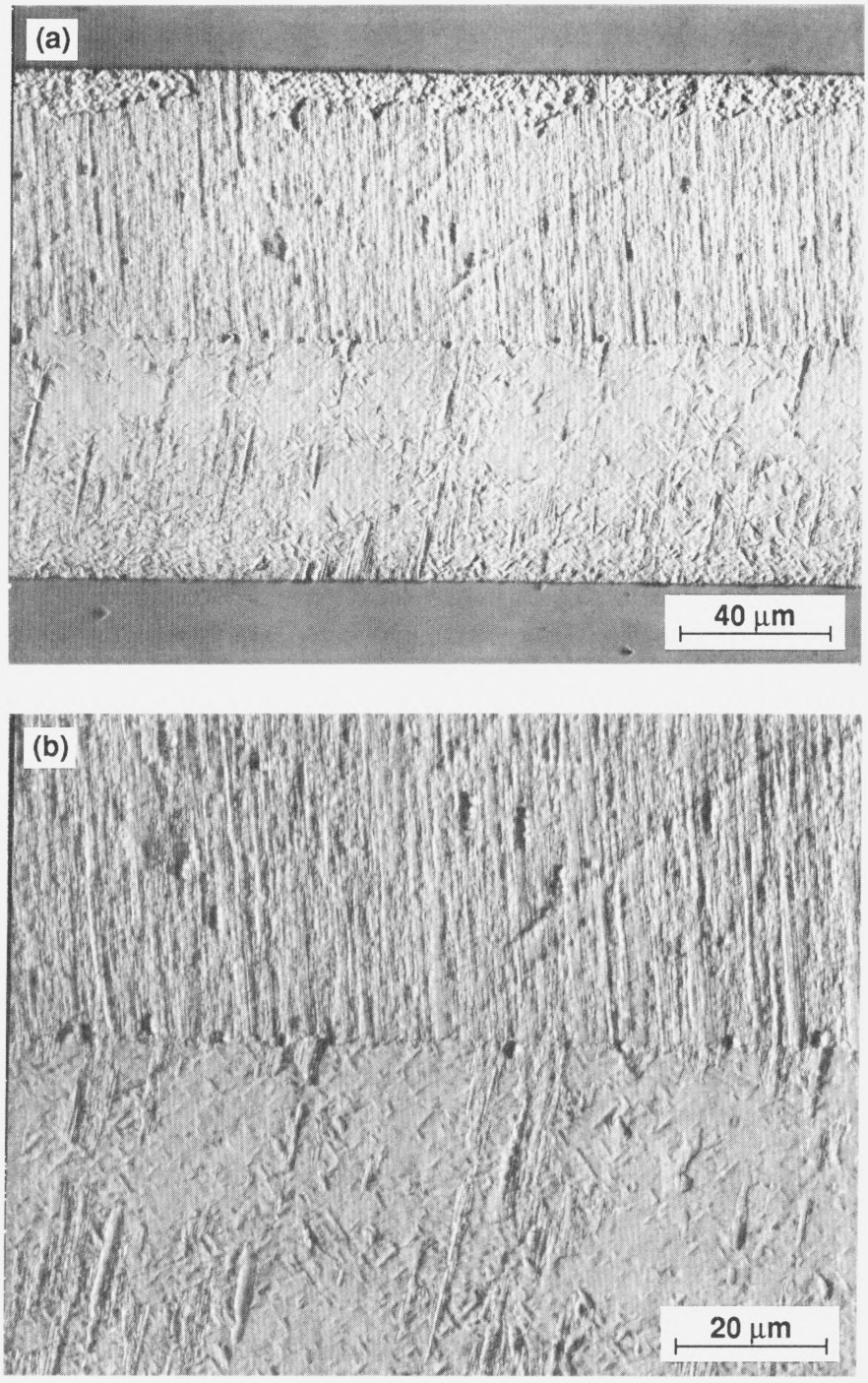

Figure 6.18. Optical micrographs showing the diffusion-welded-silver interlayer joining lapped maraging steel base metals, loaded to 25% of the expected rupture time at 552 MPa. Strings of microvoids appear along the silver-silver interface.

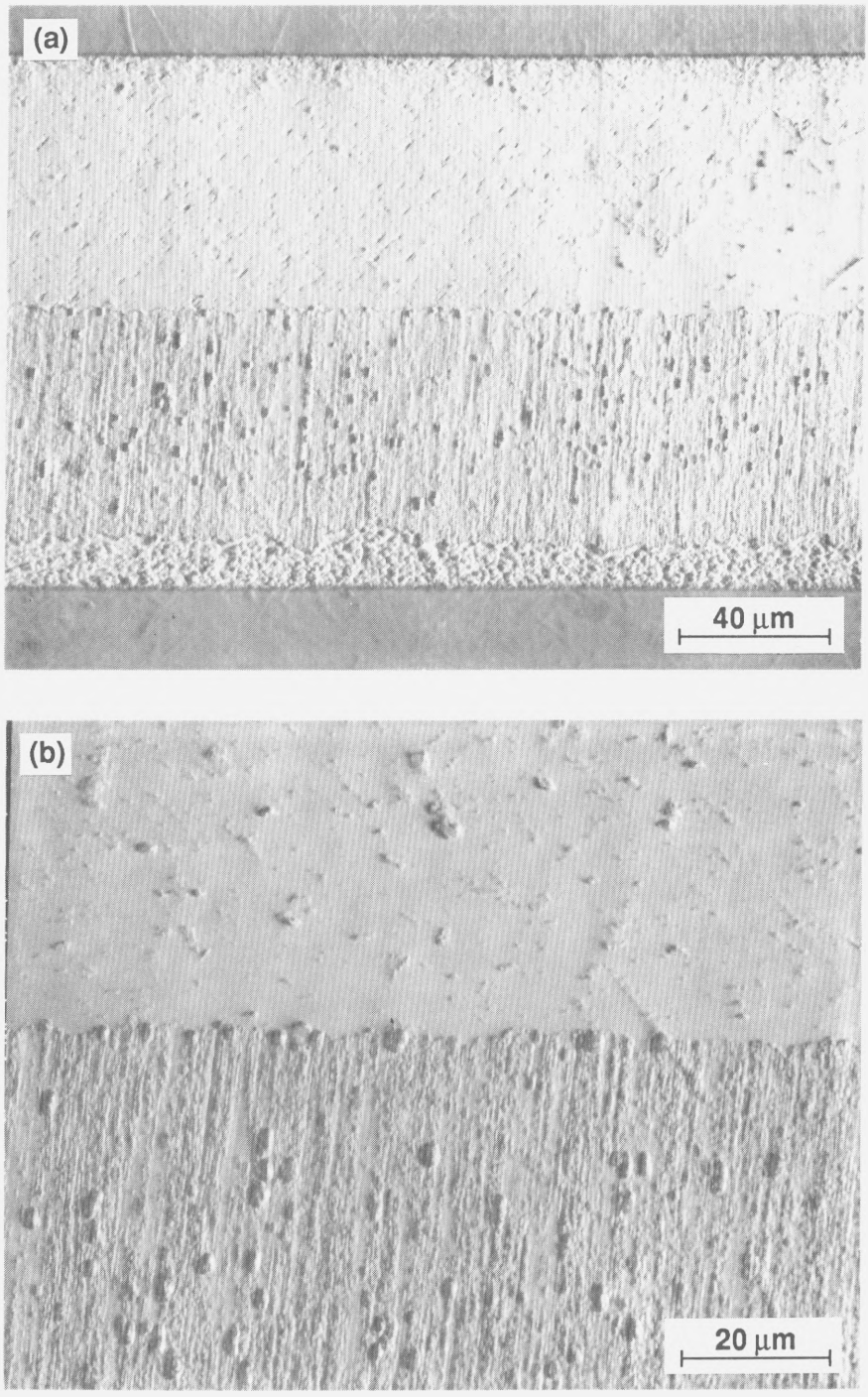

Figure 6.19. Optical micrographs showing the diffusion-welded-silver interlayer joining machined maraging steel base metals, loaded to 50% of the expected rupture time at 124 MPa. Extensive cavitation has occurred at the silver-silver interface, and also at the grain boundaries of nonrecrystallized regions.

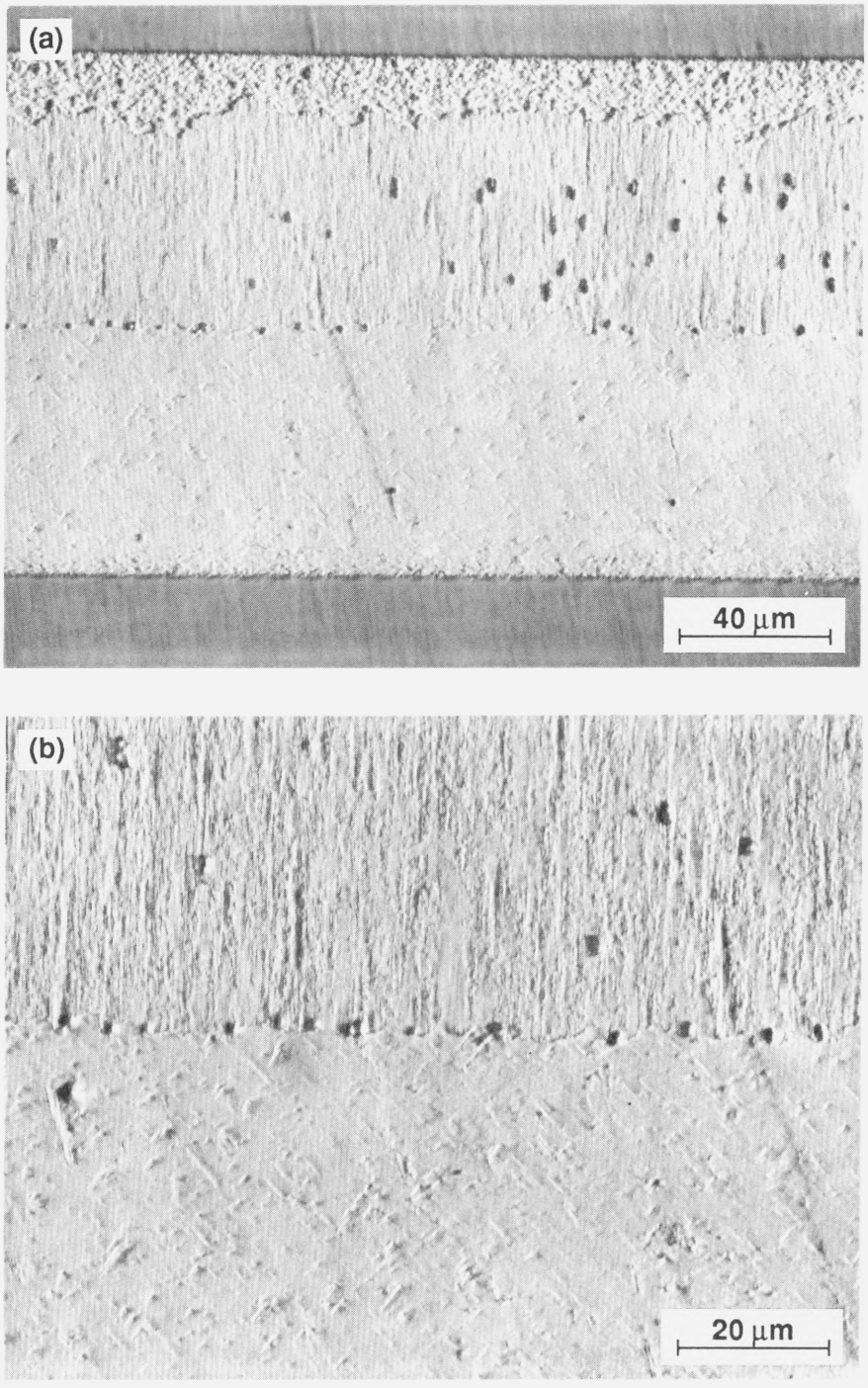

6.20. (a, b) Optical micrographs showing the diffusion-welded-silver interlayer joining machined maraging steel base metals, loaded to 75% of the expected rupture time at 483 MPa. Extensive cavitation has occurred at the silver-silver interface, and also at the grain boundaries of nonrecrystallized regions.

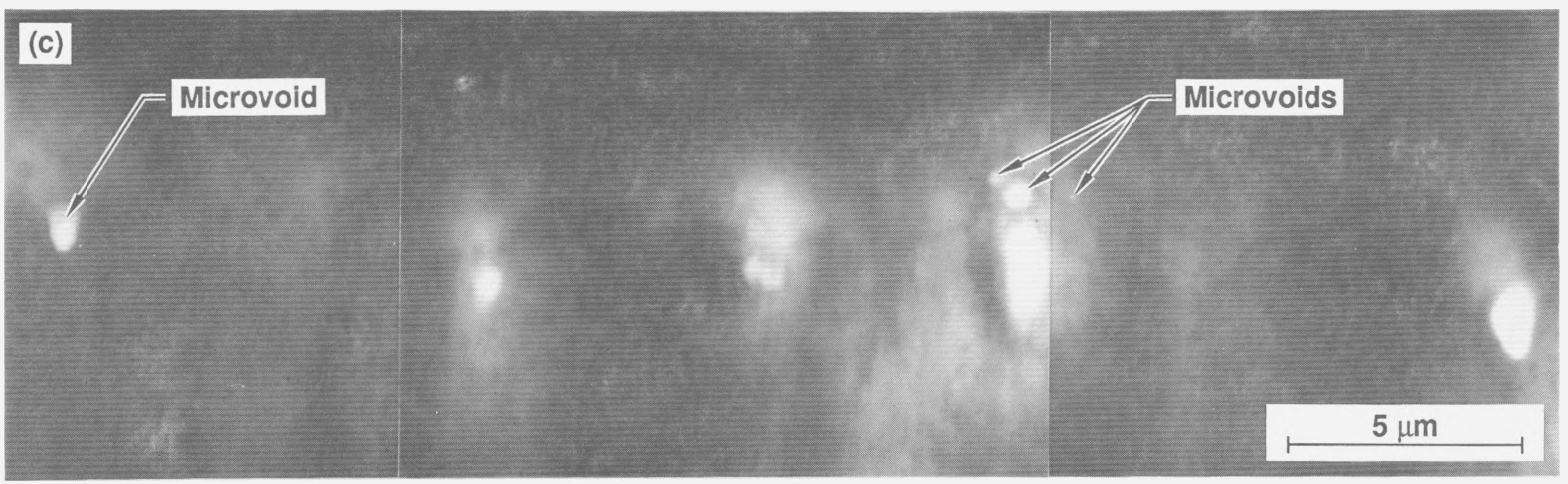

Figure 6.20. (c) Transmission electron micrograph showing a string of microvoids at the diffusion-welded-silver interlayer joining machined maraging steel base metals, loaded to 75% of the expected rupture time at 483 MPa.

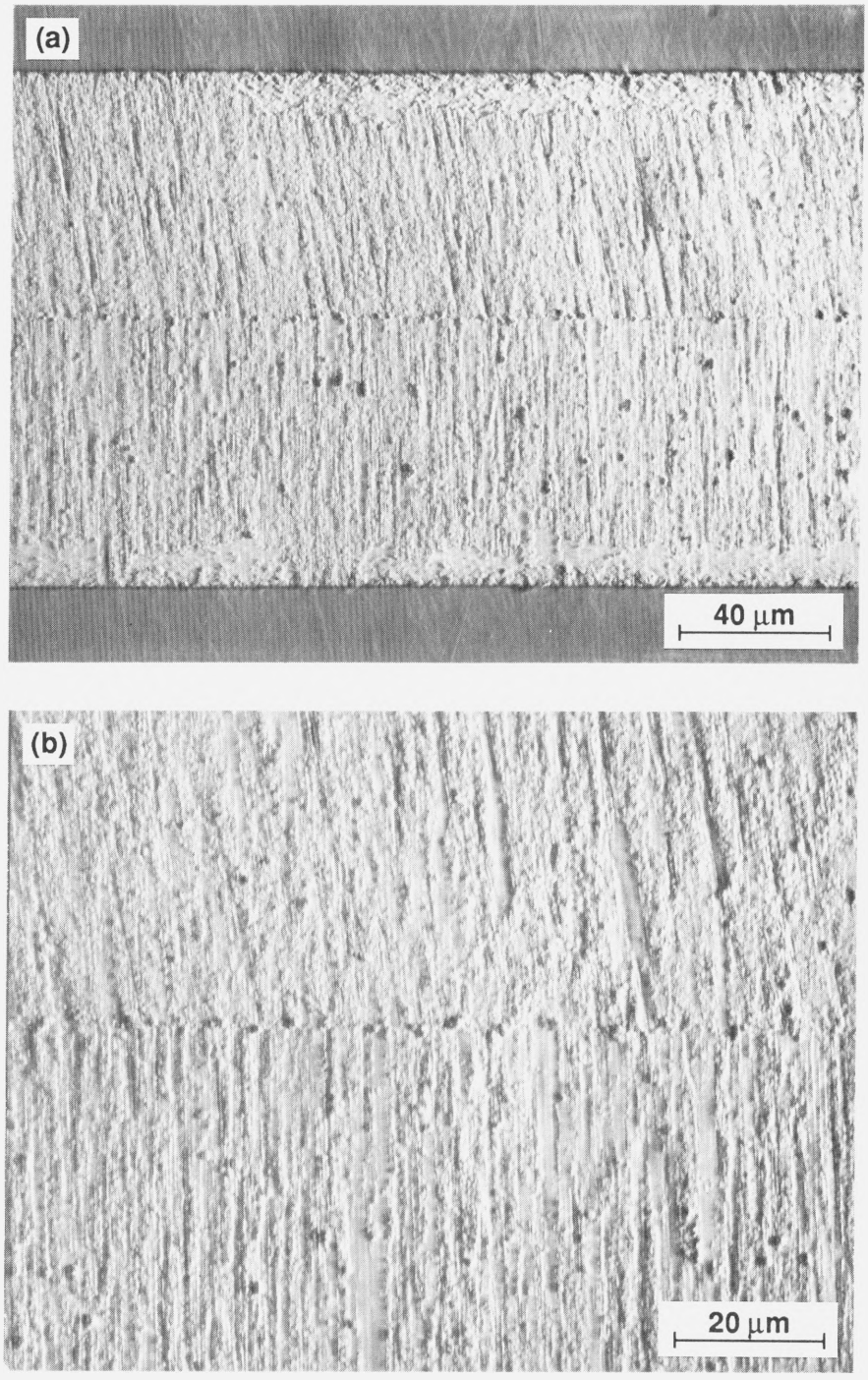

Figure 6.21. (a, b) Optical micrographs showing the diffusion-welded-silver interlayer joining lapped maraging steel base metals, loaded to 99% of the expected rupture time at 552 MPa. Extensive cavitation at the silver-silver interface results in a high density of closely-spaced microvoids. Microvoids are also evident at the grain boundaries of nonrecrystallized regions (both sides of the interlayer).

using TEM. Interestingly, the microvoids (at any interface) do not appear to grow beyond a maximum size (roughly 1 μm) already observed at 10% $t_{r,exp}$. This is an important observation which suggests that cavity nucleation rate, rather than cavity growth rate, is a more likely rate-controlling mechanism for creep rupture of the silver joints. This point will be discussed further in Section 10.1.

Transmission electron microscopy was attempted since the resolution of microvoids may be improved over SEM examination of the etched surfaces. A string of microvoids can be observed in the TEM micrograph of Fig. 6.20c (75% $t_{r,exp}$) at the silver-silver interface. Microvoids often appear in groups forming larger cavities. These cavities are small, generally 1 μm or somewhat less in diameter. Some microvoids, smaller than those resolvable with optical or scanning electron microscopy, are evident in Fig. 6.20c of about 50 nm diameter. The spacing of microvoids in interlayers close to failure is approximately between 5 and 10 μm. Some ambiguity exists in resolving microvoids less than about 50 nm, and the spacing may be actually less than 5 μm. Transmission electron microscopy of many other foils revealed that microvoids may preferentially nucleate at interfaces between columnar (nonrecrystallized) grains and recrystallized grains. Figures 6.21c and 6.21d show scanning electron micrographs of the maraging steel specimen loaded to 99% $t_{r,exp}$. Scanning electron microscopy, having the advantage of greater depth of field than optical microscopy, was used to confirm that these features are, in fact, microvoids.

Figure 6.22 shows scanning electron micrographs of a diffusion-welded-silver interlayer joining machined cold-worked stainless steel base metals, loaded at the relatively low stress level of 207 MPa, where only elastic deformation in the base metal is evident. The specimen was loaded for approximately twice the expected rupture time (assumed to be 99% $t_{r,exp}$, for convenience). This specimen contains a nonrecrystallized region at the silver-silver interface, while most of the interlayer has recrystallized. Stereoscopic photography of both of the specimens shown in Figs. 6.21 and 6.22 using the SEM confirmed that some of the larger cavities consist of clusters of smaller (<0.5 μm diameter)

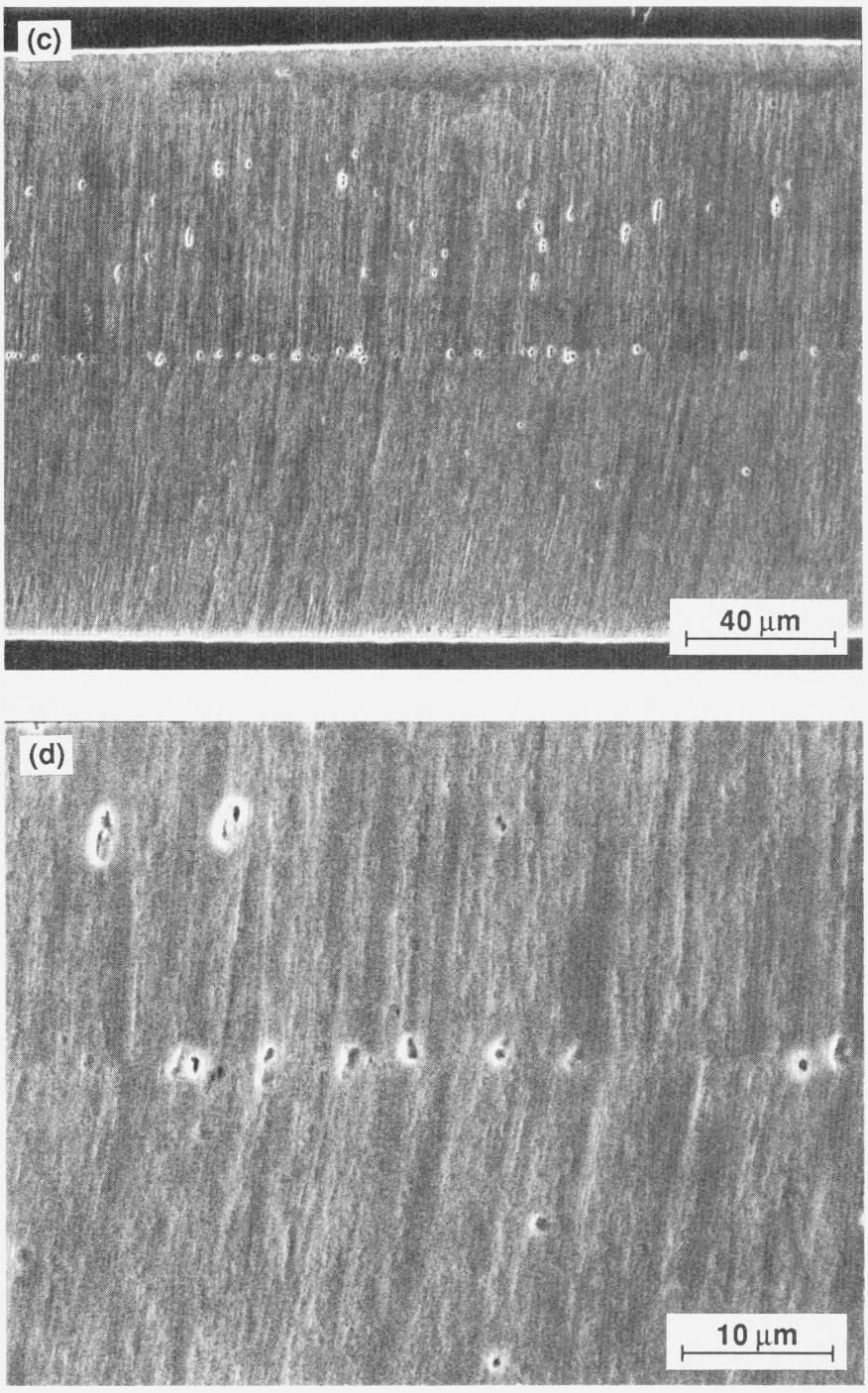

Figure 6.21. (c, d) Scanning electron micrographs showing the diffusion-welded-silver interlayer joining lapped maraging steel base metals, loaded to 99% of the expected rupture time at 552 MPa. Extensive cavitation at the silver-silver interface results in a high density of closely-spaced microvoids. Microvoids are also evident at the grain boundaries of nonrecrystallized regions (both sides of the interlayer).

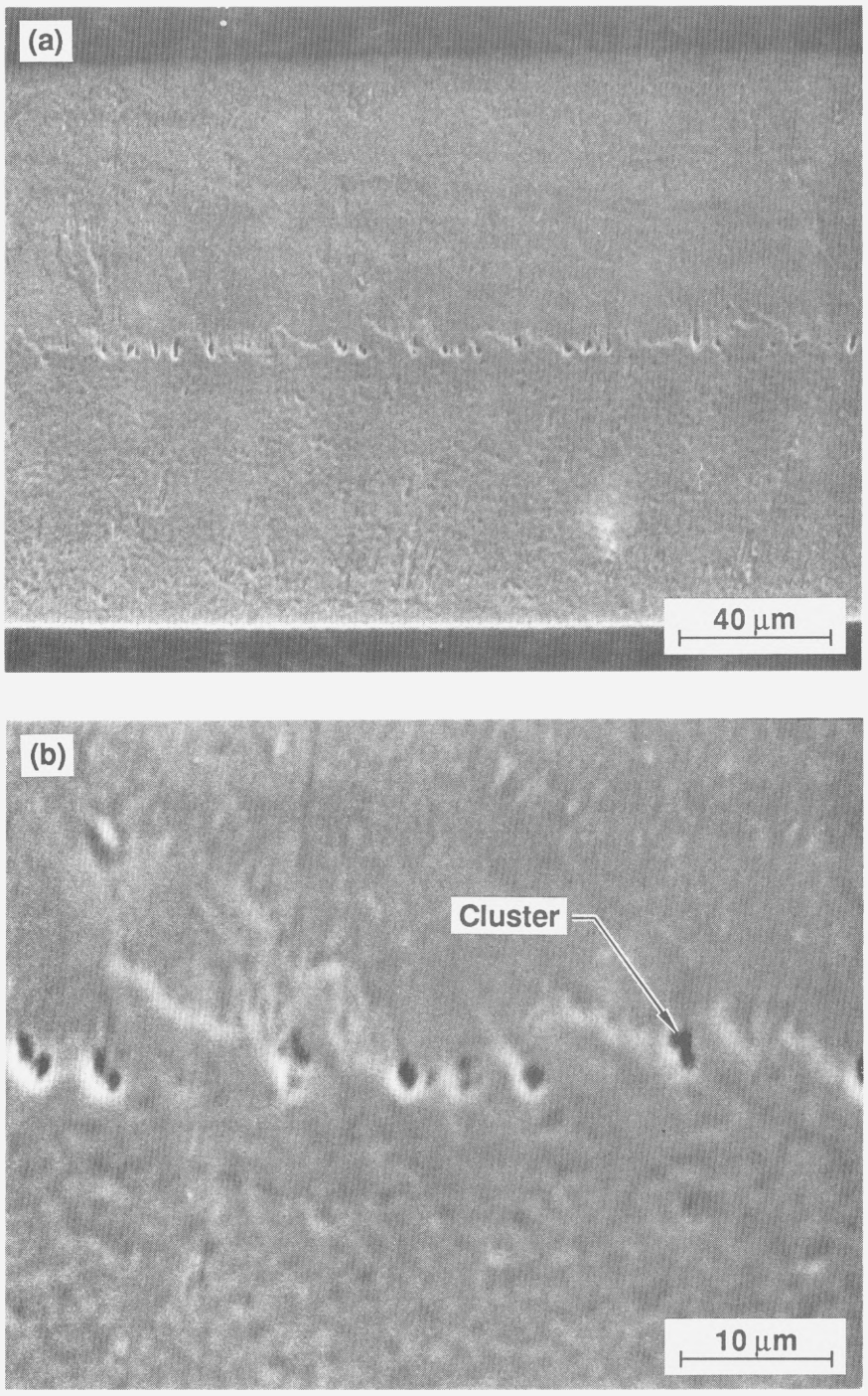

Figure 6.22. Scanning electron micrographs showing the diffusion-welded-silver interlayer joining machined cold-worked stainless steel base metals, loaded at 207 MPa (elastic behavior) for approximately twice the expected rupture time. Stereoscopic photography revealed that the larger cavities consist of clusters of smaller microvoids.

microvoids. The average cavity concentration appears to be very uniform at the silver-silver interface over most of the diameter of the specimens shown in Figs 6.16–6.22. Similarly, the fracture surface dimple sizes of specimens shown in Section 6.4 do not vary with radial distance across the specimens. Optical examination near the outer diameter (OD) of silver interlayers loaded to substantial fractions of $t_{r,exp}$ revealed that cavities are not observed within approximately 150 μm of the specimen surface. The optical micrographs in Figs. 6.23a and 6.23b were taken at the OD of the specimens shown in Figs. 6.19 (50% $t_{r,exp}$) and 6.21 (99% $t_{r,exp}$), respectively. The outer surface of the interlayer can be seen on the right-hand side of the micrograph. In both specimens, the extensive cavitation at the silver-silver and columnar grain boundary interfaces throughout the remainder of the interlayer is not present near the outer edge. The absence of cavitation near the OD of the interlayer may be related to the change in stress state as predicted by finite-element analysis (see Fig. 6.3). The hydrostatic and effective stresses in a 150-μm-thick interlayer are very nearly uniform over most of the specimen diameter. However, the hydrostatic stress begins to decrease rapidly at approximately 300 μm from the OD, while the effective stress increases slightly in this region. Eventually, the effective stress decreases also, but not until within approximately 75 μm from the OD. Therefore, although cavity nucleation resulting from dislocations pile-ups is a function of the effective stress, the magnitude of the hydrostatic stress may be important for cavity stability and, hence, the nucleation rate.

Chemical etching of the silver-base-metal interface does not appear to permit critical examination for microvoids as with the silver-silver interface by light microscopy or by SEM. However, a few foils were extracted from the silver-base-metal interface of prestressed specimens and examined in the TEM. Elongated cavities were confirmed at the nonrecrystallized-recrystallized silver interface located approximately 1 μm from the base metal (shown in Fig. 3.4c). These observations, along with the fracture surface

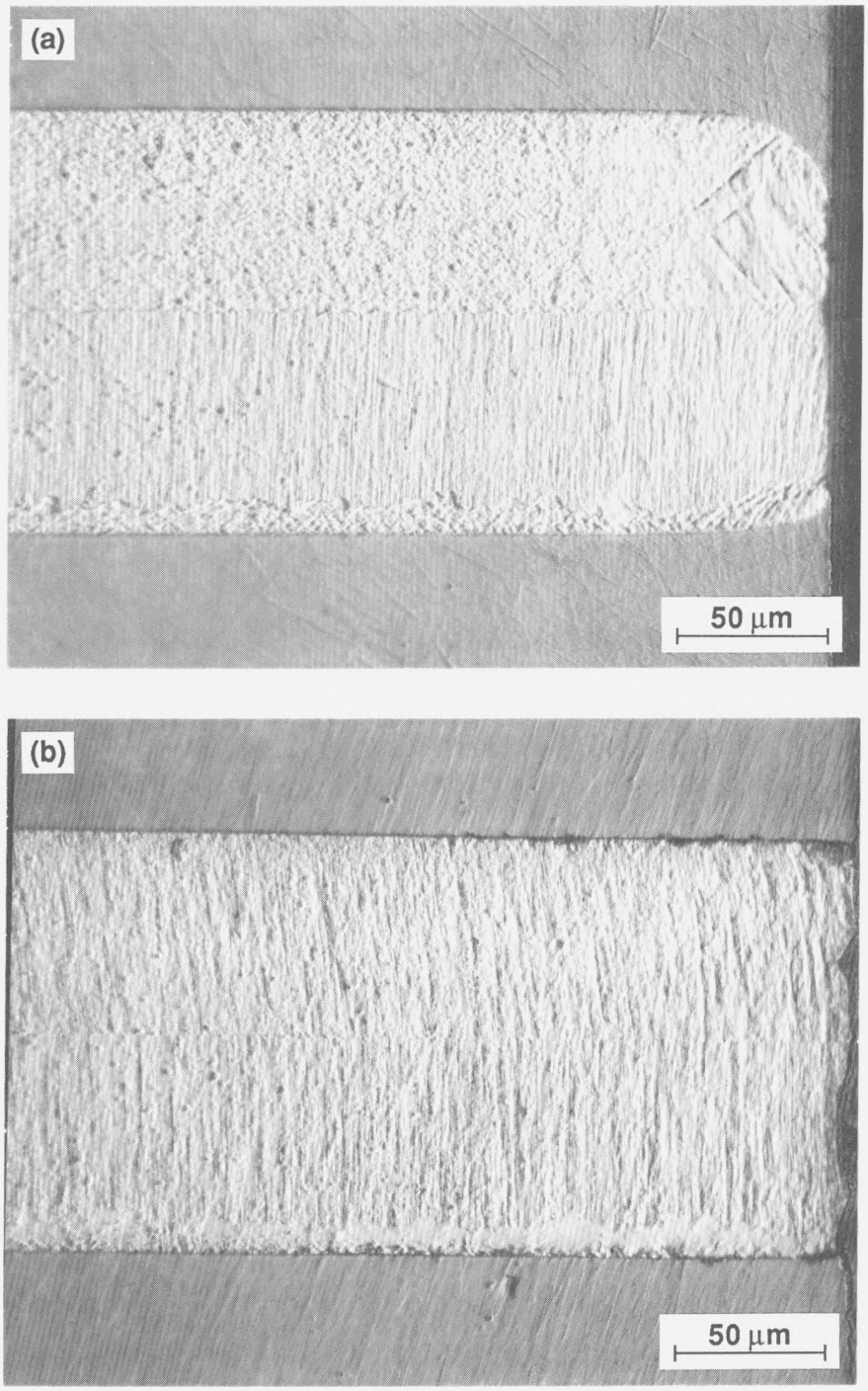

Figure 6.23. Optical micrographs taken at the outer diameter (seen on the right-hand side of the figure) of the specimens shown in (a) Fig. 6.19 and (b) Fig. 6.21. Examination of silver interlayers loaded to substantial fractions of the expected rupture time revealed that cavities are not observed within ~1 interlayer thickness (150 μm) of the specimen surface.

morphologies and nondependence of fracture location on rupture times, suggests that the same mechanism of failure is occurring at all three interfaces.

Finally, the five diffusion-welded-silver specimens utilizing maraging steel that were loaded to 1, 10, 25, 50, and 99% of the expected rupture time, along with the cold-worked stainless steel specimen loaded to 99% $t_{r,exp}$, were examined for external cracks by ultraviolet-sensitive-dye penetrant applied while the joints were loaded and by optical metallography of the joint cross sections (unloaded state). No external cracks were observed, confirming that the fracture process does not involve the (slow) growth of external cracks.

CHAPTER 7
CREEP TEST RESULTS: PLASTIC BASE METALS

7.1. Annealed Type 304 Stainless Steel

Austenitic stainless steels are known to exhibit time-dependent plasticity (creep) at ambient temperature. In one study,[43] creep tests were performed on annealed austenitic stainless steels (18-Cr) of varying nickel content. The creep rate was found to diminish very rapidly with strain, exhibiting logarithmic plastic strain versus time behavior. Deviations from logarithmic behavior were observed at strains of 8–10%, resulting in a concave downward curvature in the strain versus log time plot. The investigators concluded that the increased strain-hardening rate at strains of 8–10% was due to the appearance of deformation twins, and also to the formation of martensite (α'-BCC phase) in the γ-austenite structure. At higher strains, the strain-hardening rate, again, was found to exhibit nearly linear strain versus log time behavior.

Figure 7.1 shows the ambient-temperature creep behavior of the annealed type 304 SS base metal utilized in the present study. Plots of plastic strain versus (log) time were obtained from creep tests of base-metal tensile specimens at stresses from 241–293 MPa (solid lines), as described in Section 2.1.2. Creep data at stresses from 138–224 MPa (dashed lines) were obtained from creep rupture tests of the diffusion-welded-silver joints using the measurements of base-metal gage section diameter, as described in Section 2.7.1. The time-dependent creep deformation, shown plotted on semi-logarithmic coordinates, exhibits primary strain-hardening typical of ambient-temperature creep of austenitic stainless steels.[68] The creep rate is shown to decrease continuously with time, and also decreases with applied stress level. However, time-dependent plastic strain in the annealed SS base-metal gage section of diffusion-welded-silver joints was still recorded at stresses as low as two-thirds of the (0.2% plastic strain offset) yield stress.

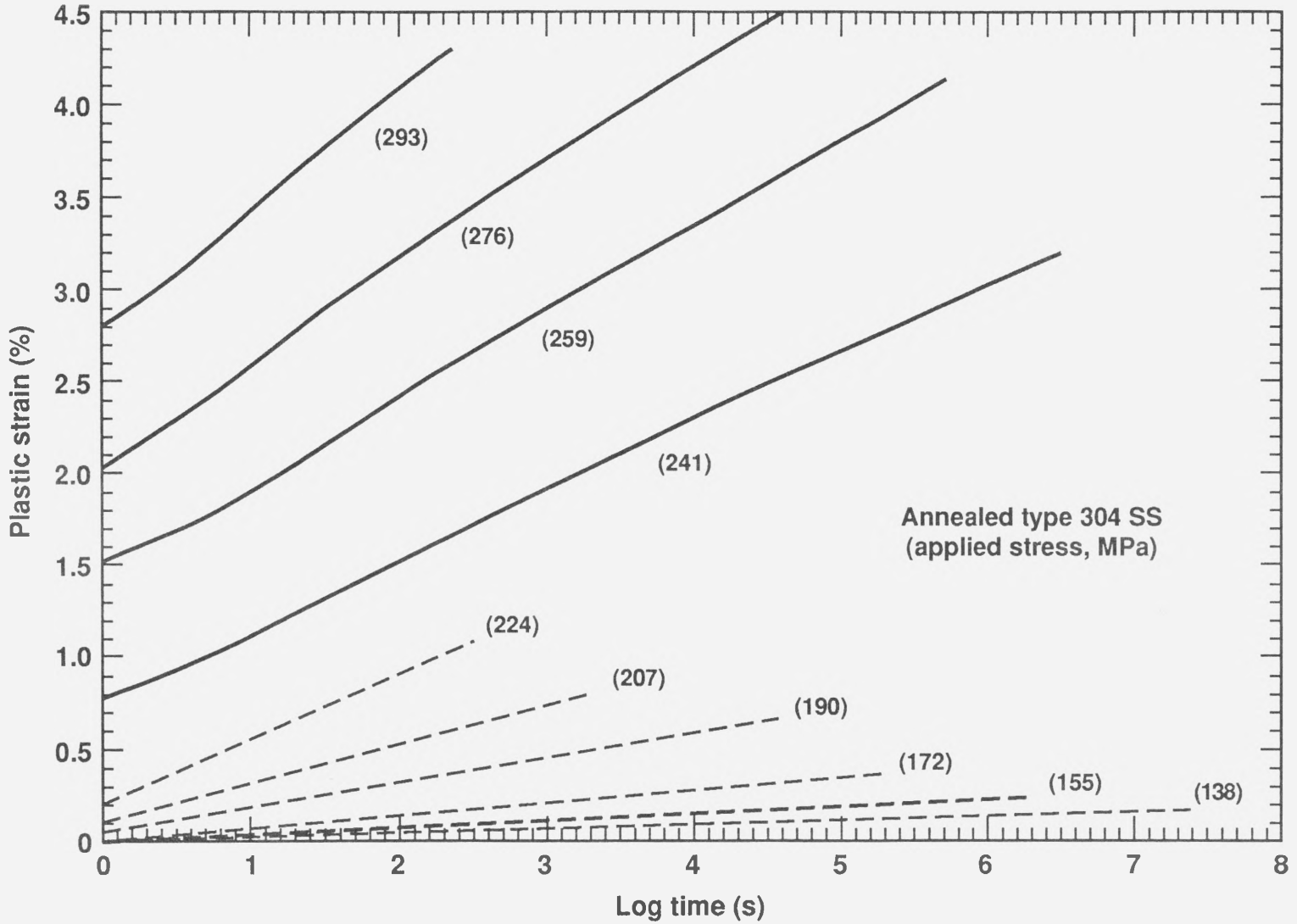

Figure 7.1. Ambient-temperature creep behavior of annealed type 304 stainless steel at a variety of applied stresses.

One of the steels tested in an earlier creep study[43] had a nominal composition of 18-Cr, 8-Ni, closely matching that of type 304 stainless steel used in the present study. The creep behavior of type 304 SS can be compared using estimations of the constant structure stress exponent:

$$N = \left[\frac{\partial \ln \dot{\varepsilon}}{\partial \ln \sigma}\right]_{T,s}, \tag{4}$$

determined by calculating the change in creep strain rate with applied stress at constant plastic strain. The creep data published in the previous study[43] was evaluated at plastic strains of 1 and 3%, and these calculations resulted in an average value of N equal to 55. Calculations of the constant structure stress exponent for the annealed type 304 SS used in the present study was determined by substituting 1/t for $\dot{\varepsilon}$ in Eq. 4. This resulted in an average value of N equal to 60 (evaluated at constant plastic strains in the range of $\varepsilon_p = 0.2–3\%$). Additionally, the stress exponent is found to increase with applied strain (or stress) over the range of data presented in Fig. 7.1, consistent with the results reported previously[43] for austenitic stainless steels of similar compositions. The significance of the relationship between the constant structure stress exponent of the SS base metal and the creep-rupture stress exponent of diffusion-welded-silver interlayers joining SS base metals, will be discussed fully in Sections 8.5.1 and 10.1.

7.2. Cold-Worked Type 304 Stainless Steel

Figure 7.2 shows the ambient-temperature creep behavior of the cold-worked type 304 SS base metal utilized in the present study. Plots of plastic strain versus (log) time were obtained from creep tests of base-metal specimens at stresses from 327–396 MPa (solid lines). Creep data at a stress of 310 MPa (dashed line) was obtained from creep rupture tests of the diffusion-welded-silver joints, using measurements of the base-metal diameter

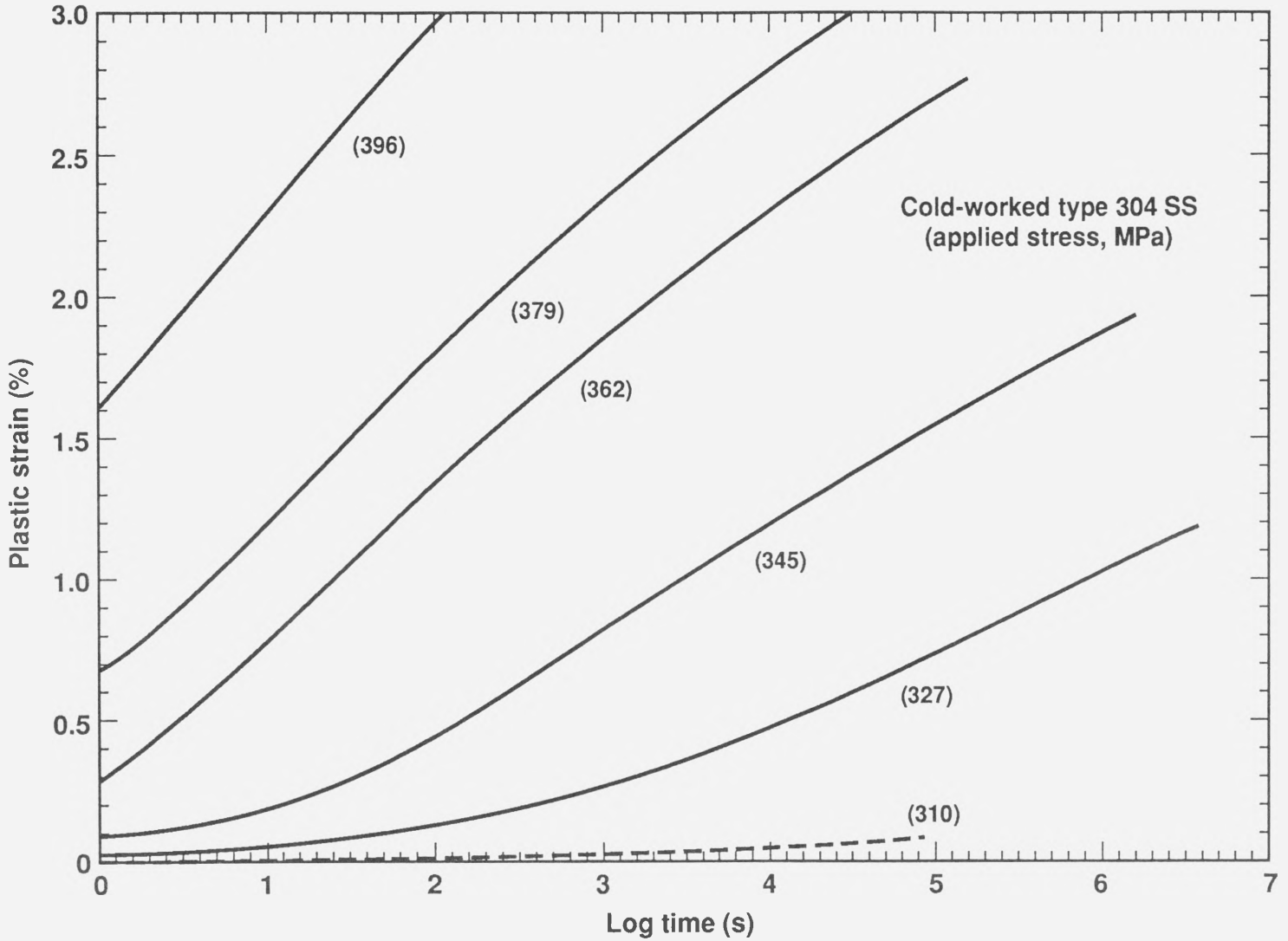

Figure 7.2. Ambient-temperature creep behavior of cold-worked type 304 stainless steel at a variety of applied stresses.

in the gage section. Calculations of the constant structure stress exponent from Fig. 7.2 (determined by substituting 1/t for $\dot{\varepsilon}$ in Eq. 4) resulted in an average value of N equal to about 80. This value is larger than that of the annealed SS discussed in the previous section, consistent with increases in stress exponent with increasing applied strain.[43] Additionally, the concave-downward curvature of the strain versus log time plots are in agreement with the results previously reported[43] for creep strains of 8–10%, as discussed in the previous section. The cold-worked type 304 SS used in the present study represents the equivalent of cold-working annealed SS to a level of 7% strain, as shown by the flow stress of 360 MPa in Figure 2.4b. Therefore, the observed deviation from purely logarithmic behavior may possibly be explained by the appearance of martensite and deformation twins, as suggested by the results of the earlier study.[43]

Calculations of the constant structure stress exponents from other previously reported stainless steel data[69–74] were performed to compare the results with those of the present study. Included in the analysis were austenitic stainless steels with compositions of the main alloying elements (Cr and Ni) similar to those utilized in the present study (e.g., type 304, 308, 310, and 316 stainless steels). The average constant structure stress exponent (and standard deviation) determined from this analysis is N equal to 70 (±34). Therefore, the constant structure stress exponent of the stainless steel utilized in the present study is found to be consistent with the results reported by others for austenitic stainless steels of similar compositions.

CHAPTER 8
CREEP RUPTURE RESULTS: PLASTIC BASE METALS

8.1. Effect of Base-Metal Properties

Figure 8.1 shows the creep-rupture behavior of 150-μm-thick diffusion-welded-silver interlayers joining one of two different strengths of type 304 stainless steel base metals: annealed (squares; σ_y = 221 MPa) and cold-worked (triangles; σ_y = 359 MPa). The specimens welded using different strength stainless steels were fabricated in an identical manner. All of the data refer to base-metal specimens that were machined prior to coating. As shown in Figs. 7.1 and 7.2, significant plastic strain (e.g., >0.2%) is occurring at most of the stresses at which creep rupture is observed. For both cases, as the applied stress decreases, time-to-rupture, t_r substantially increases. This behavior is consistent with all previous data for creep ruptures of interlayers joining plastically-deforming base metals.[20,21,40,41] (The bend or "knee" in the curve for specimens utilizing cold-worked stainless steel will be explained in Section 8.6). The creep-rupture applied stress exponents, $n_{app} = [-d (\ln t)]/[d (\ln \sigma_{app})]$ were calculated, using regression analysis, as 21 (correlation coefficient, r^2 = 0.95) for annealed SS base metals, and 42 (correlation coefficient, r^2 = 0.96) for cold-worked SS base metals ($\sigma_{app} \geq 293$ MPa). The significance of the creep-rupture applied stress exponents will be discussed in Section 8.5.

As mentioned in Section 5.3.3, the range of scatter is only a factor of about 10 in creep rupture time at any given applied stress level for diffusion-welded-silver joints between annealed type 304 SS, utilizing PM sputter-deposition from three separate coating operations. By contrast, the scatter was reported to be a factor of about 50 (from the highest to the lowest values) in creep rupture time at any given applied stress level for silver joints between uranium and type 304 SS, utilizing HHC deposition from three separate coating operations.[20,40] Therefore, diffusion-welded-silver interlayers fabricated utilizing PM sputter-deposition appear to have more reproducible creep rupture properties than those

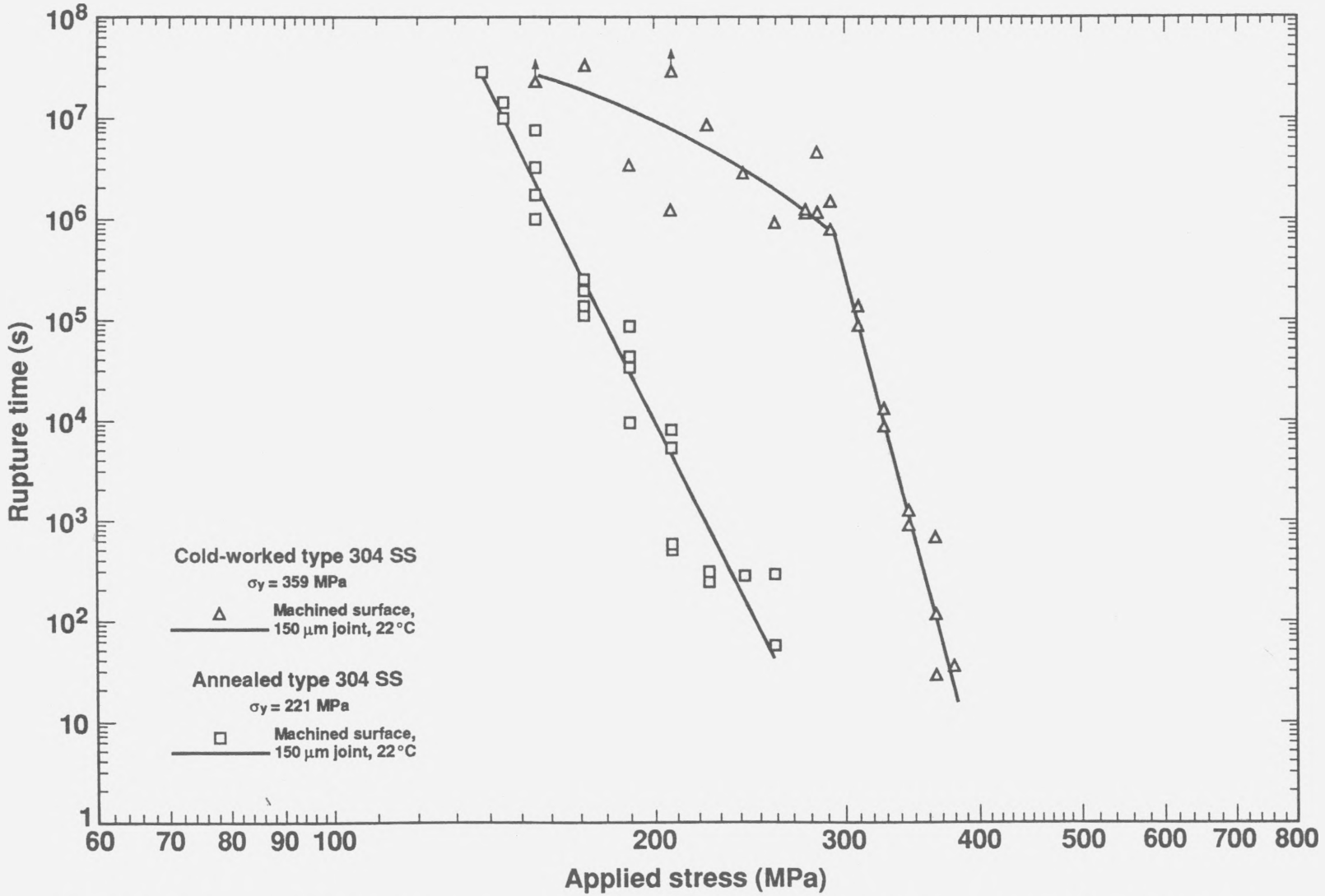

Figure 8.1. Effect of base-metal plasticity on creep rupture of diffusion-welded-silver joints between plastic base metals.

utilizing HHC deposition. This reduction in experimental scatter has the advantage of allowing more accurate assessments of the nature of the mechanical behavior of interlayer welds.

An important observation is that, for an applied stress that is common to both sets of stainless steel data (e.g., 250 MPa), the rupture times for diffusion-welded-silver joints between cold-worked stainless steel base metals are about a factor of 10^4 higher than for specimens that utilize the weaker (and less creep-resistant) annealed type 304 SS. The processing steps and specimen geometry are identical for both kinds of specimens. Therefore, the dramatic difference between the rupture times must be a consequence of the mechanical behavior of the stainless steel base metals rather than the silver interlayer. This confirms some sort of "base-metal acceleration" theory to rationalize the difference in the creep-rupture times.

The relatively high tensile strengths of the diffusion-welded-silver joints utilizing the annealed and the cold-worked stainless steels (304 and 400 MPa respectively; from results of Section 5.1), as compared to the ultimate tensile strength of bulk polycrystalline silver of approximately 150 MPa,[35] is rationalized by the constraint provided by the base metals. However, at higher stresses time-dependent base-metal plasticity (or creep) is observed in the base metals. As the base metal creeps, concomitant shear occurs within the soft silver interlayer under a state of high triaxial stress. The interlayer plasticity causes cavitation and failure just as in the elastic base-metal case, however, the rupture is accelerated or "premature" because of base-metal creep. By this reasoning, any modification in stress, temperature (to be discussed in Section 8.3), or base material selection or processing that alters the creep rate of the base metal would correspondingly alter the rupture time, as observed. For example, when the creep rate of the base metal is substantially reduced for a given applied stress, as with a substitution of annealed with cold-worked stainless steel, the time-to-rupture increases. Finite-element analyses have confirmed that plasticity in the base

metal allows the interlayer to plastically deform to a much greater extent than if the base metal deforms only elastically (this will be discussed in Section 8.5.2).

8.2. Effect of Surface Finish

Figure 8.2 shows the effect of base-metal surface finish, that is eventually coated, on the creep-rupture behavior of joints utilizing cold-worked type 304 SS. The two lapped cold-worked SS base-metal specimens (triangles with solid points) have longer rupture times than those of machined cold-worked SS, as was the case with the maraging steel specimens utilizing lapped base-metal surfaces. However, the increase in creep rupture times of specimens utilizing lapped versus machined plastic base metals is only a factor of 5, considerably less than the increase of approximately 50 for specimens utilizing lapped versus machined elastic base metals. The difference between the increases in creep rupture times for lapped plastic versus lapped elastic base-metal specimens may be due to the difference in failure processes For the case of a plastic base metal, the strain in the silver is externally and uniformly imposed on the silver by the deformation of the base metal. For elastic base metals, plasticity is caused by the effective stress within the interlayer. It is believed that the heterogeneities along the diffusion-welded-silver interface caused during the joining of the comparatively rough machined surfaces could result in regions which may be more resistant to plasticity than other regions. The heterogeneities at the diffusion-welded-silver interface may be less significant in increasing the nucleation and coalescence rate of cavities in specimens utilizing plastic base metals compared to those utilizing elastic base metals, where the strain is not imposed by base metal deformation, but is indigenous to the interlayer.

8.3. Effect of Test Temperature

Figure 8.3 shows the effect of test temperature on the creep-rupture behavior of silver joints between annealed type 304 SS base metals. The hollow points refer to ambient-

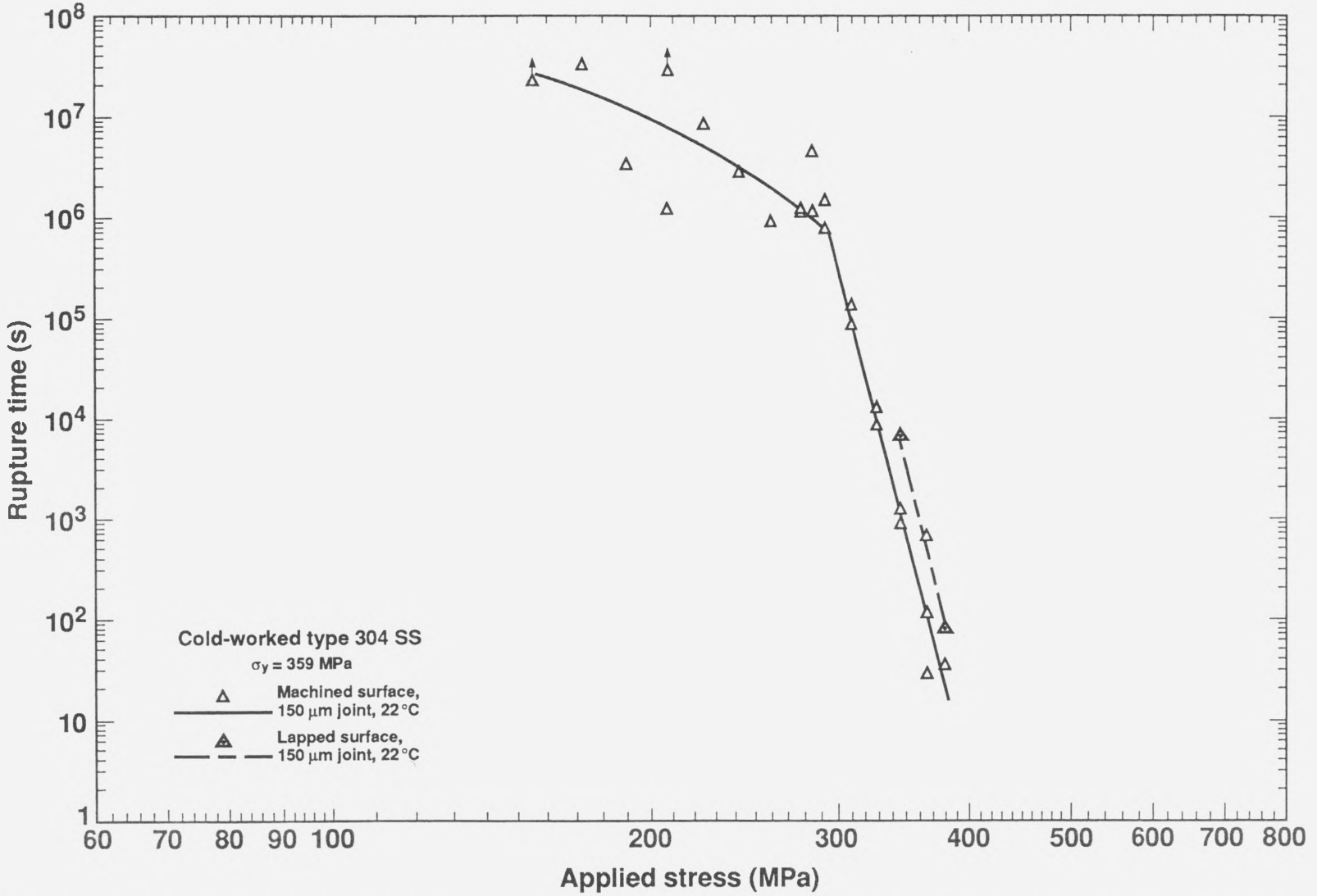

Figure 8.2. Effect of base-metal surface finish on creep rupture of diffusion-welded-silver joints between plastic base metals.

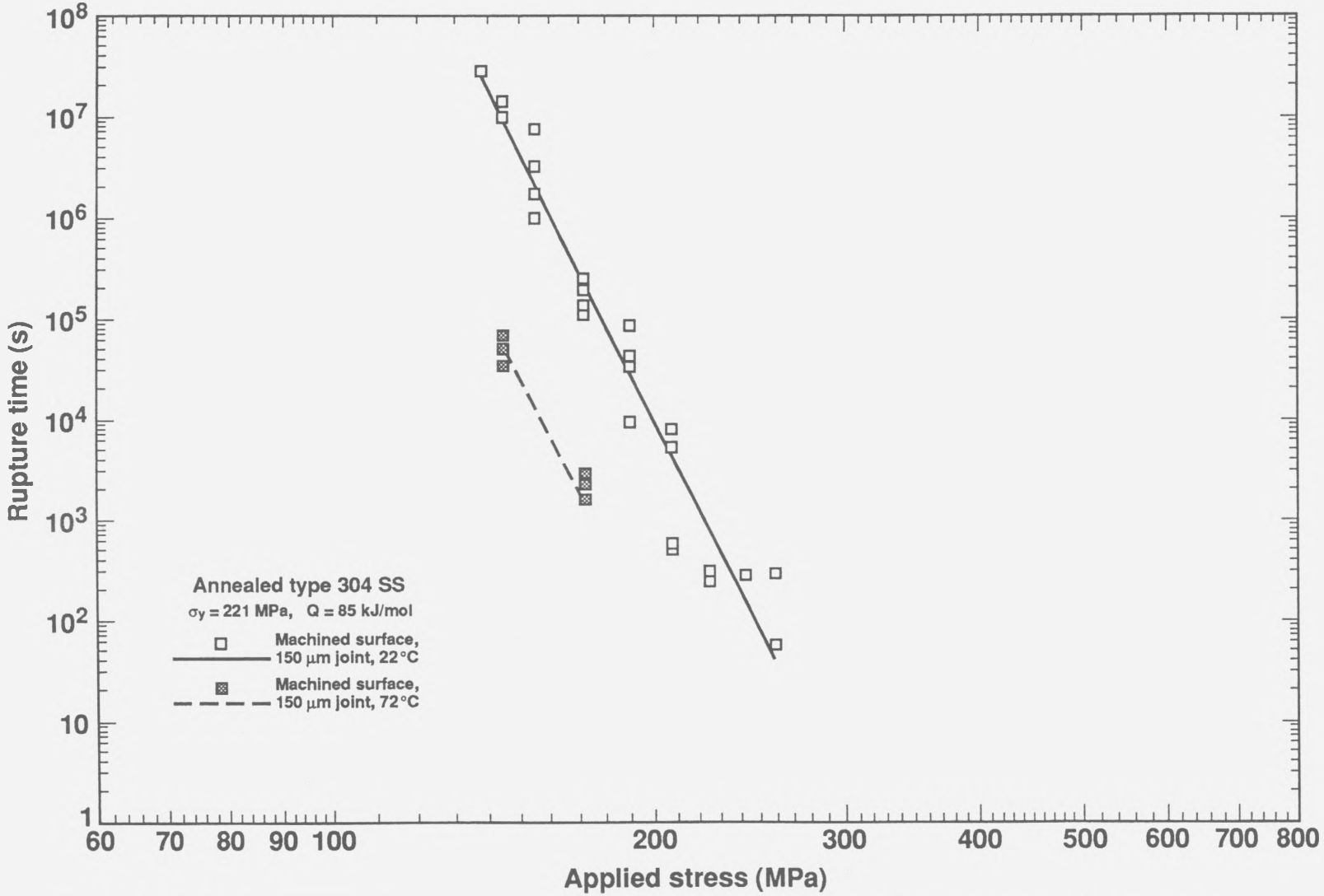

Figure 8.3. Effect of test temperature on creep rupture of diffusion-welded-silver joints between plastic base metals.

temperature tests (295 K or 22 °C); shaded points refer to 345 K (72 °C) tests. With an increase of the test temperature from 22 to 72 °C, the base-metal creep rate significantly increases and t_r decreases. The activation energy for creep rupture, Q_r (calculated using Eq. 3) equals 85 kJ/mol. This quantity is nearly identical to the activation energy for creep rupture (85.8 kJ/mol) reported[20,40] for diffusion-welded-silver interlayers joining uranium and type 304 SS base metals. It was suggested in a following study[21] that the activation energy for creep rupture more closely matches the activation energy for plastic flow in stainless steel, evaluated as equal to 68±20 kJ/mol, than that of silver (53 kJ/mol[66]). This evidence, along with the coincidence of the creep-rupture and stainless steel creep stress exponents led the investigators[21] to conclude that base metal plasticity controls the deformation and failure of silver interlayers. An analysis of previously reported data[68,74,75,76] on type 304, 304L, and 310 stainless steels was performed to determine the average activation energy for plastic flow in SS. This value was estimated using the equation:

$$Q = \left[\frac{NR\, d(\ln \sigma)}{d\left(\frac{1}{T}\right)} \right]_{\varepsilon_p}, \qquad (5)$$

where N is the constant structure stress exponent, R is the universal gas constant, σ is the flow stress at temperature T, and E is Young's modulus. Results of this analysis found that the average value of Q is approximately equal to 1500N. Assuming an average value of N equal to 70 (from Chapter 7), the average activation energy for plastic flow, Q is equal to 105 kJ/mol. Although this value is higher (by ~25%) than the value calculated from the creep-rupture data, it is subject to fairly large deviations (±35%) because of the range of experimental results. Therefore, the activation energies for creep rupture of silver interlayers between SS base metals and for plastic flow in SS are comparable, suggesting

that the temperature dependence of creep rupture is determined by creep plasticity in the stainless steel base metal.

8.4. Fracture Surface Characterization

Generally, both silver-silver and silver-base-metal separations are observed for a given specimen. Figure 8.4 shows the summary plot for creep rupture behavior of diffusion-welded-silver joints between plastic base metals. The fraction of fracture surface associated with silver-silver separation decreases from about 85% at the higher applied stresses to only 20% at the lower stresses. Figure 8.5 shows a plot of percent silver-silver fracture as a function of applied stress level for 150-μm-thick silver interlayers joining machined stainless steel base metals. This trend of decreasing percent silver-silver fracture with applied stress (also observed for the case of elastic base metals) was not observed in a prior study[40] of diffusion-welded-silver interlayers joining uranium and SS base metals. A plot of percent silver-silver fracture for these interlayers, which were prepared using hot-hollow cathode (HHC) deposition, is shown in Fig. 8.6. It was established in the earlier study[40] that the percent of fracture at the diffusion-welded-silver (silver-silver) interface was independent of the UTS and creep rupture times, and that the fracture morphologies of UTS and creep rupture specimens were indistinguishable. It is not clear why the percent of fracture at the silver-silver interface should decrease with applied stress (or time). There is no convincing evidence that the rupture times are influenced by the distribution of fracture along the three principal interfaces for interlayers between plastic or elastic base metals.

Figure 8.7 illustrates a silver-silver ductile rupture in an annealed SS base-metal specimen utilizing a machined surface, and several observations can be noted. First, classic ductile dimples are observed (see Fig. 8.7b) which is characteristic of failure by a microvoid-coalescence type mechanism. These dimples appear similar to the small dimples between the large cavities of the machined maraging steel base-metal specimens shown in Fig. 6.7e. Second, it appears that there is the same concentric pattern to the voids

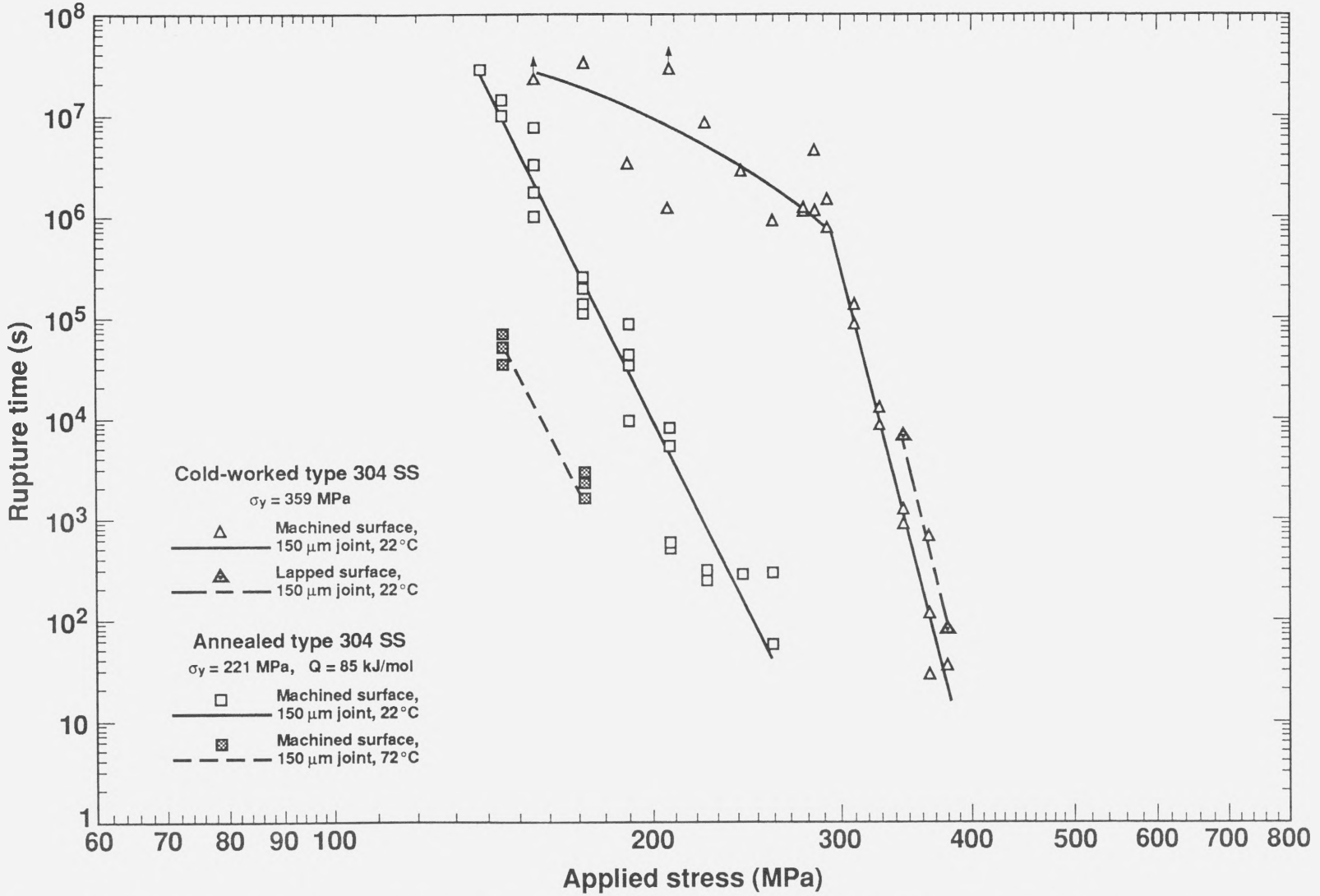

Figure 8.4. Summary plot for creep rupture behavior of diffusion-welded-silver joints between plastic base metals.

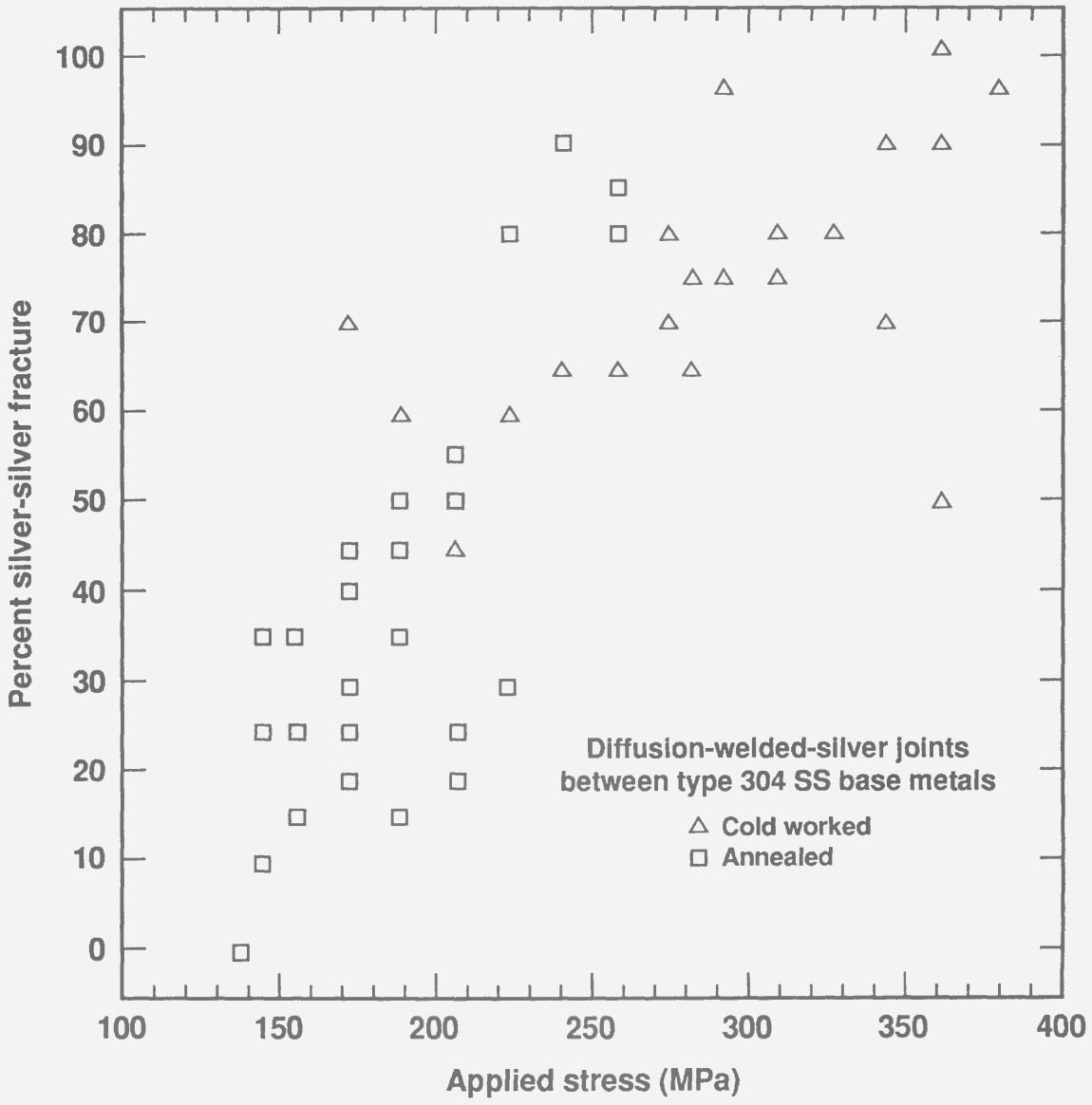

Figure 8.5. Percent silver-silver fracture as a function of applied stress level for 150-μm-thick silver interlayers fabricated by PM sputter-deposition onto machined stainless steel base metals.

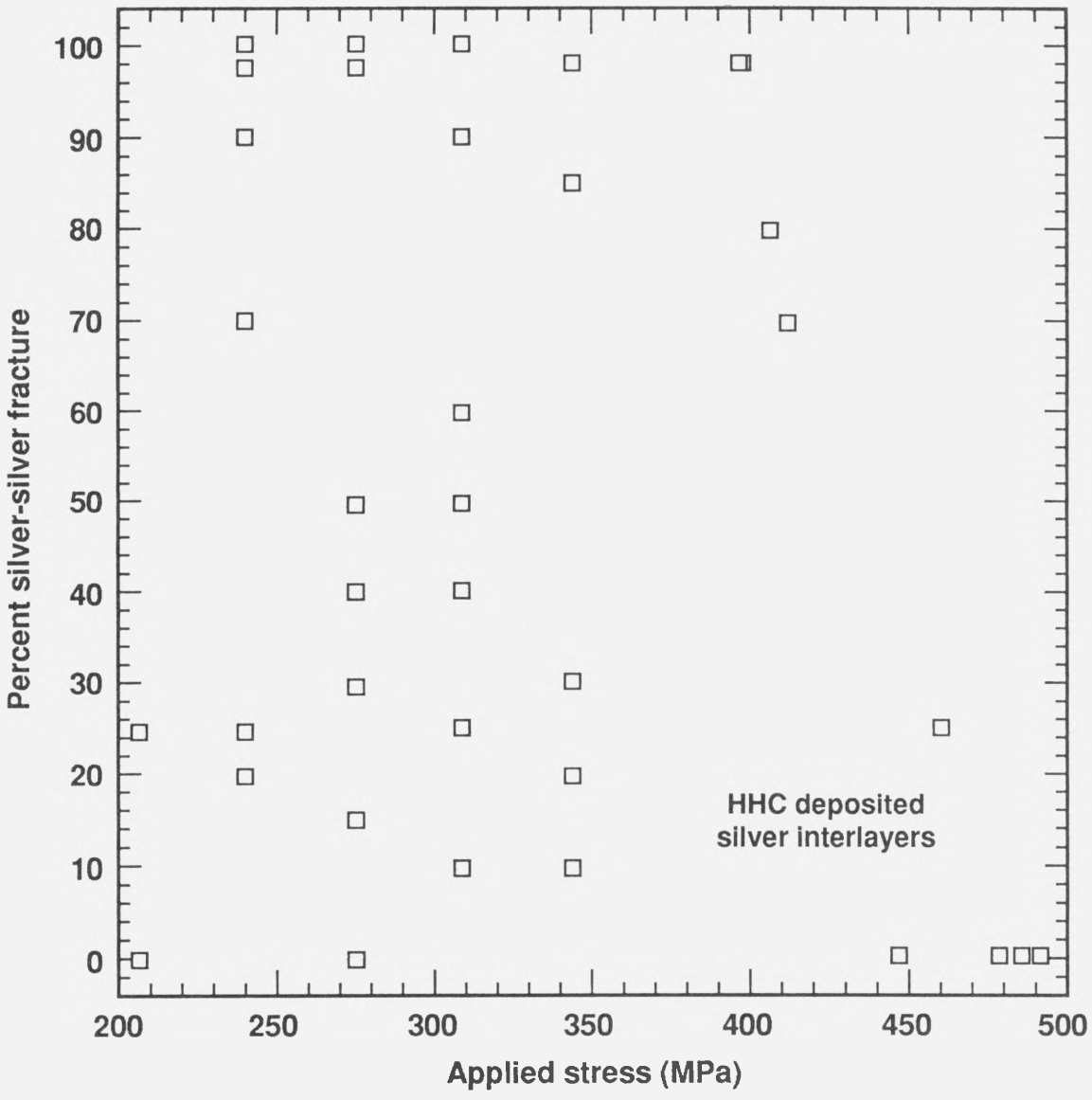

Figure 8.6. Percent silver-silver fracture as a function of applied stress level for 150-μm-thick silver interlayers fabricated by HHC deposition onto machined uranium and stainless steel base metals.

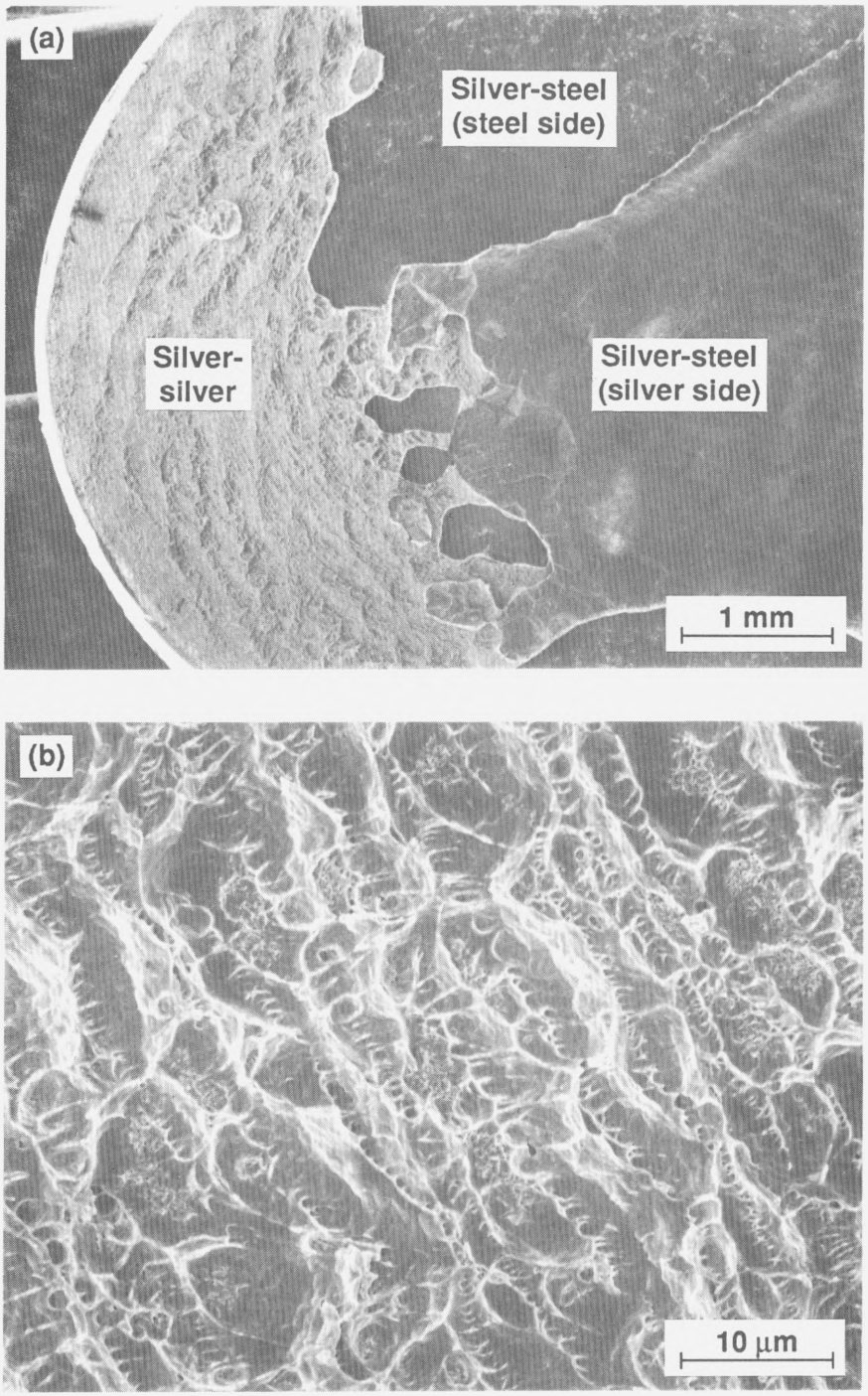

Figure 8.7. Fracture surface (155 MPa) of a specimen utilizing machined annealed type 304 stainless steel base metals showing (a) silver-silver and silver-base-metal fractures. (b) Silver-silver fracture exhibits typical ductile microvoid coalescence.

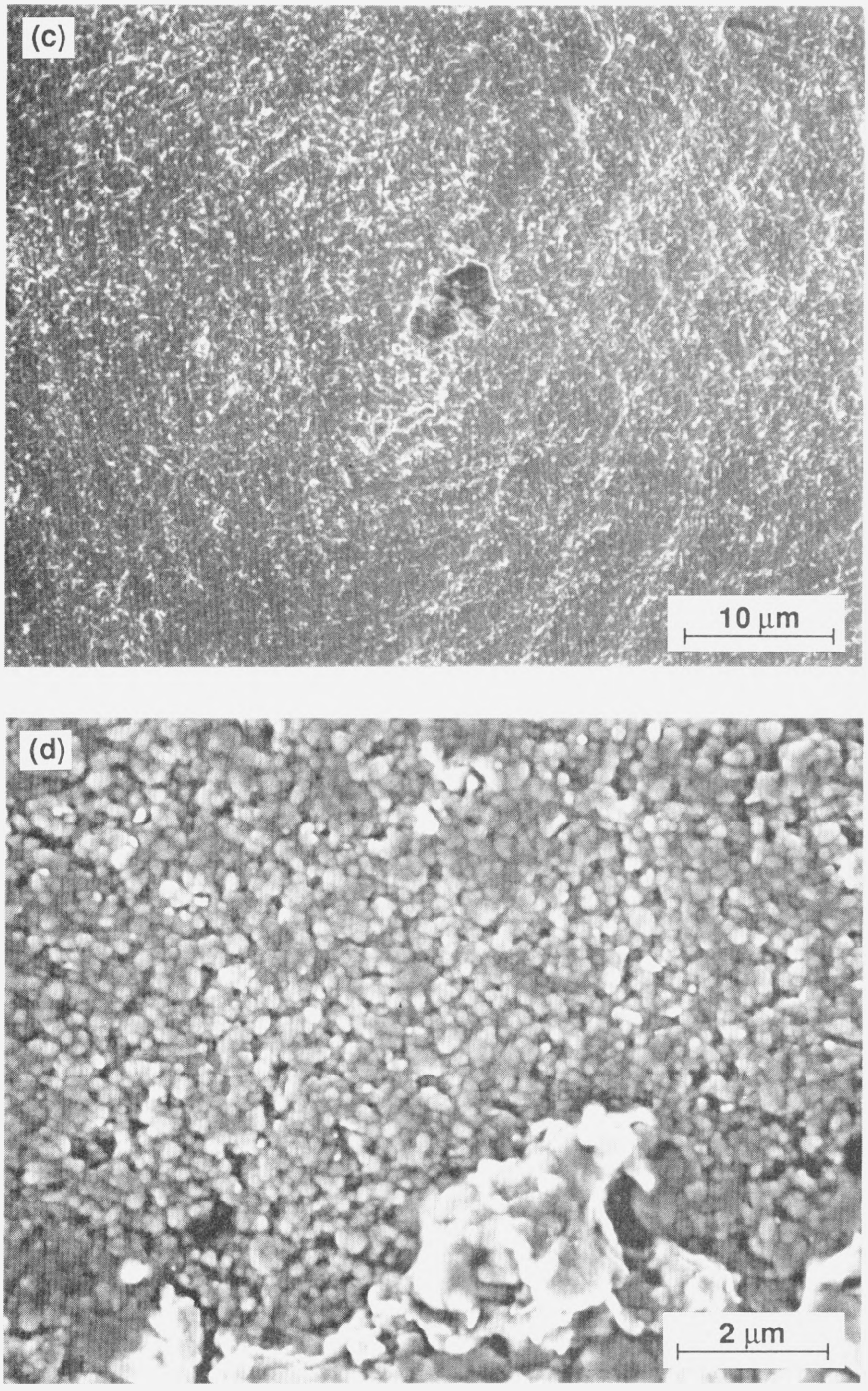

Figure 8.7. (c) Silver side of silver-base-metal fracture (155 MPa) of a specimen utilizing machined annealed type 304 SS base metals. Pronounced plasticity is not evident in these type of separations. (d) Steel side of the silver-steel fracture shows the columnar grains of nonrecrystallized silver (~1 μm thick) remaining on the steel surface.

analogous to that of the high-stress rupture of the annealed SS specimen shown in Fig. 5.3. These also appear related to the machining-lathe markings of the base-metal surface. Again, nucleation of cavities may be associated with some type of heterogeneities resulting from joining "rough" silver surfaces. The principal difference between the fracture morphologies of the low-stress (155 MPa) creep-rupture specimen shown in Fig. 8.7 and those of the high-stress specimen shown in Fig. 5.3 is in the percent silver-silver fracture (as previously discussed). Otherwise, the fracture morphologies of UTS and creep rupture specimens are indistinguishable, as reported previously for diffusion welds prepared using HHC deposition.[40] Again, the base metal side of the silver-base-metal fracture is shown in Figs. 8.7c and 8.7d. Energy dispersive spectroscopy confirmed that a thin (~1 μm) layer of silver remained adhered to the steel surface. This silver layer consists of the nonrecrystallized region as shown in Fig. 3.4c in cross section using TEM. The tops of the columnar grains can be seen in Fig. 8.7d at high magnification using SEM.

Figure 8.8 shows a typical fracture surface (mostly silver-silver) of a specimen utilizing machined cold-worked SS base metals and tested at stresses high enough to cause significant plasticity in the base metal (379 MPa and above the knee of the curve shown in Fig. 8.4). The ductile microvoid coalescence appears identical to those of annealed stainless steel fracture surfaces, and also appears related to the machining-lathe markings of the base-metal surface. Again, nucleation of cavities may be associated with some type of heterogeneities resulting from joining "rough" silver surfaces.

The silver-silver fracture morphology of specimens utilizing machined cold-worked SS base metals, tested at stresses too low to cause significant plasticity in the base metal (207 MPa and below the knee in the curve shown in Fig. 8.4), is shown in Fig. 8.9. The silver-fracture surface exhibits the same heterogeneous cavitation (large cavities and small ductile dimples) along the machining lay as those of machined maraging steel base metals. Because the cold-worked SS base metals were machined identically, the appearance of a change in fracture morphology, coupled with a bend, or knee in the rupture time versus

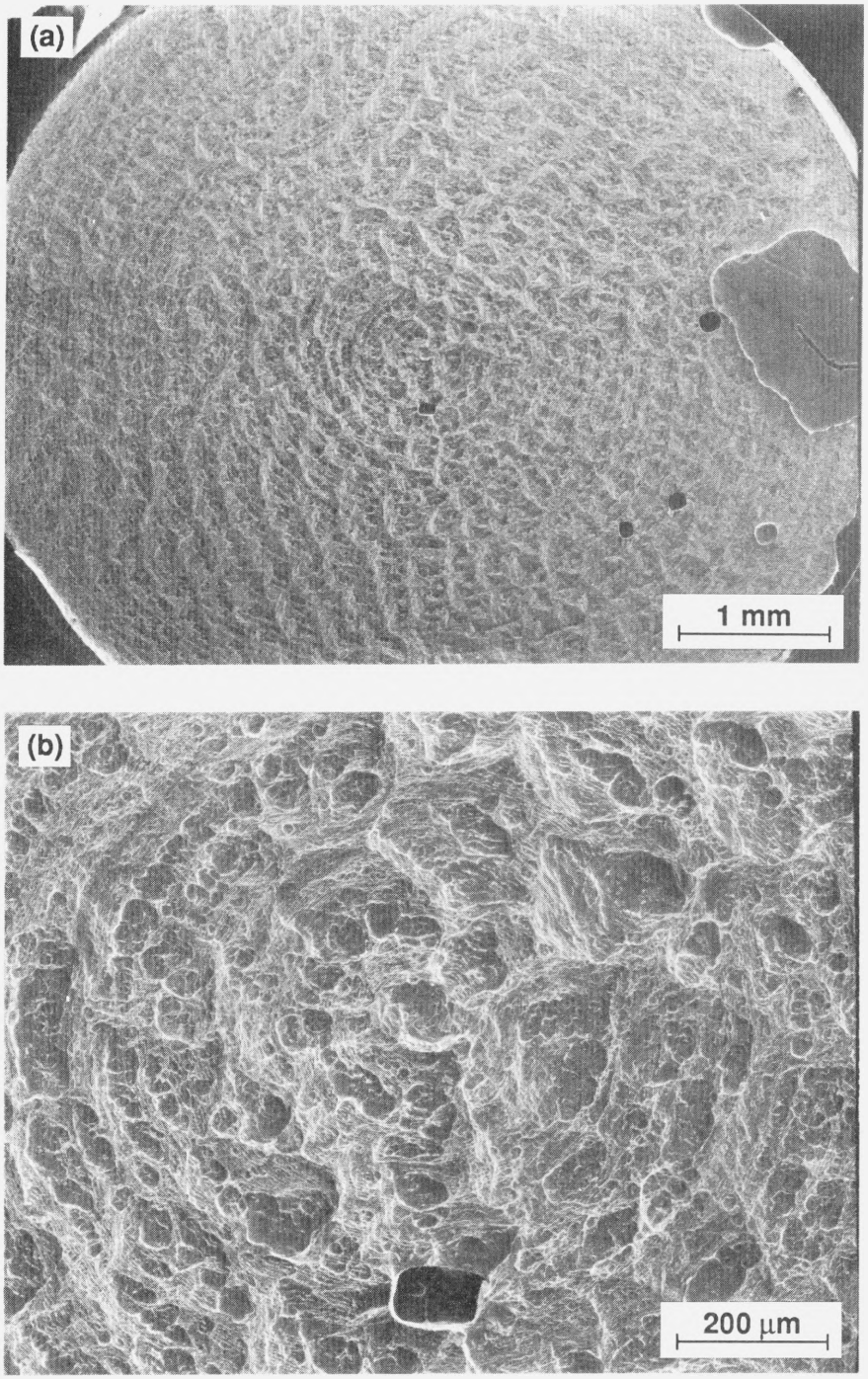

Figure 8.8. (a, b) Typical silver-silver fracture surface of specimens utilizing machined cold-worked stainless steel, and tested at stresses high enough to cause significant plasticity in the base metal (379 MPa and above the knee in the curve shown in Fig. 8.4).

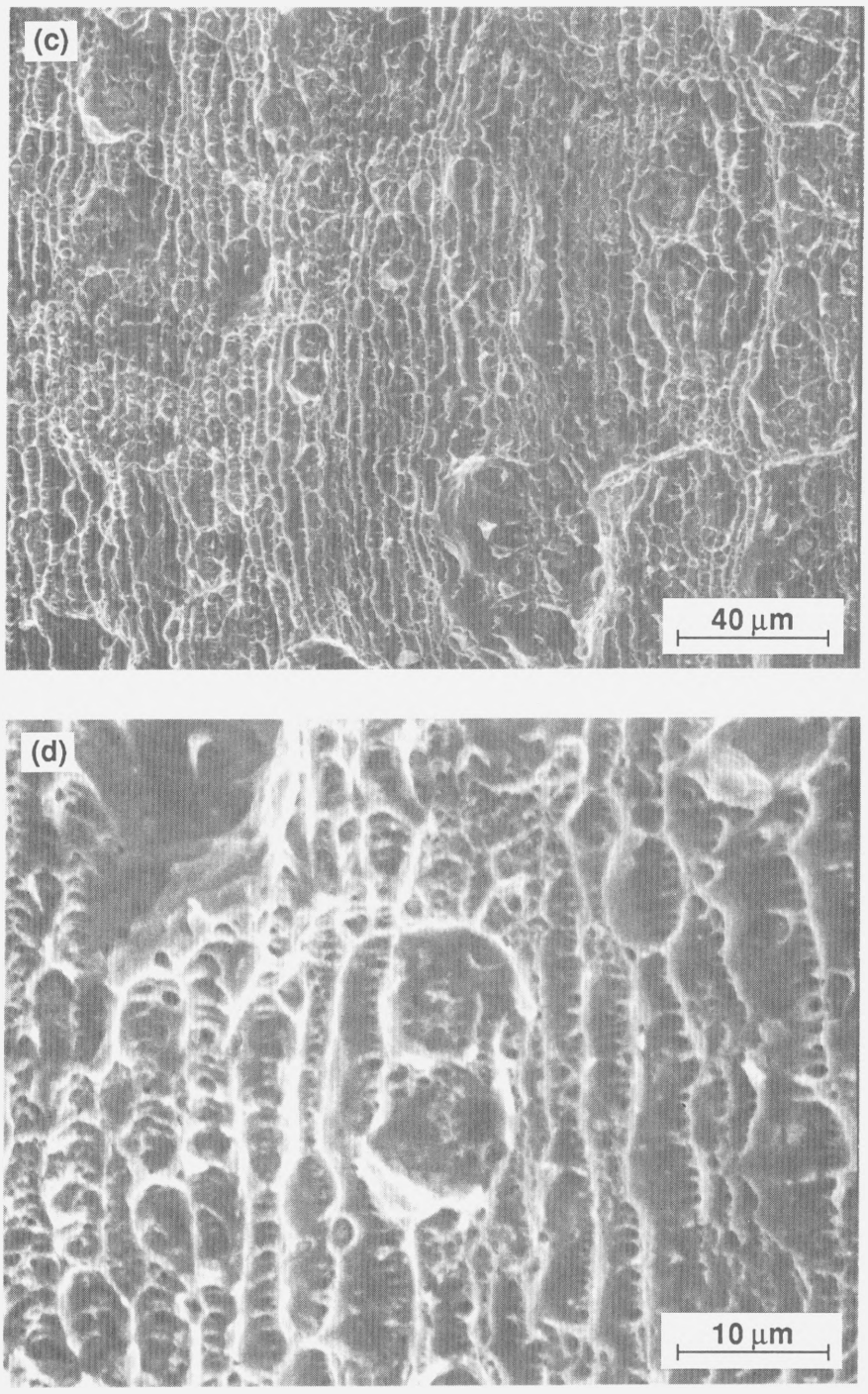

Figure 8.8. (c, d) Ductile microvoid coalescence at silver-silver fracture surface of specimens utilizing machined cold-worked stainless steel (379 MPa and above the knee in the curve shown in Fig. 8.4) appears identical to those of annealed stainless steel specimens.

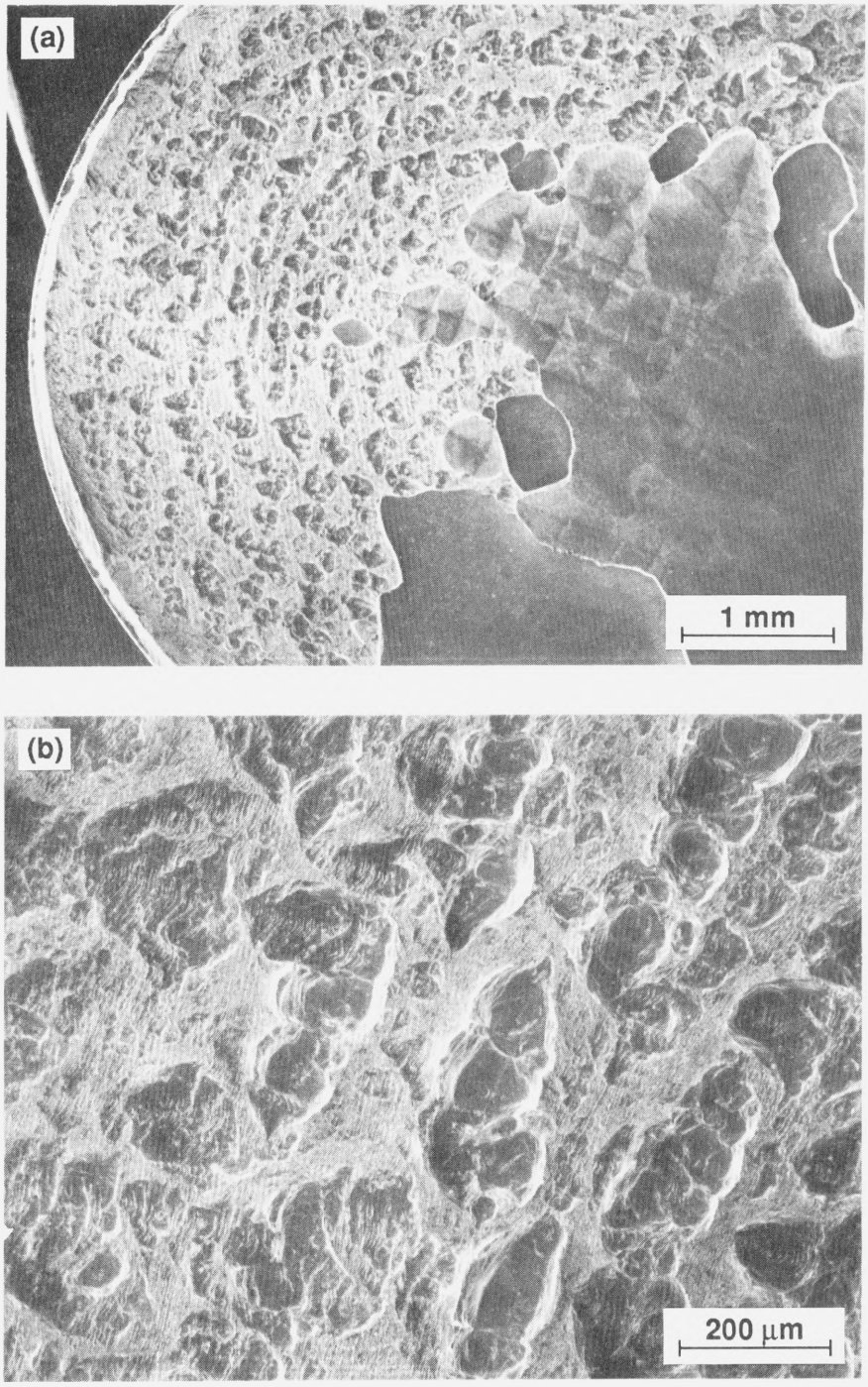

Figure 8.9. Fracture surface of specimens utilizing cold-worked stainless steel and tested at stresses too low to cause significant plasticity in the base metal (207 MPa and below the knee in the curve shown in Fig. 8.4). The silver-silver fracture exhibits the same heterogeneous cavitation (large cavities and small ductile dimples) along the machining lay as those of machined maraging steel base-metal specimens.

applied stress curve below a critical stress, strongly suggests a change in the rate-controlling mechanism of creep rupture. This point will be discussed further in Section 8.6. Energy dispersive spectroscopy revealed that the silver-base-metal fractures consisted of principally silver-silver grain boundary fracture near the steel surface, as noted previously for most of these types of fractures.

Figure 8.10 shows the silver-silver and (mostly) silver-base-metal fracture surfaces of specimens utilizing lapped cold-worked SS base metals (359 MPa and above the knee in the curve shown in Fig. 8.4). The silver side of the silver-base-metal fracture shown in Fig. 8.10b shows the third type of silver-steel fracture morphology, referred to as "pyramid-shaped" plastic deformation. This pattern can also be seen on the silver side of the silver-base-metal separations shown in Figs. 6.7a, 6.12a, 8.7a, and 8.9a. The cross-sectional view of this type of separation was shown in Fig. 6.12d, and indicates extensive plasticity in the silver side of the fracture surface. Most of the other silver-base-metal separations with this type of morphology occurred between a thin (~1 μm) layer of silver on the steel surface and the remainder of the silver interlayer. However, EDS confirmed that the steel side of the fracture surface of some specimens were not covered with a thin layer of silver, but rather contained only isolated amounts of silver "pullout." These observations are consistent with previously reported results[20,40] of silver-base-metal fractures between uranium and SS base metals. The investigators observed that varying amounts of silver were present on the base-metal surfaces after fracture, including regions of silver-base-metal "delamination." Therefore, fractures can occur along silver-base-metal interfaces and silver grain boundary interfaces very near the base metal, apparently independent of the rupture time or ultimate strength.

Fracture along the silver-silver (diffusion-welded-silver) interface of this specimen (shown in Figs. 8.10c–8.10d) exhibits the same type of uniform-size ductile microvoids as that of other specimens utilizing lapped base-metal surfaces (e.g. Figs. 5.2 and 6.10),

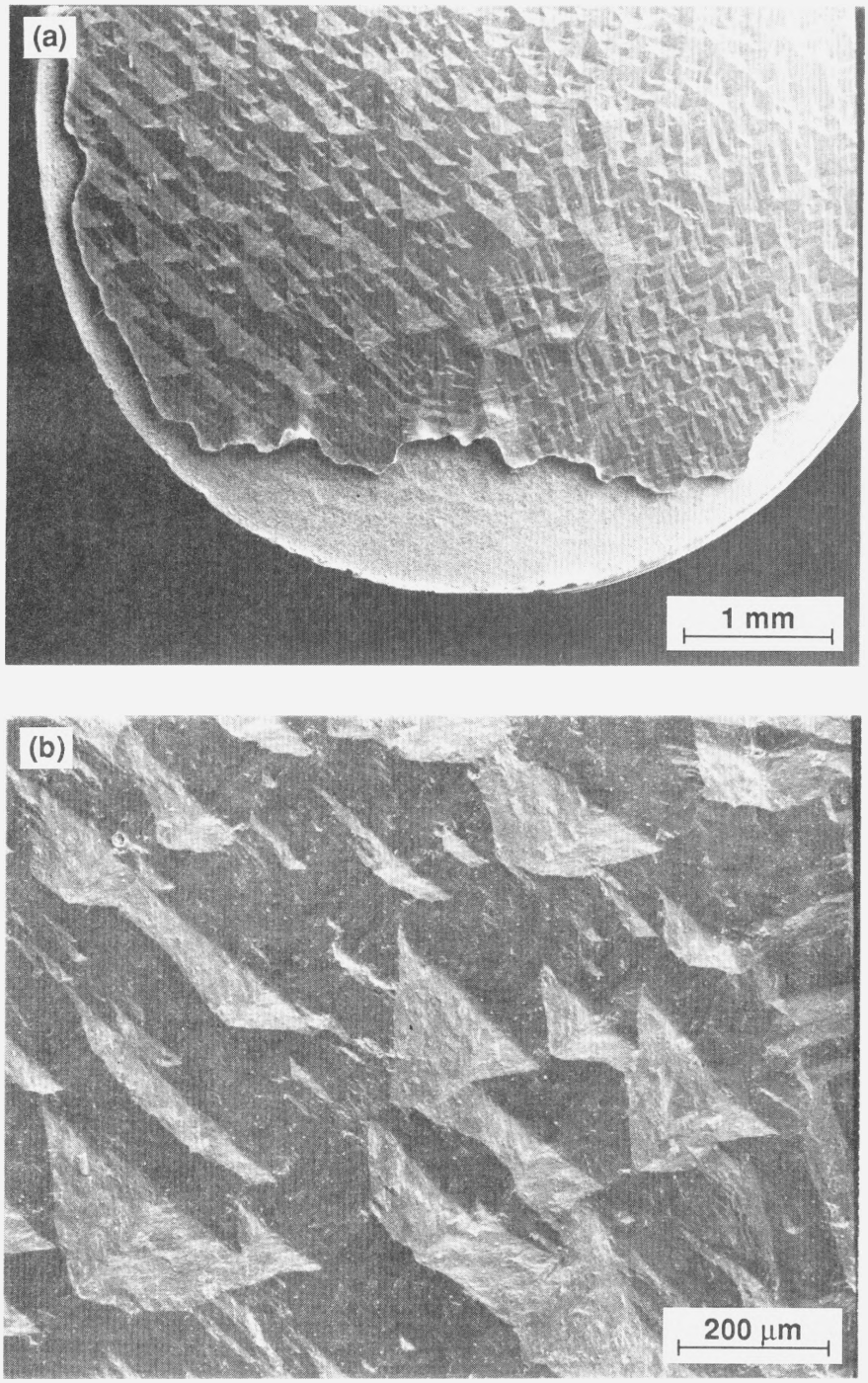

Figure 8.10. (a) Fracture surface between specimens utilizing lapped cold-worked stainless steel (359 MPa and above the knee in the curve shown in Fig. 8.4), showing silver-silver and (mostly) silver-base-metal separation. (b) The silver side of the silver-base-metal fracture exhibits a "pyramid-shaped" pattern of plastic deformation.

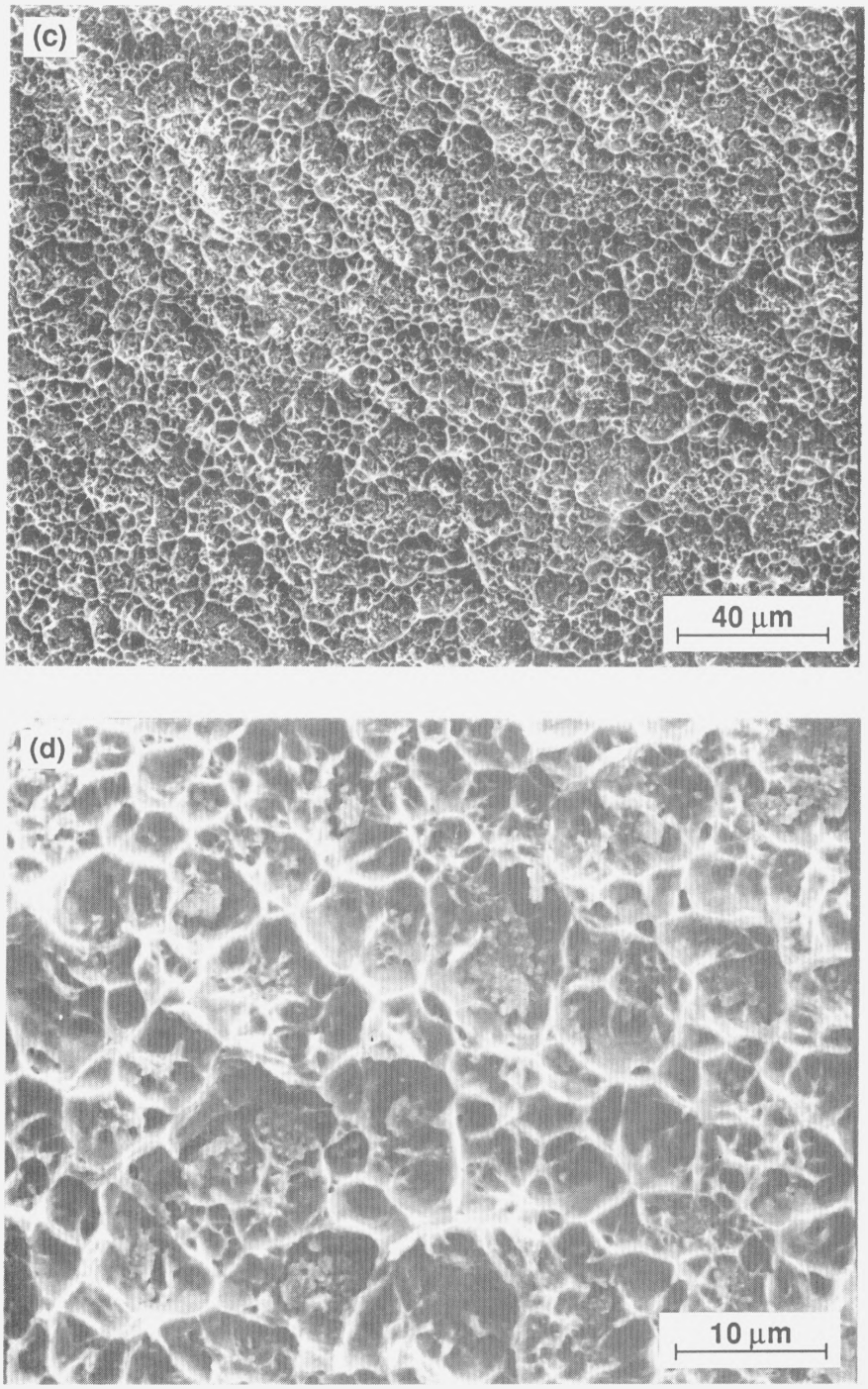

Figure 8.10. (c, d) Silver-silver fracture between specimens utilizing lapped cold-worked stainless steel (359 MPa and above the knee in the curve shown in Fig. 8.4) consists of the same uniform-size ductile microvoids as those of other lapped base-metal specimens.

although the average size of the dimples from specimen to specimen tend to vary by a factor of two or so.

8.5. Plastic Strain in the Base Metal and Interlayer

8.5.1. Experimental Results

Figures 8.11 and 8.12 show the plastic strains in the base metal and the silver interlayer as a function of time for specimens utilizing annealed and cold-worked stainless steels, respectively. The strain in the base metal is plotted both near (<50 μm) and away from (>5 mm) the interlayer-base metal interface. In both cases, the plastic strain in the stainless steel increases with time. The strain within the silver interlayer correspondingly increases. Presumably, after having reached a small, critical strain, ε_c induced by the creeping stainless steel, the silver fractures in a ductile manner. The plastic strain-to-failure in the silver (as determined prior to rupture from measurements of interlayer diameter) decreased with decreasing stress from 2.2% (259 MPa) to 0.8% (207 MPa) for the annealed SS, and from 2.8% (379 MPa) to 2.2% (362 MPa) for the cold-worked SS. The reason for the decrease in the "macroscopic" strain of the interlayer with decreasing applied stress is not clear. However, this trend explains why the rupture time versus applied stress slopes of Fig. 8.1 are a factor of 2 or 3 lower than the constant-structure stress exponent, N of stainless steel equal to about 60–80, as calculated from Figs. 7.1 and 7.2 using the substitution of $1/t_r$ for $\dot{\varepsilon}$ in Eq. 4. Correspondence between stress exponents would exist for the case in which the plastic strain-to-failure in the silver interlayer in the vicinity of the fracture interface is independent of stress.

It should be noted that, as a result of the final cavitation leading to rupture, the plastic strain in the vicinity of the interface increases substantially. Figures 8.11b and 8.12b show the plastic strain surge within the silver and in the base metal near the interlayer, respectively, occurring upon joint rupture. This surge is believed to be due to the local increase in effective stress with decreasing load carrying area, resulting from the ductile

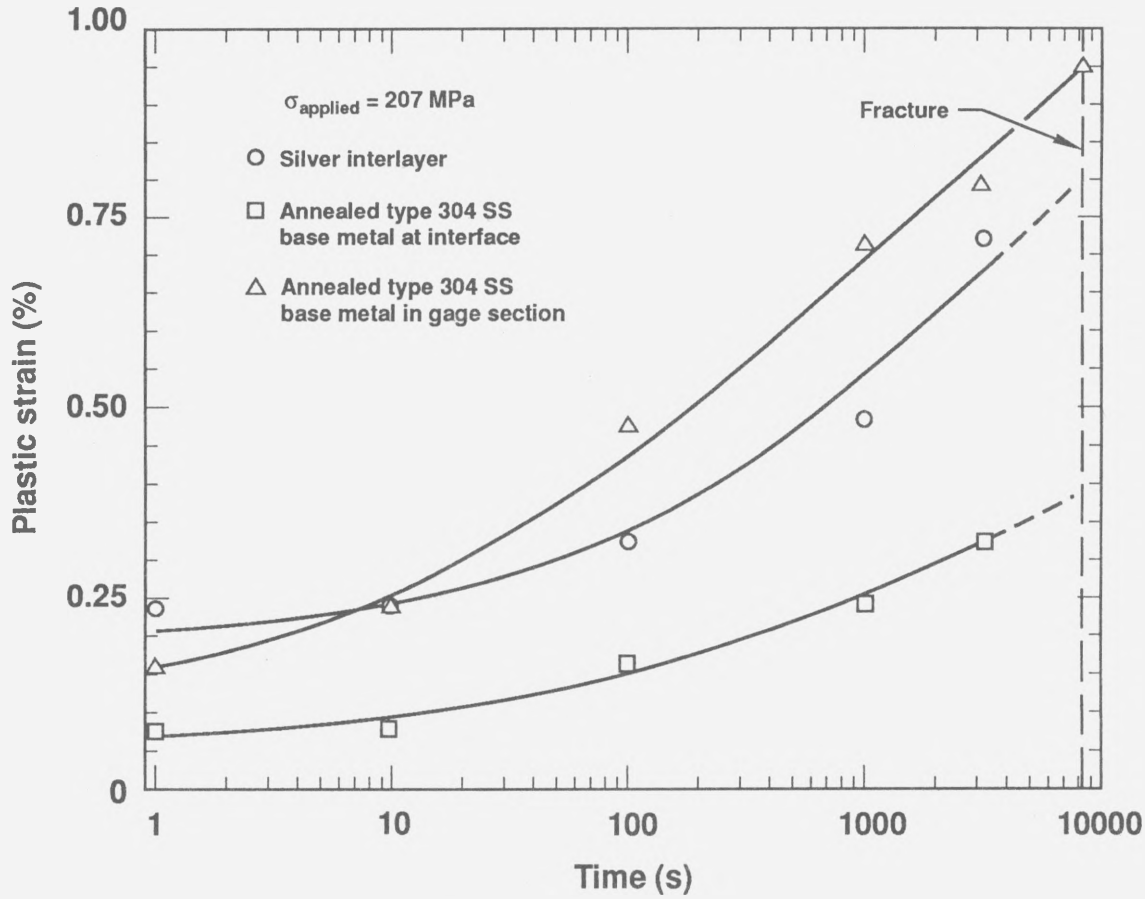

Figure 8.11. (a) Plastic strains in the silver interlayer and the base metal adjacent to the interlayer as a function of time for diffusion-welded specimens utilizing annealed type 304 stainless steel tested at 207 MPa.

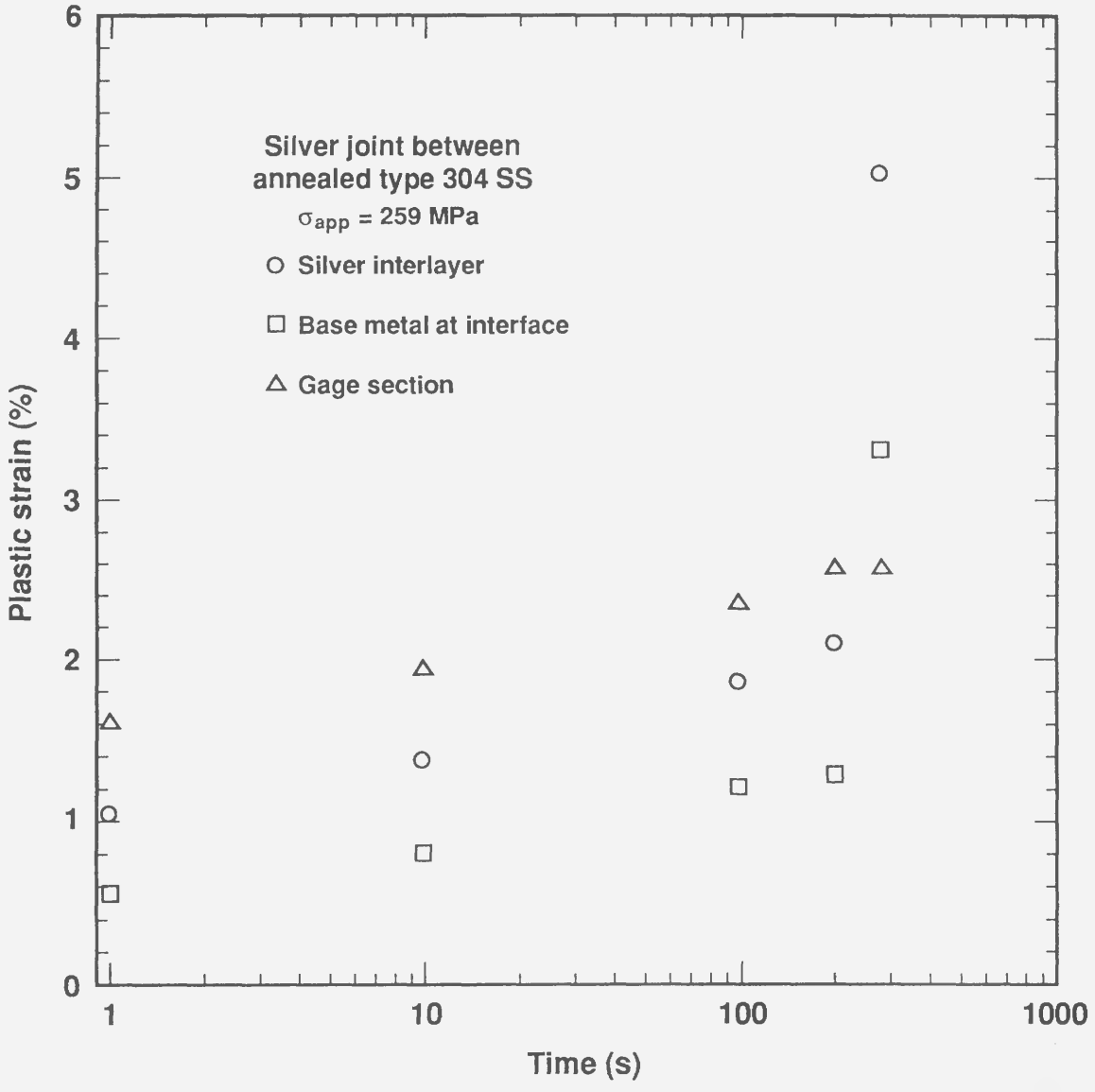

Figure 8.11. (b) Plastic strains in the silver interlayer and the base metal adjacent to the interlayer as a function of time for diffusion-welded specimens utilizing annealed type 304 stainless steel tested at 259 MPa. The plastic strain surge within the silver and base metal near the interlayer, occurring upon rupture, is shown by the final set of data points.

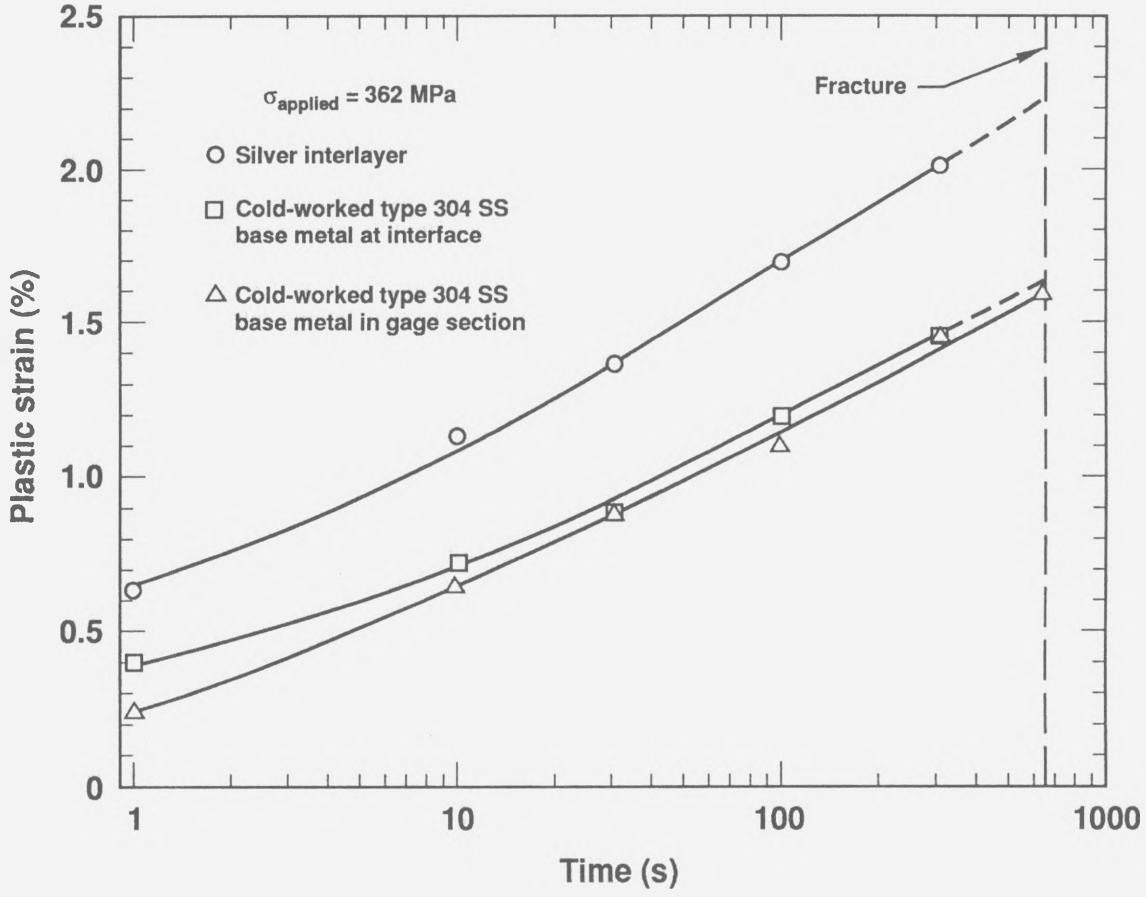

Figure 8.12. (a) Plastic strains in the silver interlayer and the base metal adjacent to the interlayer as a function of time for diffusion-welded specimens utilizing cold-worked type 304 stainless steel tested at 362 MPa.

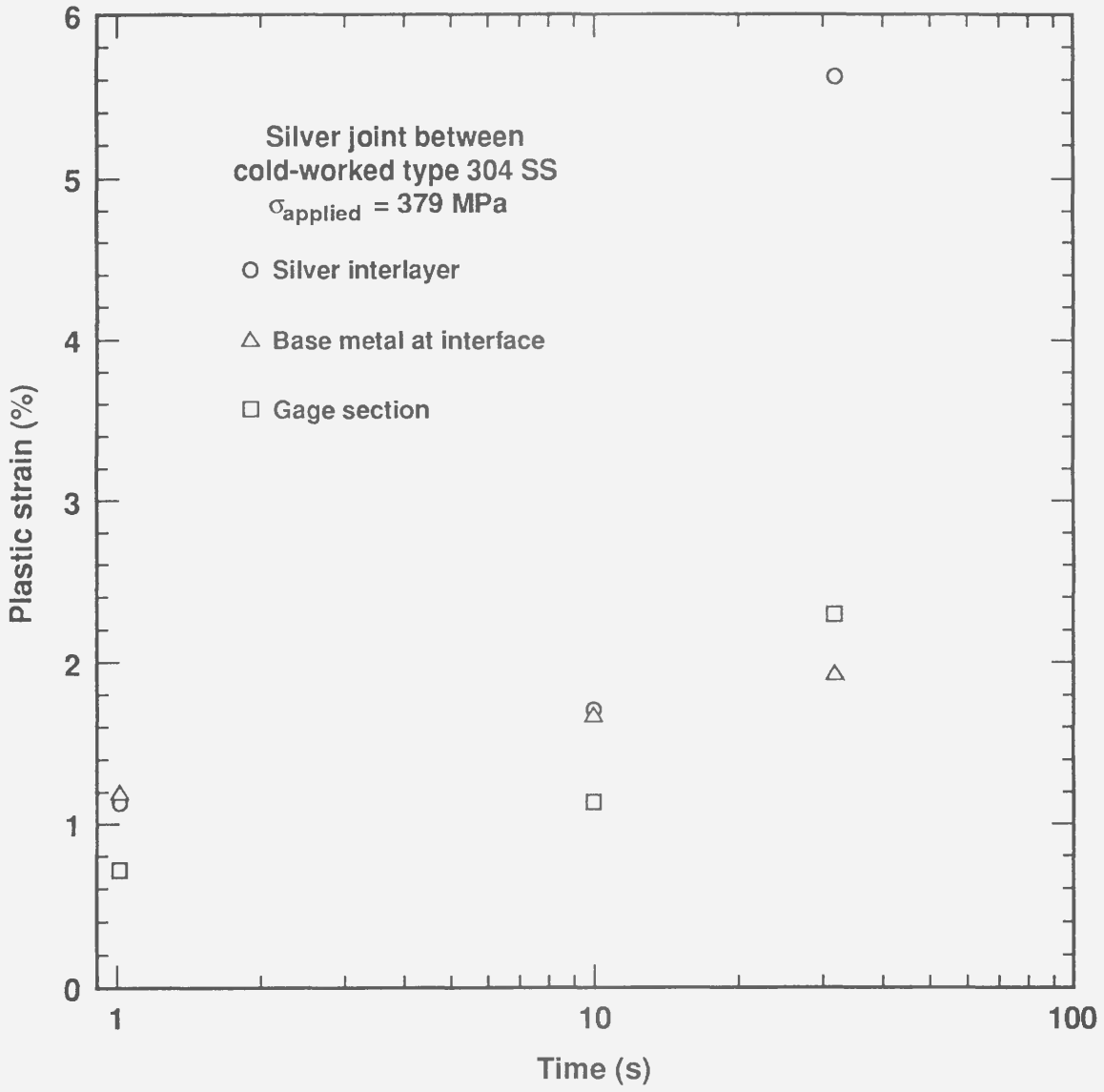

Figure 8.12. (b) Plastic strains in the silver interlayer and the base metal adjacent to the interlayer as a function of time for diffusion-welded specimens utilizing cold-worked type 304 stainless steel tested at 379 MPa. The plastic strain surge within the silver and base metal near the interlayer, occurring upon rupture, is shown by the final set of data points.

"tearing" of silver ligaments during the catastrophic failure process. Figure 8.13 shows the plastic strain in (a) annealed and (b) cold-worked SS base metals occurring in the gage section and near the interface after creep rupture of the silver interlayer. The plastic strain (to creep rupture of the joint) in the gage section decreases with increasing applied stress, although the amount of deformation near the interlayer occurring upon rupture is essentially independent of applied stress. Additionally, the plastic strains (to creep rupture of the joint) in the gage section and near the interlayer appear to be independent of temperature for tests performed at 22 and 72 °C. This latter observation is important because comparisons between the activation energy for creep rupture and the activation energy for plastic flow in SS, presented in Section 8.3, were based on the assumption of constant plastic strain (with changes in temperature) in the SS base metals.

The reduction in area of the stainless steel base metal (by creep) adjacent to the interface is smaller (by about a factor of two for the annealed SS) than that about 1 mm from the interlayer. This is probably due to strain hardening from the machining of the base-metal surface that is eventually coated. Figure 8.14a shows the microhardness (DPH) of annealed and cold-worked type 304 SS base metals as a function of distance from the machined surface (to be coated). The hardened layer extends about 200 μm (0.2 mm) from the surface, decreasing rapidly in hardness within the initial 75 μm. Figure 8.14b shows the correlation between microhardness (DPH) and flow stress (or prestress) of type 304 SS. This relationship is approximately linear over the range of flow stresses tested. Figure 8.14c combines the data from the previous two figures to present the flow stress in annealed type 304 SS base metal as a function of distance from the silver interface (machined surface). The average hardness of this "damaged" layer in the annealed SS is about that of the cold-worked SS used in this study (205 DPH or ~359 MPa). Figure 8.15 is an optical micrograph showing extensive slip lines and deformation twins in the grains of the machining-damaged layer near the silver interface for (a) annealed and (b) cold-worked SS base metals.

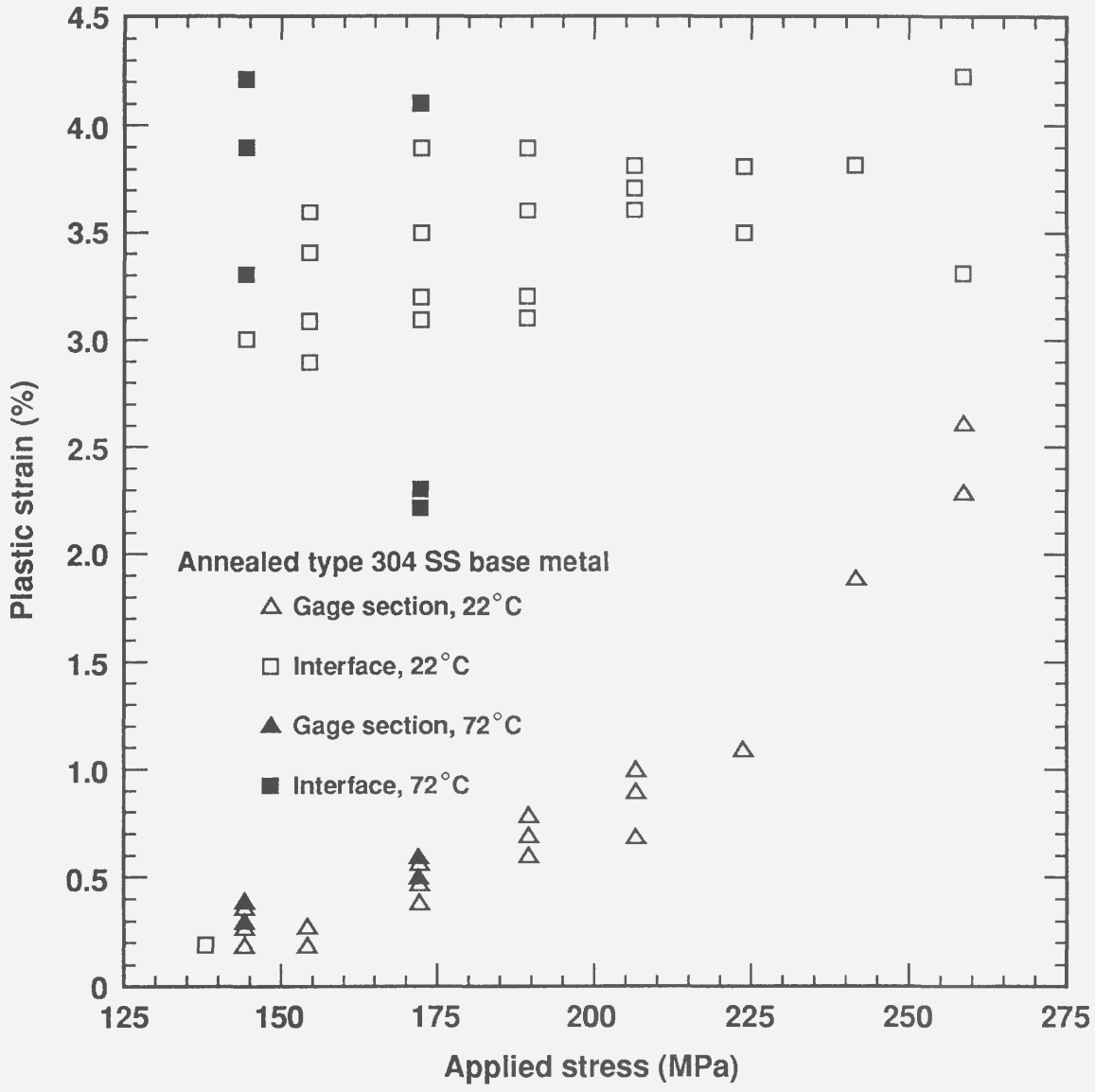

Figure 8.13. (a) Plastic strain in annealed SS base metals in the gage section and near the interface measured after creep rupture of the silver interlayer. The strain-to-failure in the gage section decreases with applied stress, although the amount of base-metal deformation near the interlayer after rupture is essentially independent of stress.

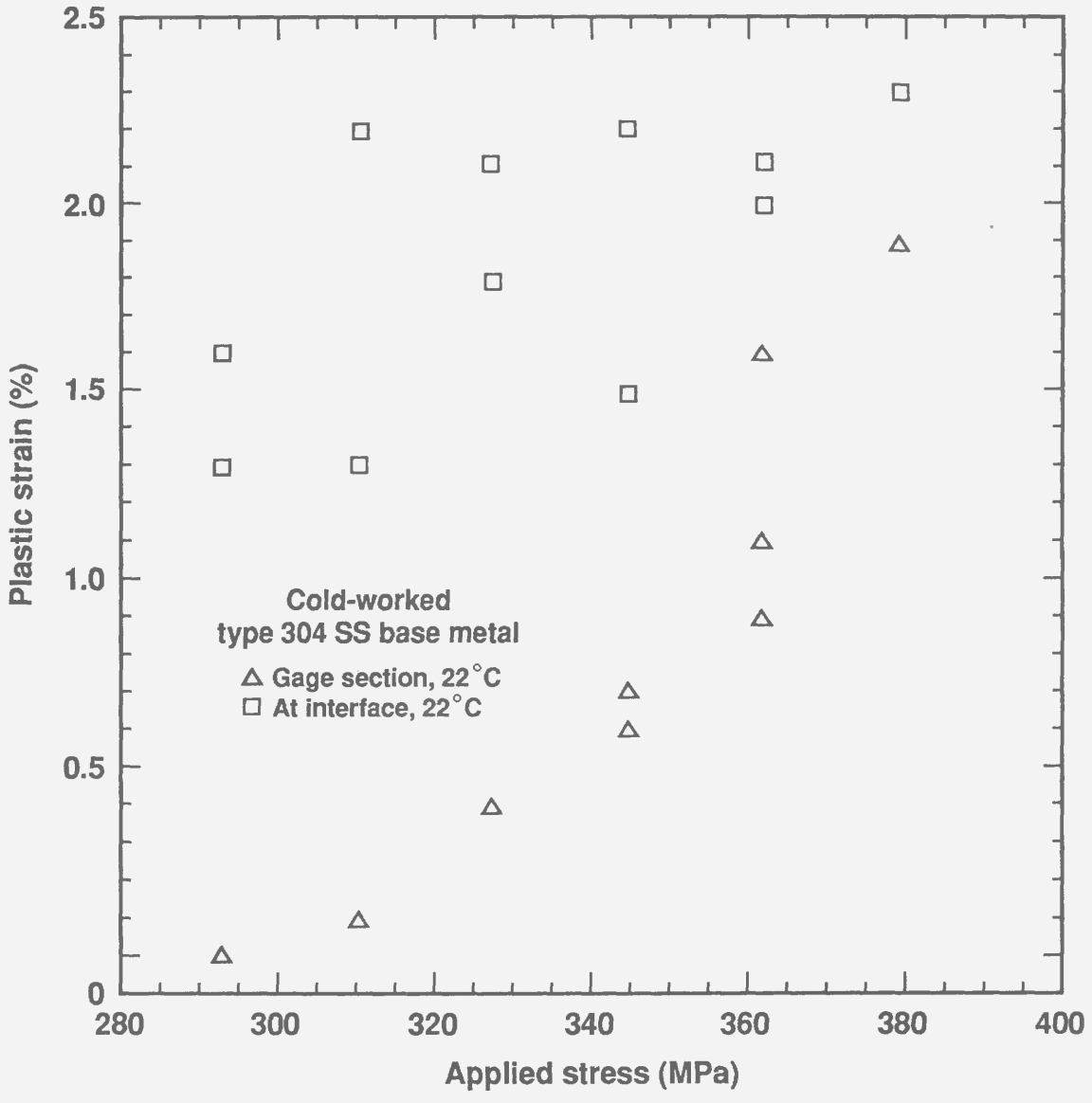

Figure 8.13. (b) Plastic strain in cold-worked SS base metals in the gage section and near the interface measured after creep rupture of the silver interlayer. The strain-to-failure in the gage section decreases with applied stress, although the amount of base-metal deformation near the interlayer after rupture is essentially independent of stress.

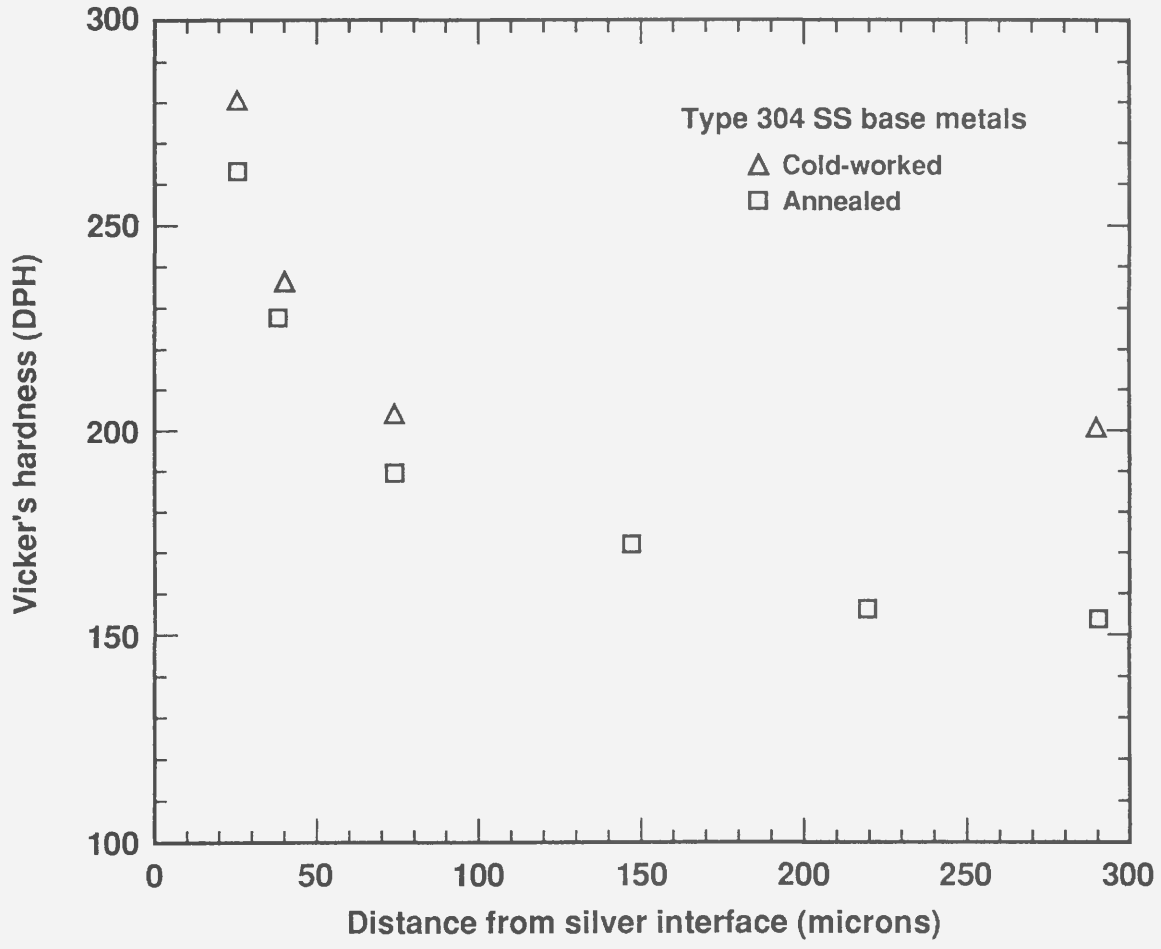

Figure 8.14. (a) Machining damage layer of type 304 stainless steel base-metal specimens as prepared prior to coating, plotted as microhardness versus distance from the coated interface.

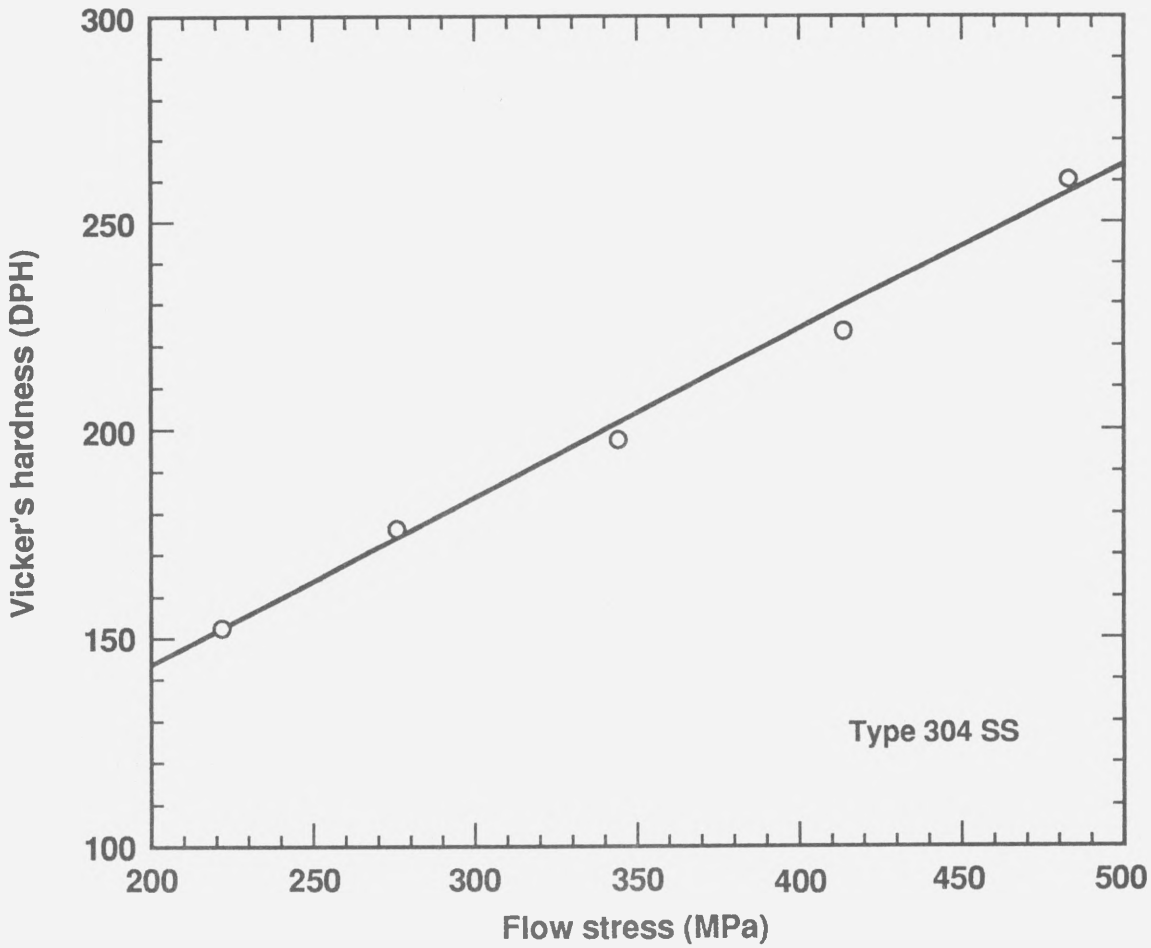

Figure 8.14. (b) Microhardness versus flow stress for type 304 stainless steel.

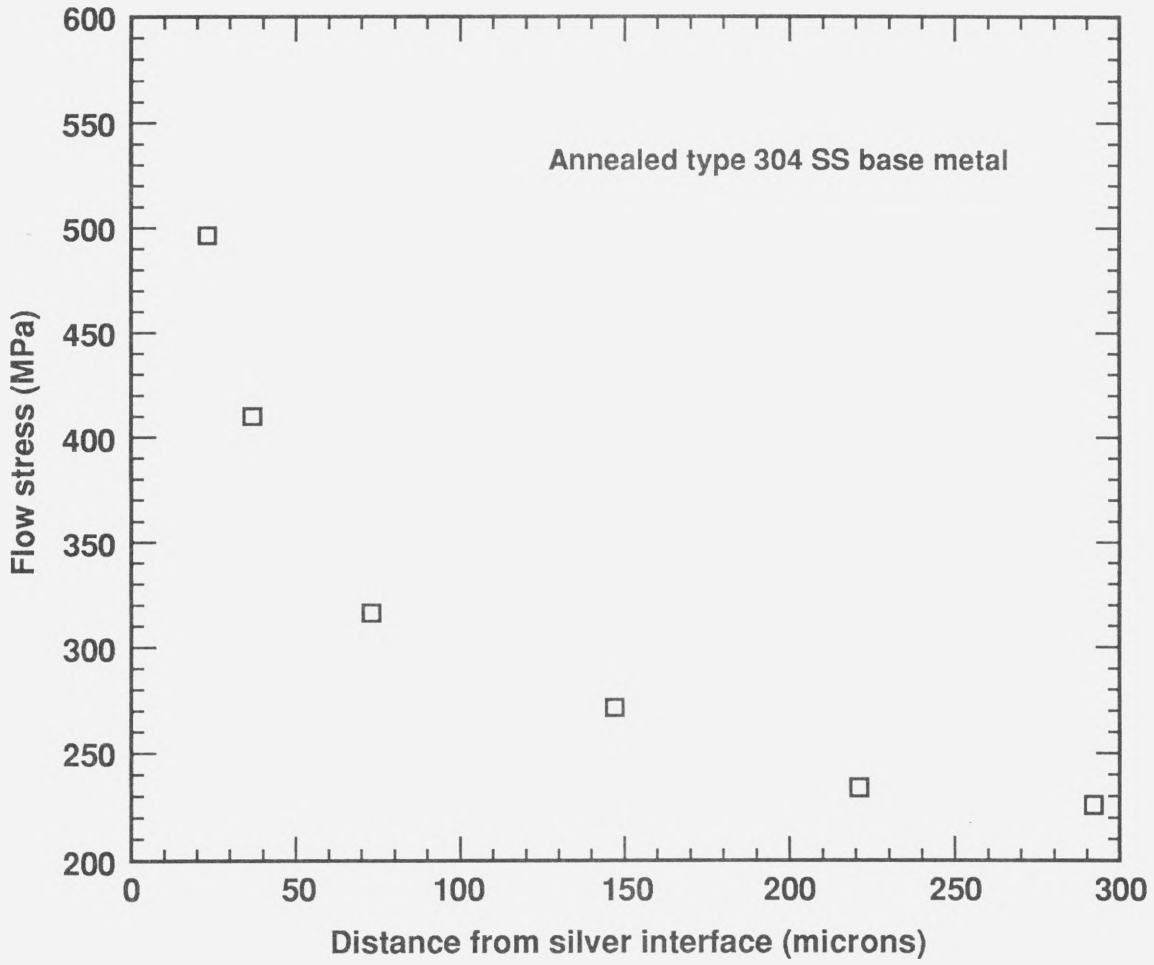

Figure 8.14. (c) Machining damage layer of type 304 stainless steel base-metal specimens as prepared prior to coating, plotted as flow stress versus distance from the silver interface by combining the data of (a) and (b).

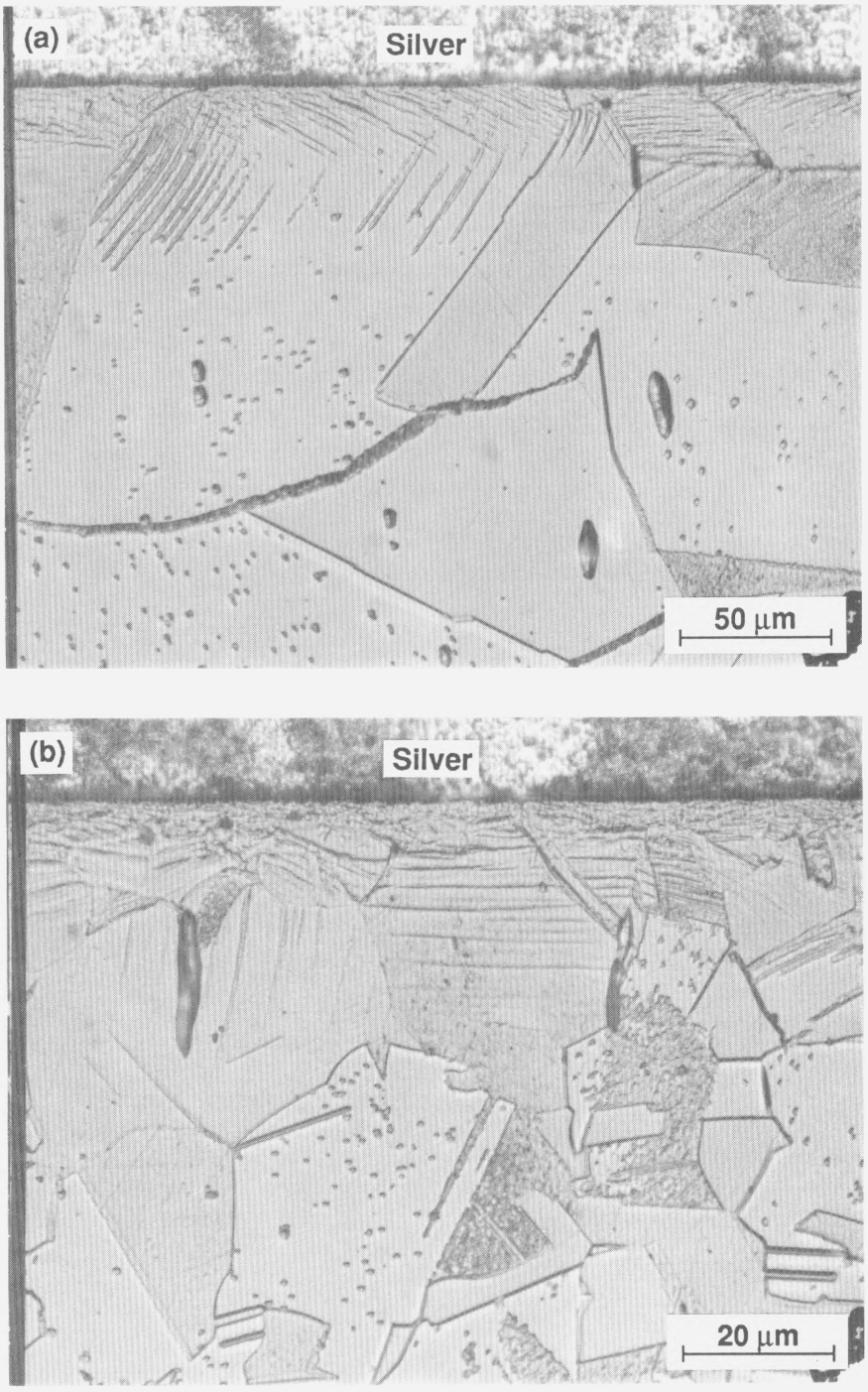

Figure 8.15. Optical micrographs showing machining-damaged layer of (a) annealed and (b) cold-worked type 304 stainless steel base-metal specimens as fabricated prior to coating. Extensive twinning is present in the grains near the interface.

8.5.2. Finite-Element Analysis

Figure 8.16 shows the plastic deformation in the diffusion-welded-silver interlayer and annealed type 304 SS base metal after 410 s of creep at 293 MPa (99% $t_{r,exp}$), using (a) mesh generated by finite-element analysis[77] and (b) optical metallography of an actual specimen. The finite-element analysis, described in detail elsewhere,[77] consisted of incorporating the time-independent (elastic-plastic) material properties for silver that were presented in Fig. 4.1 and the time-dependent (creep) properties for annealed type 304 SS that were presented in Fig. 7.1 into the two-dimensional stress analysis code (NIKE2D[59,60]) to simulate the deformation. Additionally, the increased strength of the base metal near the interface was accounted for, at least approximately, by using the creep behavior of cold-worked SS (flow stress equal to 359 MPa) for the initial 75 μm from the interface. This "step function" reasonably approximates the SS flow stress versus distance from the interface curve shown in Fig. 8.14c. Qualitatively, the shapes of the deformation by experiment and finite-element analysis are similar, confirming the expectation that the base-metal region near the interface exhibited less plastic strain (in spite of the higher effective stress) than that of the gage section due to the increased strength from machining damage.

Further evidence of the base-metal control theory for creep rupture of silver interlayers between plastically-deforming base metals is demonstrated by Fig. 8.17. This figure shows the finite-element simulation of effective plastic strain versus time for the annealed SS base-metal specimen loaded to 293 MPa for 410 s. The strain is plotted at three positions along the cylindrical axis of the specimen mesh: (1) at the center plane of the interlayer, (2) in the base metal near (7.6 μm) the interface, and (3) in the gage section (at the top of the mesh, far from the interface). The latter position represents the behavior of annealed type 304 SS as shown in Fig. 7.1. Figure 8.17 shows that the creep strain in the base metal near the interface is always less than that far from the interface, in agreement with the experimental results shown in Fig. 8.11. The most important feature of Fig. 8.17

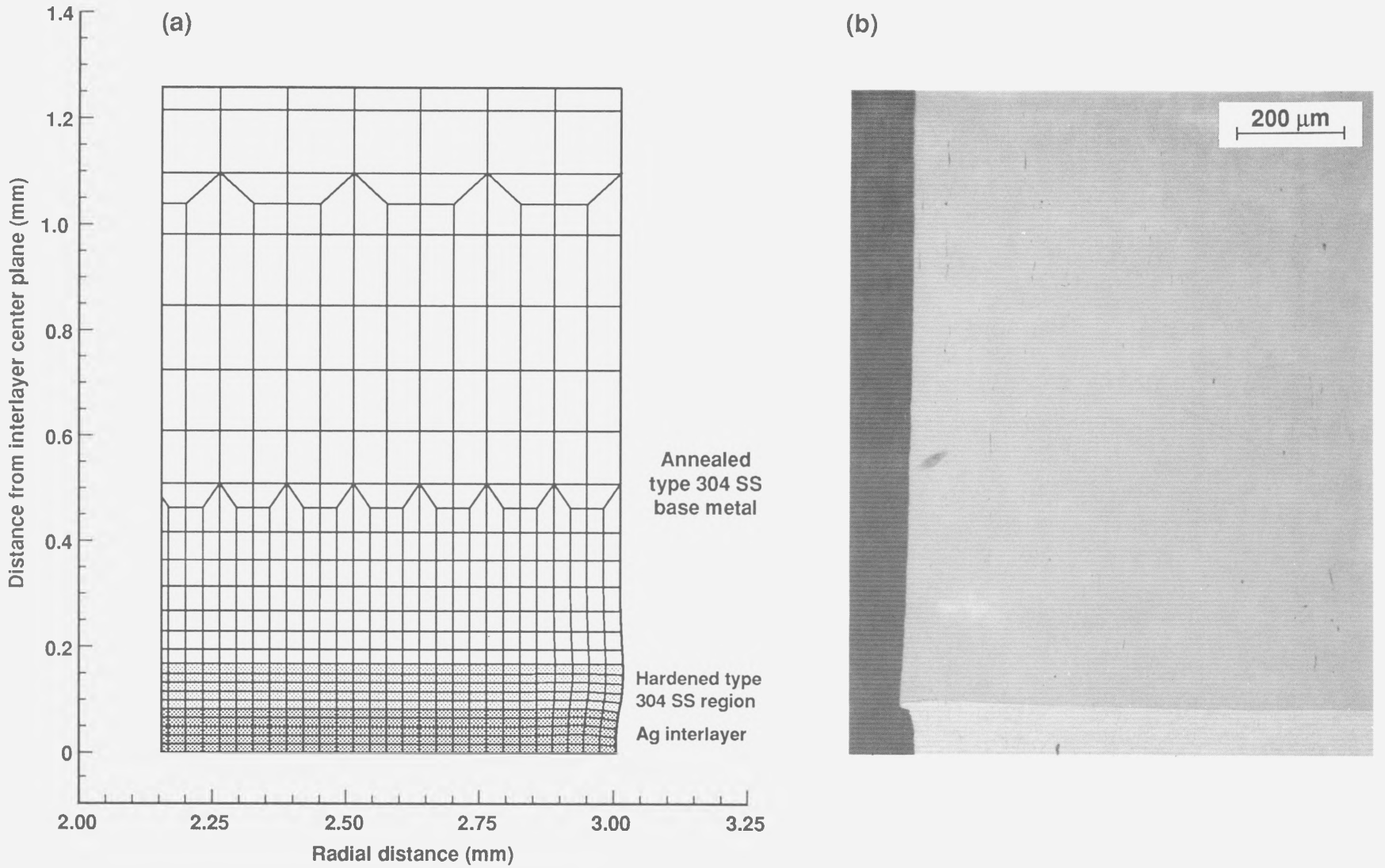

Figure 8.16. Plastic deformation in diffusion-welded-silver interlayer between annealed type 304 SS loaded to 293 MPa for 410 s.

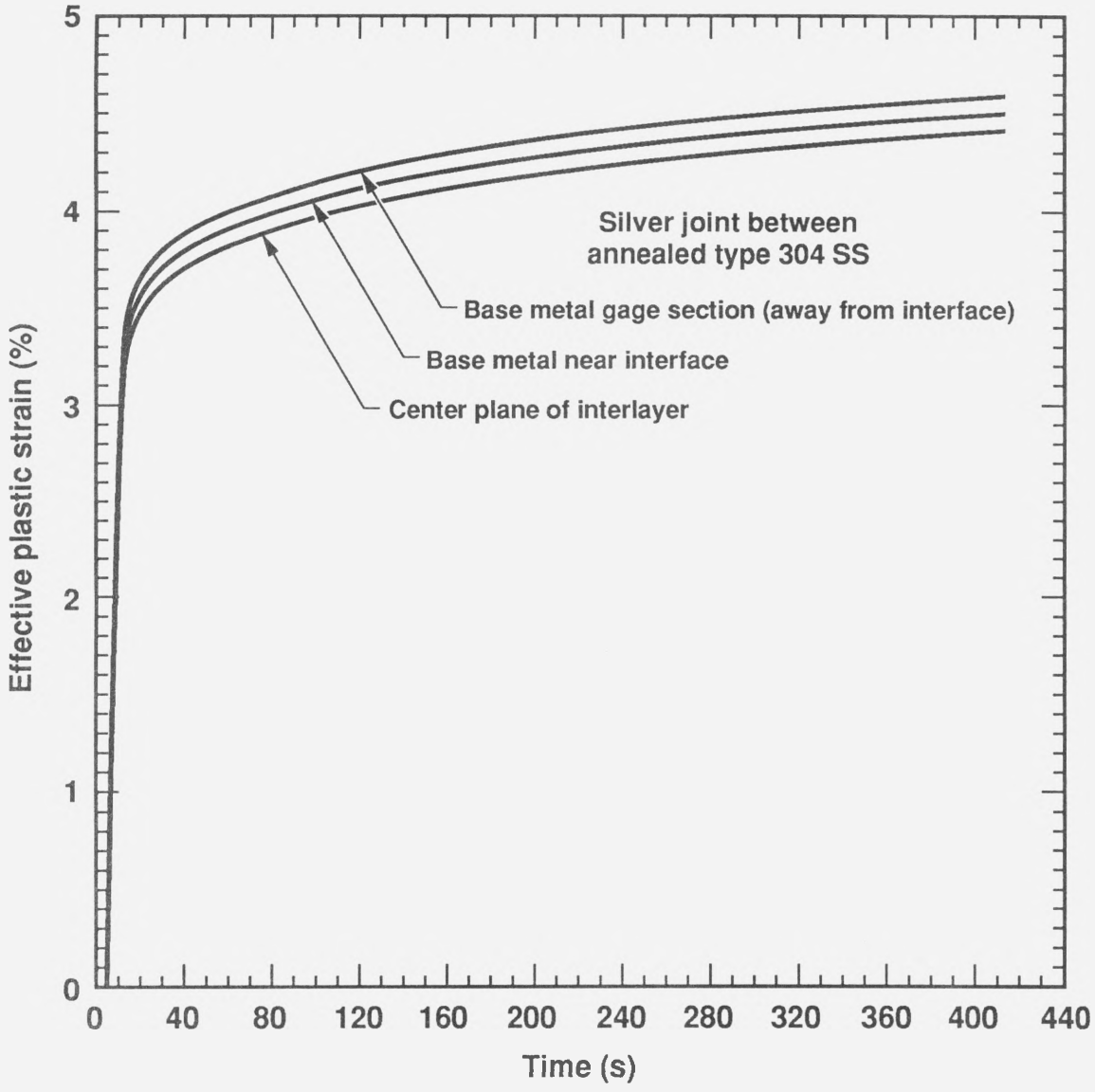

Figure 8.17. Finite-element analysis of effective (von Mises) plastic strain as a function of time for the annealed SS base-metal specimen shown in Fig. 8.15. The strain is plotted at three positions along the cylindrical axis of the specimen mesh: (1) at the center plane of the interlayer, (2) in the base metal near (7.6 μm) the interface, and (3) in the gage section (at the top of the mesh, far from the interface).

is that time-dependent plasticity (creep) of the base metal induces time-dependent plastic deformation of the interlayer, even though the interlayer alone has been modelled to deform in a time-independent manner. Note also that the creep rate of the interlayer closely follows that of the SS base metal, in agreement with the experimental results shown in Fig. 8.11.

8.6. Parallel Failure Process

For the case of elastic base materials, plasticity within the interlayer occurs under the action of the effective stress within the interlayer and cavities may be nucleated, particularly at or near the three principal interfaces. The cavity concentration presumably increases with strain and failure occurs by microvoid coalescence. For the case where significant plasticity within the base metal occurs, there is concomitant shear within the interlayer and cavity nucleation can occur more rapidly at the same applied stress level. These two processes operate simultaneously and the faster process determines the rupture time. This last point may rationalize the bend, or "knee" in the creep-rupture time versus applied stress curve for specimens that utilized cold-worked stainless steel.

Figure 8.18 contains a summary plot of the ambient-temperature creep-rupture data of specimens for which the base-metal surfaces were machined prior to coating. For the specimens utilizing annealed type 304 SS, the rupture time is determined by the creep rate of the SS base metal. In the absence of base metal creep, the rupture time at a particular stress would dramatically increase to a value predicted by the maraging steel curve. At high stresses, above the intersection of the maraging steel curve with the cold-worked type 304 SS curve, the rupture time of specimens utilizing cold-worked SS is also substantially less than that in the absence of base-metal creep. At these stresses, the creep rate of the base metal is presumably substantially higher than the creep rate of silver in the vicinity of the interface(s), deforming under the effective stresses within the interlayer in the absence of base-metal plasticity. However, at stresses below the intersection point (or knee in the curve), the rate-controlling mechanism of failure changes. In this regime, the cold-worked

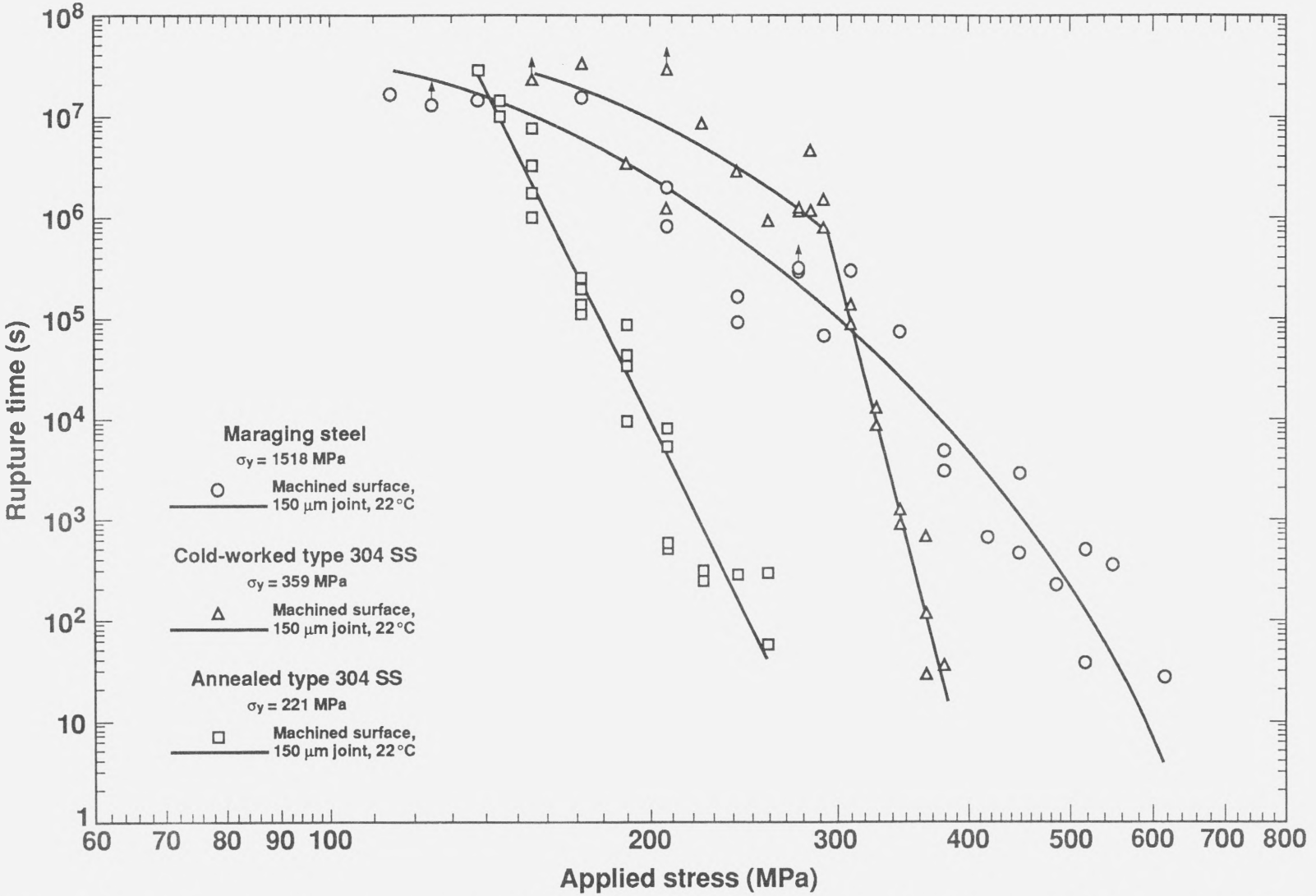

Figure 8.18. Ambient-temperature creep-rupture behavior of diffusion-welded-silver joints between machined base-metal surfaces.

SS base-metal creep rate is relatively low (see Fig. 7.2), and presumably less than that of the silver deforming under the effective stress within the interlayer. Consequently, below the crossover stress, the applied stress versus time-to-rupture trends of specimens utilizing cold-worked SS are quite similar to those utilizing maraging steel, and a bend occurs in the curve as the data more closely matches that of elastic base-metal specimens.

The change in fracture mechanism appears to be reflected in increased scatter of the rupture time values as well as in the SEM micrographs of Fig. 8.19. At the bottom of the figure is a micrograph of the silver-silver fracture surface of a diffusion weld between annealed stainless steel (tested at 207 MPa), which is representative of fractures between annealed SS base metals. This is also typical of the silver-silver separations of diffusion welds between cold-worked SS tested at higher stresses (e.g. see Fig. 8.8). An SEM micrograph of a silver-silver fracture surface of a diffusion weld joining maraging steel base metals (tested at 293 MPa) is shown at the top right of Fig. 8.19, and is representative of fractures between machined maraging steel surfaces tested at all stress levels. At the same magnification, the base-metal-accelerated (stainless steel case) fracture surface appears substantially different from the "interlayer-controlled" (maraging steel base metal case) fracture surface, reflecting the difference in the rate-controlling mechanism of failure. The micrograph at the top left of Fig. 8.19 was taken from the silver-silver fracture of a diffusion weld between cold-worked SS tested at a stress (241 MPa) below the crossover stress. The fracture process operating here is different from that above the crossover stress, and the silver-silver fracture surface exhibits the same heterogeneous cavitation as that of the interlayer-controlled (maraging steel) fracture surface.

The difference between the base-metal-accelerated silver-silver fracture surface and interlayer-controlled fracture surface for specimens utilizing machined (but not lapped) base-metal surfaces is perhaps somewhat surprising, considering that cavitation resulting from silver plasticity is common to both failure-control processes. The difference in fracture surface appearance is believed to be due, simply, to the cause of the plasticity in the

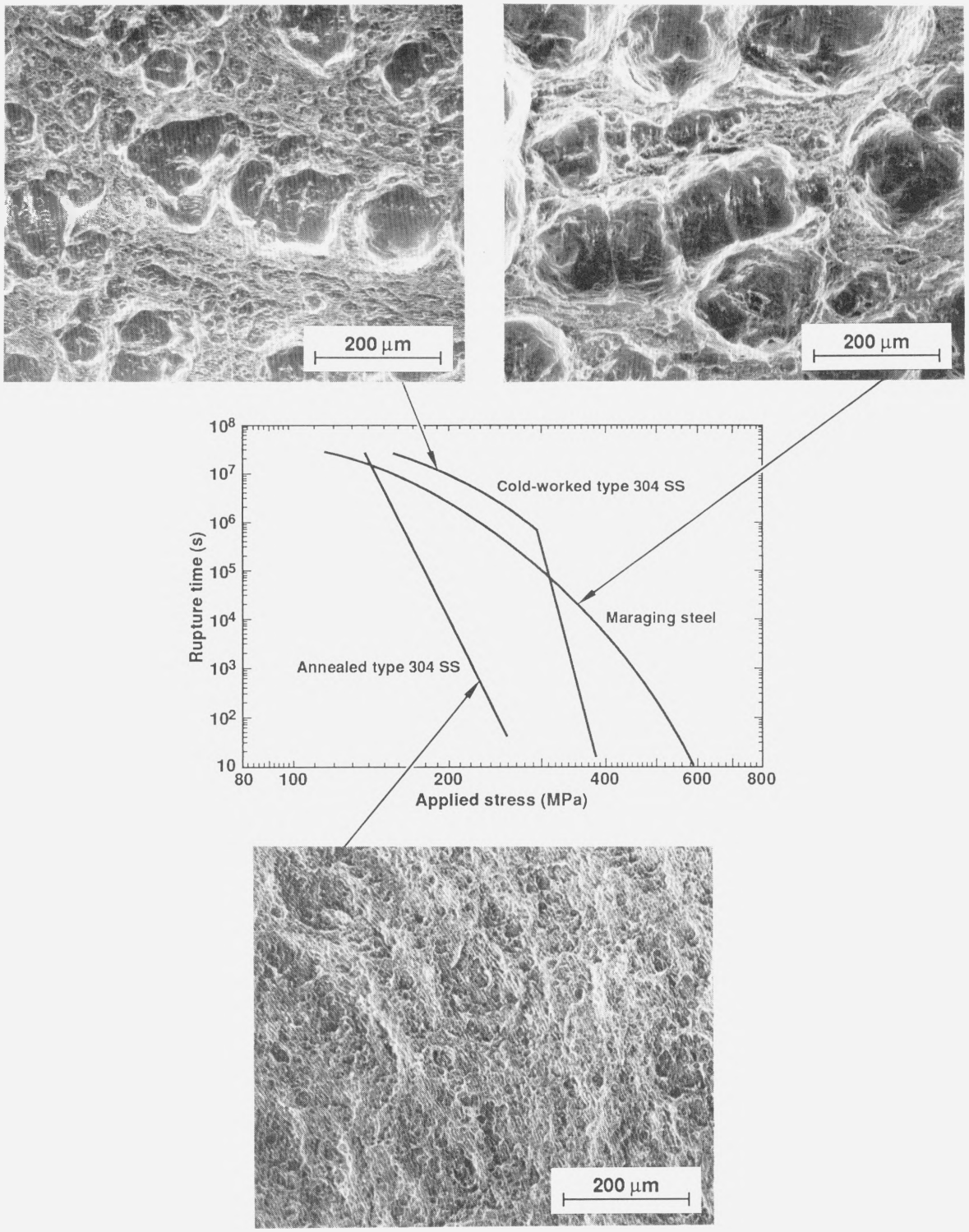

Figure 8.19. Silver-silver fracture surfaces of diffusion welds between machined base metals of annealed stainless steel (207 MPa), cold-worked stainless steel (241 MPa), and maraging steel (293 MPa).

interlayer. In the plastic base metals, the strain in the silver is externally and uniformly imposed on the silver by the deformation of the base metal. As discussed earlier for specimens utilizing elastic base metals, the strain is not imposed by base metal deformation, but is indigenous to the interlayer. It is believed that the heterogeneities along the diffusion-welded-silver interface caused during the joining of the comparatively rough machined surfaces could result in regions which may be more resistant to plasticity than other regions. Cavities may form more easily in the regions less resistant to plastic strain leading to the formation of the very large, deep cavities. When base-metal surfaces are lapped prior to coating, a more uniform silver-silver interface is created and the large cavities are not observed.

CHAPTER 9
CREEP RUPTURE RESULTS: OTHER INTERLAYERS

9.1. Diffusion Welds Utilizing Electrodeposited Silver

It is important to emphasize that the creep-rupture phenomenon is not unique to interlayers deposited by planar-magnetron (PM) sputtering. It was demonstrated that diffusion-welded-silver interlayers between uranium and stainless steel (plastic base metals) using the hot-hollow-cathode physical vapor-deposition process[20,21,40] also experience creep rupture, apparently by the same mechanism relevant to this study. Although not previously reported in the literature, creep ruptures were also observed in several maraging steel (elastic base metal) specimens utilizing silver deposited by the hot-hollow cathode process.[62] Other investigators[41] have verified creep rupture in diffusion welds between TD-nickel base metals utilizing cobalt-alloy and nickel-alloy foil interlayers. However, creep ruptures have not been reported for diffusion-welded joints utilizing electrodeposited interlayers, in spite of the many studies of ultimate tensile strengths for electrodeposited interlayers.[1,2,4,5,9–12] Therefore, joints were fabricated utilizing electrodeposited silver to determine if creep ruptures would be observed.

Figure 9.1 shows that creep ruptures are observed in diffusion-welded-silver interlayers fabricated by electrodepositing silver onto uranium and type 304 SS base metals. The base metals were selected to directly compare the creep-rupture behavior of 150-μm-thick diffusion-welded-silver interlayers fabricated using electrodeposition with those fabricated using hot-hollow cathode (HHC) deposition.[20,21,40] The rupture times of electrodeposited-silver specimens are approximately 100 times shorter than those of HHC-deposited-silver specimens (shown plotted on the same log-log figure using regression analysis of all ambient-temperature test results[40]). This observation is consistent with the lower ultimate tensile strengths of electrodeposited interlayers as discussed in Section 5.3.1. Because the base-metal properties and diffusion welding parameters of the

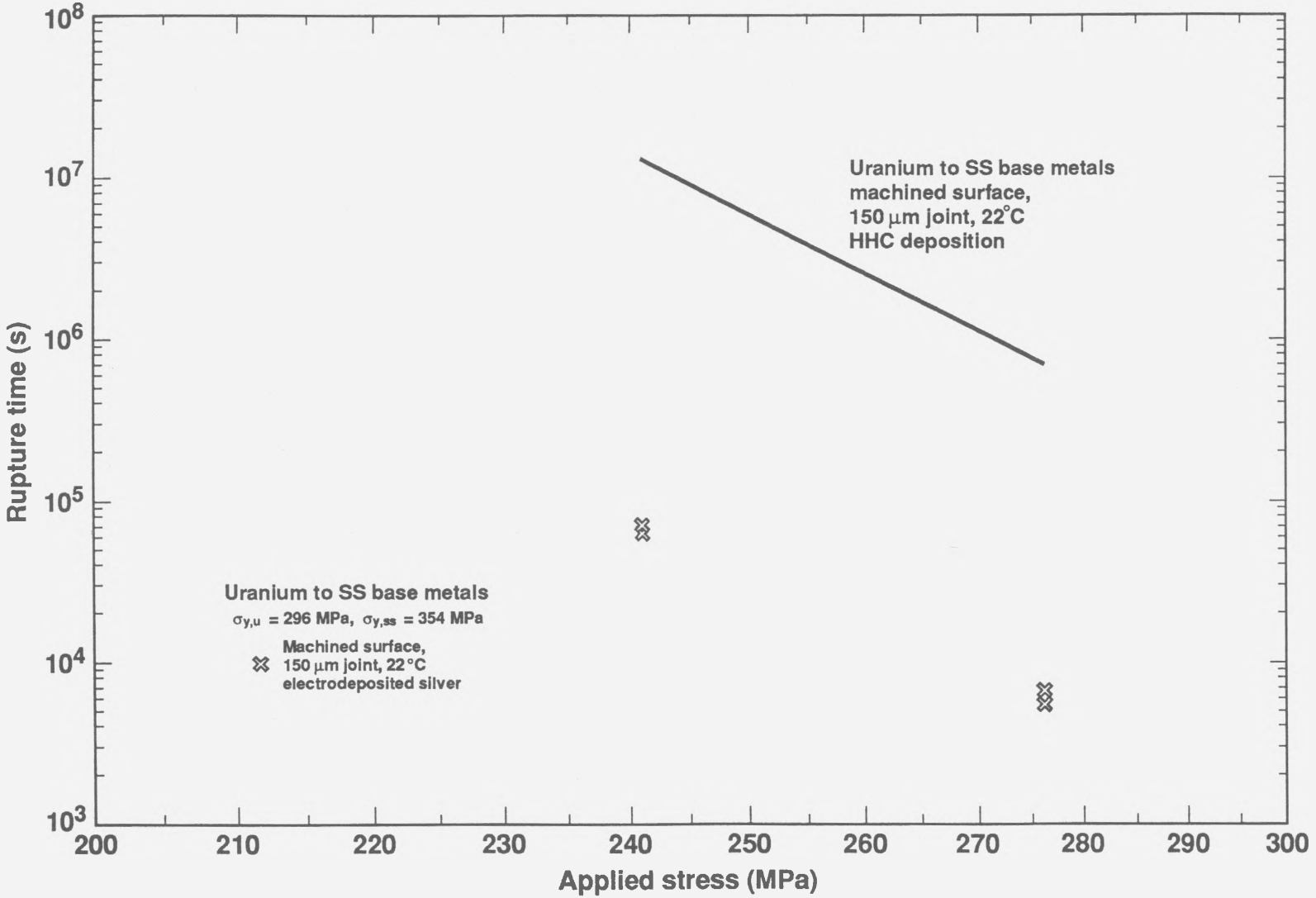

Figure 9.1. Effect of deposition method on creep rupture of diffusion welds between machined uranium and type 304 SS base metals.

two sets of specimens are identical, differences in rupture times would most likely be related to the differences in adhesion, yield stress, and strain-hardening rates between the two types of diffusion-welded-silver structures.

It is known that if the interlayer yield stress and strain-hardening rates are lowered, for example, by substitution of a softer interlayer material, then the effective stress in the base metal near the interlayer will be greater at an equivalent applied stress level than that of the higher yield-stress material (this was confirmed by finite-element analysis of the stress states in a joint substituting bulk silver properties for those of interlayer silver). In this case, the creep rate of the base metal near the interlayer, which controls the time-dependent plasticity within the interlayer (see Section 8.5), would be higher than the base-metal creep rate of a joint utilizing the stronger interlayer material. Therefore, the differences in creep rupture times between joints fabricated using electrodeposited-silver compared to those utilizing (stronger) HHC-deposited silver may be explained by the base-metal control failure theory. Although the tests of electrodeposited-silver interlayers were only conducted at two stress levels, it appears that the applied stress exponents for creep rupture are roughly comparable with those of HHC-deposited interlayers (n_{app} = 18 vs. 22).

Creep ruptures of electrodeposited-silver interlayers between uranium and SS base metals consisted of both silver-silver and silver-uranium fracture. Figure 9.2 shows the silver-silver fracture morphology. The ductile cavities are nonuniform in size, exhibiting many small microvoids which have coalesced to form larger cells. This type of ductile microvoid coalescence has been reported[20,40] for specimens utilizing HHC deposition of silver onto machined uranium and SS base metals. This nonuniformity of the silver-fracture surfaces may be related to the increased surface roughness of the base metals compared to those of the stainless steel base-metal specimens described in Section 8.4. The diffusion-welded-interlayer specimens utilizing PM sputter-deposited silver were machined flat to 2 μm, and to a surface roughness of 0.1 μm arithmetic average (AA), while those utilizing electrodeposited silver were machined flat to 5 μm, and to a surface

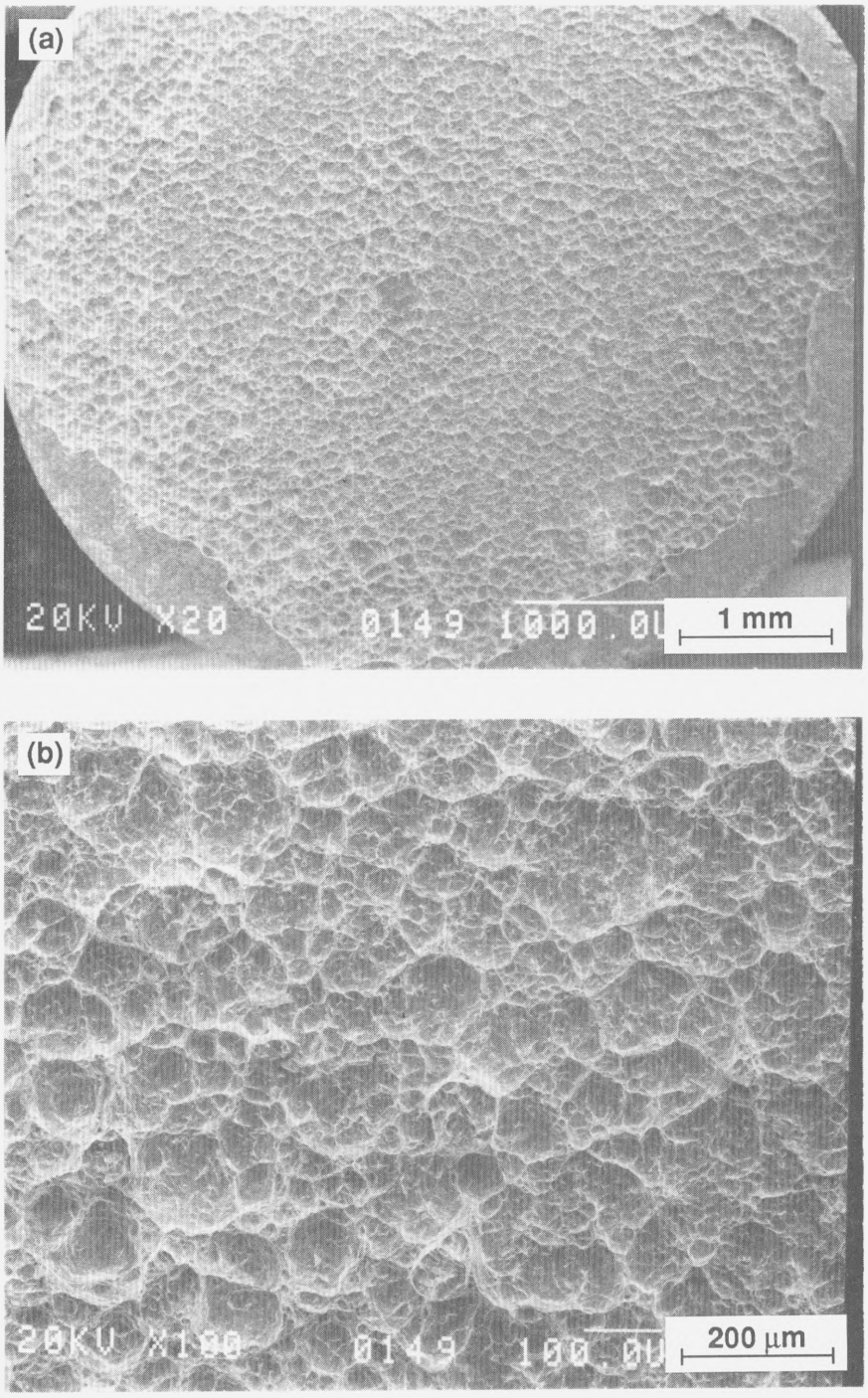

Figure 9.2. (a, b) Silver-fracture surface (241 MPa) between uranium and SS base metals which were fabricated by diffusion welding of electrodeposited silver interlayers. Approximately 90% of the fracture surface consists of silver-silver separation.

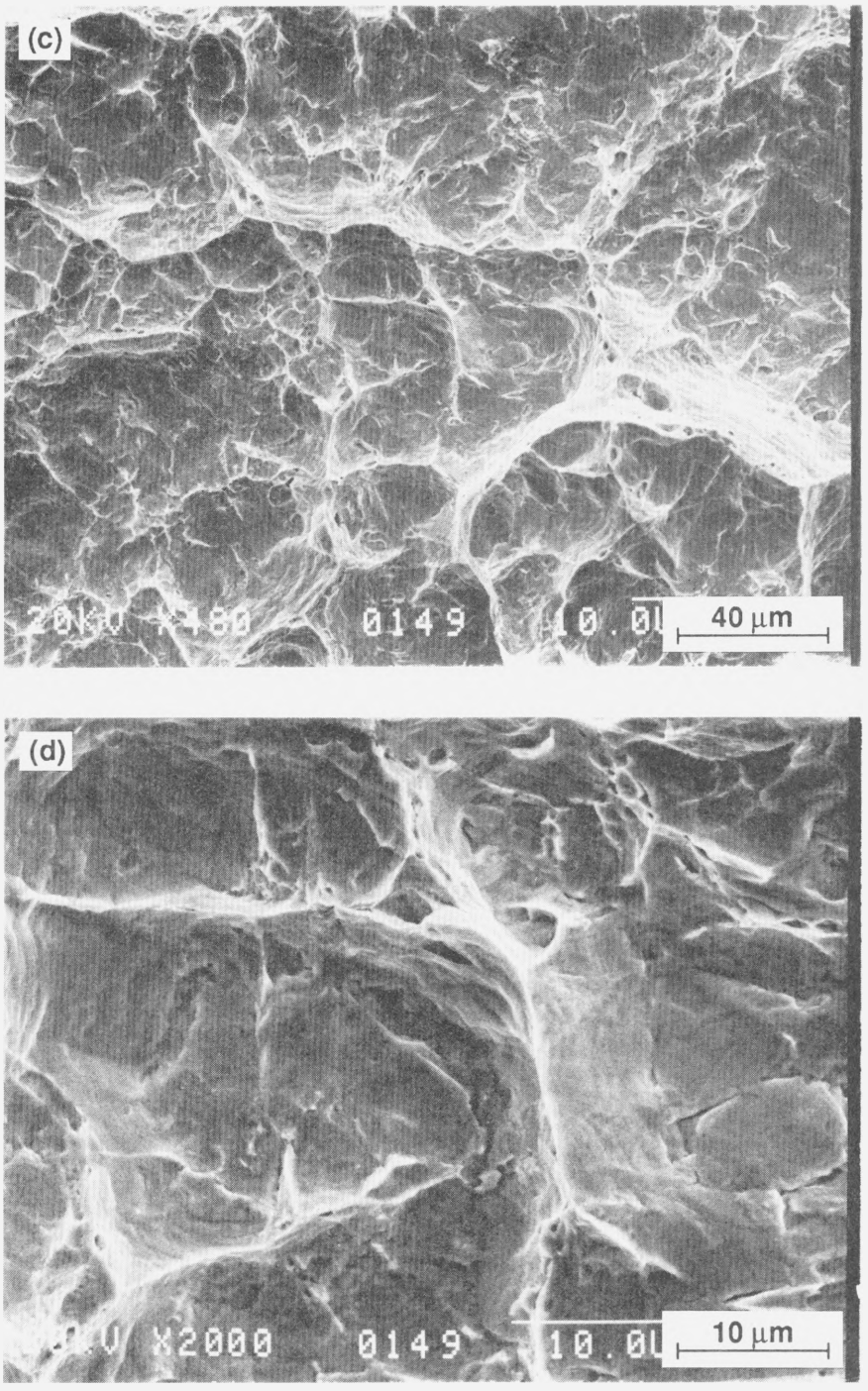

Figure 9.2. (c, d) Silver-silver fracture surface (241 MPa) between uranium and SS base metals which were fabricated by diffusion welding of electrodeposited silver interlayers. Nonuniform-size ductile microvoid coalescence is observed.

roughness of 0.4 μm AA. Additionally, the base metals utilized for electrodeposition were further roughened by acid etching prior to plating. Because specimens fabricated from plastically-deforming base metals with lapped surfaces were shown to exhibit more uniform-size ductile cells after fracturing than those utilizing machined surfaces, the silver fractures shown in Fig. 9.2 are consistent with the relatively rough base metal surface finish. The silver side of the silver-uranium fracture surface (see Fig. 9.3) shows some evidence of ductile microvoids, similar to those observed in other silver-base-metal separations (e.g., see Fig. 5.3h). Energy dispersive spectroscopy revealed substantial amounts of nickel present on the uranium side of the silver-uranium separation. This suggests that a large percentage of the fracture occurred between the nickel "strike" (6 μm thick), which was electrodeposited directly onto the uranium surface, and the silver interlayer, which was electrodeposited over the nickel deposit. However, the fraction of fracture surface associated with silver-base-metal separation (silver-nickel and nickel-uranium) varied from 0–60% for this set of specimens without changing their creep-rupture behavior.

9.2. Brazed-Silver Joints

It is also important to determine if interlayers fabricated by processes other than diffusion welding, such as brazing, exhibit time-dependent failure. If creep rupture is a general phenomenon of (soft) interlayer joints, then time-dependent failure should be (eventually) observed in all specimens subject to applied stresses (causing plasticity in the interlayer) below the UTS. To test the generality of these results, 150-μm-thick interlayer brazes made with pure silver (using titanium-hydride flux and annealed type 304 SS and maraging steel base metals) were tested to determine if creep rupture occurs.

Figure 9.4 shows that creep rupture is observed in the brazed-silver joints using both plastic and elastic base metals. At high stresses, brazed interlayer rupture times are shorter than those of diffusion-welded-silver interlayers deposited by PM sputtering. This result is

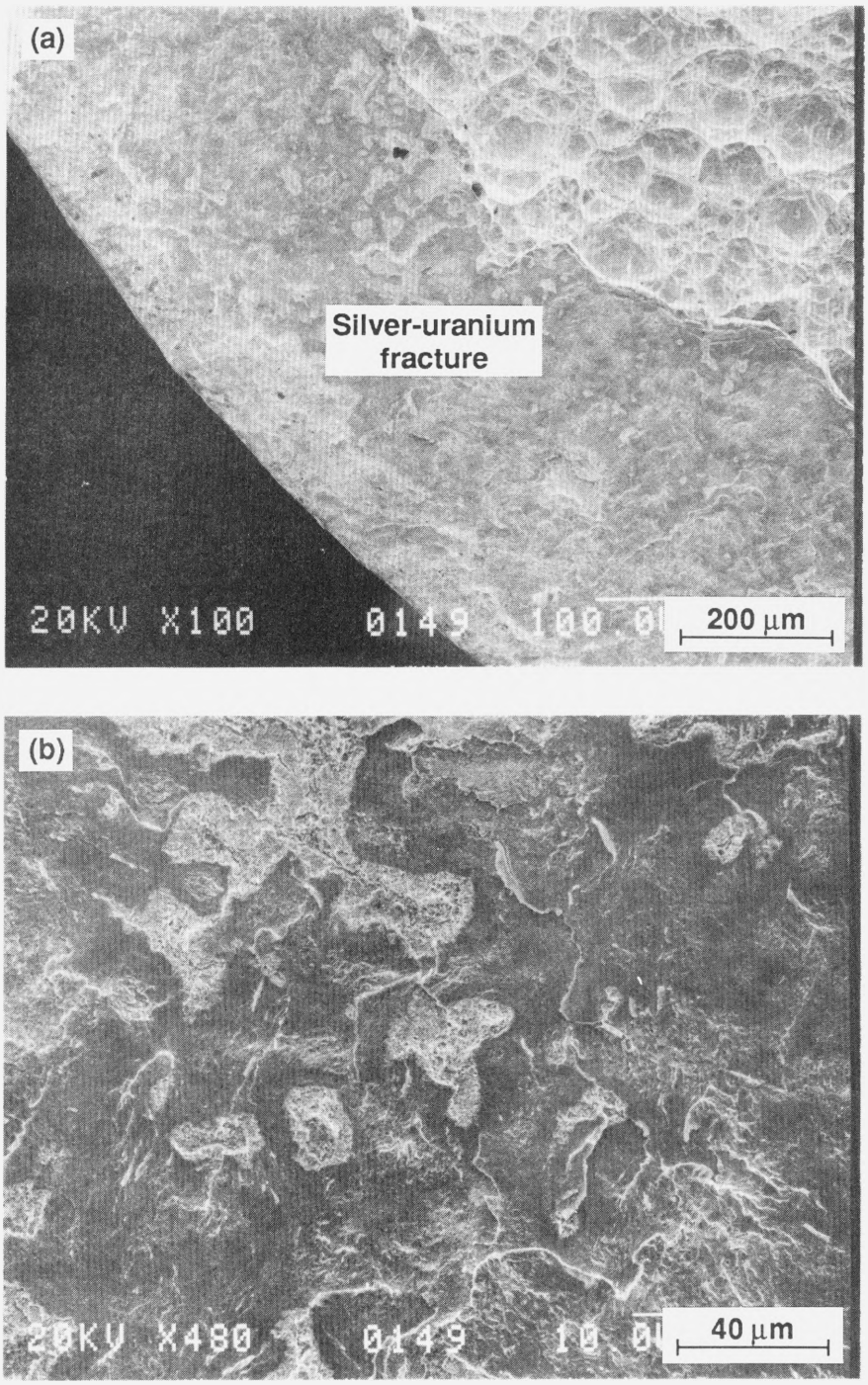

Figure 9.3. (a, b) Silver side of the silver-uranium fracture of the specimen shown in Fig. 9.2.

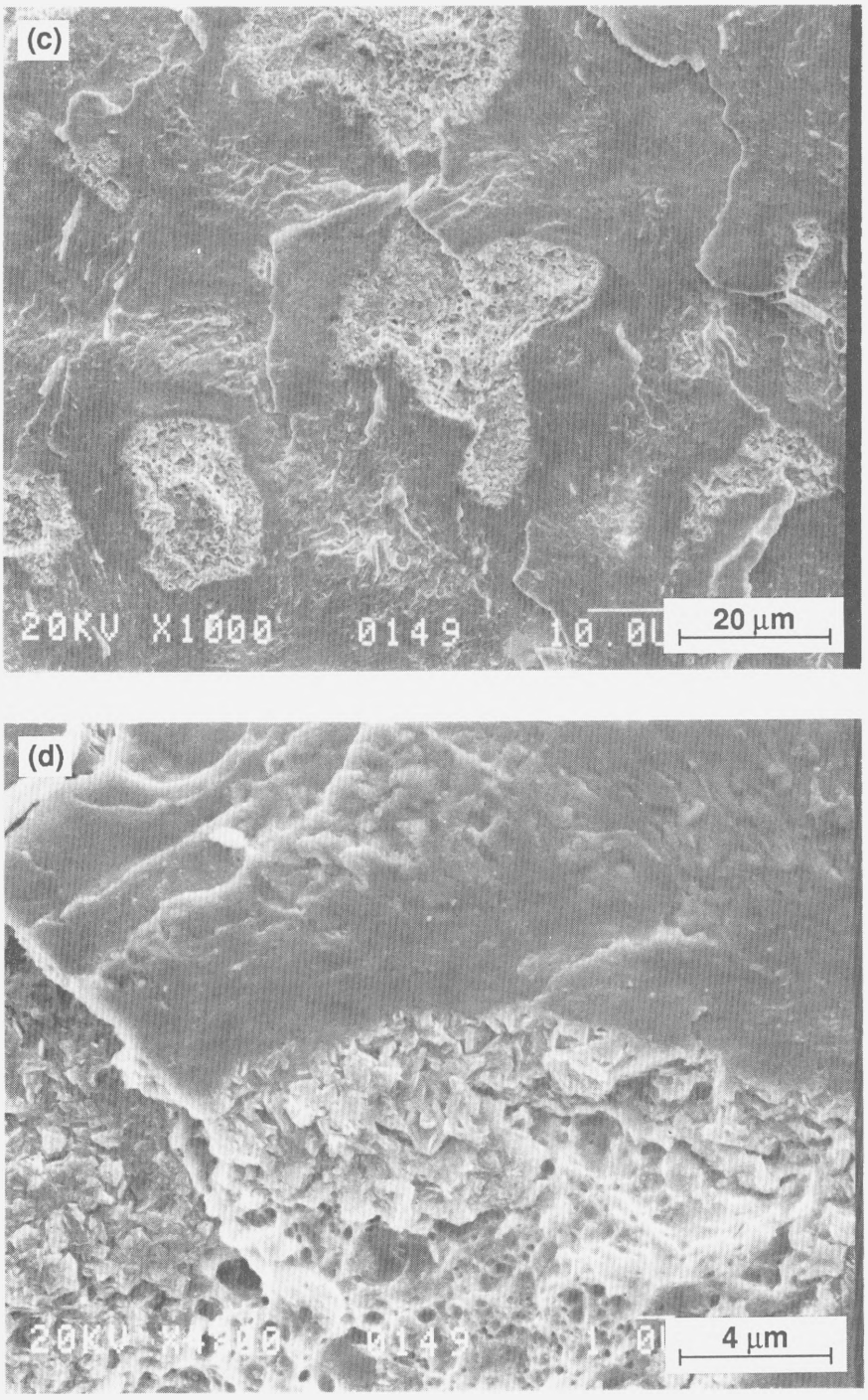

Figure 9.3. (c, d) Silver side of silver-uranium fracture of specimen shown in Fig. 9.2. Evidence of plasticity is shown by the microvoids present in some areas of the fracture surface.

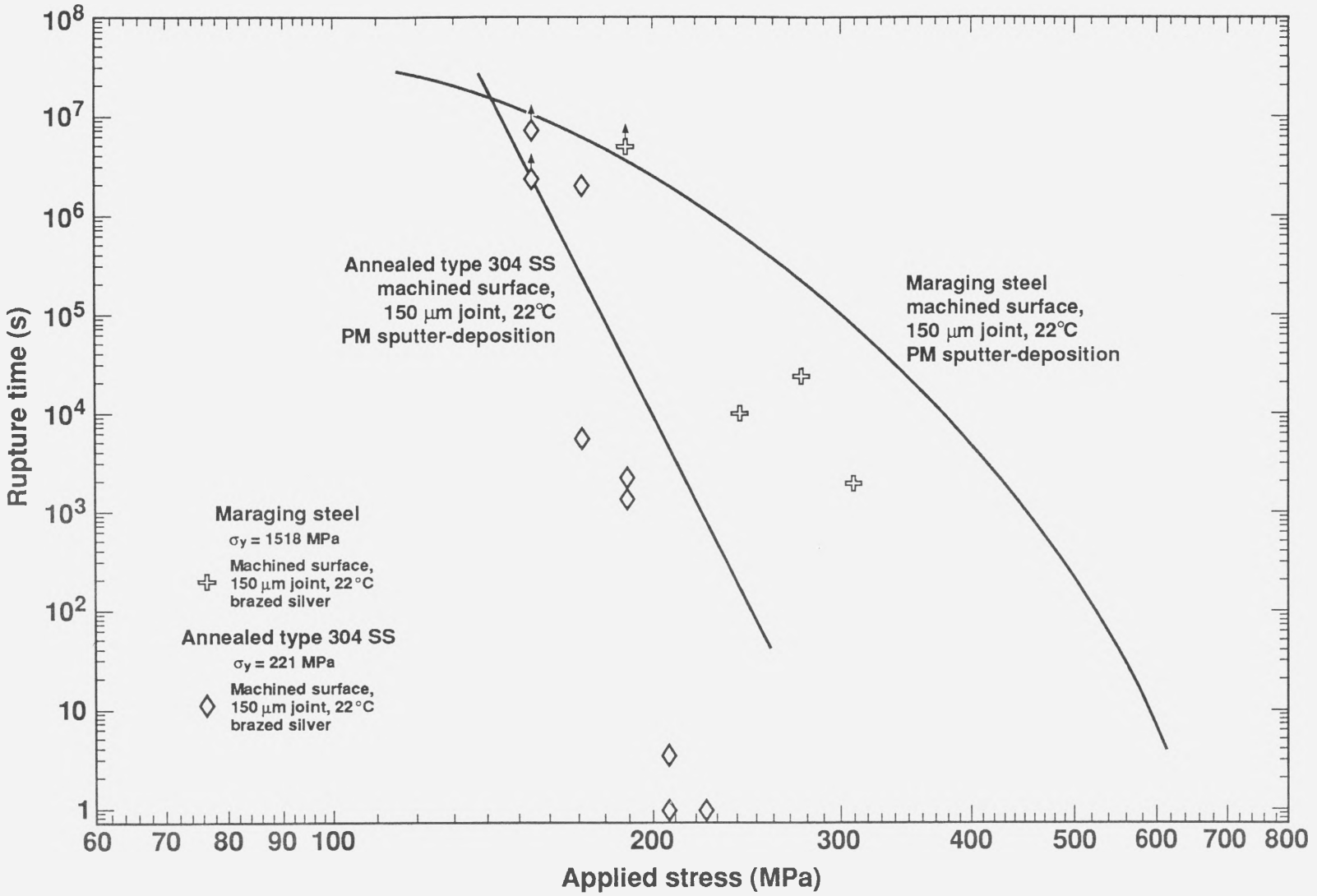

Figure 9.4. Creep rupture of brazed-silver interlayers joining steel base metals compared with those utilizing PM sputter-deposition.

consistent with the lower ultimate tensile strengths of brazed-silver interlayers compared to those of diffusion-welded-silver interlayers deposited by physical vapor deposition. Also, the brazed-silver interlayer data have higher creep rupture applied stress exponents than those of interlayers prepared by planar-magnetron (PM) sputtering. For the set of brazed-silver specimens fabricated with annealed SS, the creep-rupture applied stress exponent is approximately equal to 62, or three times higher than that of annealed SS specimens utilizing PM sputter-deposited silver.

One explanation for the higher stress exponent is that, unlike joint fractures of PM sputter-deposited interlayers, creep ruptures of brazed-silver joints tested at different stresses may occur at an approximately constant plastic strain-to-failure. This conclusion is consistent with the constant structure stress exponent, N equal to 60 for the annealed type 304 SS used in this study (see Section 7.1). The reason for the possible difference in plastic strains-to-failure between the two types of interlayers is not clear. Results of Sections 4.1 and 5.3.2 demonstrated that microstructural differences exist between the two types of silver interlayers (brazed vs. PM sputter-deposited) which gives rise to different mechanical properties. However, an explanation for the variation of plastic strains-to-failure with applied stress will require a more complete formulation of an interlayer failure mechanism (including stress state) than the model to be presented in Section 10.1. Certainly, these new data, together with the earlier observations using other processes, suggest that mechanically-induced creep rupture may be a general phenomenon in silver interlayer joints and, probably, also in joints using other interlayer materials.

Figures 9.5 and 9.6 show the fracture morphology of brazed-silver specimens utilizing elastic and plastic base metals, respectively. All of these fractures occurred at or very near the silver-base-metal interface. This result is consistent with the absence of an interface in the center of brazed-silver specimens, in contrast with the usual presence in diffusion-welded-silver interlayers utilizing PM sputter-deposition. The silver side of silver-base-metal fractures between brazed maraging steel base metals shows some evidence of ductile

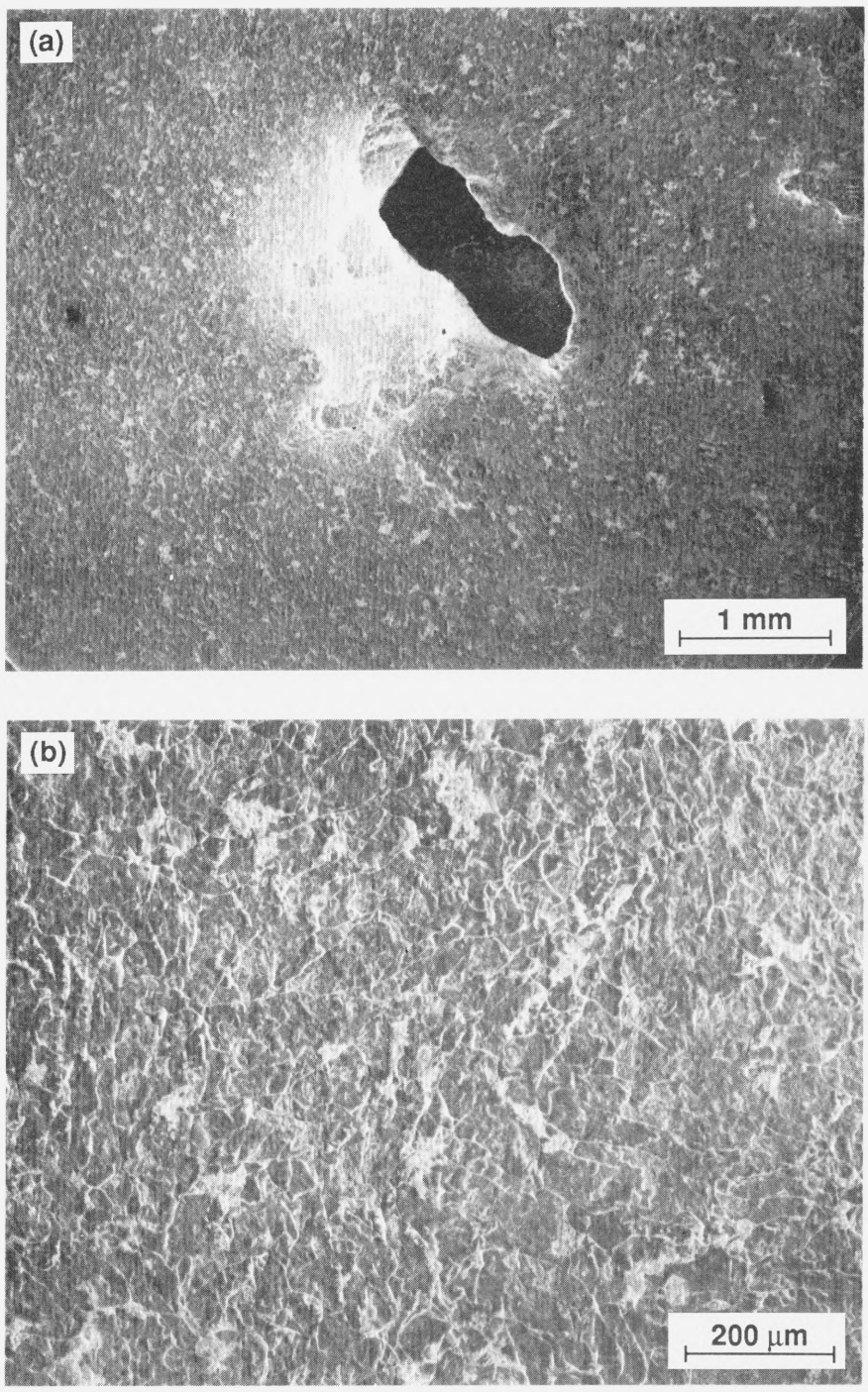

Figure 9.5. (a, b) Silver side of silver-steel fracture (241 MPa) between brazed maraging steel base metals showing some evidence of ductile microvoid coalescence.

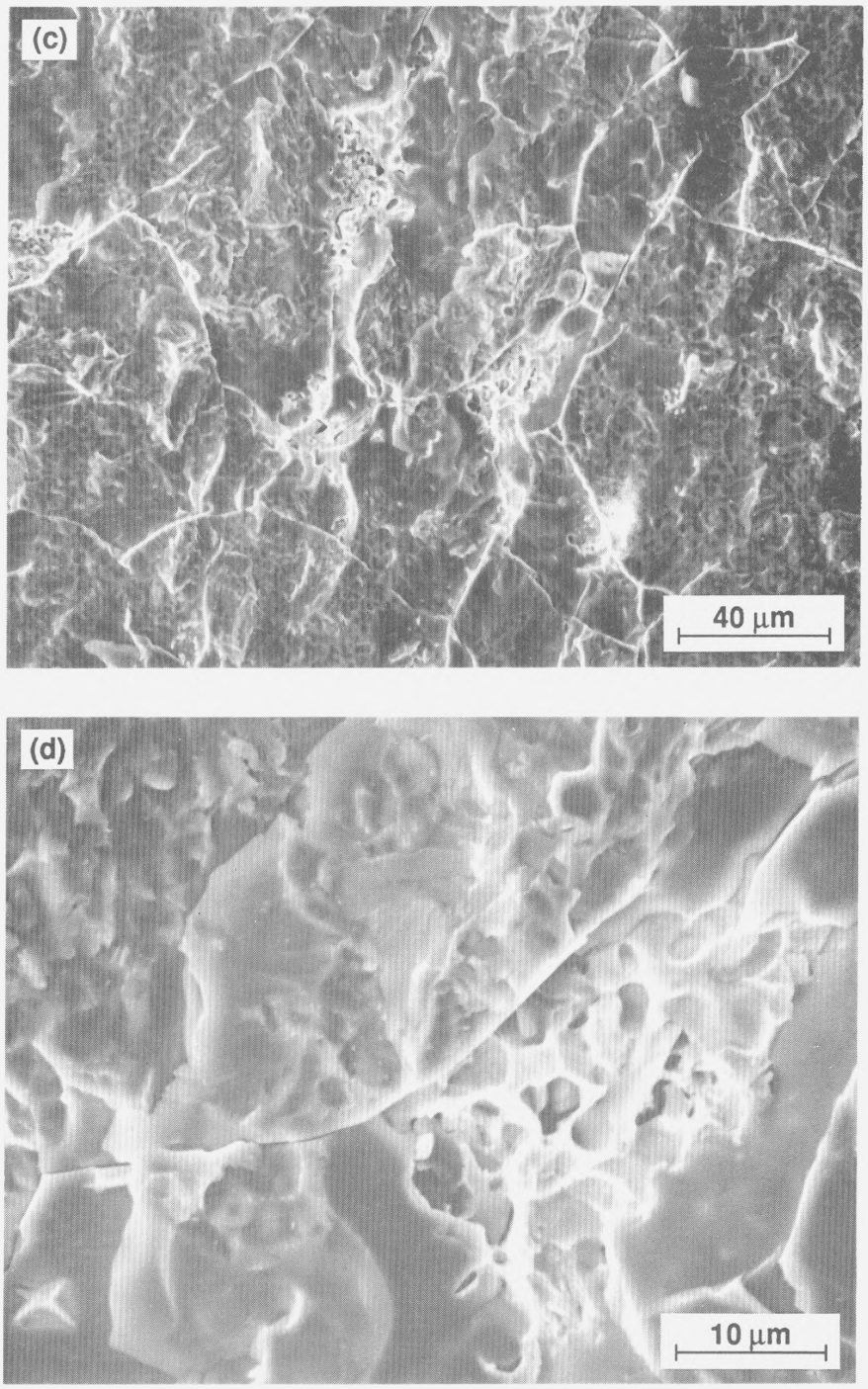

Figure 9.5. (c, d) Silver side of silver-steel fracture (241 MPa) between brazed maraging steel base metals showing some evidence of ductile microvoid coalescence.

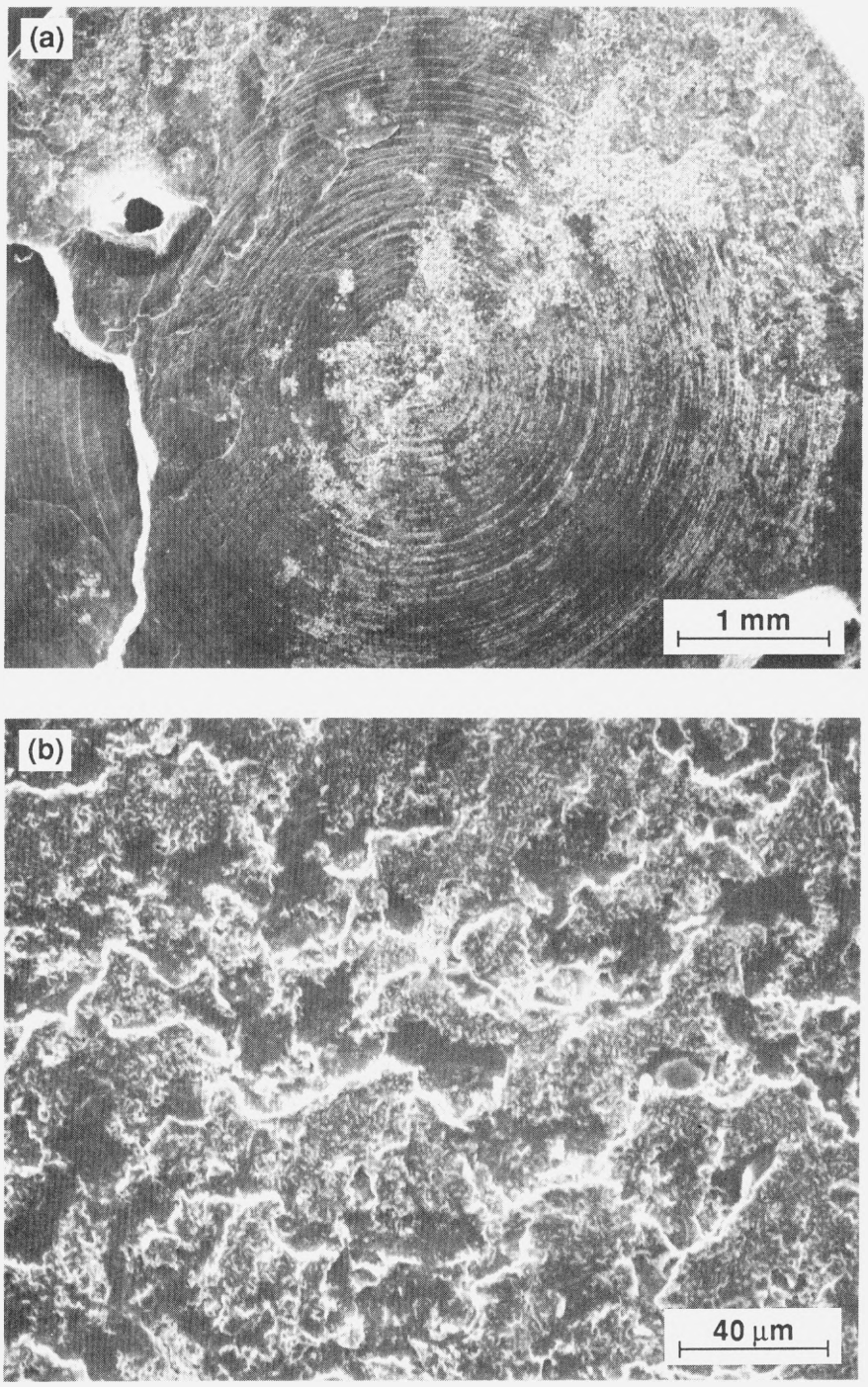

Figure 9.6. (a, b) Silver-base-metal fracture (172 MPa) between brazed (annealed) stainless steel base metals.

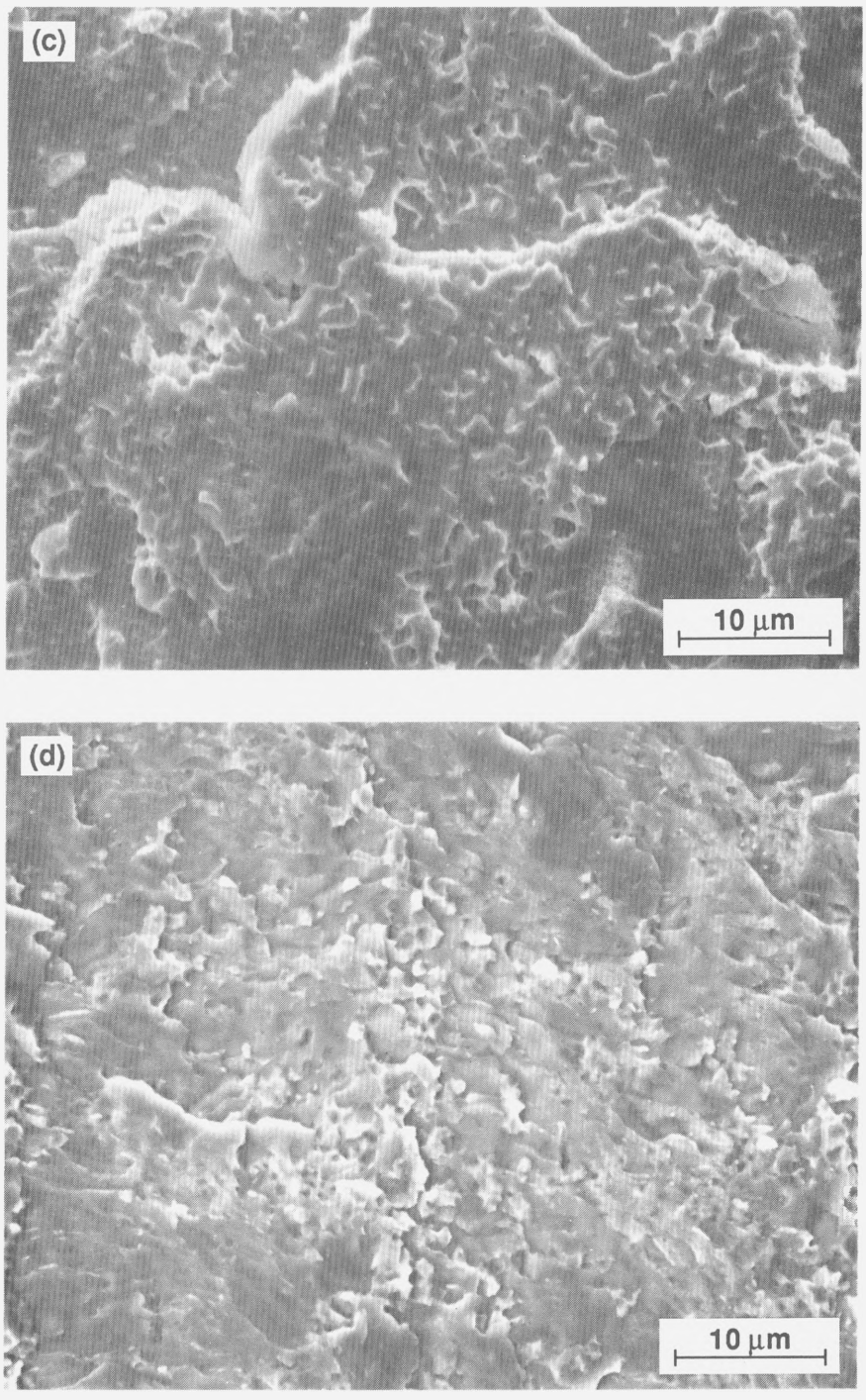

Figure 9.6. (c) Silver side of the silver-base-metal fracture (172 MPa) between brazed (annealed) stainless steel base metals shows strong evidence of ductile microvoid coalescence. (d) Steel side of the fracture surface is covered with a thin layer of silver.

microvoid coalescence, as seen in Fig. 9.5. Energy dispersive spectroscopy revealed that the maraging steel side of the fracture surface (not shown in figure) contains very little silver, although the fracture morphology replicates that of the silver side. In contrast with the fracture morphology of elastic base-metal specimens, an analysis of fractures between brazed-silver specimens utilizing annealed SS revealed that most of the steel surface was covered with a thin layer of silver. Figure 9.6 shows strong evidence of ductile microvoid coalescence occurring on the silver side of the silver-base-metal fracture interface. Microvoids are also seen in the thin layer of silver covering the steel surface, as shown in Fig. 9.6d.

CHAPTER 10
DISCUSSION OF FAILURE THEORY AND FUTURE WORK

10.1. Microvoid Nucleation and Coalescence

The previous experimental results are substantially supportive of the proposition that the observed creep ruptures of diffusion-welded-silver joints are a result of plasticity occurring in the soft interlayers under high triaxial stresses, leading to the nucleation and eventual coalescence of cavities. For diffusion-welded-silver interlayers joining elastic base metals, the temperature dependence of the rupture times, finite-element analysis, optical and electron microscopy, and the independence of the fabrication process on the phenomenon are all consistent with a creep-plasticity explanation for failure. The data for diffusion-welded-silver interlayers joining plastic base metals are also consistent with the "base-metal control" theory of joint failure, since changes in the creep rate of the base metal and, hence the silver interlayer, result in corresponding changes in the rupture times.

However, some questions remain. For example, if creep plasticity is associated with the rate-controlling process for failure of soft interlayers between elastic base metals, then the creep-rupture stress exponent should be related to the silver-plasticity stress exponent just as the activation energy for creep rupture was found to be related to the activation energy for silver plasticity. The stress exponent of a material can be described by considering the general case where specimens are deformed to the same plastic strain, ε_p at two different stresses, σ_1 and σ_2. The difference in stress results in different levels of strain hardening and different strain rates at ε_p (i.e., $\dot{\varepsilon}_1$ and $\dot{\varepsilon}_2$). The "general" stress exponent, $[\ln (\dot{\varepsilon}_2/\dot{\varepsilon}_1)]/[\ln (\sigma_2/\sigma_1)]$, will quantitatively be between the "steady-state" stress exponent, n_{ss}, and the "constant-structure" stress exponent, N. These quantities are described in the following way: mechanical steady state occurs when the strain rate reaches a minimum or saturation value, $\dot{\varepsilon}_{ss}$, at a fixed stress, σ_{ss}. Here, hardening processes are

balanced by dynamic recovery. The steady-state stress exponent is defined by:

$$n_{ss} = \left[\frac{\partial \ln \dot{\varepsilon}_{ss}}{\partial \ln \sigma} \right]_{T,\, s} . \tag{6}$$

The values of N from Eq. 4 indicate the increase in strain rate associated with an increase in flow stress for a particular substructure, s. In contrast, the steady-state stress exponent indicates the increases in steady-state strain rate with increases in steady-state stress. Different steady-state stresses are associated with different microstructures. Therefore,

$$n_{ss} \leq \frac{\ln\left(\frac{\dot{\varepsilon}_1}{\dot{\varepsilon}_2}\right)}{\ln\left(\frac{\sigma_1}{\sigma_2}\right)} \leq N . \tag{7}$$

The constant-structure stress exponent of silver at ambient temperature has been determined to be about 200, whereas the steady-state stress exponent is between about 10 and 40.[47,66] Figure 4.1 shows that saturation or steady state is achieved by effective plastic strains between 5 and 10%. Therefore, for interlayer silver, as ε_p approaches zero, the general stress exponent is about 200; for strains near 5%, the general exponent is between about 10 and 40.

The effective stress exponent for creep rupture, as determined from the slopes of Fig. 6.14 (rupture time vs. the effective stress), varies from about 60 at high stresses to between 10 and 15 at low stresses. These values appear roughly consistent with the established steady-state stress exponent of silver, but not with the constant-structure stress exponent. Therefore, consistency with the silver-plasticity theory of failure is realized provided that the plastic strain accumulated to the onset of catastrophic ductile rupture is near 5% or so. As mentioned earlier, the measured average plastic strains at higher applied stresses over the entire interlayer were only about 0.2% (perhaps even smaller at lower

stresses), which is less than that which would appear to bring consistency. It appears that consistency is only realized between theory and the observed stress exponent if the plastic deformation in the vicinity of the interfaces is higher (e.g., a few percent) than the macroscopic strain.

Another difficulty is an explanation for the apparent cavity growth. As illustrated in the previous figures, cavities with diameters between 0.2 and 1 μm are frequently observed. If dislocation pile-ups are responsible for cavity nucleation, then the nuclei size might be expected to be of the order of 1 nm or so. As discussed earlier, an increase of 2 or 3 orders of magnitude in size cannot be readily rationalized by vacancy accumulation. Furthermore, this increase would not seem to be easily explained by "uniform" plastic deformation of the interlayer matrix. Large plastic strains are clearly not observed uniformly over a 150-μm-thick interlayer, nor is there obvious evidence that sufficient strains exist in the vicinity of the interfaces.

One possible explanation for the "expansion" of cavities is the coalescence of small nuclei or cavities. On loading an interface, small cavities may nucleate in groups in which the spacing may be small. The coalescence is possible by plasticity in the region between the small nuclei. Thus "growth" or cavity expansion may occur by coalescence (aided by the increased effective stress between the voids) rather than the traditional concept of a uniformly expanding cavity surface. Therefore, the failure steps may be reasonably described by cavity nucleation and coalescence. The micrographs of Figs. 6.21d and 6.22b show some evidence of clustering of cavities. In addition, SEM stereo pairs of the silver-silver fracture surface provide evidence that large (1-μm-diameter) cavities result from the coalescence of several smaller cavities.

Figure 10.1 illustrates this process in the simplest form. Dislocations are activated by the effective stress, move on various slip-planes, and pile-up at the three principal interfaces. This leads to the nucleation of cavities of diameter, d. With increasing plastic strain, ε_p, more cavities are nucleated. As the spacing between cavities, l decreases, the

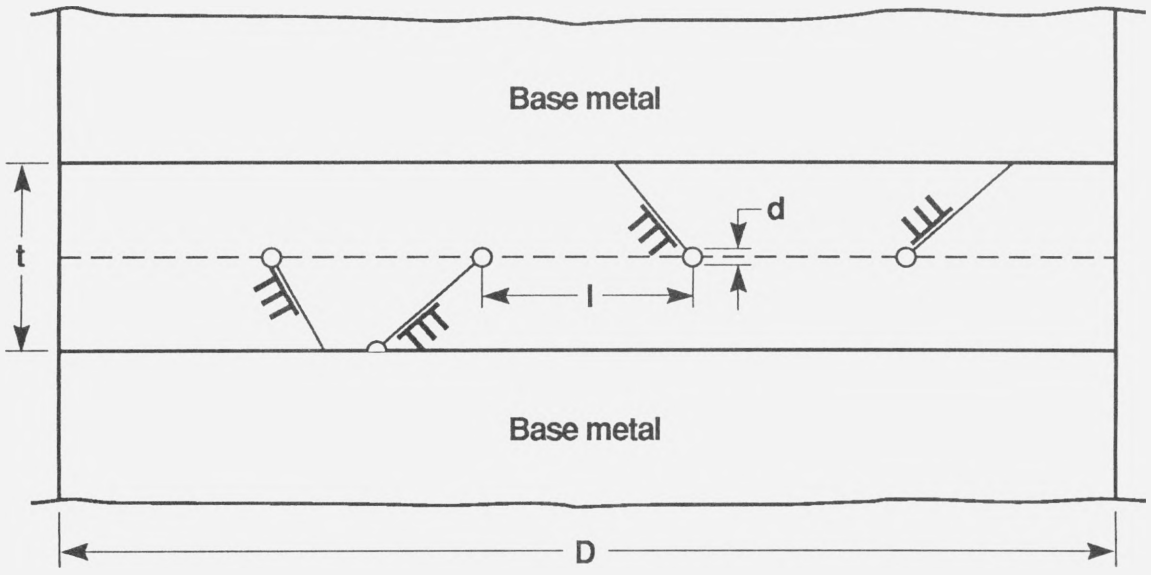

Figure 10.1. Schematic showing model of time-dependent plasticity controlled failure in diffusion-welded-silver interlayers. Dislocation pile-ups at the three principal interfaces lead to the nucleation of microvoids. Continued nucleation results in microvoid coalescence and eventual interfacial failure after extensive cavitation.

stress between the cavities increases until local rupture occurs. The plastic strain necessary for this process to occur over a sufficient fraction of the interface, so that catastrophic failure occurs over the entire interface, is calculated in the following way. First, consider the simplified geometry shown in Fig. 10.1 with slip lines at a 45° angle to the interlayer-base-metal interface. The shear strain, γ_p produced by the motion of N_d dislocations in the interlayer of thickness, t and diameter, D is:[78]

$$\gamma_p = \frac{N_d b \bar{x}}{Dt} , \tag{8}$$

where b is the Burgers vector, and $\bar{x}$ is the average distance of dislocation glide. The shear strain in the interlayer can be converted to uniaxial strain using the von Mises criterion:

$$\varepsilon_p = \frac{N_d b \bar{x}}{Dt\sqrt{3}} . \tag{9}$$

The number of dislocations in the interlayer, N_d is:

$$N_d = \left(\frac{\sqrt{2}t}{2}\right) n_p P D , \tag{10}$$

where n_p is the number of mobile dislocations per slip-line length and P is the number of slip planes per silver-silver interfacial line-length. Based on the model shown in Fig. 10.1, $\bar{x} = \sqrt{2}t/4$. Equation 9 can then be written:

$$\varepsilon_p = \frac{n_p P b t}{4\sqrt{3}} . \tag{11}$$

Assuming that movement of half of the dislocations on a slip plane lead to formation of a cavity at the silver-silver interface, and the other half to formation of a cavity at the interlayer-base-metal interface, then:

$$\frac{d}{l} = \frac{\sqrt{2}}{4} n_p P b t , \tag{12}$$

where d is the cavity diameter and l is the cavity spacing at the silver-silver interface. Combining Eqs. 11 and 12 produces an expression directly relating the plastic strain in the interlayer to the cavity spacing and diameter:

$$\varepsilon_p = \frac{1}{\sqrt{6}}\left(\frac{d}{l}\right). \tag{13}$$

Depending on the applied stress, there will be a critical diameter-to-spacing ratio for local instability or rupture to occur:

$$\left(\frac{d}{l}\right)_{local}^{critical} = f(\sigma). \tag{14}$$

Catastrophic failure occurs when $(d/l)_{local}^{critical}$ is satisfied over a sufficient fraction of the interface approximately given by $(1-\sigma_{app}/\sigma_{uts})$, where σ_{app} is the load divided by the original cross-sectional area, and σ_{uts} is the ultimate tensile strength of the joint. From the above, the critical plastic strain to failure in interlayers is given by:

$$\varepsilon_p^{fail} = \left(\frac{d}{l}\right)_{local}^{critical}\left(1-\frac{\sigma_{app}}{\sigma_{ult}}\right)\left(\frac{1}{\sqrt{6}}\right). \tag{15}$$

Predicting $(d/l)_{local}^{critical}$ is difficult, at least partially because a failure criterion as a function of the stress state and the defect configuration has still not been established. Transmission electron micrographs of specimens loaded to near rupture (within a factor of 2 or so of the rupture time, t_r) reveal d/l values in the "higher concentration" locations to be between 0.1 and 0.2. Interestingly, critical d/l values in this same range were reported previously using analytical techniques.[36] If $(d/l)_{local}^{critical}$ is estimated to be about 0.15, then the ε_p for failure over the relevant applied-stress levels is estimated to range from 0.9 to 5%. This suggests that the above described mechanism can account for both small plastic strains to failure and, perhaps, sufficiently large strains to imply steady-state mechanical behavior of the silver.

The fact that the observed strains appear lower than these values may be because the strain becomes localized as cavities nucleate. Localization can be demonstrated by calculating the plastic strain rate near the cavitating interface for elastic base-metal specimens:

$$\dot{\varepsilon}_p^{int} = \left(\frac{\sigma_{int}}{\sigma_{app}}\right)^n \dot{\varepsilon}_{bulk} , \qquad (16)$$

where $\dot{\varepsilon}_{bulk}$ is the strain rate in the interlayer away from the interface, σ_{int} is the applied load divided by the unseparated area at the interface, and n is defined by Eq. (6). At the intermediate stress levels of 300-400 MPa and at $t_r/2$, $(\dot{\varepsilon}_{int}/\dot{\varepsilon}_{bulk}) \approx 400$. Therefore, because of the high general stress exponent, n (or low strain-rate sensitivity, m = 1/n) of silver, plasticity becomes very localized at the interface during fracture. Therefore, the low strains predicted by Eq. (13) may be even lower in the bulk, as observed. This may bring consistency between the very low measured bulk plastic strains and the observation of the creep-rupture stress exponent being coincident with n_{ss} (i.e., local strains of near 5% or so). The localization may also rationalize the observation of decreasing interlayer strain-to-failure with decreasing stress. As the strain becomes localized, the bulk strain in the interlayer approaches zero. The macroscopic strain may, then, be related to a strain "surge" on loading, which would naturally decrease with the applied stress.

The suggestion of a non-growth control for failure has, of course, been suggested in other simpler systems such as uniaxial creep.[79] This explanation is speculative and is an important new area for further investigation.

10.2. Future Work

10.2.1. In-Situ Deformation Experiments

The formation of microvoids at the principal diffusion-welded-silver interface has been confirmed in elastic base-metal specimens loaded to various fractions of the expected

rupture time. Additionally, the density of these microvoids has been shown to increase with increasing percentage of creep rupture time. Stereoscopic scanning electron microscopy has revealed that the microvoids tend to cluster (local coalescence) with increasing percentage of creep rupture time. These observations have been shown to be consistent with the model presented for dislocation-controlled cavity nucleation and coalescence. However, the small plastic strains, known to vary with radial distance across the interlayer, have not been measured accurately as a function of creep time.

One recommendation for future study is an assessment of the plastic strain versus time in the silver interlayer by performing in-situ creep experiments of specimens in a scanning electron microscope. The specimen could have a grid etched onto the surface of the silver interlayer to measure total deformation (elastic and plastic) as a function of stress during loading. The plastic deformation could be determined by unloading the specimen upon reaching the desired load. The time-dependent plastic deformation could then be monitored during the creep portion of the test. These results could, possibly, be used to verify the finite-element analysis of deformation in the interlayer.

10.2.2. Creep Rupture Threshold Stress

As discussed in Section 6.3, a specimen loaded to 62 MPa at 72°C had not failed (as of the submission date of this document) after 1.6×10^7 s, or approximately 4 times longer than expected based on an extrapolation of the 72 °C creep-rupture curve. If creep plasticity within the silver interlayer determines the time-to-rupture then, it might be supposed that, creep ruptures may not occur below stress levels necessary to cause dislocation motion. Plasticity within the silver interlayer is observed, from ambient temperature torsion test results reported in Section 4.1, at stresses as low as 95 MPa (0.1% plastic strain), and possibly at stresses as low as 40 MPa (0.01% plastic strain). Results of the finite-element analysis shown in Fig. 6.13 indicate that the effective stress in the interlayer of a specimen loaded to 62 MPa is approximately 40 MPa. Because the yield stress of silver at 72 °C is

nearly equal to the value at 22 °C, the specimen loaded to 62 MPa may be at or below a threshold stress level necessary to cause dislocation motion in the interlayer. Therefore, creep rupture may not occur in this specimen.

The existence of a threshold stress level for creep ruptures would have important consequences in engineering design. Currently, soft interlayer joints cannot be recommended for applications requiring sustained tensile stresses (residual or applied). Low-stress extrapolations based on the high-stress creep-rupture behavior of interlayers utilizing plastic base metals are particularly erroneous due to the change in rupture mechanism from base-metal to interlayer control. Additionally, the stress exponent for creep rupture appears to decrease continually with applied stress level suggesting, perhaps, that silver interlayer joints between machined base metals may exhibit creep ruptures even at low tensile stress levels (<50 MPa) within 10 years or so.

Because creep rupture times at ambient temperature may exceed 10^8 s (~3 years) at possible threshold stress levels, testing at 72 °C may aid in confirming the existence of a threshold stress in a substantially shorter time. The determination of a threshold stress level at ambient temperature (22 °C) using test data from 72 °C may be complicated by the possibility of annealing (softening) of the silver microstructure at elevated temperature over very long times (>10^7 s). If the specimen loaded at 62 MPa ruptures, then the occurrence of time-dependent plasticity within the silver may be due to softening (lowering of the yield stress) with time, as opposed to creep occurring continuously over the entire time of the test. To determine if the former possibility may have occurred, a second, nonloaded specimen has been placed in the furnace at 72 °C for the duration of the creep test. If the loaded specimen ruptures, then the nonloaded specimen will be tested in torsion at 22 °C to determine the post-soak yield stress. The results of this test would be compared with those of an as-fabricated (nonsoaked) specimen as shown in Fig. 4.1. Additionally, a third specimen fabricated at the same time as the first two, and not having been subjected to an

elevated-temperature soak, would be tested in torsion at 72 °C to confirm the effect of temperature on flow properties.

10.2.3. Biaxial Creep Rupture Testing

All of the creep testing of soft interlayers in the present study, in addition to most of the other results reported, have been performed using applied tensile loads. In a previous study, several ambient-temperature creep tests of diffusion-welded-silver interlayers were performed in torsion to determine the creep-rupture behavior.[21] Creep rupture times in torsion (determined by the onset of tertiary creep) were found to be approximately 100 times shorter than those of identical base metal (uranium-to-stainless steel) joints tested in tension, as compared using effective (von Mises) stress for the torsion data. The investigators[21] concluded that creep ruptures in torsion were controlled by the steady-state creep plasticity in the silver interlayer. However, creep tests were not reported for biaxial loading states (combined tension and torsion).

Biaxial creep rupture testing could provide more insight into the failure criteria for thin, soft interlayers between elastically-deforming base metals as a function of multiaxial stress states. The stress state in the interlayer could be determined using a 3-dimensional finite-element analysis (due to the nonaxisymmetric shear stresses). The contributions of effective and hydrostatic stresses to the nucleation, coalescence, and resultant creep ruptures may be determined by varying the shear stress (torsional load) level. In principle, for a given effective stress, larger shear components should reduce the creep-rupture time.

10.2.4. Hardenable Interlayer

An important improvement in the mechanical properties of soft interlayer materials would be to decrease the nucleation and coalescence rate of cavities at the interfaces. Because this mechanism is believed to be controlled by creep plasticity in the interlayer,

modifications to the interlayer structure which increase the yield stress and strain-hardening rates should decrease the creep rate and, hence, increase the resultant creep-rupture times.

One method of strengthening the silver is by additions of an alloying element, such as aluminum, that would be in substitutional solution at the diffusion-welding temperature and not expected to affect welding, but would precipitate out on cooling to ambient temperature. Examination of the silver-aluminum phase diagram suggests that 10–15 at.% aluminum would provide a single-phase solution at diffusion-welding temperatures from 200–400 °C, and then would precipitate out into a two-phase mixture of silver and the μ-phase which is a hard intermetallic. The advantage of using a precipitation-hardening interlayer is that the silver remains soft and weldable at joining temperature, but then strengthens after quenching by precipitation of the supersaturated element into a dispersed phase. The μ-phase may precipitate during continuous cooling at an appropriate rate, possibly eliminating the need to quench and then age at an elevated reaction temperature.

10.2.5. Alternative Interlayers

Other noble metals such as gold and copper have been used as interlayers for diffusion welding.[13,39] Both of these metals have higher yield stresses than silver and may, perhaps, provide increased resistance to creep rupture. Determining whether time-dependent failure occurs with these interlayers would test the generality of creep rupture. Copper has the disadvantage of requiring higher diffusion-welding temperatures than that of silver, due to the higher dissociation temperature of copper oxide. Gold, on the other hand, has the advantage of being able to be diffusion welded at ambient temperatures due to the lack of a surface oxide. For the most part, the vast majority of research into the joining and mechanical properties of low-temperature interlayer diffusion welds has been performed using silver.

These metals (Au and Cu), along with other candidate metals and alloys (e.g., Pt and Pt alloys), may provide interlayer materials that can be easily diffusion welded and may

exhibit superior creep resistance properties than those of pure silver. Any metal or alloy that can be fabricated into a bulk target geometry should be able to be sputtered using a planar magnetron configuration. Similarly, using the in-situ etching and coating procedure developed in this study, any base metal or alloy may be sputter-etched and then coated with an interlayer material for subsequent joining by diffusion welding. Perhaps pure silver, utilized frequently as an "optimum" interlayer material, may eventually be supplanted by a more creep-resistant material.

SUMMARY AND CONCLUSIONS

Various base metals were diffusion welded using silver interlayers deposited by planar-magnetron (PM) sputtering. The properties of these joints were determined and compared with silver joints fabricated using other methods. The following conclusions are based on experiments in which the diffusion-welded-silver joints were loaded to various stresses up to the ultimate tensile strength. These conclusions were substantiated by careful analyses of the stress and temperature dependence of the rupture times, finite-element analysis of the stress and strain states within the interlayer, scanning electron microscopy of the fracture surfaces, and optical, scanning electron, and transmission electron microscopy of the silver interlayer loaded to various fractions of the expected rupture time.

1. Silver coatings deposited by PM sputtering consist of heavily-twinned fine columnar grains that grow perpendicular to the base-metal surface, with the axes of the columns oriented along the [111] crystallographic direction. This type of structure is typical of sputter deposits on low-temperature substrates using a low working-gas pressure. Diffusion-welded-silver interlayers consist mostly of large recrystallized grains containing a high twin-density and a somewhat high dislocation density. However, a substantial portion of the interlayers contain nonrecrystallized columnar grains that retain the same microtwinned structure. Considerable recrystallization occurs across the diffusion-welded-silver interface. Microvoids are rarely observed in nonloaded diffusion-welded-silver interlayers. The absence of microvoids is believed to improve the mechanical properties of the joints compared with other fabrication processes. Silver deposited by PM sputtering was found to be very pure compared to hot-hollow cathode (HHC) deposited or electrodeposited silver.

2. The yield stress and strain-hardening rate of diffusion-welded-silver joints fabricated using PM sputter-deposited interlayers are much higher than values for annealed bulk silver or brazed-silver joints, although the maximum (steady-state) stresses are nearly

identical. The harder yield stress may be explained by the many dislocation barriers in the diffusion-welded-silver structure. Joints fabricated using HHC deposition achieved higher steady-state stress levels, presumably due to tantalum impurities introduced during the deposition process, and also the greater amount of nonrecrystallized silver retained after diffusion welding. Tensile strengths of diffusion-welded-silver joints fabricated using PM sputter-deposition are equal to or greater than those utilizing electrodeposition or other vapor deposition methods. The ultimate tensile strength of diffusion-welded-silver joints between elastic base metals (>750 MPa) was found to exceed those fabricated by brazing, which produces a lower interlayer yield stress and a high concentration of shrinkage voids. Relaxation of triaxial constraint in the silver interlayer by plastic deformation in the base metals resulted in lower joint strengths. Base metal surfaces machined by single-point turning prior to silver deposition, provided sites for subsequent nucleation and coalescence of microvoids at the silver-silver interface, thereby (slightly) lowering joint strengths compared to those utilizing lapped base metal surfaces. Silver joints fabricated using PM sputter-deposition were found to have more reproducible mechanical properties than those utilizing HHC deposition. The high purity of PM sputter-deposits is believed to contribute to the improved reproducibility of diffusion-welded-silver joints fabricated by this method.

3. Ambient-temperature creep rupture of diffusion-welded-silver interlayers joining maraging steel base metals was observed at applied tensile stresses as low as 17% of the ultimate tensile strength. Rupture times of diffusion-welded-silver joints were found to decrease with increasing base-metal surface roughness, interlayer thickness, and test temperature. However, joints fabricated using very thin interlayers between elastic base metals exhibited no appreciable increase in tensile strength or rupture times. Finite-element analysis of the stress state within the silver interlayer confirmed that only slight increases in triaxial constraint occur with decreasing interlayer thickness for very thin interlayers. The time-to-rupture appears to be controlled by the creep rate of silver near grain boundary interfaces in the interlayer, which is determined by the effective stress within the interlayer.

Plastic deformation causes cavity nucleation. Cavity nucleation continues with creep (time-dependent plasticity) of the silver interlayer until the concentration of nuclei is sufficiently high to lead to instabilities and eventual rupture. The microvoid nucleation and coalescence process leading to joint rupture occurs at both the silver-silver and at or near the silver-base-metal interfaces.

4. Creep rupture of diffusion-welded-silver joints may be accelerated by time-dependent plasticity in the base metal, resulting from the effective stress in the base metal near the interlayer. Plastic deformation of the base metal causes concomitant shear, or corresponding deformation in the soft interlayer, and rupture occurs by cavity nucleation and coalescence as with diffusion-welded-silver interlayers joining elastic base metals. These two processes are parallel mechanisms, and the faster one controls the rupture time of the interlayer. Further evidence for the "base-metal control" theory was provided by a finite-element analysis of plastic strain in the joint, whereby time-dependent plasticity (creep) of the base metal was shown to induce time-dependent plastic deformation of the interlayer, even though the interlayer alone had been modelled to deform in a time-independent manner.

5. Creep rupture has been confirmed in silver-interlayer joints prepared by processes other than those utilizing diffusion welding of physical-vapor-deposited interlayers. In the present study, creep ruptures were observed in joints fabricated by diffusion welding of electrodeposited-silver interlayers between plastic base metals, and also in joints utilizing brazed-silver interlayers between both plastic and elastic base metals. These findings also appear applicable to joints prepared with other soft interlayer materials.

REFERENCES

[1] J. T. Niemann, R. P. Sopher, and P. J. Rieppel, "Diffusion Bonding Below 1000 °F," Weld. J. **37** 337s–342s (1958).

[2] I. M. Barta, "Low Temperature Diffusion Bonding of Aluminum Alloys," Weld. J. **43** 241s–247s (1964).

[3] D. Hauser, P. A. Kammer, and J. H. Dedrick, "Solid-State Welding of Aluminum," Weld. J. **46** 11s–22s (1967).

[4] P. A. Kammer, R. E. Monroe, and D. C. Martin, "Further Studies of Diffusion Bonding Below 1000 °F," Weld. J. **48** 116s–124s (1969).

[5] C. L. Cline, "An Analytical and Experimental Study of Diffusion Bonding," Weld. J. **45** 481s–489s (1966).

[6] A. T. D'Annessa, "The Solid-State Bonding of Refractory Metals," Weld. J. **43** 232s–240s (1964).

[7] M. G. Nicholas and R. M. Crispin, "Diffusion Bonding Ceramics with Ductile Metal Interlayers," Proc. Inter. Conf. on Diffusion Bonding, R. Pearce, ed., Cranfield, U. K. (1987).

[8] B. Derby, "Zirconia/Metal Diffusion Bonds," Proc. Inter. Conf. on Diffusion Bonding, R. Pearce, ed., Cranfield, U. K. (1987).

[9] R. A. Morley and J. Caruso, "The Diffusion Welding of 390 Aluminum Alloy Hydraulic Valve Bodies," Weld. J. **59**, 29–34 (1980).

[10] C. H. Crane, D. T. Lovell, W. A. Baginsky, and M. G. Olsen, "Diffusion Welding of Dissimilar Metals," Weld. J. **46**, 23s–31s (1967).

[11] M. O'Brien, C. R. Rice, and D. L. Olson, "High Strength Diffusion Welding of Silver Coated Base Metals," Weld. J. **55**, 25–27 (1976).

[12] J. W. Dini, W. K. Kelley, W. C. Cowden, and E. M. Lopez, "Use of Electrodeposited Silver as an Aid in Diffusion Welding," Weld. J. **63**, 26s–34s (1983).

[13] J. L. Knowles and T. H. Hazlett, "High-Strength Low-Temperature Bonding of Beryllium and Other Metals," Weld. J. **49**, 301s–310s (1970).

[14] P. S. McLeod and G. Mah, "The Effect of Substrate Bias Voltage on the Bonding of Evaporated Silver Coatings," J. Vac. Sci. Technol. **11**, 119–121 (1974).

[15] G. Mah, P. S. McLeod, and D. G. Williams, "Characterization of Silver Coatings Deposited from a Hollow Cathode Source," J. Vac. Sci. Technol. **11**, 663–665 (1974).

[16] D. G. Williams, "Vacuum Coating with a Hollow Cathode Source," J. Vac. Sci. Technol. **11**, 374–377 (1974).

[17] E. R. Naimon, D. Vigil, J. P. Villegas, and L. Williams, "Adhesion Study of Silver Films Deposited from a Hot Hollow-Cathode Source," J. Vac. Sci. Technol. **13**, 1131–1135 (1976).

[18] E. R. Naimon, J. H. Doyle, C. R. Rice, D. Vigil, and D. R. Walmsley, "Diffusion Welding of Aluminum to Stainless Steel," Weld. J. **60**, 17–20 (1981).

[19] D. T. Larson and H. L. Draper, "Characterization of the Be-Ag Interfacial Region of Silver Films Deposited Onto Beryllium Using a Hot Hollow Cathode Discharge," Thin Solid Films **107**, 327–334 (1983).

[20] R. S. Rosen, D. R. Walmsley, and Z. A. Munir, "The Properties of Silver-Aided Diffusion Welds Between Uranium and Stainless Steel," Weld. J. **65**, 83s–92s (1986).

[21] J. W. Elmer, M. E. Kassner, and R. S. Rosen, "The Behavior of Silver-Aided Diffusion-Welded Joints under Tensile and Torsional Loads," Weld. J. **67**, 157s–162s (1988).

[22] J. Harvey, P. G. Partridge, and A. M. Lurshey, "Factors Affecting the Shear Strength of Solid State Diffusion Bonds Between Silver-coated Clad Al-Zn-Mg Alloy (Aluminum Alloy 7010)," Mater. Sci. Eng. **79**, 191–199 (1986).

[23] P. G. Partridge and D. V. Dunford, "On the Testing of Diffusion-Bonded Overlap Joints Between Clad Al-Zn-Mg Alloy (7010) Sheet," J. Mater. Sci. **22**, 1597–1608 (1987).

[24] D. V. Dunford and P. G. Partridge, "The Peel Strengths of Diffusion Bonded Joints Between Clad Al-Alloy Sheets," J. Mater. Sci. **22**, 1790–1798 (1987).

[25] P. G. Partridge and J. Harvey, "Process for the Diffusion Bonding of Aluminum Materials," UK Patent Application GB 2117691 A (1983).

[26] E. Orowan, J. F. Nye, and W. I. Cairns, Theoretical Research Report, Arman. Res. Dept. Min. of Supply, London, 16pp. (1945).

[27] E. Orowan, "Fracture and Strength of Solids," Reports on Progress in Physics, The Physical Society **12**, 185–231 (1948-49).

[28] E. Orowan, "Fundamentals of Brittle Behavior of Metals," in *Fatigue and Fracture of Metals*, John Wiley & Sons, NY, 139–167 (1952).

[29] N. Bredz, "Investigation of Factors Determining the Tensile Strength of Brazed Joints," Weld. J. **33**, 545s–563s (1954).

[30] W. G. Moffatt and J. Wulff, "Strength of Silver Brazed Joints in Mild Steel," Trans. AIME **209**, 442–445 (1957).

[31] N. Bredz and H. Schwartzbart, "Triaxial Tension Testing and The Brittle Fracture Strength of Metals," Weld. J. **35**, 610s–615s (1956).

[32] R. Z. Shron and O. A. Bakshi, "The Problem of Gauging the Strengths of Welded Joints in Which There is a Soft Interlayer," Weld. Prod. **9**, 19–23 (1962).

[33] W. G. Moffatt and J. Wulff, "Tensile Deformation and Fracture of Brazed Joints," Weld. J. **42**, 115s–125s (1963).

[34] O. A. Bakshi and A. A. Shatov, "The Stressed State in Welded Joints with Hard and Soft Interlayers," Weld. Prod. **13**, 13–19 (1966).

[35] H. J. Saxton, A. J. West, and C. R. Barrett, "Deformation and Failure of Brazed Joints—Macroscopic Considerations," Met. Trans. **2**, 999–1007 (1971).

[36] A. J. West, H. J. Saxton, A. S. Tetelman, and C. R. Barrett, "Deformation and Failure of Thin Brazed Joints—Microscopic Considerations," Met. Trans. **2**, 1009–1017 (1971).

[37] V. S. Golovchenko and B. A. Gololobov, "The Use of Silver as an Intermediate Layer for Joining Titanium to Other Metals," Weld. Prod. **18**, 55-57 (1971).

[38] R. A. Musin, V. A. Antsiverov, Y. A. Belikov, Y. V. Lyamin, and A. N. Solokov, "The Effects on the Strength of the Joint of the Thickness of the Soft Interlayer in Diffusion Welding," Automat. Weld. **32**, 38–40 (1979).

[39] E. A. Almond, D. K. Brown, G. J. Davies, and A. M. Cottenden, "Theoretical and Experimental Interlayed Butt Joints Tested in Tension," Int. J. Mech. Sci. **25**, 175–189 (1983).

[40] R. S. Rosen, "An Investigation of the Properties of a Silver-Aided Solid-State Bond Between Uranium and Stainless Steel," Lawrence Livermore National Laboratory Rept. UCRL-53458, Livermore, CA, 103 pp.(1983).

[41] T. J. Moore and K. H. Holko, "Solid-State Welding of TD-Nickel Bar," Weld. J. **49**, 395s–409s (1970).

[42] R. K. Waits, "Planar Magnetron Sputtering," in *Thin Film Processes*, J. L. Vossen and W. Kern, eds., Academic Press, Inc., Orlando, 564 (1978).

[43] R. Castro, R. Tricot, and D. Rousseau, "Creep of Austenitic Stainless Steels at Room Temperature," in *Steel Strengthening Mechanisms*, Climax Molybdenum Co., Greenwich, CN, 117-134 (1969) (in French).

[44] A. T. Kuhn and R. M. Trimmer, "Review of the Aqueous Corrosion of Stainless Steel — Silver Brazed Joints," Br. Corros. J. **17**, 4–8 (1982).

[45] T. Takemoto and I. Okamoto, "Effect of Composition on the Corrosion Behavior of Stainless Steels Brazed with Silver-Base Filler Metals," Weld. J. **64**, 300s–307s (1984).

[46] D. S. Fields and W. A. Backofen, "Determination of Strain-Hardening Characteristics by Torsion Testing," Proc. ASTM **57**, 1259–1272 (1957).

[47] M. E. Kassner, "The Rate-Dependence and Microstructure of High-Purity Silver Deformed to Large Strains Between 0.16 and 0.30 T_m," Metall. Trans., **20A**, 2001-2010 (1989).

[48] J. A. Thornton, "High Rate Thick Film Growth," Ann. Rev. Mater. Sci. **7**, 239–260 (1977).

[49] M. E. Kassner and J. J. Oldani, "High-Strain Steady-State Flow in Silver at Ambient and Near-Ambient Temperatures," Scripta Met. **22**, 41–46 (1988).

[50] C. W. Shaw, L. A. Shepard, and J. Wulff, "Plastic Deformation of Thin Brazed Joints in Shear," Trans. ASM **57**, 94–109 (1964).

[51] C. A. Colmenares, Lawrence Livermore National Laboratory, Livermore, CA, private communication (1986).

[52] E. R. Naimon, R. G. Kurtz, D. Vigil, and L. Williams, *Silver Films for Solid State Bonding*, Rockwell International, Rocky Flats Plant, Golden, CO, Report RFP-3125 (1981).

[53] W. M. Leher and H. Schwartzbart, "Static and Fatigue Strength of Metals Subjected to Triaxial Stresses," Proc. ASTM **60**, 610–626 (1960).

[54] E. P. Lautenschlager, B. C. Marker, B. K. Moore, and R. Wildes, "Strength Mechanism of Dental Solder Joints," J.Dent. Res. **53**, 1361–1367 (1974).

[55] H. J. Saxton, A. J. West, and C. R. Barrett, "The Effect of Cooling Rate on the Strength of Brazed Joints," Met. Trans. **2**, 1019–1028 (1971).

[56] R. M. Trimmer and A. T. Kuhn, "the Strength of Silver-Brazed Steel Joints—A Review," Brazing & Soldering **2**, 6–13 (1982).

[57] Z. Nisenholtz, J. Mironi, and N. Nir, "Diffusion Bonding of Stainless Steel 304L to Ti-6Al-4V Alloy," Proc. 3rd Inter. Conf. on Isostatic Pressing, London, UK (1986).

[58] R. S. Rosen and M. E. Kassner, Lawrence Livermore National Laboratory, Livermore, CA, unpublished results (1986).

[59] G. L. Goudreau and J. O. Hallquist, "Recent Developments in Large Scale Finite Element Hydrocode Technology," J. Comp. Meths. Appl. Mechs. Eng. **30**, 725-757 (1982).

[60] J. O. Hallquist, "NIKE2D: An Implicit, Finite Deformation, Finite Element Code for Analyzing the Static and Dynamic Response of Two-Dimensional Solids," Lawrence Livermore National Laboratory, Rept. UCRL-52678 Rev. 1 (1986).

[61] R. S. Rosen, S. Beitscher, and M. E. Kassner, "Stress Corrosion Cracking of Uranium-Silver Interfaces in Silver-Aided Diffusion Welds," *Proc. Inter. Conf. Environment-Induced Cracking of Metals,* Kohler, Wisconsin (1988).

[62] R. S. Rosen, Lawrence Livermore National Laboratory, Livermore, CA., unpublished results (1983).

[63] P. G. Shewmon, *Diffusion in Solids*, J. Williams, Jenks, OK (1983).

[64] A. C. F. Cocks and M. F. Ashby, "On Creep Fracture by Void Growth," Prog. Mater. Sci. **27**, 189-244 (1982).

[65] W. D. Nix, Mater. Sci. and Eng. **A103**, 103–110 (1988).

[66] R. W. Logan, R. G. Castro, and A. K. Mukherjee, "Mechanical Properties of Silver at Low Temperatures," Scripta Metall. **17**, 63–66 (1983).

[67] D. Turnbull and R. E. Hoffman, "The Effect of Relative Crystal and Boundary Orientations on Grain Boundary Diffusion Rates," Acta Metall. **2**, 419–426 (1954).

[68] P. Marshall, *Austenitic Stainless Steels: Microstructure and Mechanical Properties*, Elsevier Applied Science, London, 431 pp. (1984).

[46] D. S. Fields and W. A. Backofen, "Determination of Strain-Hardening Characteristics by Torsion Testing," Proc. ASTM **57**, 1259–1272 (1957).

[47] M. E. Kassner, "The Rate-Dependence and Microstructure of High-Purity Silver Deformed to Large Strains Between 0.16 and 0.30 T_m," Metall. Trans., **20A**, 2001-2010 (1989).

[48] J. A. Thornton, "High Rate Thick Film Growth," Ann. Rev. Mater. Sci. 7, 239–260 (1977).

[49] M. E. Kassner and J. J. Oldani, "High-Strain Steady-State Flow in Silver at Ambient and Near-Ambient Temperatures," Scripta Met. **22**, 41–46 (1988).

[50] C. W. Shaw, L. A. Shepard, and J. Wulff, "Plastic Deformation of Thin Brazed Joints in Shear," Trans. ASM **57**, 94–109 (1964).

[51] C. A. Colmenares, Lawrence Livermore National Laboratory, Livermore, CA, private communication (1986).

[52] E. R. Naimon, R. G. Kurtz, D. Vigil, and L. Williams, *Silver Films for Solid State Bonding*, Rockwell International, Rocky Flats Plant, Golden, CO, Report RFP-3125 (1981).

[53] W. M. Leher and H. Schwartzbart, "Static and Fatigue Strength of Metals Subjected to Triaxial Stresses," Proc. ASTM **60**, 610–626 (1960).

[54] E. P. Lautenschlager, B. C. Marker, B. K. Moore, and R. Wildes, "Strength Mechanism of Dental Solder Joints," J.Dent. Res. **53**, 1361–1367 (1974).

[55] H. J. Saxton, A. J. West, and C. R. Barrett, "The Effect of Cooling Rate on the Strength of Brazed Joints," Met. Trans. **2**, 1019–1028 (1971).

[56] R. M. Trimmer and A. T. Kuhn, "the Strength of Silver-Brazed Steel Joints—A Review," Brazing & Soldering **2**, 6–13 (1982).

[57] Z. Nisenholtz, J. Mironi, and N. Nir, "Diffusion Bonding of Stainless Steel 304L to Ti-6Al-4V Alloy," Proc. 3rd Inter. Conf. on Isostatic Pressing, London, UK (1986).

[58] R. S. Rosen and M. E. Kassner, Lawrence Livermore National Laboratory, Livermore, CA, unpublished results (1986).

[59] G. L. Goudreau and J. O. Hallquist, "Recent Developments in Large Scale Finite Element Hydrocode Technology," J. Comp. Meths. Appl. Mechs. Eng. **30**, 725-757 (1982).

[60] J. O. Hallquist, "NIKE2D: An Implicit, Finite Deformation, Finite Element Code for Analyzing the Static and Dynamic Response of Two-Dimensional Solids," Lawrence Livermore National Laboratory, Rept. UCRL-52678 Rev. 1 (1986).

[61] R. S. Rosen, S. Beitscher, and M. E. Kassner, "Stress Corrosion Cracking of Uranium-Silver Interfaces in Silver-Aided Diffusion Welds," *Proc. Inter. Conf. Environment-Induced Cracking of Metals,* Kohler, Wisconsin (1988).

[62] R. S. Rosen, Lawrence Livermore National Laboratory, Livermore, CA., unpublished results (1983).

[63] P. G. Shewmon, *Diffusion in Solids*, J. Williams, Jenks, OK (1983).

[64] A. C. F. Cocks and M. F. Ashby, "On Creep Fracture by Void Growth," Prog. Mater. Sci. **27**, 189-244 (1982).

[65] W. D. Nix, Mater. Sci. and Eng. **A103**, 103–110 (1988).

[66] R. W. Logan, R. G. Castro, and A. K. Mukherjee, "Mechanical Properties of Silver at Low Temperatures," Scripta Metall. **17**, 63–66 (1983).

[67] D. Turnbull and R. E. Hoffman, "The Effect of Relative Crystal and Boundary Orientations on Grain Boundary Diffusion Rates," Acta Metall. **2**, 419–426 (1954).

[68] P. Marshall, *Austenitic Stainless Steels: Microstructure and Mechanical Properties*, Elsevier Applied Science, London, 431 pp. (1984).

[69] A. Miller, "An Inelastic Constitutive Model for Monotonic, Cyclic, and Creep Deformation: Part II — Application to Type 304 Stainless Steel," Trans. ASME **98**, 106–113 (1976).

[70] E. Krempl, "An Experimental Study of Room-Temperature Rate Sensitivity, Creep and Relaxation of AISI Type 304 Stainless Steel," J. Mech. Phys. Solids **27**, 363–375 (1979).

[71] G. Mura, P. Olla, and P. F. Virdis, "Stress Relaxation of AISI 308 Stainless Steel Between 25 and 250 C," Avesta Stainless Bulletin **6**, 3–7 (1982).

[72] A. M. Eleiche, C. Albertini, and M. Montagnani, "The Influence of Strain-Rate History on the Ambient Tensile Strength of AISI Type 316 Stainless Steel," Nuclear Engineering and Design **88**, 131–141 (1985).

[73] M. G. Stoudt, and P. S. Follansbee, "Strain Rate Sensitivity, Strain Hardening, and Yield Behavior of 304L Stainless Steel," Trans. ASME **108**, 344-353 (1986).

[74] M. R. Lin, and R. H. Wagoner, "Effect of Temperature, Strain, and Strain Rate on the Tensile Flow Stress of I. F. Steel and Stainless Steel Type 310," Scripta Metall. **20**, 143–148 (1986).

[75] H. E. Boyer, ed., *Atlas of Stress-Strain Curves*, ASM International, 630 pp. (1987).

[76] Battelle Columbus Laboratories, eds., *Aerospace Structural Metals Handbook* **2**, Army Materials and Mechanics Research Center, Watertown, MA, (1979).

[77] G. A. Henshall, R. S. Rosen, M. E. Kassner, and R. G. Whirley, "Finite-Element Analysis of Interlayer Welds Loaded in Tension," Lawrence Livermore National Laboratory Rept. UCRL-102280, Livermore, CA, 38 pp. (1990), submitted to Weld. J.

[78] G. E. Dieter, *Mechanical Metallurgy*, McGraw-Hill, 751 pp. (1986).

[79] B. F. Dyson, "Continuous Cavity Nucleation and Creep Fracture," Scripta Metall. **17**, 31–37 (1983).

APPENDIX

A. Creep Rupture Test Data: Elastic Base Metals

Table A.1. Creep rupture data for diffusion-welded-silver joints using maraging steel.

Applied Tensile Stress, MPa	Base-Metal Surface Finish	Interlayer Thickness, μm	Test Temperature, °C	Creep Rupture Time, s	Percent Silver-Silver Fracture[a]
517	Machined	150	22	3.5E1	99
483	Machined	150	22	2.2E2	90
448	Machined	150	22	4.6E2	100
414	Machined	150	22	6.3E2	97
379	Machined	150	22	2.9E3	75
517	Machined	150	22	5.0E2	85
552	Machined	150	22	3.4E2	90
448	Machined	150	22	3.0E3	85
379	Machined	150	22	4.4E3	80
345	Machined	150	22	7.5E4	75
310	Machined	150	22	2.9E5	60
621	Machined	150	22	2.6E1	95
293	Machined	150	22	6.7E4	60
241	Machined	150	22	9.2E4	55
207	Machined	150	22	8.3E5	55
241	Machined	150	22	1.6E5	60
207	Machined	1000	22	2.1E4	0
276	Machined	1000	22	4.7E4	0
414	Machined	1000	22	3.3E1	100
207	Machined	150	22	2.0E6	70
172	Machined	150	22	1.5E7	70
207	Machined	150	72	1.3E4	70
207	Machined	150	72	7.0E4	75
207	Machined	150	72	5.2E4	80
293	Machined	150	72	1.9E3	85
293	Machined	150	72	2.6E3	85
293	Machined	150	72	6.2E2	80

Table A.1. (Continued)

Applied Tensile Stress, MPa	Base-Metal Surface Finish	Interlayer Thickness, μm	Test Temperature, °C	Creep Rupture Time, s	Percent Silver-Silver Fracture[a]
379	Machined	150	72	1.3E2	95
138	Machined	150	72	3.5E5	55
103	Machined	150	72	7.5E5	45
138	Machined	150	22	1.3E7	60
276	Machined	150	22	2.9E5	(b)
276	Machined	150	22	2.9E5	75
124	Machined	150	22	1.2E7	(b)
448	Machined	150	72	5.0E1	92
62	Machined	150	72	1.6E7	(c)
110	Machined	150	22	1.6E7	50
483	Lapped	150	22	9.5E3	85
621	Lapped	150	22	1.0E3	80
345	Lapped	150	22	1.1E6	75
276	Lapped	150	22	3.6E6	75
689	Lapped	150	22	1.7E2	96
758	Lapped	150	22	4.0E0	97
414	Lapped	150	22	7.4E4	10
689	Lapped	150	22	3.0E0	8
552	Lapped	150	22	1.1E3	(b)
552	Lapped	150	22	1.1E3	85
758	Lapped	150	22	2.7E0	10
689	Lapped	50	22	1.5E1	20
552	Lapped	50	22	9.9E2	25
448	Lapped	50	22	1.2E4	50
379	Lapped	50	22	6.5E4	98
310	Lapped	50	22	6.5E5	99

[a] Refers to diffusion-welded-silver interface; remainder of fracture occurred ~1 μm from the silver-base-metal interface.

[b] Removed from load and examined for microvoids.

[c] Plotted as of December 1, 1989.

B. Creep Rupture Data: Plastic Base Metals

Table B.1. Creep rupture data for diffusion-welded-silver joints using cold-worked SS.[a]

Applied Tensile Stress, MPa	Base-Metal Surface Finish	Plastic Strain in Gage Section, %	Plastic Strain Near Interface, %	Creep Rupture Time, s	Percent Silver-Silver Fracture[b]
362	Machined	0.9	2.1	2.7E1	50
276	Machined	0.0	0.7	1.2E6	80
345	Machined	0.7	1.5	1.1E3	90
362	Machined	1.1	2.0	1.0E2	100
293	Machined	0.0	1.6	7.3E5	75
328	Machined	0.4	1.8	1.4E4	80
310	Machined	0.1	2.2	8.9E4	75
328	Machined	0.4	2.1	8.8E3	80
310	Machined	0.1	1.3	1.2E5	80
293	Machined	0.0	1.3	1.4E6	96
345	Machined	0.6	2.2	8.6E2	70
283	Machined	0.0	1.4	4.1E6	75
207	Machined	0.0	(c)	2.5E7	(c)
362	Machined	1.6	4.2	6.5E2	90
379	Machined	1.9	2.3	3.2E1	97
207	Machined	0.0	1.5	1.2E6	45
224	Machined	0.0	1.5	8.2E6	60
259	Machined	0.0	1.8	9.0E5	65
241	Machined	0.0	1.4	2.6E6	65
276	Machined	0.0	1.9	1.2E2	70
283	Machined	0.0	1.7	1.1E6	65
190	Machined	0.0	2.1	3.2E6	60
172	Machined	0.0	0.2	2.9E7	70
155	Machined	(d)	(d)	2.2E7	(d)
352	Lapped	0.4	1.8	6.6E3	10
379	Lapped	1.8	2.2	7.3E1	0

[a] Tested at 22 °C.

[b] Refers to diffusion-welded-silver interface.

[c] Removed from load and examined for microvoids.

[d] Plotted as of December 1, 1989.

Table B.2. Creep rupture data for diffusion-welded-silver joints using annealed SS.[a]

Applied Tensile Stress, MPa	Test Temperature, °C	Plastic Strain in Gage Section, %	Plastic Strain Near Interface, %	Creep Rupture Time, s	Percent Silver-Silver Fracture[b]
145	22	0.2	3.0	1.0E7	25
207	22	0.7	3.8	5.8E2	50
155	22	0.2	2.9	9.9E5	35
207	22	0.9	3.6	5.4E3	55
190	22	0.7	3.6	3.4E4	35
155	22	0.2	3.6	1.7E6	15
190	22	0.7	3.1	4.2E4	15
190	22	0.6	3.9	9.9E3	45
172	22	0.4	3.5	1.4E5	20
172	22	0.4	3.1	1.2E5	25
207	22	0.7	3.7	5.4E2	20
241	22	1.9	3.8	2.7E2	90
259	22	2.3	4.2	6.1E1	85
207	22	1.0	3.8	8.1E3	25
155	22	0.3	3.1	3.2E6	25
259	22	2.6	3.3	2.8E2	80
172	22	0.4	3.2	2.0E5	45
145	22	0.3	3.0	1.3E7	35
224	22	1.1	3.5	2.6E2	80
224	22	1.1	3.8	3.1E2	30
138	22	0.2	0.2	2.5E7	0
190	22	0.8	3.2	8.9E4	50
172	22	0.4	3.9	2.3E5	40
145	72	0.3	3.3	5.1E4	10
145	72	0.4	3.9	3.4E4	25
172	72	0.6	2.3	3.0E3	30
172	72	0.6	4.1	1.4E3	20
145	72	0.3	4.2	6.7E4	25
172	72	0.5	2.2	2.3E3	20
155	22	0.3	3.4	7.4E6	25

[a] Machined base-metal surfaces.

[b] Refers to diffusion-welded-silver interface.

C. Creep Rupture Data: Other Interlayers

Table C.1. Creep rupture data for brazed-silver joints.[a]

Applied Tensile Stress, MPa	Type of Base-Metal Deformation[b]	Base-Metal Surface Finish	Interlayer Thickness, μm	Creep Rupture Time, s	Percent Silver-Steel Fracture[c]
310	Elastic	Machined	150	1.4E3	100
241	Elastic	Machined	150	8.5E3	100
276	Elastic	Lapped	150	2.0E4	100
190	Elastic	Machined	150	4.6E6	(d)
207	Plastic	Machined	150	1.0E0	100
207	Plastic	Machined	150	3.2E0	100
224	Plastic	Machined	150	1.0E0	100
190	Plastic	Machined	150	1.7E3	100
172	Plastic	Machined	150	4.6E3	100
155	Plastic	Machined	150	6.6E6	(d)
190	Plastic	Machined	150	1.1E3	100
172	Plastic	Machined	150	1.9E6	100
155	Plastic	Machined	150	2.1E6	(d)

[a] Tested at 22 °C.

[b] Elastic: maraging steel; plastic: annealed type 304 stainless steel.

[c] Refers to both silver-steel fractures and silver-silver fractures less than 1 μm from the base-metal interface.

[d] Plotted as of December 1, 1989.

Table C.2. Creep rupture data for diffusion-welded-silver (electrodeposited) joints.[a]

Applied Tensile Stress, MPa	Base-Metal Surface Finish	Interlayer Thickness, μm	Test Temperature, °C	Creep Rupture Time, s	Percent Silver-Silver Fracture[b]
276	Machined	150	22	5.8E3	50
276	Machined	150	22	6.8E3	40
241	Machined	150	22	6.4E4	100
241	Machined	150	22	7.1E4	90

[a] Joints fabricated between uranium and hot-rolled type 304 stainless steel base metals.

[b] Refers to diffusion-welded-silver interface; remainder of fracture occurred at the silver-uranium interface.